Growth and Investigations of Rare Earth doped Orthovanadate Laser Host Single Crystals

By
Mohammad Soharab
Enrolment No: PHYS03201604006

Raja Ramanna Centre for Advanced Technology
Indore-452013, India

A thesis submitted to the
Board of Studies in Physical Sciences

In partial fulfillment of requirements
for the Degree of
DOCTOR OF PHILOSOPHY
of
HOMI BHABHA NATIONAL INSTITUTE

March, 2021

Homi Bhabha National Institute[1]

Recommendations of the Viva Voce Committee

As members of the Viva Voce Committee, we certify that we have read the dissertation prepared by **Mohammad Soharab** entitled "**Growth and Investigations of Rare Earth doped Orthovanadate Laser Host Single Crystals**" and recommend that it may be accepted as fulfilling the thesis requirement for the award of Degree of Doctor of Philosophy.

Chairman - Dr. Arup Banerjee, RRCAT, Indore	Arup Banerjee, 02/09/2021
Guide / Convener/ Member 1- Dr. A.K. Karnal, RRCAT, Indore	2/9/2021
Examiner - Prof. A. Thamizhavel, TIFR, Mumbai	2 Sep 2021
Member 2- Dr. Tapas Ganguli, RRCAT, Indore	02/09/2021
Member 3- Dr. S.M. Gupta, RRCAT, Indore	2/9/2021
Member (Ext.) 4- Dr. S. Ganesamoorthy, IGCAR, Kalpakkam	S. Ganesamoorthy 2/9/21

Final approval and acceptance of this thesis is contingent upon the candidate's submission of the final copies of the thesis to HBNI.

I hereby certify that I have read this thesis prepared under my direction and recommend that it may be accepted as fulfilling the thesis requirement.

Date: 2/9/2021

Place: Indore

2/9/2021

Dr. A.K. Karnal

Guide

[1] This page is to be included only for final submission after successful completion of viva voce.

STATEMENT BY AUTHOR

This dissertation has been submitted in partial fulfillment of requirements for an advanced degree at Homi Bhabha National Institute (HBNI) and is deposited in the Library to be made available to borrowers under rules of the HBNI.

Brief quotations from this dissertation are allowable without special permission, provided that accurate acknowledgement of source is made. Requests for permission for extended quotation from or reproduction of this manuscript in whole or in part may be granted by the Competent Authority of HBNI when in his or her judgment the proposed use of the material is in the interests of scholarship. In all other instances, however, permission must be obtained from the author.

Mohammad Soharab

Mohammad Soharab

DECLARATION

I, hereby declare that the investigation presented in the thesis has been carried out by me. The work is original and has not been submitted earlier as a whole or in part for a degree / diploma at this or any other Institution / University.

Mohammad Soharab

Mohammad Soharab

List of Publications arising from the thesis

A. International Journals

1. "Effect of Yb doping on the crystal structure, polarization dependent optical absorption and photoluminescence of Yb:YVO_4 single crystal grown by optical floating zone technique" M. Soharab, Indranil Bhaumik, R. Bhatt, A. Saxena, A.K. Karnal, S. Satapathy, P.K. Gupta, *Journal of Alloys and Compounds*, **2015**, *649*,766-771.
2. "Effect of Yb doping on the refractive index and thermo-optic coefficient of YVO_4 single crystals" M. Soharab, Indranil Bhaumik, R. Bhatt, A. Saxena, A. K. Karnal, and P. K. Gupta, *Applied Optics,* **2017**, *56*, 1682-1688.
3. "Effect of Yb co-doping on the spectral properties of Er:YVO_4 single crystal: A Judd-Ofelt analysis", M. Soharab, Indranil Bhaumik, R. Bhatt, A. Saxena, A.K. Karnal, *Journal of Luminescence*, **2018**, *200*, 280-286.
4. "Effect of Nd doping on the refractive index and thermo-optic coefficient of $GdVO_4$ single crystals", M. Soharab, Indranil Bhaumik, R. Bhatt, A. Saxena, A.K. Karnal, *Applied Physics B*, **2019**, *125*, 84-98.
5. "Spectroscopic properties and Judd-Ofelt analysis of Nd doped $GdVO_4$ single crystals grown by OFZ method", M. Soharab, Indranil Bhaumik, R. Bhatt, A. Saxena, S. Khan, A.K. Karnal, *Optical Materials,* **2019**, *92*, 379-385.
6. "Anomalous effect of growth ambience on the optical absorption characteristics of Cr-co-doped Nd:YVO_4 crystal", Indranil Bhaumik", M. Soharab, R. Bhatt, A. Saxena, Kamlesh Gupta, A.K Karnal, *Applied Physics A*, **2019**, *125*, 347-356.
7. "Growth and optical investigation of Nd co-doped Yb:YVO_4 crystal: A promising material for laser gain medium", M. Soharab, Indranil Bhaumik, R. Bhatt, A. Saxena, S. Khan, A. Sagdeo, A.K. Karnal, *Optical Materials,* **2020**, *109*, 110183-110190.
8. "Investigation of optical and spectroscopic properties of Nd co-doped Yb:YVO_4 single crystals grown by OFZ method", M. Soharab, Indranil Bhaumik, R. Bhatt, A. Saxena, S. Khan. U. K. Goutam, A.K.

Karnal, *Journal of Luminescence*, **2021,** *231*, 117736-117743.

9. "Unusual absorption and emission characteristics of Cr co–doped Nd:$GdVO_4$ laser gain crystal", M. Soharab, Indranil Bhaumik, R. Bhatt, A. Saxena, A.K. Karnal, *Journal of Alloys and Compounds*, **2021,** *886*, 161182-161188.

B. AIP Conference Proceedings

10. "Growth and investigation of Nd doped $GdVO_4$ single crystals grown by OFZ technique", M. Soharab, Indranil Bhaumik, R. Bhatt, A. Saxena, A. K. Karnal, and P. K. Gupta, *AIP Conference Proceedings*, **2017,** *1832*, 100018.
(The work was selected for oral presentation and awarded BEST POSTER in DAE-SSPS 2016.)

11. "Fabrication of "a-cut" laser element from in-house grown Nd doped $GdVO_4$ crystals and demonstration of lasing, M. Soharab, Indranil Bhaumik, R. Bhatt, A. Saxena, A.K. Karnal , A.J. Singh, S.K. Sharma, C. Mukherjee, K. Rajiv and M.P. Kamath, *AIP Conference Proceedings*, **2020,** *2265*, 030416.

C. Conference/Symposium

1. "Growth of 1.0 at.% Nd doped $GdVO_4$ single crystal and lasing performance of fabricated c-cut element", M. Soharab, Indranil Bhaumik, R. Bhatt, A. Saxena, A.K. Karnal, A.J. Singh and S.K. Sharma, *27th DAE-BRNS National Laser Symposium (NLS-27)*, **2018,** RRCAT, Indore, Dec., 3-6.
2. "Effect of Nd doping concentration on the absorption and emission properties of Nd: $GdVO_4$ single crystals for laser application", M. Soharab, Indranil Bhaumik, R. Bhatt, A. Saxena and A.K. Karnal, *26th DAE-BRNS National Laser Symposium (NLS-26)*, **2017**, at Bhabha Atomic Research Centre, Mumbai, Dec. 20-23.
3. "Growth and investigation of thermo-optic coefficient of Yb doped

YVO_4 single crystal", M. Soharab, Indranil Bhaumik, R. Bhatt, A. Saxena, A.K. Karnal and P.K. Gupta, *20th National Seminar on Crystal Growth and Applications,* **2016**, BARC Mumbai, Jan. 19-21.

4. "Effect of Yb co-doping on spectroscopic properties of Er:YVO_4 single crystals grown by optical floating zone technique", M. Soharab, Indranil Bhaumik, R. Bhatt, A. Saxena, A.K. Karnal and P.K. Gupta, *24th National Laser Symposium (NLS-26),* **2015**, RRCAT, Indore, Dec. 2-5.
5. "Effect of Er and Cr co-substitutions on the transmission property of Yb:YVO_4 crystal grown by OFZ technique", M. Soharab, Indranil Bhaumik, R. Bhatt, A. Saxena, A.K. Karnal and P.K. Gupta, *60th DAE SSPS,* **2015**, Amity University, Noida, Dec. 21-25.

Mohammad Soharab

Mohammad Soharab

Name & Signature of the student

DEDICATIONS

I dedicate this Thesis to

My Parents and

Wife

ACKNOWLEDGEMENTS

First, I would like to express my sincere heartfelt gratitude and regards to my Supervisor Dr. A.K. Karnal for his excellent guidance, expert suggestions and continuous cooperation during the research work. I would never be able to forget his affectionate and friendly behavior towards me.

I place my deep sense of gratitude towards Dr. Indranil Bhaumik for suggestions and guidance through various stages of difficulty during my Ph.D work and his valuable discussion related my research work.

I would like to give extremely thank to Dr. Rajeev Bhatt for continuous support and valuable guidance during this Ph.D work.

I am also thankful to Mr. Amit Saxena for his help during the single crystal growth process. I am also grateful to Mr. S.R. Bagade and Kum. Ratna Kumari Karn for their help for the preparation of the feed rods and synthesis of materials during the experiment. I would like to thank Mr. B.K Sajith and Mr. M.K Sharma for their helps throughout my research work.

I am grateful to Dr. Gurvinderjit Singh and Mr. Prem Kumar, LFMD for helping me to carry out the XRD experiments. I am also grateful to Dr. S. Satapathy for his help in carrying out the PL measurements. I deeply thanks to Shri Amarjeet Singh for help and support for testing of lasing of grown crystals and Dr. Salahuddin Khan for helping the fluorescence life measurements. I also put my regards to Shri M.P. Kamath, Shri Y. Pawan Kumar, Dr. Chandrachur Mukherjee, and Shri Rajiv Kamparath for doing the optical polishing and antireflection coating on the laser elements.

I am thankful to Dr. M.K. Tiwari, Kum. Ayushi Trivedi, Mr. Ajit and Mr. Ajay for the XRF experiments on BL-16 and to Dr. A.K. Sinha, Dr. (Smt.) Archna Sagdeo for

helping me in carrying out the Rocking curve experiments in Indus-2 BL-12. I am also grateful to Shri Uttam Kumar Goutam for facility the XPS measurement at BL-14 of Indus- 2.

I am also thankful to all the members of the Doctoral Committee for their fruitful motivation and valuable suggestions.

I place lots of thank to my friends, my colleagues and beloved family who always provided unlimited moral support without which I could not have made this Ph.D work a success.

Finally, I thank Almighty for all His blessings and the successful completion of this research work.

Mohammad Soharab

Mohammad Soharab

Table of Contents

Summary of Thesis

The thesis presents a systematic study of the growth of RE doped orthovanadate single crystals e.g. YVO_4, $GdVO_4$ and $LuVO_4$ by optical floating zone (OFZ) technique for laser application. The growth challenges such as, the presence of secondary phase due to volatile nature of V_2O_5, melt overflow problem, bubble & core formation, low angle grain boundary and cracking of crystals have been overcome by optimizing the process parameters. The oriented elements have been fabricated from the grown crystals and subjected to various characterization.

In Yb doped YVO_4 the absorption studies depict that the absorption cross-section at 952, 972 and 985 nm is maximum at ~3 at.% of Yb doping and beyond this it decreases due to quenching. The emission spectra depicts higher PL intensity at 1010 nm for excitation at 952 and 972 nm in comparison to that at 985 nm. The refractive index (RI) studies show that extraordinary RI (n_e) varies marginally in comparison to ordinary RI (n_o) as the doping concentration of Yb is increased. The thermo-optic coefficient (dn/dT) of Yb:YVO_4 crystal is one order higher than that of undoped YVO_4. The Yb co-doped Er:YVO_4 have been grown to study the effect of Yb doping on the pumping efficiency of Er:YVO_4. It was observed from the absorption, emission and Judd-Ofelt (JO) analysis that Yb co-doping of Er:YVO_4 is helpful in achieving efficient pumping and hence acts as a good sensitizer. Also, the JO analysis reveals that the value of spectroscopic quality factor of Er:YVO_4 improves with Yb doping but remains invariant with increasing Yb concentration. The radiative lifetime and emission cross-section of $^4I_{13/2} \rightarrow {}^4I_{15/2}$ transition of Er ions was also found to be independent of Yb doping concentration. In addition, Nd co-doped Yb:YVO_4 single crystals have been grown for the first time by using OFZ method to the best of our knowledge. PL study reveals that Nd^{3+} ion effectively excites the Yb^{3+} ion in YVO_4. The measured fluorescence life-time of Nd and Yb in Nd (0.8 at.%)co-doped Yb(0.8 at.%):YVO_4 crystal is around 66 and 581 μs, respectively with energy transfer efficiency ~35%.

In Nd doped $GdVO_4$ crystals the spectroscopic properties have been evaluated by JO analysis using polarized absorption spectra. Spectroscopic quality factor was found to be maximum for 0.8 at.%Nd doped $GdVO_4$ crystals. The emission study shows that PL intensity at 1062 nm increases with the doping concentration of Nd up to 0.8 at.% and beyond that it decreases. Also, the fluorescence life-time ~ 101 μs was found maximum for 0.8 at.% of Nd doping indicating optimum concentration of Nd in $GdVO_4$ is 0.8 at.%. RI measurements crystals depict slight variation in n_e with Nd doing whereas a significant change was observed in n_o within the measurement limits. Further, *c*- and *a*-oriented elements have been fabricated from the grown Nd:$GdVO_4$ crystals and CW laser emission at 1064 nm was demonstrated. The laser output power for *c*-oriented element was 2.7 W at 11.2 W of incident pump power with slope efficiency ~ 39%. The laser output power for *a*-oriented element was 4.57 W at 11.94 W of incident pump power with slope efficiency ~ 49.7%. In addition, Cr co-doped Nd:$GdVO_4$ crystals were also grown to study for self Q-switching application. The absorption spectra show multiple peaks due to Nd^{3+}ion and a broad peak centred at 1100 nm due to Cr^{5+} ion. It was observed that the lower concentration of Cr exhibits larger absorption whereas the higher concentration have smaller absorption for Cr^{5+} ion when grow at lower oxygen ambience (10%). The saturation absorption characteristics of Nd:Cr:$GdVO_4$ was evaluated by recording intensity dependent transmittance. An increase of transmission from 0.57 to 0.66 (9%) was observed for an incident power of 200 mW at 1064 nm. The increase in transmittance is attributed to saturation of absorption of the Cr^{5+} ions at 1064 nm that give rise to self-passive Q-switching phenomenon.

Finally, Nd:$LuVO_4$ crystals have been evaluated for the absorption and emission characteristics. A strong absorption band is observed at 810 nm which can be used for pumping to the Nd:$LuVO_4$ gain medium. The emission spectra show highest emission at 1065 nm for both excitation at 810 and 880 nm. The lasing has been demonstrated at 1066 nm from fabricated elements with output power of 360 mW from 13.6 W of pump power with slope efficiency ~ 32%.

List of Figures

List of Tables

Chapter-1 Introduction and Motivation

Most of solid materials possess crystalline structure that means spatial periodicity and translation symmetry. Single crystals find applications in several important areas in scientific and technological domains due to their superior optical, thermal, electrical, mechanical, and other properties. Hence, the growth of innovative and technologically important materials in the form of single crystals is essential for the development of science & technology and the related applications such as integrated optics, solid state laser, microelectronics, optical communication, radiation detection, nuclear imaging, drug designing etc. [1-2]. The growth of high-optical quality laser host single crystals and their characterization towards the fabrication of laser gain medium and the development of solid-state lasers have attracted great impetus due to their important applications in medical eg. eye surgery, skin therapy, cancer treatment; defense communication; industries, etc., and other applied research [1-2].

1.1 Introduction to the laser host single crystals

Single crystal laser gain mediums are attractive and worth full choice for making the solid-state lasers [1,2]. Although a wide variety of lasers exist, but the solid-state lasers are better choice because these are more efficient, rugged, compact and easy to use. This has motivated a great deal of R&D on the synthesis of solid-state gain medium such as garnet, orthovanadate, molybdates, tungstate, phosphate, etc., with improved performance [1-2].The laser operation of any crystal depends on the optical properties of material, which have energy levels of a particular doped ion, between which electrons or atoms can do transitions. Usually these energy levels arise due to the doping of impurity ions in the laser host crystal. Once an impurity ion is doped in the laser host, a

very large number of energy levels are created due to the crystals field of host. Therefore, the pumping in gain medium and laser processes in a particular laser systems, have a complex excitation processes and cascaded relaxation processes among all available energy levels. The laser operation of an actual laser material can be properly described by different energy level diagram. The main features can be understood through the familiar three-level and four-level idealizations. The three-level and four-level diagram are shown in the following Figure 1.1 to understand the laser operation.

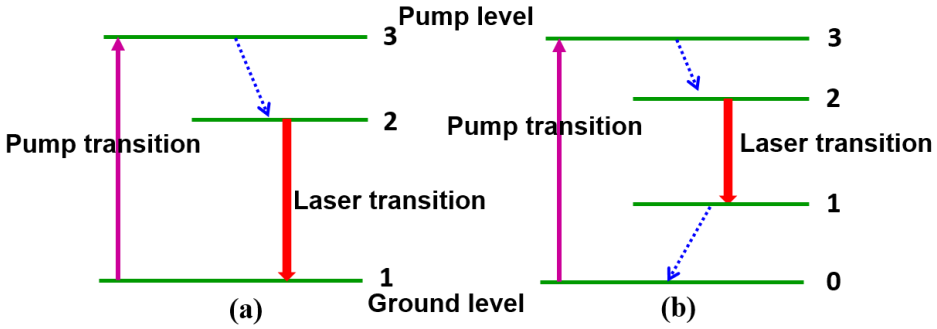

Figure 1.1 Energy levels of three and four level laser system

The population inversion in the excited level is essential for starting the laser action. Initially all ions or atoms of the laser material for three-level or four-level laser system, are present in the ground level i. e. 1 of (a) or 0 of (b). The energy level 3 of ions are populated by pumping source via stimulated absorption mechanism. The excited ions come down to the intermediate level 2 by fast non-radiative transition. This intermediate level 2 also called metastable level, has long fluorescence life-time. Finally, all the ions present in the energy level 2 returns to the energy level 1 by stimulated emission of photon. This stimulated emission transition is only responsible for the starting the laser action under essential conditions [1-2].The laser action is started when the pumping power is above the laser threshold power and ions from the

long-lived energy level (level 2) decay by stimulated as well as spontaneous emission. The laser output is obtained when the stimulated radiation is dominant.

In the three-level laser system high-intensity source is required for pumping because the laser transition in gain medium takes place between the metastable energy level 2 and the final ground energy level 1, the lowest energy level of the system with high population which leads to low efficiency. In case of the four-level laser system the stimulated or pump absorption transition occurs from the ground state (level 0) to the energy level 3. The excited atoms in level 3 will proceed rapidly to the level 2 as in the case of the three-level system. But in the four-level laser system, laser transition takes place between the excited laser level 2 and the level 1 and the energy level 1 of the system is not highly populated and hence in this case population inversion occurs even at low pump power and high pump rate. Therefore, such a laser system offers high efficiency. Further, the ions in level 1 undergoes a non-radiative transition to the ground level via rapid non-radiative transition [1,2]. Therefore, four level laser system have less threshold value compared to three level laser system for any lasers.

Further, the solid-state laser consists of three components: (i) an active medium having energy levels that can be selectively populated by excitation, (ii) an optical pumping source to excite the active medium and to produce the required population inversion between some of the energy levels and (iii) a resonant electromagnetic cavity that contains the active medium and provides feedback to amplify and maintain the coherence of the emitted light. Therefore, the active medium or laser gain medium is one of the important component for achieving the laser action. The lasing properties of gain medium depend on the materials. The energy level present in the active medium are decided by the active ion, which are being doped into the active medium. Hence,

the materials used as active medium and doped active ion in the gain medium are very important for designing and developing laser system.

1.2 Materials characteristics for laser gain medium

The materials used as laser gain medium, should have strong absorption bands, sharp fluorescent lines, long fluorescence lifetime and reasonably high quantum efficiency for desired transitions. The above properties of materials are generally found in the solid materials with incorporation of some impurity elements, or dopant ion, into the laser host. The dopant ions are called active ion and the energy levels of active ions are created due to the crystal field of the host and responsible for the optical transitions between these energy levels for the laser operation. The active ions, doped in the crystalline hosts, replace some of the sites of the host lattice. There are several parameters, which decides the compatibility of the active ion and crystalline host, such as ionic sizes, valency of ions and spectral properties of the crystal host and type of doped active ion. Therefore, a few active ion and host material-combinations are used for efficient laser operation. Therefore, the properties of host materials and active ions for making the efficient laser gain medium are given in the next section.

1.2.1 Host materials

The solid-state laser host materials may generally be classified into two categories, the crystalline and non-crystalline solid materials. The several crystalline host materials have been investigated for solid-state laser applications after the discovery of first ruby laser. There are several advantages of crystalline laser hosts materials as compared to the other form of materials like glasses (non-crystalline solids). The crystalline laser host materials exhibit higher thermal conductivity,

narrower fluorescence linewidths, and better optical properties. Important key points for choosing a suitable crystalline host materials for laser applications are [1,2]:

1. The optical properties of the crystal host should be favorable as per the requirement of laser operation. In this regards the refractive index of crystal host should not vary in the crystal and with the temperature of crystal, otherwise it leads to inhomogeneous propagation of light through the crystal. The absorption by host at lasing and pump wavelengths should be minimum.

2. The mechanical and thermal properties of the crystal host should be such that it allows the operation at high-average power without damaging the crystal. Many important parameters such as high thermal conductivity, high hardness and high fracture strength of laser host governs the output power of the medium. In addition to this, the thermal expansion and stress optic coefficient of the host must be small to avoid the lensing effect in the anisotropic crystals.

3. The crystal structure and lattice sites of laser host should be such that dopant active ions can accommodate in the lattice site, and the host ions produce local crystal fields of symmetry for generating the desired spectroscopic properties.

4. The chemical stability of the host medium is also important property for minimizing the radiation-induced color centers.

5. The smooth fabrication of laser host is also one of important considerations during the development of solid state-laser.

There are few important and popular host materials such as $Y_3Al_5O_{12}$ (YAG), $YAlO_3$, orthovanadate (YVO_4, $GdVO_4$ and $LuVO_4$, etc.) $YLiF_4$ (YLF), tungstates [$KGd(WO_4)_2$ and $KY(WO_4)_2$] for solid state laser applications.

1.2.2 Active ions

The selection of suitable active ions is important for laser gain medium. Hence the following properties must be considered at time of choosing the active ions [2]:

1. The active ions should have efficient absorption at pumping wavelength.

2. There should be efficient internal conversion of excited ions to metastable state from the excited energy level and also, it should have minimum quantum defect.

3. The radiative emission cross-section of active ions at lasing wavelength should be maximum and it should have high quantum efficiency.

4. The active ion should not have any absorption at lasing wavelength neither-ground state nor excited state.

The rare earth and transition metals elements are important candidates for the laser applications. The lanthanide ions are naturally excellent species and act as an active ions in solid-state laser materials because they show sharp fluorescent transitions in the wide range from the ultraviolet region to the near-infrared region of the electromagnetic spectrum [1–4].

1.3 Literature survey and selection of material as a laser gain medium

In the field of solid-state laser, there are various laser host materials as mentioned in the previous section. Among these, the rare earth ($Yb^{3+,}$ Nd^{3+}, Er^{3+}, etc.)

doped orthovanadate single crystals such as YVO_4, $GdVO_4$, $LuVO_4$, etc. have attracted considerable attention due to their long fluorescence lifetime, low threshold, large emission cross section and high absorption coefficient [1–3,5–14]. The development of laser diode (LD) creates effective and tunable pumping in the solid-state lasers. Recently, solid state lasers with an emission wavelength of near ~ 1 μm and its second harmonic generation (SHG) are progressing toward the practical use in various applications such as industry and medical treatment [15].

Further, multiple doping in the laser host orthovanadate also plays crucial role to increase the functionality and the efficiency of the gain medium. Therefore, different co-dopant are doped in the gain medium and these are being investigated for sensitizer application and development of the functionality in the gain medium such as, self Q-switching, self-mode locking, self-frequency-doubling and self-Raman conversion [16]. As an example, when Er^{3+} doped gain medium is co-doped with Yb^{3+} ions, the efficiency of pumping of Er^{3+} ions can be increased due to the strong absorption band of Yb [17,18]. Similarly, co-doping of Cr^{5+} ion in the gain medium, with strong absorption band at ~ 1 μm, can be utilized for generating pulsed lasers directly by self Q-switching mechanism [19,20].

1.3.1 Yttrium orthovanadate (YVO_4) laser gain medium

Among the orthovanadates, the yttrium orthovanadate (YVO_4) single crystals are widely investigated as a promising and an excellent laser host material for the last two to three decades. YVO_4 single crystals have attractive physical properties for polarizers, gas sensors, phosphors and laser applications (with trivalent, rare earth ion doping) [8–10,21]. The attractive properties being larger birefringence [22,23], higher damage threshold and ease of processing as compared with other birefringent crystals

namely, $LiNbO_3$, $CaCO_3$ and TiO_2 [8,21,23–31]. Further, YVO_4 has high chemical stability and wide optical transparency (340–5000 nm) [14,15]. YVO_4 has been utilized for light communications [15,16], light isolator and light circulator applications [14,15]. The yttrium orthovanadate (YVO_4) crystals have tetragonal zircon type crystal structure with space group D_{4h}^{19}- $I4_1/amd$ and four formula units per unit cell [32,33][Figure 1.2-1.4]. The tetragonal zircon type structure of YVO_4 shows significant anisotropy in the various properties like optical absorption, refractive indices, thermal conductivity and thermal expansion coefficients and direction dependent growth rate [34,35].

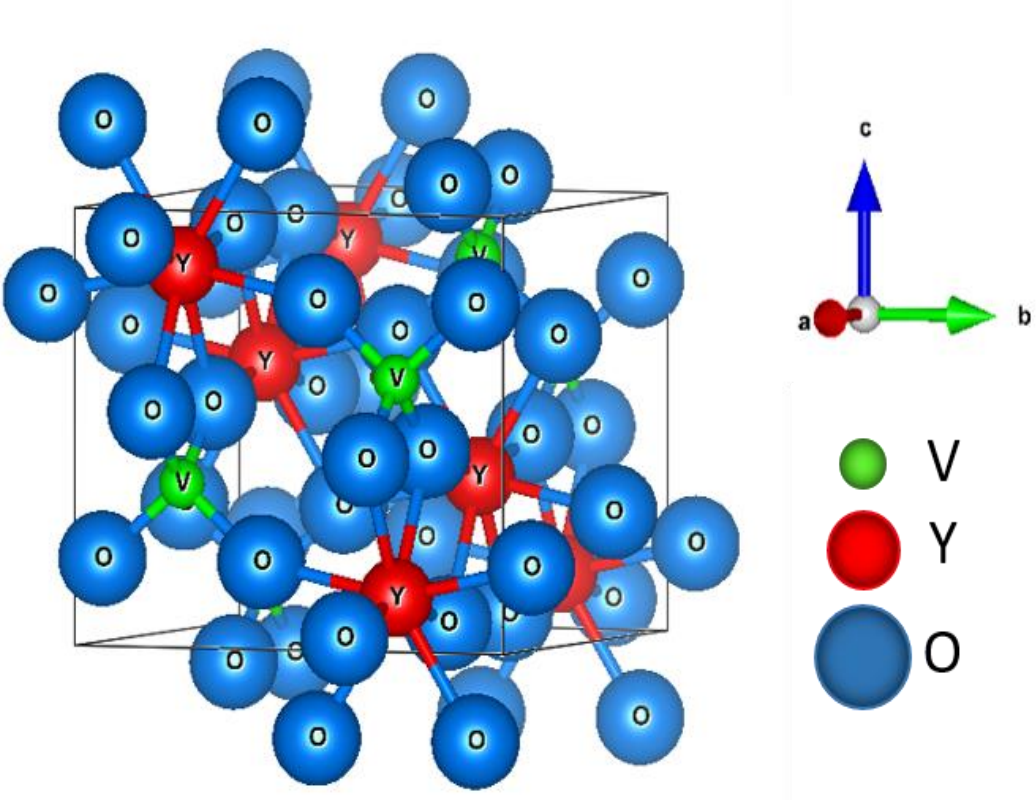

Figure 1.2 Structure of YVO_4 crystal

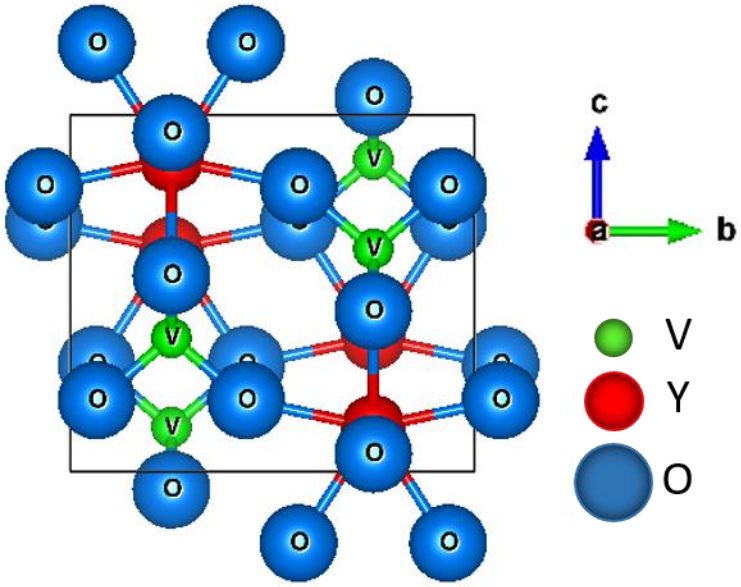

Figure 1.3 Structure of YVO_4 crystal, [100]-projection.

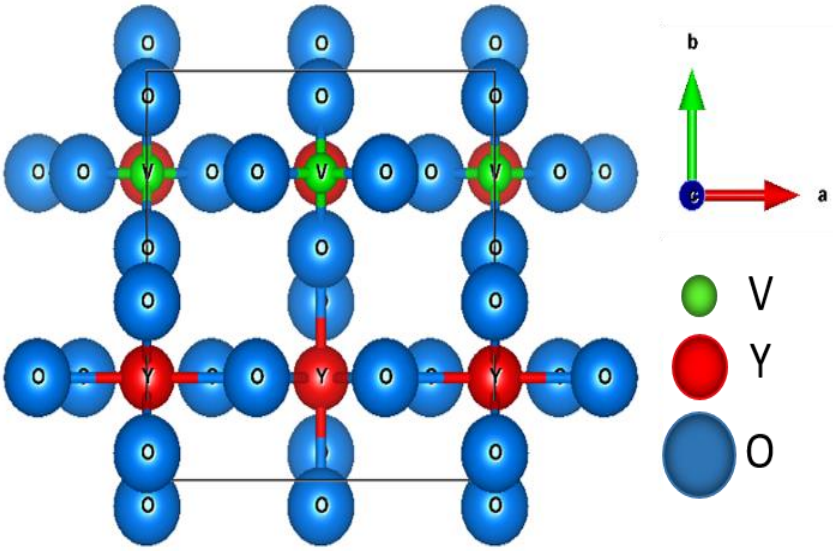

Figure 1.4 Structure of YVO_4 crystal, [001]-projection.

Further, at the beginning of research work on YVO_4 crystals, the growth of high quality single crystal of YVO_4 was difficult but presently these growth difficulties have been solved [22,23,33]. As YVO_4 is not a naturally occurring mineral, hence this material was synthesized for first time by Goldschmidt and Haraldsen in 1928 [32,33,36]. The phase diagram of YVO_4 was explained by Levin using the Y_2O_3-V_2O_5 binary system [8,9,23,24,26–31] and it is shown in the Figure 1.5.

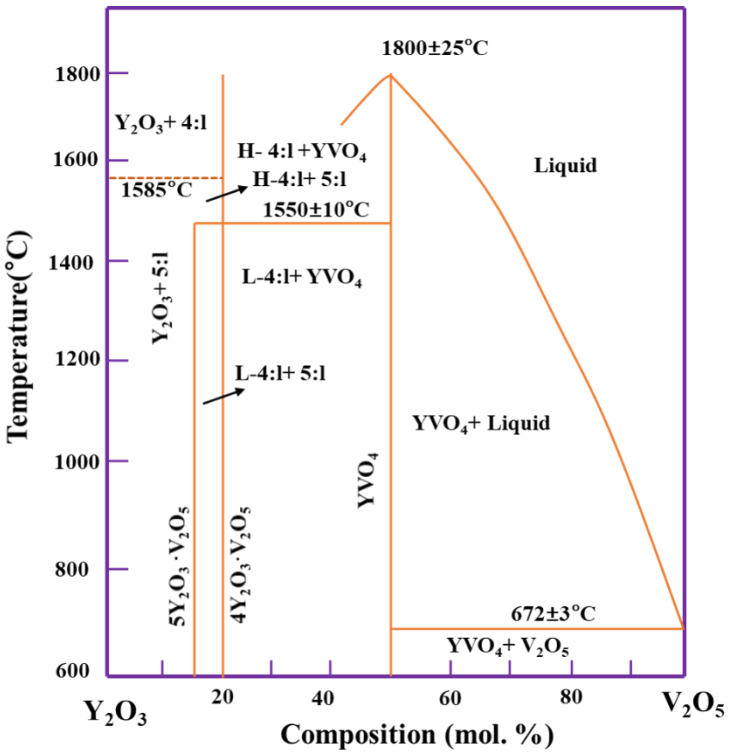

Figure 1.5 Phase diagram Y_2O_3-V_2O_5 binary system [26]

The year 1973, pure and rare earth doped of YVO_4 crystals were grown by K. Chow et al. [29]. Nd doped YVO_4 laser host medium has favorable laser characteristics which are better than the widely used Nd:YAG laser gain medium. There are three emission wavelengths of Nd^{3+} ion at around 914, 1064 and 1340 nm. The stimulated emission cross section at 1064 nm of Nd^{3+} ion, doped in the YVO_4 host medium is found

to be around 3 to 4 times higher than that of the Nd^{3+} ion doped in YAG host [21–23,25]. The Nd:YVO_4 laser with emission at 1340 nm is also useful for the development of eye-safe laser [21–23,25]. The higher absorption coefficient at 808 nm makes the crystal suitable for diode-laser end pumped solid state laser with a low threshold, a high efficiency and a compact size [9,24]. Nd:YVO_4 laser generates linear polarized laser emission which helps for electro-optic Q-switching without special intracavity polarizers [9]. A lot of the research works and reports on Nd doped YVO_4 crystals have been published [21–23,25]. Yb^{3+} ion among the rare earth elements, which has emission around 1 μm, can also be used in place of Nd^{3+} ion. Also, the Yb^{3+} ion has higher solubility in YVO_4 compared to the other rare earth ions which makes it possible to prepare a laser gain medium with high dopant concentration, resulting in a compact solid state-laser system. The broad absorption around 985 nm (used for pumping) of Yb^{3+} ion eliminates the necessity for a precise temperature control of the laser diodes used for pumping. The wide emission band (1010 nm) of Yb^{3+} ion provides the option of tunability in laser emission and short pulse generation. The long fluorescence lifetime of Yb^{3+} ion gives low laser threshold, and low quantum defect of Yb line creates minimum thermal load in the crystal during the operation of laser. Due to the favorable properties, Yb:YVO_4 is attracting lot of attention. Although, a few reports on the investigation of optical properties of Yb doped YVO_4 single crystals are available [10,15,25,37,38], there is so far no systematic investigation reported on the structural and optical properties of Yb doped YVO_4 laser crystal as a function of Yb doping concentration over its wide range of solubility in the host.

In view of the above, in the present work, Yb:YVO_4 crystals with varied Yb doping concentration of 0.8, 1.5, 3.0, 5.0, 8.0 and 15.0 at.% are grown by the optical

floating zone technique and subsequently detailed investigations like, absorption, refractive index for two polarizations (parallel and perpendicular to the optic axis), emission characteristics with different excitation and structural properties are carried out and are discussed in the **Chapter 4**.

Co-doping in the laser host medium plays a crucial role to increase the efficiency of the gain medium and its functionality for applications, such as self Q-switching, self-frequency doubling, self-Raman conversion and self-mode locking [16–20]. Co-doping in a laser host medium as a sensitizer is utilized for enhancing the efficiency of pumping in the gain medium. As an example, when Er doped gain medium is co-doped with Yb, the efficiency of pumping increases due to the strong absorption band of Yb utilized for pumping [17,18]. Er doped YVO_4 laser medium has two main laser emission lines, one at ~1.55 μm wavelength used in the field of high speed optical fiber communication systems, whereas the 3.0 μm wavelength is used for gas sensing application [39–43]. The Er doped YVO_4 laser gain medium is generally pumped by 808 nm diode laser but the absorption cross-section at 808 nm of Er^{3+} ion is very weak and it can be enhanced by increasing the Er concentration. However, Er concentration beyond 1 at.% creates undesirable cross-relaxation and up-conversion processes resulting in depopulation in the excited energy level $^4I_{13/2}$ of Er^{3+} ion [Figure 1.6] [21,22]. The population density of Er^{3+} ion in the excited energy level $^4I_{13/2}$ can be increased with addition of Yb co-doping. The strong absorption of Yb level at 985 nm transfers its energy to Er^{3+} ion at $^4I_{11/2}$ level for efficient pumping. The probability of reverse energy transfer to Yb^{3+} ions from Er^{3+} ions and the excited state absorption to the level $^2H_{11/2}$ is considerably reduced if the lifetime of the $^4I_{11/2}$ energy level is lower than a few μs ($\sim < 27\mu s$)[8,17,44]. Recently, the investigation of the down-conversion by Stokes emission as well as up-conversion

by anti-Stokes emission by energy transfer from Yb^{3+} to Er^{3+} has been reported in the Yb co-doped Er:YVO_4 single crystal [17,44].

Hence, in view of the importance of Yb co-doped Er:YVO_4 laser gain medium, the spectroscopic properties of the grown Yb co-doped Er:YVO_4 crystals (with different Yb doping concentration from 1.5 to 12.0 at.%) are carried out by Judd-Ofelt theory. The obtained parameters from unpolarized and polarized absorption data are compared with Er doped YVO_4 crystals in the present work and discussed in the **Chapter 4.**

Yb doped YVO_4 single crystals having emission around ~1 μm offers some important advantages [45–49]. However, Yb:YVO_4 single crystal faces many challenges for the laser design. In the Yb:YVO_4 single crystal, the absorption line for pumping radiation and the laser emission wavelengths of Yb^{3+} ion are very close to each other which creates complexity in the optics design of laser cavity for the laser operation. To overcome this issue, a suitable rare earth (RE) ion, called sensitizer is generally introduced as co-dopant in the Yb doped laser gain medium [50,51]. Therefore, in the present work, Nd^{3+} ion is incorporated in the lattice of Yb doped YVO_4 crystal for efficient pumping of laser gain medium.

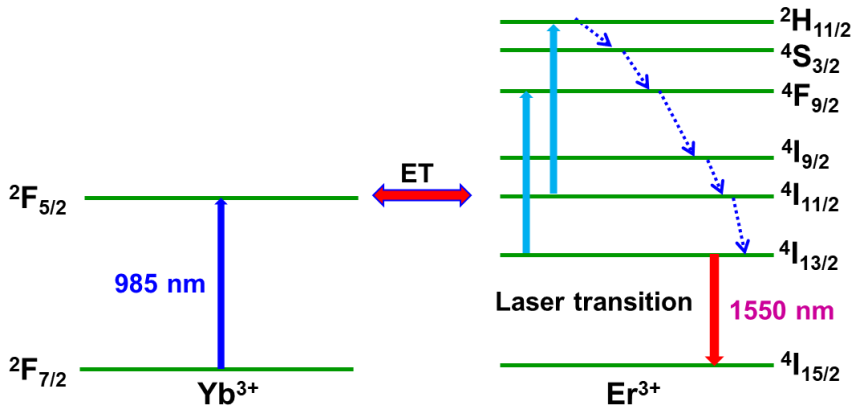

Figure 1.6 Energy levels of Yb and Er

The doping of Nd^{3+} ions creates a channel of pumping for Yb doped host crystals. Nd^{3+} ions absorb the pump energy and transfer to the nearby Yb^{3+} ions. Also, multiple options of pumping in Nd;Yb co-doped laser host, such as excitation with absorption line of Yb^{3+} and Nd^{3+} ion results in efficient pumping in the laser gain medium [50–52]. Though, there are a few reports on the Nd and Yb co-doped laser gain medium [50,53–57], only one report discusses the energy transfer process from Nd (1.0 at.%) to Yb (1.0 at.%) ions doped in YVO_4 crystal [50].

In view of the importance of Nd-Yb co-doped laser gain medium, the growth of Nd co-doped Yb:YVO_4 (0.8 at.% Nd and 0.8 & 3.0 at.% Yb) crystals by the optical floating zone method and investigation of the effect of co-doping on various properties like lattice parameters of YVO_4, crystalline quality of the crystal, etch pit dislocation density, the refractive index, optical homogeneity, fluorescence lifetime and optical absorption characteristics of Nd co-doped Yb:YVO_4 crystals have been carried out. Further, spectroscopic properties of Nd ion in Yb:YVO_4 crystals are also evaluated by Judd-Ofelt theory and details are discussed in the **Chapter 4.**

1.3.2 Gadolinium orthovanadate ($GdVO_4$) laser gain medium

Another important orthovanadate laser host single crystal is rare earth doped gadolinium orthovanadate ($GdVO_4$), due to its excellent thermal properties, high optical absorption and emission cross-section [58,59]. The thermal conductivity of $GdVO_4$ single crystal is nearly two times to that of YVO_4 and comparable to YAG crystal [60,61]. In addition, Nd:$GdVO_4$ crystals show higher slope efficiency, higher efficiency in energy conversion and lower laser threshold compared to that of YAG crystals. Further, the solubility or the segregation coefficient of Nd^{3+} ion in $GdVO_4$ crystals is

higher than that in YVO_4 and YAG crystals, thereby helping in the growth of high optical quality single crystals with uniform doping concentration [12–15,62].

The $GdVO_4$ crystal belongs to the zircon type structure having tetragonal crystal system with point group 4/mmm (D_{4h}) and space group $I4_1/amd$ (D_{4h}^{19}) [15,62] [Figure 1.7-1.9].

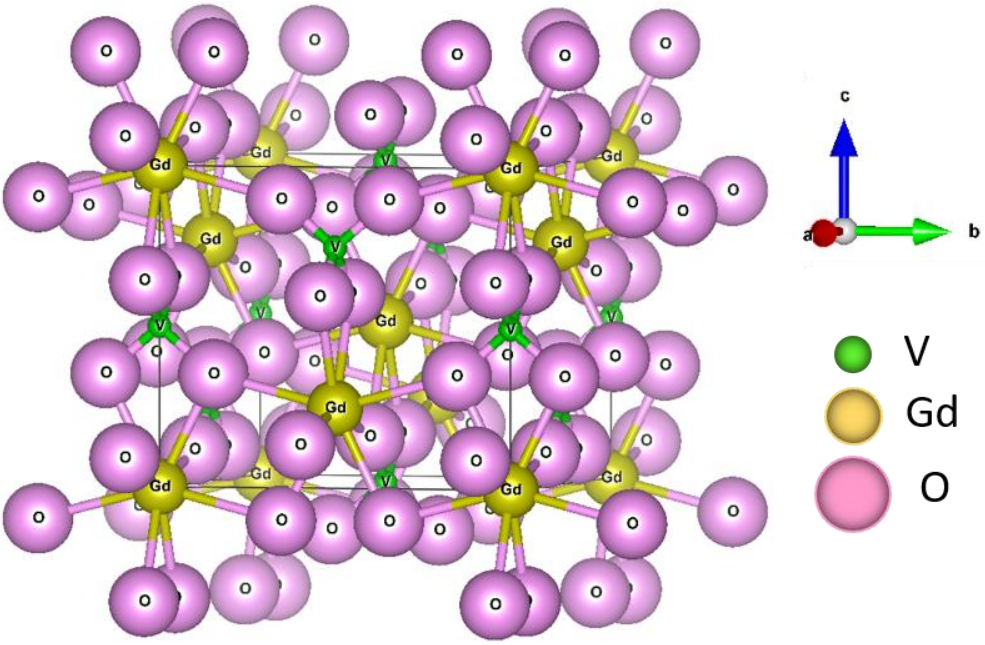

Figure 1.7 Structure of $GdVO_4$ crystal

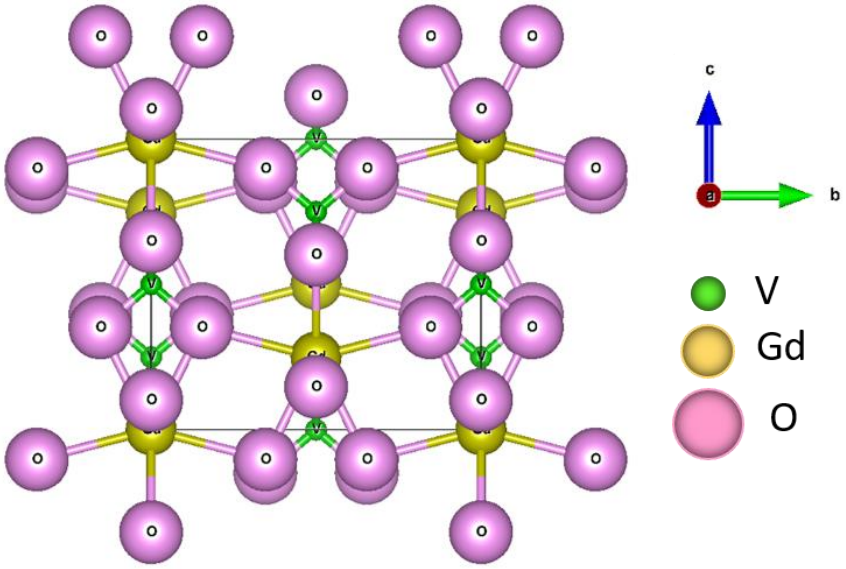

Figure 1.8 Structure of $GdVO_4$ crystal; [100] projection

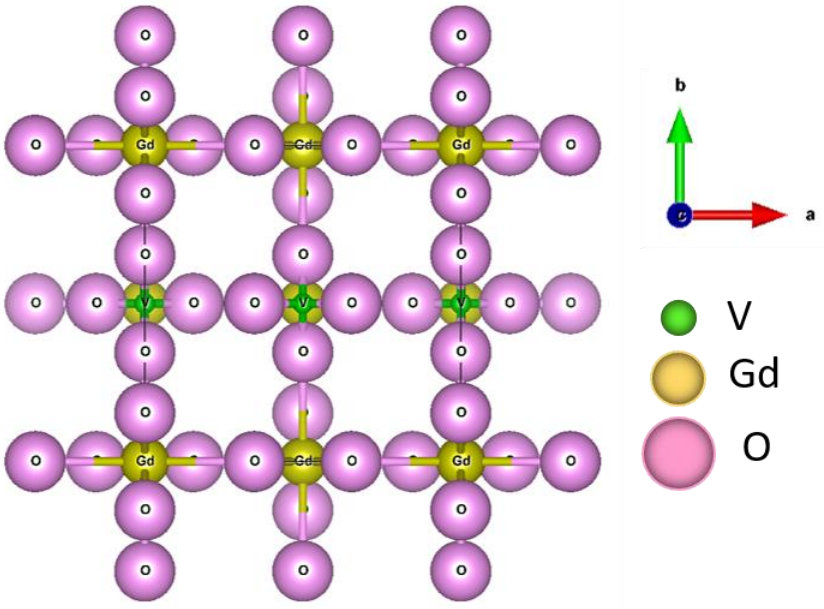

Figure 1.9 Structure of $GdVO_4$ crystal; [001] projection

Generally, f-f transitions of rare earth are not allowed according to the Laporte rule but if the rare earth ion such as Nd ion, doped in the $GdVO_4$ crystals, f-f sharp transitions of rare earth ion are possible due to the presence of strong tetragonal crystal field with a site symmetry D_{2d}. The various optical properties such as the emission cross-section, intensity of Nd emission and fluorescence lifetime intensely depend on the concentrations of the Nd ion, doped in laser gain medium. During laser operation, the performance of lasers depends on the thermal loading in the laser gain medium, which adversely affects the beam quality of laser emission. Hence, the investigation of thermal properties of the laser gain medium are important pre-requisite for designing the laser systems. Parameters such as thermo-optic coefficient (dn/dT), thermal expansion and thermal conductivity are required to be estimated accurately for an efficient laser system [12–14,58–66].

In view of this the growth of Nd:$GdVO_4$ crystals by optical floating zone (OFZ) method and a systematic investigation on the effect of Nd doping concentration (0.2, 0.6, 0.8, 1.0, 1.2 and 1.6 at.%) on refractive index, thermo-optic coefficient and spectroscopic properties using Judd-Ofelt theory are carried out. The details are discussed in the **Chapter 5**.

Further, to explore the multi-functionality such as self-Q-switching in the laser crystals (Nd:$GdVO_4$, Nd:YVO_4, etc.), Cr ion has been co-doped in the gain medium [67–72]. Literature reports suggest that Nd^{3+} and Cr^{4+} co-doped YAG crystals has been recognized as a promising self-Q-switched laser gain medium [67–72]. However, a charge imbalance is created due to the substitution of Cr^{4+} ions for a fraction of Al^{3+} ions in its lattice. Therefore, Ca^{2+} or Mg^{2+} ions are co-doped in YAG crystals to retain the charge neutrality. The co-doping of an extra divalent ion creates complexities in the

growth of good quality single crystals and impedes the development of laser. Hence, it is important to explore a new laser crystal, which can be used for self Q-switching applications. Interestingly, in the $GdVO_4$ crystals or other orthovanadate, Cr^{5+} substitutes V^{5+} ions, and charge neutrality is maintained. Absorption spectra of Cr^{5+} doped $GdVO_4$ show that the absorption of Cr^{5+} ion is polarization sensitive and its absorption bands for π-polarized (E//c) light is located in the range 900-1300 nm [23,40]. Therefore, this Cr^{5+} absorption band can be used as the passive Q-switching for laser emission at 1 μm [19,73,74]. So Cr co-doped Nd:$GdVO_4$ is a promising laser gain medium to investigate for the passively self-Q-switching application [13,60].

Therefore, in the present work, Cr co-doped Nd:$GdVO_4$ single crystals with 0.5 at.% of Nd and 1.0, 1.2 & 1.5 at.% of Cr are carried out under oxygen/nitrogen ambience using optical floating zone technique and investigated the optical properties. Details are discussed in the **Chapter 5**.

1.3.3 Lutetium orthovanadate ($LuVO_4$) laser gain medium

Further, a comparatively new laser host that falls in the same family of orthovanadate crystals is lutetium orthovanadate ($LuVO_4$). The rare earth doped $LuVO_4$ crystal shows superior lasing property due to its higher absorption at pumped wavelength and larger emission cross section in comparison to the other orthovanadate crystals. Particularly, the neodymium-doped $LuVO_4$ (Nd:$LuVO_4$) with zircon-structure has larger emission cross-section than those of Nd:YVO_4 and Nd:$GdVO_4$ and exhibits high damage threshold [5–7]. It also possesses excellent thermal properties. Hence, Nd:$LuVO_4$ is one of the excellent laser material for generating laser emission near 1 μm and this was investigated for the first time by Maunier et al. [5]. The structure of $LuVO_4$ crystal is zircon-structure (D_{4h}^{19}- $I4_1/amd$) and is shown in the Figure 1.10-1.12.

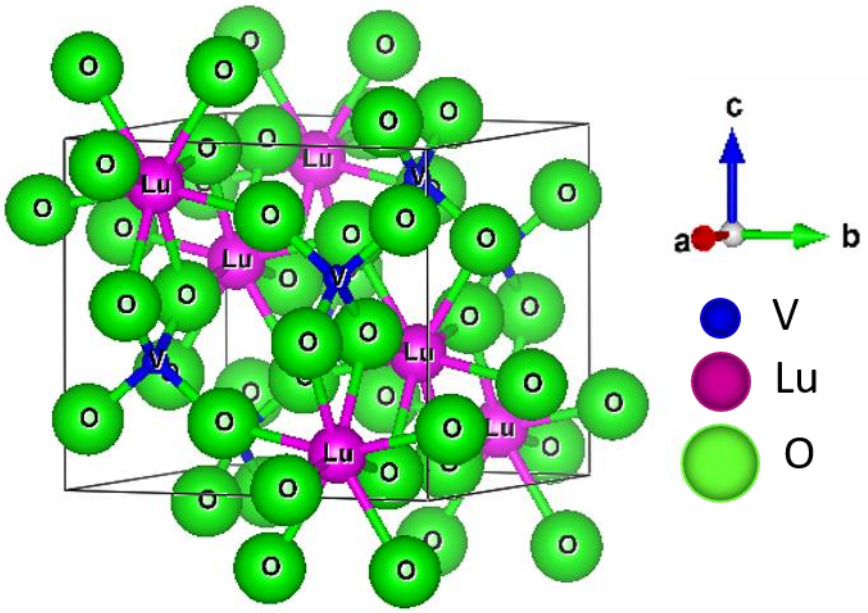

Figure 1.10 Structure of $LuVO_4$ crystal

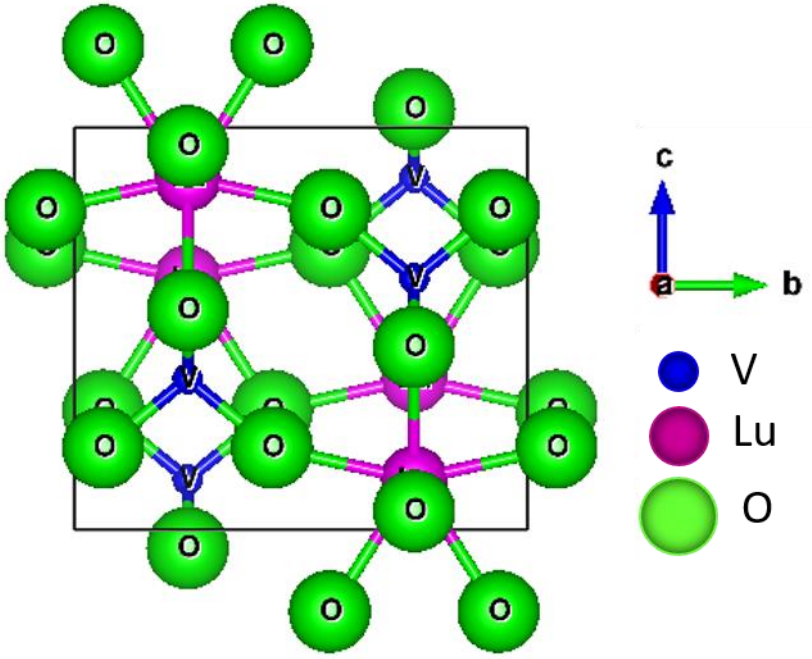

Figure 1.11 Structure of $LuVO_4$ crystal; [100] projection

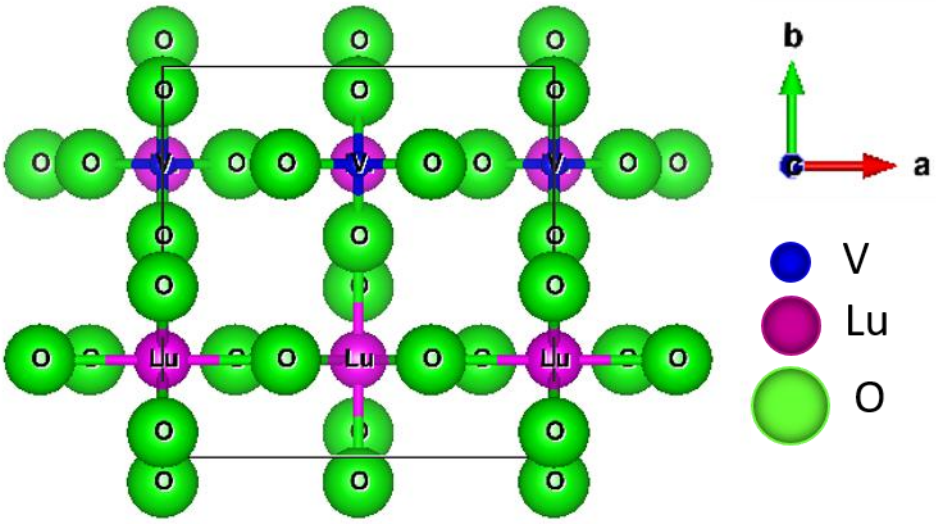

Figure 1.12 Structure of $LuVO_4$ crystal; [001] projection

Recently literature reports suggest that the Nd^{3+} doping concentration in $LuVO_4$ laser host is generally kept below 1.0 at.% for getting higher laser output [5–7,75–78].

Therefore, in the present work, the growth of single crystal of Nd:$LuVO_4$ with 0.25 and 0.5 at.% of Nd are carried out under oxygen/nitrogen ambience using optical floating zone technique. The optical properties like absorption, emission, fluorescence life-time measurements are investigated. Details of investigation are discussed in the **Chapter 6.**

1.4 Comparison of rare earth doped various laser host materials

There are various laser host materials such as garnet, orthovanadate, tungstate, etc. The rare earth doped orthovanadate shows excellent optical and thermal properties as compare to the other available laser host materials [1–4,8–10,21,79–95]. The comparisons for Nd and Yb doped into the different laser host materials are given in Table 1.1 and Table 1.2 respectively.

Table 1.1 Comparison of properties of Nd doped laser host gain mediums

	Nd:Glass	**Nd:YAG**	**Nd:YLF**	**Nd:KGW**	**Nd:YVO_4**	**Nd:$GdVO_4$**	**Nd:$LuVO_4$**
Emission-cross section ($\times 10^{-20} cm^2$)	2.7-4.3	28	12	38	156	76	14.6
Fluorescence lifetime (μs)	290-340	230	480	110	100	95	95
Thermal conductivity (W/m◦K)	1.3	14	6	2.8 [100]	5.23 [100]	11.7 [110]	7.96 [100]
Thermal expansion coefficient ($10^{-6}/^{\circ}C$)	9	7.5	13	4.0 [100]	4.3 [100]	1.5 [100]	1.7 [100]
dn/dT ($10^{-6}/^{\circ}C$)	2.9	7.3	−6.6	-16.0	8.5 [100]	4.7 [100]	6.7 [100]
Peak absorption coefficient (cm^{-1})	2-4	7.1	3.5	---	31 (π – polarization	74(π – polarization	61(π – polarization)
Hardness(Mohs)	5.5	8.5	4-5	4	5	5	~ 5-6
Slope efficiency	12-18%	38.6	47%	41%	48.5%	60%	58%

Table 1.2 Comparison of properties of Yb doped laser host gain mediums

	Yb:Glass	**Yb:YAG**	**Yb:YLF**	**Yb:YVO_4**	**Yb:KGW**
Emission Cross section ($\times 10^{-20} cm^2$)	2.0	2.2	0.75	4.2	2.6
Fluorescence lifetime (μs)	700	967	2000	951	600
Thermal conductivity (W/m °C)	1.3	14	6	5	2.8
Thermal expansion coefficient (10^{-6}/°C)	9	7.5	13	4.43 [100]	4[100]
dn/dt (10^{-6}/°C)	2.9	7.3	-6.6	8.5	-16.0
Emission band width	22-35	6-9 nm		2-9	----
Slope efficiency	18%	35	59	76%	60-66

1.5 Objective of the present work

The objective of the present research work is to carry out a detailed investigation of the optical properties like absorption, emission, refractive index, and fluorescence life characteristics and the structural properties like lattice parameters, oxidation state of vanadium ion, etc., of rare earth ions (Nd and Yb) doped YVO_4, $GdVO_4$ and $LuVO_4$ single crystals over a long range of doping concentration after their single crystal growth. Further, to include the co-doping of Er and Cr ion in the doped laser host crystal and investigate for efficient laser, optical devices, and multifunctional laser crystals. Finally, to fabricate the laser elements from one of the grown crystals and perform the testing of laser characteristics.

Chapter-2 Theory and Experimental Techniques

2.1 Introduction to crystal growth

In the past few years, with increasing demand of materials in form of single crystals there has been attaining a lot of interest on the growth of single crystals for technological applications. Hence, good quality single crystals are needed for achieving high performance of a device. There are various theories and processes to understand the growth of single crystals and also various techniques have evolved over the years to grow the promising materials in the form of single crystals [96–98].

2.1.1 Fundamental of nucleation

Growth of single crystals is a controlled process of solidification of materials from a disordered fluid phase with high atomic mobility [96]. If three phases such as solid, liquid and gas of any material are in equilibrium condition then it is called triple point. The equilibrium condition breaks and phase transformation occurs if the temperature or pressure or both are changed. The breaking of equilibrium condition usually occurs with a change in temperature, pH, pressure, electrochemical potential, strain, chemical potential, etc. [96,99]. The single solid phase transformation may occur from solid, liquid or gaseous phase at a suitable physical condition in crystal growth process. For the growth of single crystal, generally the liquid-to-solid or gas-to-solid transformation occurs. There are three basic steps involved for starting the growth of the single crystal from disordered phase [96,98].

- Achieving super-saturation or super-cooling condition.
- Nucleation.
- Growth.

The super-saturation or super-cooling condition acts as driving force for the crystallization process. The formation of crystallization centers or nucleus is the one of the most important features of crystal growth [96,98]. The process of formation of a nuclei is known as Nucleation. Nucleation may occur either spontaneously or it may be induced artificially [96–98]. Nucleation can generally be induced by friction, agitation mechanical shock, impurity, and extreme pressure within solution and melts. Nucleation can be broadly classified into two categories [Figure 2.1]. The first one is the 'primary nucleation' and it can be observed in the systems which do not have any crystalline matter. The second one is secondary' nucleation in which the nuclei are generated in a supersaturated system in presence of the crystals [96–98].

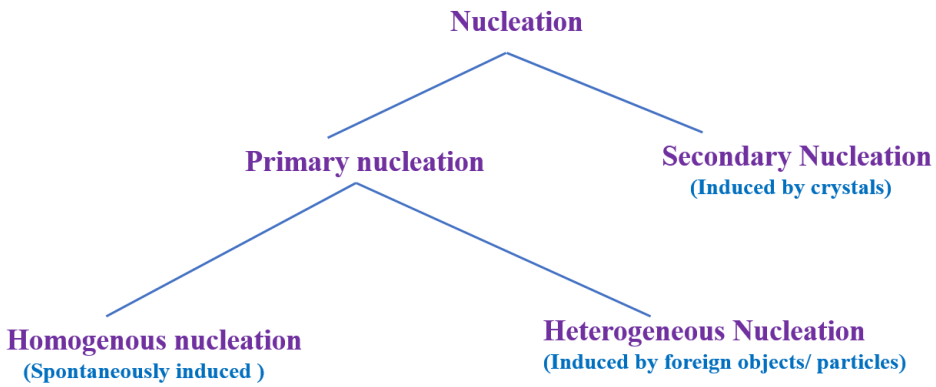

Figure 2.1 Classification of nucleation

2.1.2 Homogeneous nucleation

Homogeneous nucleation is the spontaneously formation of crystalline nuclei in the supersaturated solution or super-cooled melt. There are several theories like surface energy theory, diffusion theory and adsorption layer theory on the formation of nucleus and the rate of crystal growth. Among the different crystal growth theories, the surface energy theory (thermodynamics approach), which was proposed by Gibbs [100], is the

best approach to explain the nucleation process. Gibbs proposed that whenever atoms (solutes) present in solution, assemble and combine then they release energy from the cluster to achieve the stability. In the solutions, the molecules and ions, which are called as growth unit (GU) continuously form small solid clusters and release the energy in the form of Gibbs free energy. The Gibbs free energy (ΔG_t) has two energy terms. The first term, surface free energy (ΔG_s), which is the energy required for the formation of an interface between the new solid phase and the solution, and second term accounts for the volume free energy accompanying the transfer from the solution into the bulk solid phase (ΔG_v). The sum of these two terms reaches a maximum value at a particular particle size, called the critical size, in the supersaturated solution, as depicted in Figure 2.2.

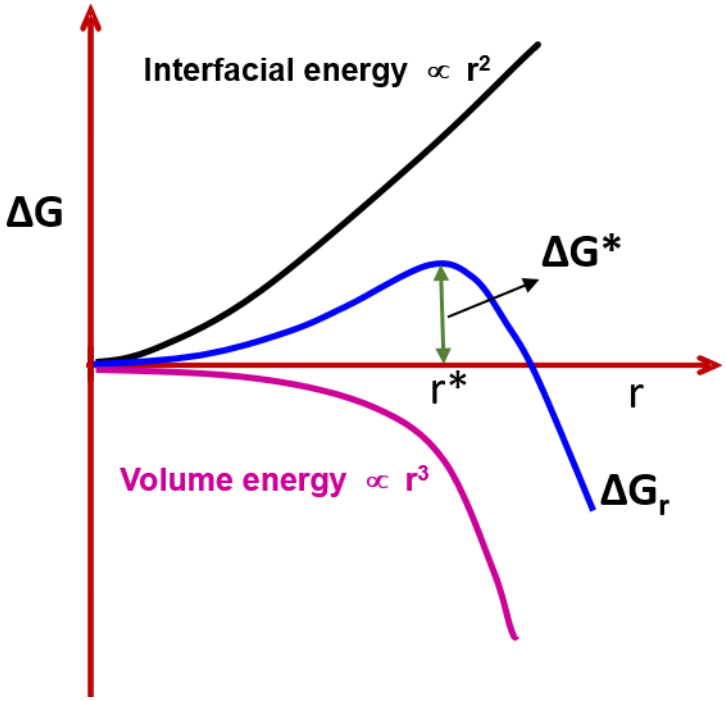

Figure 2.2 Change in Gibbs free energy during nucleation

Figure 2.2 shows variation of Gibbs free energy [ΔG_v, ΔG_s and (ΔG_t=ΔG^*)] as a function of the cluster radius (r), for a supersaturated solution. As the size of the cluster

increases, the volume Gibbs free energy (ΔG_v) of the cluster decreases, whereas surface Gibbs free energy (ΔG_s) increase due to an increase in the surface area of the cluster (interfacial energy). The sum of both free energies results that the net Gibbs free energy ($\Delta G_t = \Delta G^*$) is maximum at a critical size of nuclei. For a size greater than the critical size (nuclei), the crystals grow spontaneously and the Gibbs free energy decreases and the expression for Gibbs free energy can be written as [96,98]:

$$\Delta G_t = \Delta G_v + \Delta G_s \dots\dots\dots\dots\dots (2.1)$$

The smaller or sub-critical cluster of atoms or molecules is called an embryo. When it reaches the critical cluster size, then cluster is called a nucleus. Further, the growth of the crystal is started when size of cluster is greater than the critical nucleus. Basically, the growth of crystal starts with decrease of the Gibbs free energy of the system. The above process is called spontaneous nucleation. The spontaneous nucleation is given in the form of Gibbs free energy of a cluster or nuclei. The bulk energy term, ΔG_v, is proportional to the number of constituent GU.

Assuming the formation of a spherical cluster, the bulk energy term, ΔG_v is given as

$$\Delta G_v = \frac{4\pi r^3}{3} \Delta g_v \dots\dots\dots\dots (2.2)$$

where Δg_v is the free energy change of the transformation per unit volume, *r* is the radius of the cluster.

The surface Gibbs free energy, ΔG_s, is always a positive value and directly proportional to the cluster surface area:

$$\Delta G_s = (4\pi r^2)\gamma \dots\dots\dots\dots (2.3)$$

In this equation γ is the surface Gibbs energy per unit area, also known as the surface tension. The overall change of the total Gibbs free energy of the cluster is given by

$$\Delta G_t = \left(\frac{4\pi r^3}{3}\right)\Delta g_v + (4\pi r^2)\gamma \ldots\ldots\ldots\ldots (2.4)$$

As seen in the Figure 2.2, for a maximum value of ΔG_t, the $d\Delta G_t$ /dr must be zero and the critical size of the particle (r_{crit}) is given by

$$r_{crit} = \left(\frac{2\gamma}{\Delta g_v}\right) = \frac{2\gamma v}{kTln\left(\frac{C}{C_0}\right)} \ldots\ldots\ldots\ldots (2.5)$$

$$\Delta g_v = \left(\frac{2\gamma}{r}\right) = \frac{kTln(S)}{v} \ldots\ldots\ldots\ldots (2.6)$$

where, S (=c/c_o), corresponds to the degree of supersaturation (S), v is the molecular volume

The critical activation energy of nucleation can be calculated in terms of S by using equation (2.6) and equation (2.5).

$$\Delta G_{crit} = \left(\frac{16\pi v^2\gamma^3}{3[kTln(S)]^2}\right) \ldots\ldots\ldots\ldots (2.7)$$

It follows from equations (2.5) and (2.7) that both r_{crit} and ΔG_{crit} decrease with increasing supersaturation (Figure 2.3).

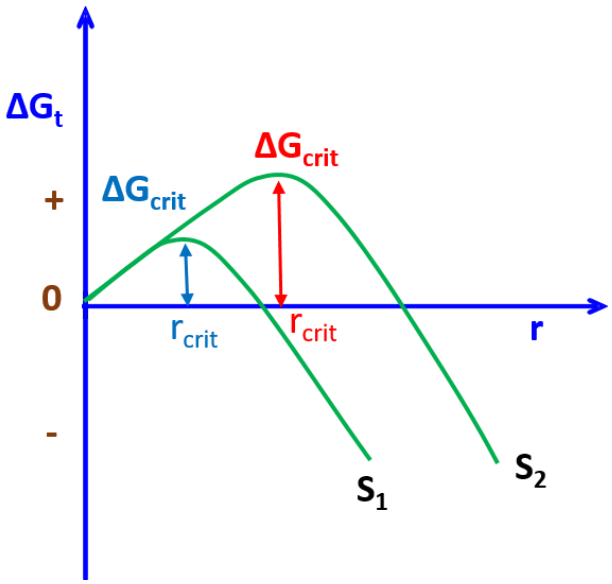

Figure 2.3 Change in Gibbs free energy with respect to supersaturation

The rate of nucleation (J) e.g. the number of nuclei formed per unit time per unit volume, can be given as

$$J = A\ exp\left(\frac{-\Delta G}{kT}\right) \ldots\ldots\ldots\ldots (2.8)$$

$$J = A\ exp\left(-\frac{16\pi v^2\gamma^3}{3k^3T^3[ln(S)]^2}\right) \ldots\ldots\ldots\ldots (2.9)$$

where v is Arrhenius reaction velocity equation and it is used for the rate of a thermally activated process. The rate of nucleation is decided by three main variables, which are temperature (T), degree of supersaturateion (S) and interfacial tension (γ).

Similar expression for the melt in terms of supercooling may be derived from homogeneous nucleation. The volume free energy ΔG_v is given as

$$\Delta G_v = \left(\frac{-\Delta H_f \Delta T}{T^*}\right) \ldots\ldots\ldots\ldots (2.10)$$

where T^* is solid-liquid equilibrium temperature expressed in kelvins, $\Delta T=T^*-T$ is supercooling and ΔH_f is latent heat of fusion.

The radius of critical nucleus is given by

$$r_c = \left(\frac{-2\gamma T^*}{\Delta H_f \Delta T}\right) \ldots\ldots\ldots\ldots (2.11)$$

And the rate of nucleation, from equation (2.9) may be expressed as

$$J = A\, exp\left(-\frac{16\pi\gamma^3}{3kT^*[\Delta H_f T_r \Delta T_r]^2}\right) \ldots\ldots\ldots\ldots (2.12)$$

where T_r is reduced temperature defined by $T_r=T/T^*$ and $\Delta T_r=\frac{\Delta T}{T_*}$ i.e $\Delta Tr = 1 - Tr$. This equation indicates the dominant effect of supercooling on the nucleation rate.

The critical nucleus size and the critical Gibbs free energy as a function of supercooling can be given by:

$$r r_c = (\Delta T)^{-1} \ldots\ldots\ldots\ldots (2.13)$$

$$\Delta G_{crit} = (\Delta T)^{-2} \ldots\ldots\ldots\ldots (2.14)$$

The above equation (Eq. 2.13) indicates that the size of a critical nucleus increases with the increase in the temperature. As per Eq. 2.12, the nucleation rate should always increase with the increase of supercooling but, the actual curve shows an anomaly such that it increases initially upto a certain maximum value and then subsequently decreases. This is attributed to an increase in viscosity of the solution with an increase in the supercooling, which restricts the mass flow, i.e. the molecular movement in the solution inhibits the growth or formation of ordered structures [99].

$$J = A\ exp\left(-\left[\frac{16\pi\gamma^3}{3kT^*\left[\Delta H_f T_r \Delta T_r\right]^2}\right] + \frac{\Delta G'}{kT}\right) \ldots\ldots\ldots\ldots (2.15)$$

The anomaly is resolved by adding the viscosity correction term in the Eq. 2.12, where $\Delta G^{'}$ is the activation energy for molecular motion across the embryo-matrix interface, which is exceptionally large for highly viscous liquids and the other exponential term is small. Under such circumstances, when S is generally very large, then ΔG' becomes dominant factor in the rate equation and controls the nucleation process.

2.1.3 Heterogeneous nucleation

Heterogeneous nucleation occurs due to the presence of foreign bodies in the solution like surface of different substances, such as a dust particle, impurities or the wall of the container that acts as nucleation sites over which atoms, ions, or molecules get deposited in an oriented manner. Heterogeneous nucleation therefore, occurs much more easily than homogeneous nucleation and commonly encountered in liquid-solid transformation. These solid surfaces or impurities act as preferential sites having lower surface energy and offer reduced free energy barrier and facilitates nucleation. The contact angles between surfaces of sites are greater than zero and they encourage the particles to nucleate. The presence of foreign substrates in the supersaturated solution induces nucleation at lower energy in case of heterogeneous nucleation than that required for spontaneous nucleation.

The free energy change associated with critical nucleus in the heterogeneous nucleation ΔG^*_{het} is less than the corresponding free energy change ΔG^*_{hom} associated with homogeneous nucleation.

$$\Delta G^*_{het} = \phi \Delta G^*_{hem} \ldots\ldots\ldots\ldots (2.16)$$

where the factor ϕ is less than unity and is given as

$$\phi = \frac{(2 + cos\theta)(1 - cos\theta)^2}{4} \ldots\ldots\ldots\ldots (2.17)$$

where θ is the contact angle between liquid and solid surface. The contact angle θ is determined by Young's relation.

$$cos\theta = \frac{\sigma_{sl} - \sigma_{cs}}{\sigma_{cl}} \ldots\ldots\ldots\ldots (2.18)$$

where σ_{sl} is the solid-liquid interfacial tension, σ_{cs} is crystal-solid interfacial tension and σ_{cl} crystal-liquid interfacial tension.

2.1.4 Secondary nucleation

Secondary nucleation occurs only in the presence of crystals of the material being grown or crystallized. The secondary nucleation is described by the mechanisms such as initial breeding as crystalline dust swept off a newly introduced seed crystal in the solution [43,96,97].

2.2 Fundamental of crystal growth techniques

Single crystals and growth of single crystals have attracted considerable attention of the researchers due to the strategic applications. It has become the thrust area of research & demands advancement in the crystal growth technologies. There are various techniques for growing crystals that have been developed over the decades depending on the material and its applications. Scientists and researchers are constantly working on the existing technologies along with new one and doing research on different materials based on their requirement for societal as well as commercial

applications. Researchers are still striving to get high quality single crystals for its best performance because the development of device quality single crystal is basically a challenging task.

The single crystal can be grown from a polycrystalline material by slow and gradual transformation from melt, solution or vapor phase [50]. Any growth technique for a particular crystal is decided by material properties like congruent melting, thermal conductivities, thermal expansion, viscosity of melt, chemical stabilities of melt or solid, etc. There are different growth methods, which are selected on the basis of growth from solution, growth from vapor and growth from melt [99]. Figure 2.4 shows the flow chart of various crystal growth techniques.

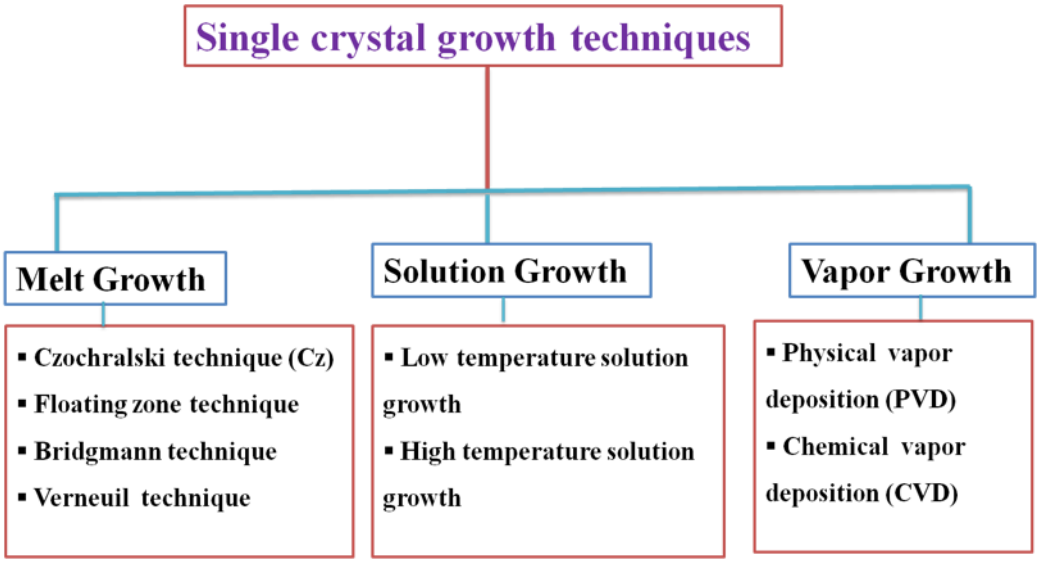

Figure 2.4 Flow chart of various crystal growth techniques

2.2.1 Melt growth technique

Among various growth techniques to grow the single crystals, the melt growth technique is the most well-known and versatile method of growing bigger size crystals with relatively high growth rate. Materials having congruent melting, manageable vapor

pressure, no polymorphic transitions and without undergoing any decomposition are usually grown by melt growth techniques. Melt growth method is mostly used for growing metals oxides, halides, semiconductors, etc.

In this technique, an orientated seed crystal is touched to the melt for initiating the growth. The problem of uncontrolled nucleation is also suppressed in the melt growth due to large super-cooling of melt phase. Here, crystals are grown in a temperature gradient to achieve super-heated fluid and super-cooled crystal. This super-cooling provides the necessary atomic driving force for crystallization.

There are number of melt growth techniques such as Czochralski (Cz), Zone melting, Bridgman, Verneuil, etc. [96–98]. The particular technique is selected on the basis of the physical and chemical properties of material to be grown [98]. The details of few melt growth techniques are explained in the following section 2.3.

2.2.2 Solution growth technique

The most general and familiar technique for growing single crystals is solution growth. This technique is based on the precipitation of solute from the solution. In this technique, single crystals are usually grown at a temperature, which is well below the melting point of the material. Most of the crystals using these techniques are grown at room temperature and this is one of the biggest advantage of solution growth method. The nucleation in the solution and subsequent growth of crystal occurs from the critically supersaturated solution. The supersaturation of solution can be achieved by the decreasing the temperature or slow evaporation of the solution. The solution growth methods can be classified on basis of the temperature and the nature of the solvents used. So, the solution growth is broadly categorized as low temperature and high

temperature solution growth. The most common solution growth techniques used to grow the crystals are named as slow cooling, slow evaporation method, hydrothermal growth, gel growth and high temperature solution growth. The solution growth techniques are characterized with slow growth rates. The typical growth duration is in the range of days to months. The crystals grown from solution are very good quality in optical as well as other physical properties.

2.2.3 Vapor growth technique

The vapor growth technique is generally used for growing those materials which have high vapor pressure and suitable solvents are not available. This growth method is utilized to grow the bulk crystals, semiconductor, photonic devices, and complex thin layers on crystal substrate having a high degree of crystalline quality and purity. Generally, the crystal growth from vapor phase is broadly classified into two techniques named as physical vapor transport (PVT) and chemical vapor transport (CVT). Using this technique very fine and complex structure for photonic applications can be grow in the form of single crystals.

2.3 Melt growth techniques

In the melt growth techniques, single crystal is formed by re-solidification of the melted polycrystalline material. All materials, which melt congruently without any decomposition at the melting point and have no phase transformation can be grown in the form of single crystal. The growth rate in the melt growth method is fastest as compared to all other growth techniques. The single crystals with high quality and purity can be grown using melt growth techniques. These techniques are mostly used to

develop commercially important laser host, nonlinear optical, semiconductor and metals crystal. The most common melt growth techniques are

- Czochralski technique
- Zone melting technique
- Bridgman technique
- Verneuil technique

2.3.1 Czochralski technique

The Czochralski (CZ) method is the most versatile and preferred technique for the growth of single crystals. The bigger size and high-quality silicon, other semiconductors and optical single crystals are grown by Czochralski technique. This method is used for those materials, which are congruent melting, having high melting point and volume expansion coefficients. This technique was first developed by Jan Czochralski, a polish chemist, in 1918.

2.3.1.1 Growth process

The material or polycrystalline powder is melted in a suitable non-reacting crucible (platinum or iridium) under a controlled atmosphere. Heating of crucible is done by induction or resistive heating, mostly induction heating is preferred. For the growth, a seed crystal with preferred orientation is used. When the temperature of the molten charge, which is just above the M.P., is stabilized, seed crystal is touched to molten charge and withdrawn slowly with the proper pulling and rotation. Rotation of seed crystal is given to control the interface shape of the growing crystal for minimizing the defects. The pulling and rotations rate depend on the material to material. When the crystal of desired length is grown, the growth process is terminated by rapid pulling of

the crystals with slight increase in the melt temperature. After that, it is retained close to the melt surface and cooled down to the room temperature with proper cooling rate. In the Cz technique, the diameter of the crystals are controlled by automatic diameter control software. The growth condition like temperature gradient, growth orientation and ambience can be modified depending on the material to grow. In this method, the crystallization establishes a dynamic equilibrium between the two phases. Figure 2.5 shows the typical growth of crystals by Cz technique.

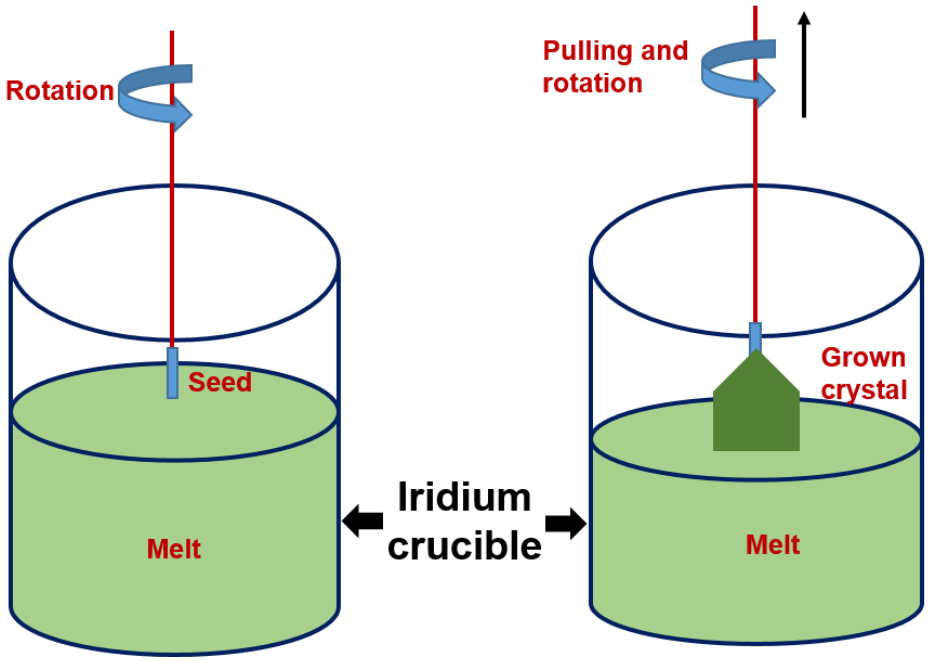

Figure 2.5 The schematic of CZ growth process

2.3.1.2 Fundamental consideration for the growth

In Cz technique the parameters for growing the crystals are selected on basis of (a) chemical properties of material (b) thermal conductivity of material in the solid and liquid phase (c) segregation coefficient of dopant (d) melt viscosity (e) anisotropy in thermal expansion (f) requirement of size and quality of crystal, etc. The shape of solid-liquid interface during growth may be flat, convex or concave as shown in Figure 2.6.

The interface shape decides the stability of growth process & the quality of crystals. The interface generates strain and dislocation in growing crystals. The flat interface is ideally desirable as it provides homogeneity in the crystal and minimal lattice stresses. The convex shape interface towards the melt gives the stable molten zone for growth, though it leads to dislocation and lattice defects in the crystals. If the interface shape is highly concave then the growing crystal can get detached from the melt unpredictably (Figure 2.6) [96–98].

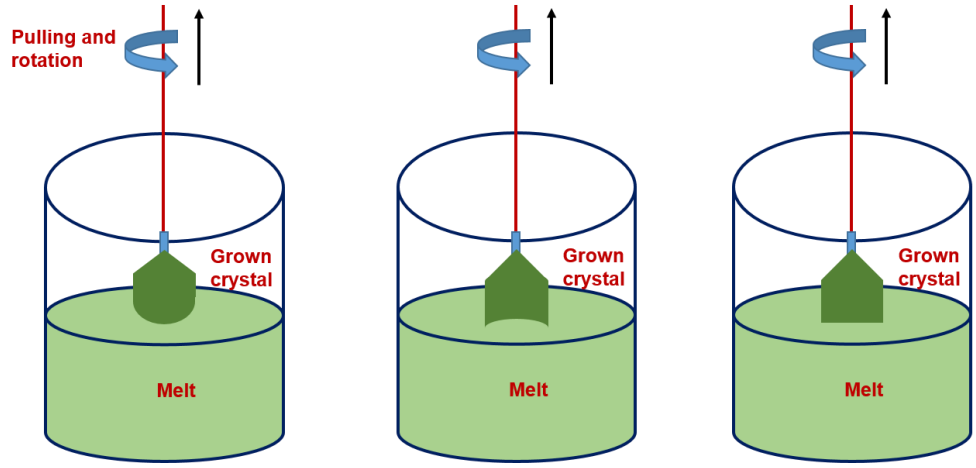

Figure 2.6 The different growth interface shape

The heat/mass flow pattern decides the shape of the interface. The various possible heat flow paths are shown in the Figure 2.7 during growth of single crystals by CZ technique [99–104]. These heat flow patterns depend on the temperature gradients, crystal rotation, viscosity and thermal conductivity of the melt. It is a complex function of radial and axial thermal gradients. This can be changed by modify the insulation geometry of growth station, pulling and rotation of seed crystal and gas flow rate [99–104]. The schematic of Cz equipment is shown in the Figure 2.8.

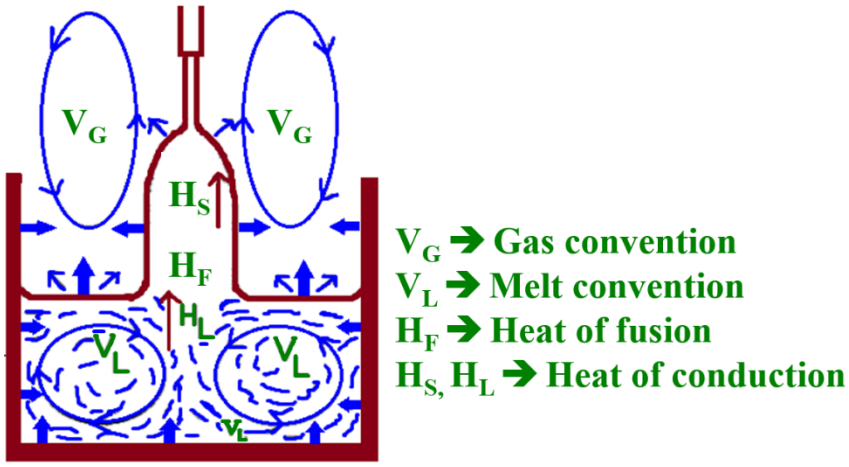

Figure 2.7 Various possible heat flow paths

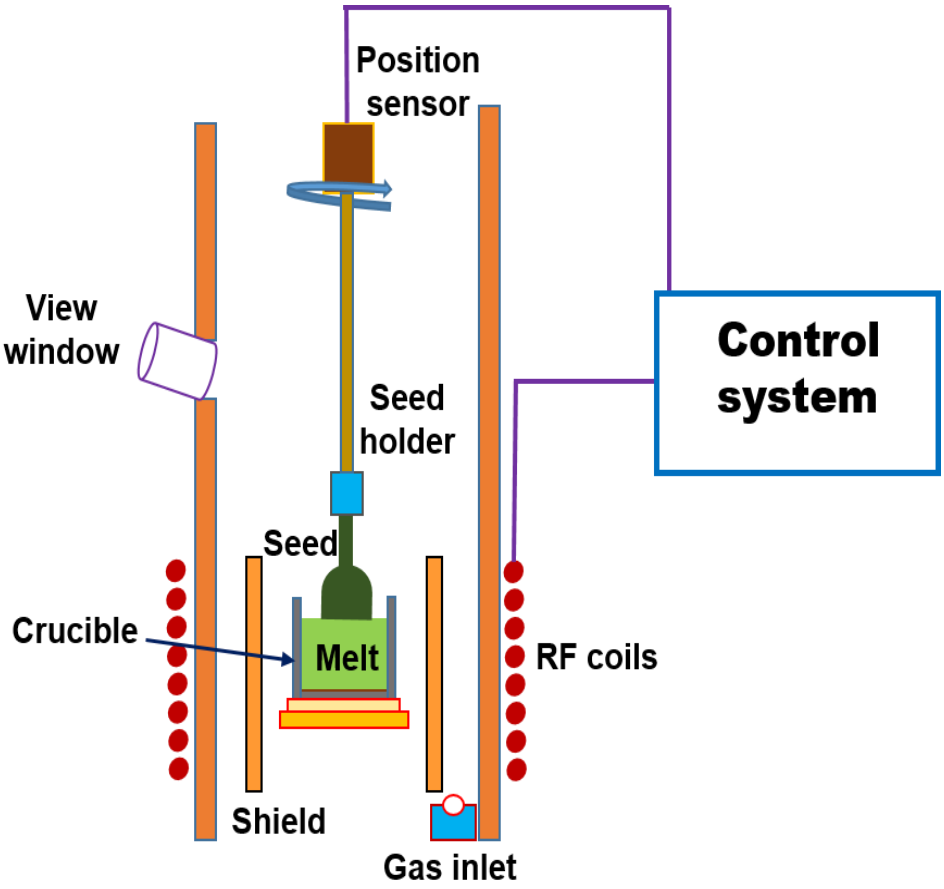

Figure 2.8 Crystal growth by Cz machine

2.3.1.3 Advantages of Cz technique

- High quality single crystals can be grown
- High melting compound can be grown
- High vapor pressure material with modified Cz technique can be grown

2.3.2 Zone melting technique

Zone melting technique is another melt growth technique for growing single crystals and it is well known for refining or purification of the materials. In this technique, the 'zone' means molten zone. For the purification of the materials, a portion of the solid material is first melted and then the molten zone is passed along the length together with heating elements. The floating zone technique is being used since half a century ago. Now a day the commercial equipment of floating zone technique is available with adaptability, compactness of design and high efficiency. Therefore, this technique is excessively used to grow single crystals of variety of oxides materials, metals, inter-metallics, etc. This method is usually applied to materials having large surface tension.

2.3.2.1 Fundamental consideration for growth

In the floating zone technique, the refinement or purification of material depends on the segregation coefficient of the impurity present in the material. When crystallization takes place, it rejects impurities on basis of distribution coefficient at the interface. If the zone refining is applied to a crystal having impurity with low segregation coefficient, then the resulting crystal is more pure compared to the original one. The crystals of high degree of purity can be obtained by more than one pass. Such

process is called 'zone refining'. For getting the high purity silicon and germanium, zone refining process is used. The simplicity of the process, the capability to produce a variety of organic and inorganic materials of extreme high purity is the main reasons for the importance of zone refining. This technique is able to produce dislocation free crystal with a low defect density. Keck [105] proposed floating zone technique and Golay [106] used a variant of the zone melting technique in which there is no need of crucible. Optical floating zone technique is one of its variants, which is a crucible less growth technique. In this technique, heating of material is done by the optical lamps [105,106].

In the optical floating zone technique, the heating of material is done by IR radiation, which is produced by a set of halogen/xenon lamps. Halogen/Xenon lamps (which may be either two or four depending on the system) are placed at one of the focal points of ellipsoid mirrors [Figure 2.9]. The radiation is reflected from the mirrors and focused at the other focal point of the mirrors, where the material to be grown is placed. The temperature profile can be changed by the adjustment of the power of the

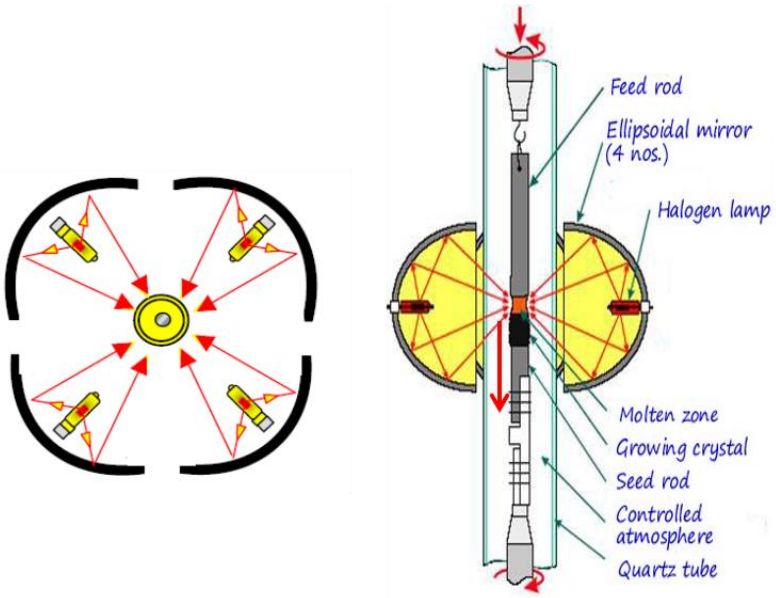

Figure 2.9 Schematic of the Optical floating zone process

lamps on the basis of our requirements. The schematic of four halogen lamps with ellipsoidal mirror based optical floating zone machine is shown in Figure 2.9.

2.4 Introduction of optical floating zone technique

2.4.1 Details of optical floating zone technique

The different types of the single crystals are grown by using optical floating zone (OFZ) technique. OFZ technique is a crucible less technique; hence it allows accessibility of favorable oxygen-rich ambience during the growth that leads to high quality single crystals. The crystals grown by OFZ method are free from impurities arising from the crucible material and defects such as oxygen vacancies and color centers. The three orthovanadate single crystals like YVO_4, $GdVO_4$ and $LuVO_4$ (part of the present work) are grown by OFZ technique in our Lab. The available OFZ equipment used for the growth single crystals is a four halogen lamped based machine. The photographs of the complete and inside view of floating zone are shown in the Figure 2.10-2.11 respectively.

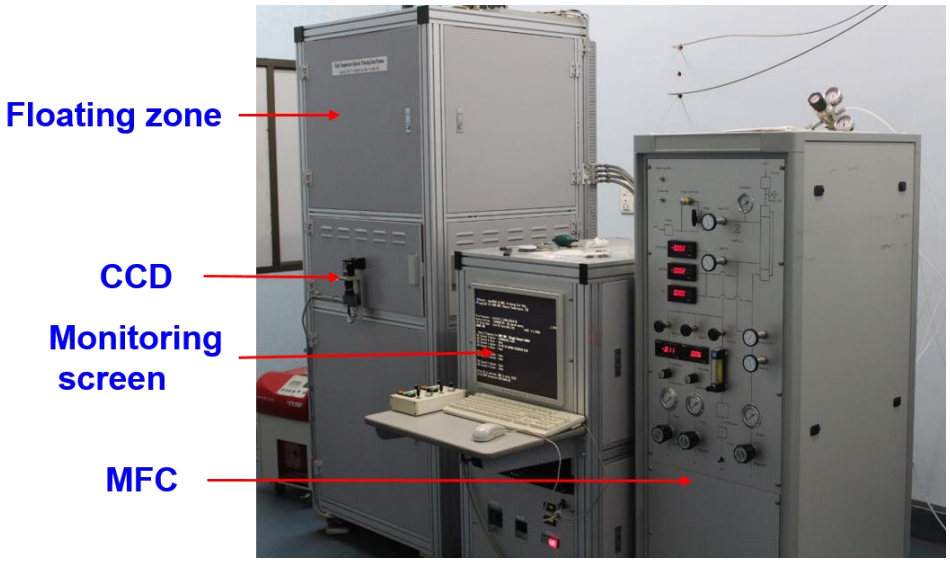

Figure 2.10 Complete setup of the optical floating zone equipment (MFC: Mass flow controller)

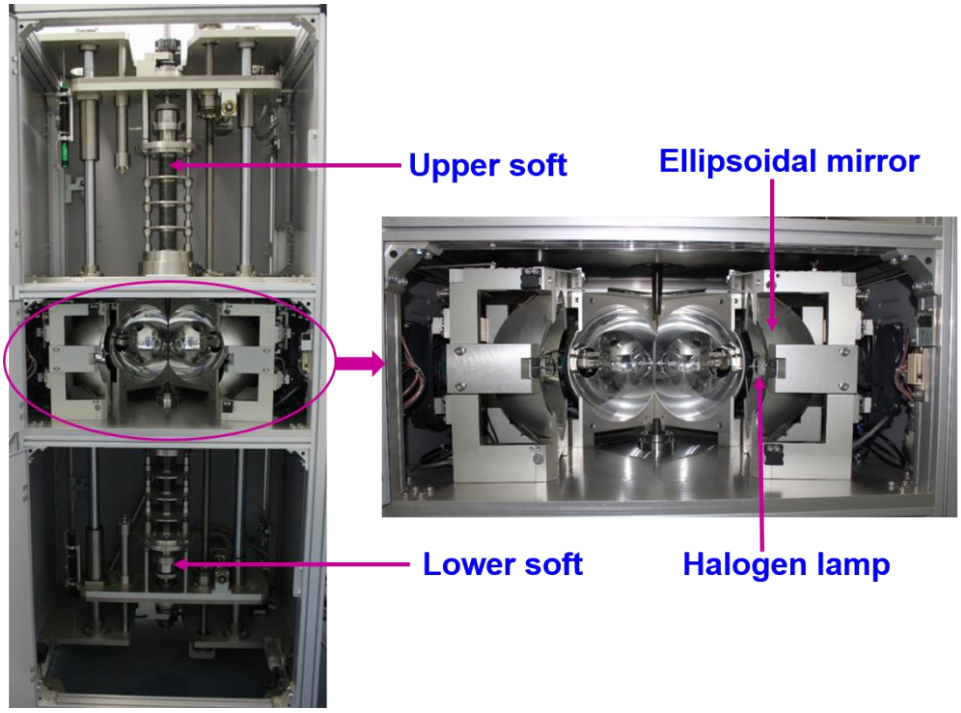

Figure 2.11 An inside view of the optical floating zone equipment

For growth of single crystal using floating zone technique, there is requirement of the polycrystalline feed rod in the form of cylindrical shape. The feed-rod is prepared from synthesized powder and sintered. Subsequently this feed rod is hanged in the holder of the upper shaft of machine. The seed crystal of a particular orientation is kept in the seed holder of the lower shaft (Figure 2.11). IR radiation of halogen lamps is focused at the focal point of the mirrors and at this point, the temperature is maximum because of the absorption of light by the material which is under growth. The tip of the feed rod and seed crystal are kept at the focal point to melt the feed rod for the growth of single crystals. The power of the lamps is increased slowly and melting of feed rod started as soon as the temperature at the feed rod reaches to the melting point of the material corresponding to a particular power of the lamps. The pulling rate, counter

rotation rate of feed rod and seed crystal are optimized for the growth of single crystal. The growth of single crystal is started with optimized translation rate of both shafts. The molten materials start solidifying at the melt–seed interface and growth of the single crystal begins on the seed crystal. The feeding of the material is stopped after the growth of crystal upto the desired length, and detached from the grown crystals. The quality of single crystal highly depends on quality of the feed rod, growth rate or pulling rate, rotation rate, growth ambience, temperature profile of molten zone and pressure of applied gas. A set of mass-flow controllers, are attached with OFZ machine, which controls the flow rates and pressure of gas atmosphere or mixture of gas (N_2, O_2) or dry air. The floating of molten materials against the gravity, which is sustained by the higher surface tension of the molten materials, is the foundation of the growth of single crystal in optical floating zone technique. Further, during the growth of crystal, the stability of the molten zone is very crucial parameter for avoiding over-flow of melt. In the OFZ techniques, there are three possible shapes of melt-solid interface such as convex, flat or concave interface like Cz technique. The most stable molten zones are observed in the slightly concave interface whereas the convex interfaces are not considered for growth of crystals. There are many advantage and disadvantage of floating zone technique, which have been listed below [98,102]:

2.4.2 Advantages of OFZ method

- As it is crucible free growth, hence there is no impurity imbedded from crucible.
- Higher level of oxygen ambient can be used even for high melting oxide material.
- Faster growth rate is possible in this technique.

- Both the congruent and incongruent melting materials can be grown by OFZ method.

2.4.3 Drawbacks of OFZ method

- OFZ technique is not able to grow large diameter size crystals.
- The low surface tension or high viscosity materials is difficult to grow by OFZ technique.

The specifications of OFZ equipment which is available in our Lab, LFMD, RRCAT are listed in the following Table 2.1.

Table 2.1 Specifications of OFZ equipment (FZ-T-10000-H-HR-I-VPM-PC)

1	Maximum operating temperature	2200 ˚C
2	Maximum crystal growth length	250 mm
3	Maximum gap adjusting length	250 mm
4	Growth speed	0.1-300 mm/hr.
5	High speed movement	1-160 mm/min.
6	Rotation rate	3-100 rpm
7	Number of mirrors / lamps	4 sets
8	Ultimate achievable vacuum	$5x10^{-5}$ torr
9	Maximum Pressure	9.5 atm
. 10	Monitoring	CCD camera

2.5 Introduction of experimental techniques for characterization

2.5.1 X-Ray diffraction techniques

In 1913, W. L. Bragg used the diffraction of X-ray light from the single crystals to explore structural properties of the various material. W. L. Bragg and his father was awarded the Nobel Prize in the field of Physics in 1915. Their works were published and formed abridged in X-rays and crystal structure. After the discovery of diffraction of X-rays from the crystal, the X-ray diffraction has been widely used for the analysis of molecular structure of different kind of materials in form of monocrystalline or polycrystalline powder forms. W. L. Bragg demonstrated the diffraction of X-ray light from a single crystal, which behave like the diffraction grating such as the individual atoms periodically aligned on plane of the crystal. X-ray is diffracted from these lattice planes and interfered constructively as per the condition of Bragg's law

$$n\lambda = 2\, d_{hkl}\, sin\theta \ldots\ldots\ldots\ldots (2.19)$$

where n integer number, λ is X-ray wavelength, d_{hkl} is the spacing distance between to consecutive lattice planes, and θ is the incident angle of the X-ray beam [107,108]. Further, there are different type of X-rays diffraction based techniques for analyzing the structure of the materials.

2.5.1.1 Powder X-Ray diffraction measurement

The powder X-ray diffraction (XRD) method is the most common and efficient technique for the determination of phase identification of the materials as well as structure. The powder XRD is an appropriate method to examine whether the particular material has form of amorphous or crystalline. Crystalline phases or phase formation of the materials can be identified with the comparison of the powder XRD pattern of the

samples along with the fundamental data available in Joint Committee on Powder Diffraction Standards (JCPDS). The XRD technique is also used to live analysis of the cell parameters of material as a function of the temperature, pressure and phase diagrams & phase transitions. Also, effect of the doping concentration, on the lattice parameters and structure of materials can be determined.

In the present research work, the powder X–rays diffraction (XRD) patterns were recorded for the synthesized powder and powder of grown crystals using a Rigaku Ultrax-18 powder diffractometer operated at 40 kV, 50 mA in Bragg–Brentano geometry with a curved crystal graphite 224-R monochromator. The XRD data were recorded using Cu-K_α in the range 20-70^o with step of 0.01° and a scan rate of 1° min^{-1}. All the measurements were carried out under the similar conditions. The photograph of Rigaku Ultrax-18 powder diffractometer is shown in Figure 2.12 [109–111].

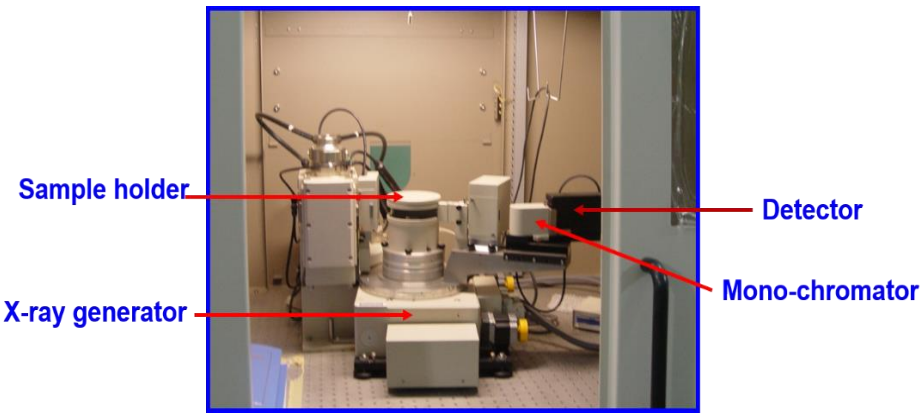

Figure 2.12 Powder X-ray diffractometer set up

2.5.1.2 High-resolution X-rays diffraction method (HRXRD)

High-resolution X-rays diffraction method (HRXRD) is used for the assessment of crystalline quality of single crystal and characterization of thin film. In this technique,

the monochromatic and highly collimated X-rays light is used. Principle is similar to the powder x-rays diffraction. This method is based on Bragg's condition. Whenever Bragg's condition is satisfied, the Bragg's peak appears. HRXRD usually measures scattered X-ray intensity as a function of omega and/or 2theta. This technique is used to check the strain, mismatch of lattice of thin film and orientation, strain and crystalline quality of grown crystals. When diffracted X-rays intensity at angle 2theta is measured with respect to omega (angle between the incident x-ray and surface of the sample) then it is called the rocking curve.

In the present work, for evaluating the crystalline quality of grown crystals the rocking curve measurements of three orthovanadates crystals were carried out using the synchrotron radiation source INDUS-2 on [100] sample for the (200) diffraction peak. The experiments were performed in the ADXRD beam-line (BL-12) of the Indus-2 synchrotron facility at RRCAT, Indore, India. The ADXRD beam-line (BL-12) has a Si (111) double crystal monochromator and a six circle Huber (model 5020) diffractometer. The instrumental broadening was found to be <15". The wavelength of the X-ray used for the rocking curve measurement was ~0.857Å (14.43 keV) [112].

2.5.1.3 Laue diffraction method

Laue diffraction method is the oldest technique of X-rays diffraction. First, X-ray diffraction experiments were carried out by M. von Laue. He did experiments using the continuous X-ray spectrum called Bremsstrahlung. In the experiment, he obtained a picture containing a pattern of spots and each spots corresponds to coherent reflection or diffraction of the X-ray light from one set of the crystal planes. In the Laue method, a continuous spectrum of X- rays is incident in a fixed angle on the single crystal and for each set of planes (hkl), the inter-planer distance d, and the Bragg's angle are fixed.

The diffracted x-rays spots are obtained whenever the Bragg's condition is satisfied. The symmetry pattern of diffracted spots on the photographic plate make it possible to deduce whether the crystals are cubic, tetragonal, or other crystal structures in the sample [109].

In the present work, Proto make Laue machine has been used to record the Laue pattern of the plate of grown crystals. The machine has Mo source used as target for X-rays and is operated in the reflection geometry. The photograph of instrument is shown in the following Figure 2.13.

Figure 2.13 Proto-make Laue instruments

2.5.1.4 X-ray photo-electron spectroscopy Measurements

X-ray Photoelectron spectroscopy is used for finding the elemental composition, chemical and electronic state of elements. In this method, photo-ionization of atoms and analysis of the kinetic energy distribution of the emitted photoelectrons are involved. This technique is generally used to study the electronic state of elements on the surface of a sample [113]. The elemental composition of samples upto around 1000 ppm levels can be obtained by using this technique. In the X-ray photoelectron spectroscopy (XPS), the excitation photon energy is normally used in the range from 200 to 2000 eV [113]. A photon with energy of $E=h\,v$ [h-Planck constant= 6.62 x 10^{-34} J-s and v– frequency] is incident on the sample surface, which is absorbed by an atom of sample that results ionization with ejection of an inner shell (core) electron [113]. When the kinetic energy of photo-electrons is more than the work-function of the sample and it comes out from the surface of the sample with a finite kinetic energy. The distribution of kinetic energy of the emitted photoelectrons (i.e. the number of emitted photoelectrons as a function of their kinetic energy) can be measured using any appropriate electron energy analyzer and a photoelectron spectrum.

The equation for conservation of energy is given as

$$hv = KE + \phi + BE \quad \text{.....(2.20)}$$

Now using above formula, the binding energy (BE) of the emitted photo-electron are written as

$$BE = hv - KE - \phi \quad \text{.....(2.21)}$$

For each and every element, there will be a characteristic binding energy associated with each core atomic orbital electron that will be emitted with specific

kinetic energy. Therefore, these emitted photo-electrons with specified kinetic energies, will give rise to a characteristic set of peaks of each element in the photoelectron spectrum. The presence of peaks at particular energies indicates the presence of a specific element and specific oxidation state in the sample, and also the intensity of the peaks is related to the concentration of the elements in sample. Hence the XPS technique provides a quantitative analysis and qualitative analysis of elements present on the surface (in depth around 30-50A) of the sample.

In the present work, X-ray photoelectron spectroscopy measurements were carried using hard x-ray photoelectron spectroscopy (HAXPES) beamline BL-14, at synchrotron radiation facility Indus-2 (2.5 GeV, 200 mA) [113]. The excitation energy of X-rays from double crystal monochromator (Si(111)) was 4.311 keV. The experimental station of beamline is equipped with Hemispherical analyzer and detector system (Phoibos 225, Specs make). The typical pressure in the experimental station is 5×10^{-9} mbar. Initially, the survey spectra were recorded over a range of 0 to 1000 eV for each sample. The energy calibration has been done with respect to the reference (C_{1s} peak at a binding energy value of 284.8 eV adventitious carbon) for all edges [113].

2.5.1.5 X-ray fluorescence (XRF) measurements

X-ray fluorescence spectrometry (XRF) is a non-destructive and most efficient method to find composition of the elementals present in the materials by measuring the emission of characteristic X-rays from the relevant materials, which have been excited by high-energy X-rays radiations [114]. Qualitative and quantitative analysis can be done for all elements starting from beryllium (Z= 4) to uranium (Z= 92). This technique offers high accuracy and precision for the detection of wide range of elements beyond beryllium in the periodic table with concentration as low as the ppm-level depending

upon the source intensity. When materials are excited with X-ray with energy higher than the respective absorption edge of elements under investigation, the tightly-held inner electrons are dislodged and the atom becomes unstable [109,110]. Subsequently an electron in the outer shell occupies the inner shell with the missing electron via emission of X-ray photon as shown in Figure 2.14.

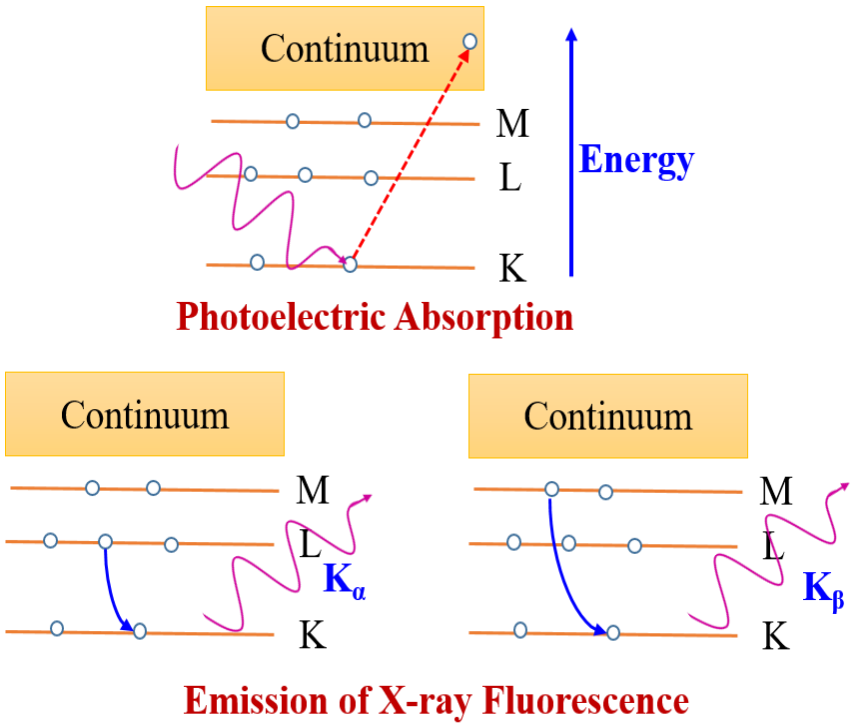

Figure 2.14 X-ray fluorescence process

The emitted X-ray photon is X-ray fluorescence whose energy is lower than the primary incident X-rays but is the characteristic to the individual elements. So the emitted fluorescent X-rays are used for detection of the elements present in the sample. A typical X-ray fluorescence spectrum consists of multiple peaks at different energy and of different intensities resulted from several transitions [109,110]. In most of the cases, the fluorescence from the innermost K and L shells are used in XRF detection. The name of the X- ray emission lines or transitions, are labeled by K, L, or M, which corresponds to the shell from which the electrons are initially removed. The X-ray

photons emitted from K lines are the highest energy, and then followed by L, then M and so on. Further the different transitions to the particular shell from the upper energy shells are denoted by the subscripts α, β, γ etc. and this subscripts indicate the quantum state of that upper energy shell [109,110].

2.5.1.5.1 Qualitative and quantitative Analysis

The X-rays fluorescence wavelength is the characteristics of the particular elements present in the sample. Therefore, the qualitative analysis of elements can be obtained with help of the wavelength of characteristic fluorescence. The quantitative analysis of elements can be done by comparing the sample spectra with the known standard reference spectra. The concentration of each element upto ppm level in the sample can be determined from area under the peak. In the present study, to estimate the dopant concentration in the grown crystals, X-ray fluorescence measurements were carried out on the samples obtained from the grown single crystals and prepared standard samples. The experiments were performed in the Microprobe X-ray fluorescence Beam-line (BL-16) of the Indus-2 synchrotron facility. The beam-line works in the X-ray energy range of 4-20 keV. The beam-line (BL-16) layout is shown in Figure 2.15 [114,115].

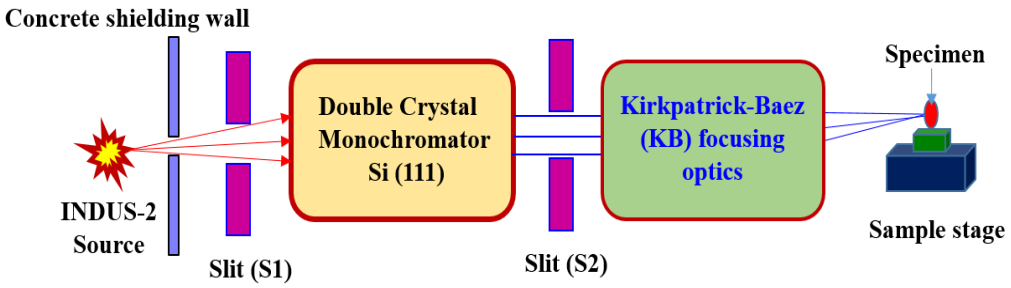

Figure 2.15 Schematic of beam-line 16 [114]

2.5.2 Refractive index measurements

Refractive index (RI) and thermo-optic coefficient of the gain medium are important parameters for the designing of a laser system. The temperature dependent refractive indices of the grown crystals are determined along the principal directions using Prism coupling technique at different wavelengths. The basic schematic and mechanism of RI measurements by Prism coupling technique is shown in the Figure 2.16-2.17. In this technique, an oriented polished sample plate of thickness preferably 0.5 to 1mm fabricated from the grown crystals is brought in intimate contact with the optical prism having known refractive index (n_p) using an in-built coupling head, which is pressed pneumatically with a pressure typically of the order of 4-6 bar. A monochromatic laser beam with selected polarization TE (s) or TM (p) is directed into the sample prism-plate interface through the prism. The intensity of the reflected light from the prism sample interface is recorded at various incident angles with an appropriate detector [Figure 2.17] and critical angle (θ_c) is monitored. As the angle of incidence (θ_i) is decreased with respect to critical angle (θ_c), a fraction of the incident light will propagate along the interface that results in an abrupt decrease in the reflected light at the detector [116] and a knee is observed in the reflected intensity vs incident angle plot. A typical intensity vs angle of incidence plot of the laser light from the sample surface is shown in Figure 2.17.

The refractive index of the specimen of interest (n_s) is estimated by detecting the critical angle for both TE and TM modes of incident light i.e orthogonal polarization mode. From the measured θ_c the refractive index along two orthogonal principle direction depending on the sample orientation can be determined using the relation $n_s = n_p \sin\theta c$ [116]. The value of n_x (n_e) of a–cut uniaxial crystals is obtained for TE mode

and n_y (n_o) of same crystal is obtained for the TM mode of incident light. This technique is simpler compared to minimum deviation method as it avoids the need of fabrication of prism of the material under investigation.

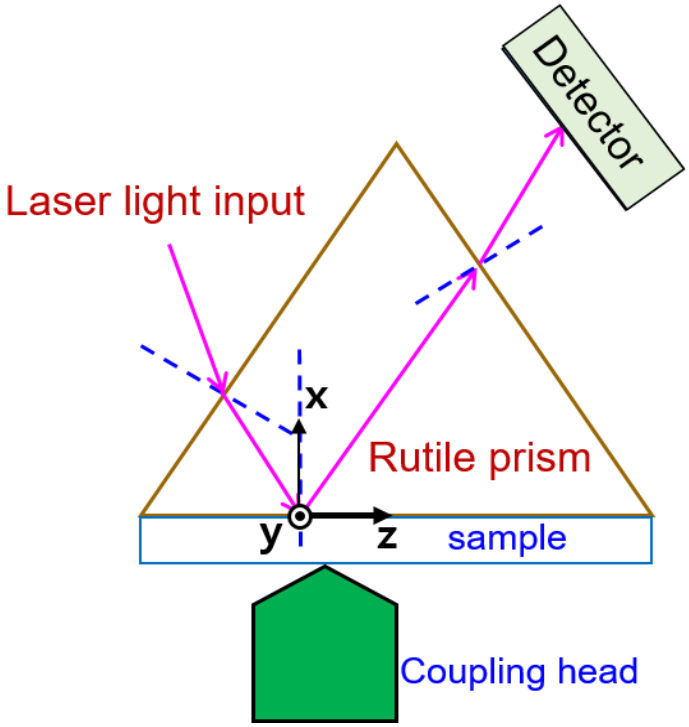

Figure 2.16 Schematic of RI measurements by Prism coupling technique

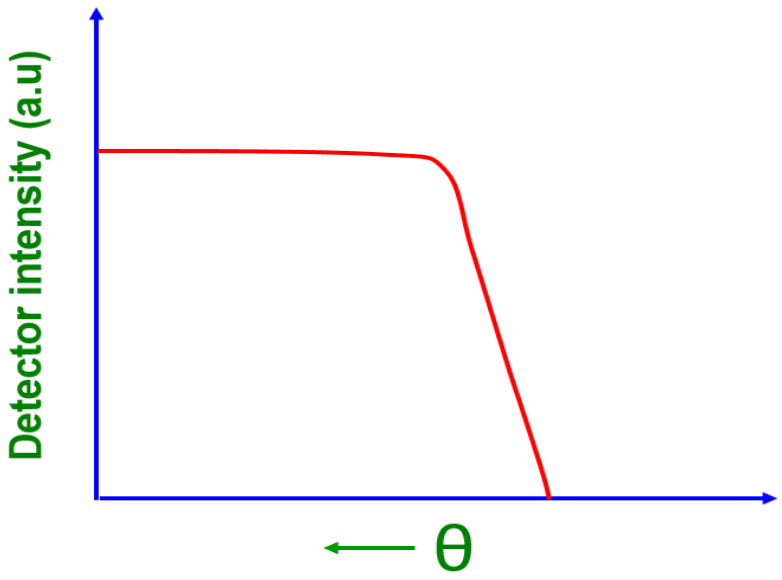

Figure 2.17 RI reflectivity curve

Onodera et al. [117] have shown that the accuracy of the prism coupling method is comparable to that of the minimum deviation method if the prism refractive index and coupling-prism apex angle are known with accuracy better than 10^{-4} and 10s, respectively [117–120].

In the Crystal Growth Laboratory, at LFMD, for measurement of refractive index a commercial Prism coupler (model 2010/M; manufactured by Metricon Corporation, UK) equipped with five laser inputs (wavelengths 408, 532, 828, 1064 and 1551 nm) is available as shown in Figure 2.18.

In the equipment, a Rutile (TiO_2) prisms, (200-P-4) which have refractive index higher than most of the samples, was used. The refractive index calibration of the instrument was done by using standard fused silica (ICS 14) and the experimental error was estimated by comparing the measured refractive index of Schott LASF18A with the data sheet. The error is ~$1x10^{-3}$. During the measurement of the refractive index of material, two major sources of error are [116,121–123]:

- The inaccuracy in the orientation of the sample
- The inaccuracy in temperature value during measurements

Figure 2.18 RI measurements setup

2.5.3 Optical transmission and absorption measurement

The absorption characteristics of the gain medium provide useful information in context to the pumping of the gain medium. As population inversion is achieved in the gain medium via absorption of pumping light, an amplified emission of light at the laser wavelength via stimulated emission takes place. Therefore, it is mandatory to investigate the absorption properties of the gain medium. Absorption characteristics are measured by Ultraviolet, visible and NIR (UV-VIS-NIR) absorption spectroscopy.

In this measurement the possible spectral ranges (wavelengths) of interest are:

- Ultraviolet (UV) 200-400 nm
- Visible (VIS) 400-700 nm
- NIR 700-3000 nm

When electromagnetic radiation is passed through a sample and selective absorption takes place depending upon the transitions associated with dopant or in the impurities in materials. These absorption lines or bands are the direct manifestation of the sample absorption characteristics. The inter band transitions corresponding the band gap of the materials occur from the valance band to conduction band and other transitions occur by the impurity or defect levels and molecular vibration levels associated with host medium [124,125].

The UV-VIS-NIR spectrophotometer made by JASCO (model no. JASCO 670) has two light sources, a deuterium (D) lamp for ultraviolet light and a Halogen lamp to cover the visible and NIR spectrum [124,125]. The photograph of JASCO 670 is shown in the Figure 2.19

Figure 2.19 UV-visible-NIR spectrophotometer set up

2.5.3.1 Principle

When light is incident on a homogeneous dielectric medium, a part of incident light is reflected, a part is absorbed by the medium and remaining part is transmitted (Figure 2.20). The absorption of light by an optical medium is quantified by absorption coefficient α. This is defined as the fraction of light absorbed per unit length of medium.

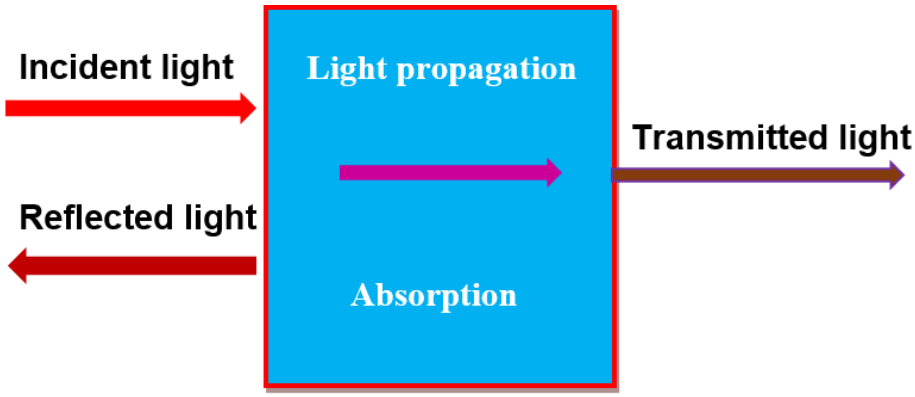

Figure 2.20 Light through an optical medium

Let us consider an incident light having intensity I_0 is propagating into the sample along the z direction and intensity of light at a depth z inside the sample is given as I(z) as shown in Figure 2.21.

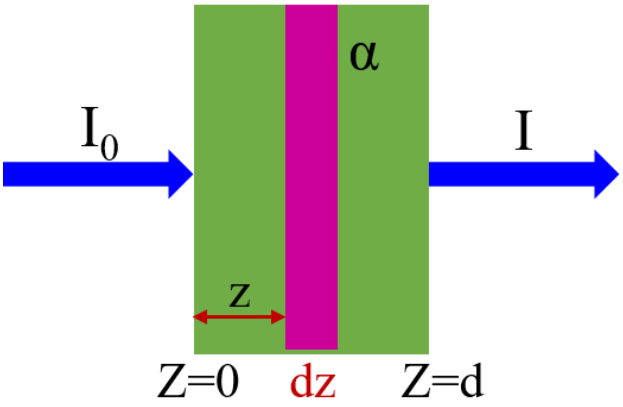

Figure 2.21 Schematic of propagation of light inside the sample

Now the change of intensity with the propagation light of an infinitesimal small distance dz (neglecting both the scattering and reflection loss) is

$$dI = -\alpha\, dz\, I(z) \quad \text{.....(2.22)}$$

On the integration from Z=0 to d, we get

$$I = I_0 e^{-\alpha d} \quad \text{.....(2.22)}$$

This equation is called Beer's law.

Now consider the reflection loss (R_1 and R_2) from the both the front and back surface of the sample, the transmittance of light is given as

$$T = (1-R_1)e^{-\alpha d}(1-R_2) \quad \text{.....(2.23)}$$

If the front and back surfaces have equal reflectivity R, then equation becomes:

$$T = (1-R)^2 e^{-\alpha d} \quad \text{.....(2.24)}$$

Using the above equation the absorption coefficient can be calculated as per the following [126–129]:

$$\alpha = \frac{1}{d} ln\left[\frac{(1-R)^2}{T}\right] \quad \text{.....(2.25)}$$

where, T is transmittance, R is reflectivity [calculated from Sellmeier's equation using, $R \sim (n-1)^2/(n+1)^2$] and d is the sample thickness [126–129].

2.5.4 Photoluminescence measurement

Fluorescence property of the gain medium is important parameters for designing and assembling the laser cavity and fabrication of laser system, particularly for selecting

the pumping and lasing wavelength. Photoluminescence (PL) is one form of luminescence (light emission) and is distinguished by photo-excitation (excitation by photons). Photoluminescence (PL) is a process in which the active ions absorb photons and go to a higher energy state and then come down to an intermediate state or metastable state via radiation less transition. The excited atoms finally relax into the lower or ground state via emission of photons [130]. In the PL process, the time of relaxation is extremely short and it may be the of order of ~ns, µs, second, minutes depending on the material as well as active ion. The main requirement for the measuring the photoluminescence are stable monochromatic light source, optic to focus light on the sample, sample holder, collection optics, monochromator and detector. Actual excitation and emission wavelength and collection optics for emission of light depends on the nature of the materials. Typically, the excitation and collection of emission of light are at 90 degrees. Figure 2.22 shows photograph of PL setup.

Figure 2.22 Schematic of PL measurements setup

In the present study, for investigating the emission characteristics of the samples, photoluminescence (PL) spectra of grown crystals of orthovanadate are

recorded for the [100] oriented plates at room temperature using Edinburg instrument PL spectrometer (FL-FS90-S). The samples are excited at desired wavelength and the corresponding PL spectra are recorded. An InGaAs with integrated lock-in steady state (NIR 300/2, G5852-23) is used to detect IR luminescence spectra. [130].

2.5.5 Fluorescence life time measurement

The fluorescence lifetime is a measure of the time a fluorophore that spends in the excited state before returning to the ground state by emitting a photon. Absorption and emission processes are related to the populations or number density of atom or molecules available in ground or excited state [130]. In general, the behavior of an excited population of fluorophores (atoms or molecules) is described by the rate equation:

$$\frac{dn^*(t)}{dt} = -kn^*(t) + f(t) \dots\dots\dots\dots (2.26)$$

where n* is the number of excited atoms at time t, k is the rate constant of all de-excitation processes and f(t) is an arbitrary function of the time, describing the time course of the excitation. The dimensions of k are s^{-1} (defined as number of transitions per molecule per unit time).

If excitation is switched off at t = 0, then above equation becomes

$$\frac{dn^*(t)}{dt} = -kn^*(t) \dots\dots\dots\dots (2.27)$$

and the solution of this equations becomes

$$n^*(t) = n^*(0)exp(-kt) \dots\dots\dots\dots (2.28)$$

The lifetime τ is equal to $\boldsymbol{k}^{-1}$.

The lifetime of excited fluorophores (atoms or molecules) is the time that it takes for the number of excited molecules to decay to 1/e or 36.8% of the original population according to the following equation

$$\frac{n^*(t)}{n^*(0)} = \boldsymbol{e}^{-t/\tau} \ldots\ldots\ldots\ldots\ldots\ldots (2.29)$$

The de-excitation rate k is the sum of the rates of all possible de-excitation paths:

$$k = k_f + k_i + k_x + k_{ET} = k_f + k_{nr} \ldots\ldots\ldots\ldots (2.30)$$

where k_f is the rate of fluorescence, k_i the rate of internal conversion and vibrational relaxation, k_x the rate of intersystem crossing, k_{ET} the rate of inter-molecular energy transfer and k_{nr} is the sum of rates of radiation less de-excitation paths. Atoms or molecules also decay via non-radiative process in addition to the radiative process. The non-radiative process occurs under different conditions, such as in the case of isolated molecules in "gas-phase" where they decay due to only internal conversion and intersystem crossing. In the case of condensed phase, an additional pathway of decay of atoms or molecules is due to interaction with molecular environment via excited state reactions, energy transfer, etc. In addition to this, the non-radiation transition occurs due to the presence of polar environment that results into the decrease in the fluorescence lifetime. It happens because of larger dipole moments of surrounding molecules that can increase the efficiency of energy transfer. Therefore, the radiative lifetime $t_r = k_f^{-1}$ for a given molecule is a constant.

The fluorescence lifetime of molecules or atoms is given as

$$t = k^{-1} = (k_f + k_{nr})^{-1} \ldots\ldots\ldots\ldots (2.31)$$

It depends on the environment of the molecule through k_{nr}. The fluorescence quantum yield (QY) is proportional to the fluorescence lifetime:

$$QY = \frac{k_f}{k_f + k_{nr}} = \frac{k_f}{k} = \frac{t}{t_r} \approx t \ldots\ldots\ldots\ldots (2.32)$$

However, the measurement of fluorescence lifetime is more robust than measurement of fluorescence intensity (from which the QY is determined), because it depends on the intensity of excitation and the concentration of the fluorophores [130].The fluorescence intensity $I(t) = k_f\, n^*(t)$ is proportional to $n^*(t)$. There are various techniques to measure the lifetime of excited atoms or molecule. In the present study the pulsed (or time) excitation technique was used to measure the fluorescence life time of excited atoms or molecule.

In this method the atoms or molecules are excited by a very short pulse (at t = 0) and the decay of florescence intensity with de-excitation of atoms or molecules is measured using a detector based on time correlated single photon counting [Figure 2.23].

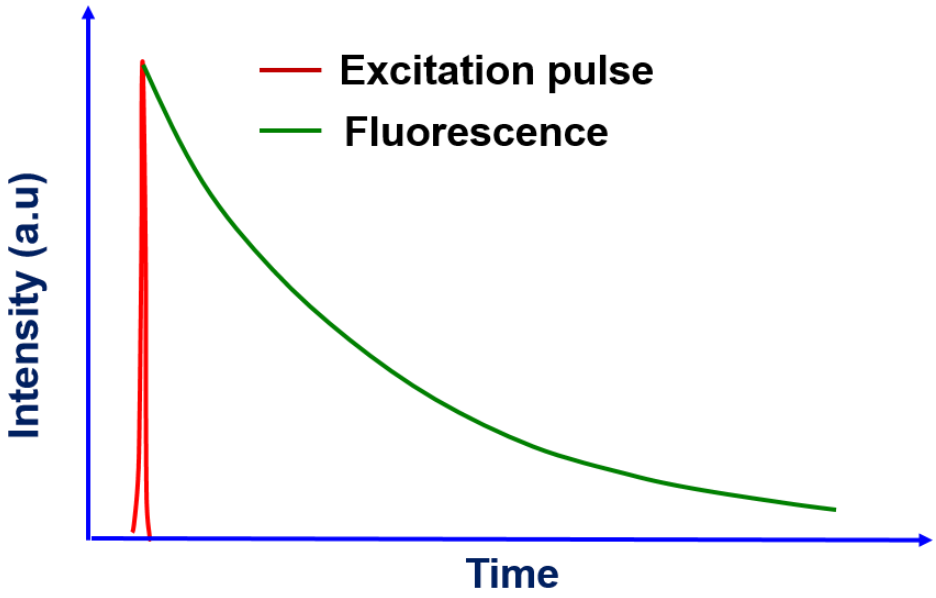

Figure 2.23 Fluorescence decay of atoms or molecules

The decay of fluorescence intensity (at t = 0) is given as [130]

$$I(t) = I(0)\exp\left(-\frac{t}{\tau}\right) \ldots\ldots\ldots (2.33)$$

The instrument response function (i_{REF}) is measured as a response of the instrument to scattered excitation pulse. The parameters of I(t) (the lifetime τ) are usually obtained by nonlinear fitting combined with a deconvolution procedure. The deconvolution is not necessary, when the excitation pulse is very short (fs-lasers) compared to the lifetime (τ) and/or high precision of lifetime determination is not required.

In the present works, the fluorescence lifetime measurements were carried out using ultrafast technique. In this measurement the sample was excited using a Ti:Sapphire femto-second laser operating at desired wavelength with 35 fs pulse width (FWHM) and repetition rate of 1 kHz (Coherent legend Elite, USA). The fluorescence decay profile of the emission of rare earth ion was recorded using IR detector and 1 GHz bandwidth oscilloscope.

2.5.6 Optically homogeneous measurement by birefringence interferometry

Optically homogeneous crystal is an important requirement for laser application. As a part of checking the quality of the grown crystal, the optical homogeneity of the crystal can be further investigated by birefringence interferometry as it provides qualitative assessment about the overall optical uniformity of the crystal [130].

Birefringence interferogram, which is a set of fringes, gives a collective information about all the flaws or defects in crystals.

The optical homogeneity/birefringence of crystal is influenced by residual stress, micro-cracks, inclusions, bubbles, spatial variation in the defects density across the crystal, and sub grain structures in the lattice (misorientation) due to these defects. Any type of optical inhomogeneity in the crystal is clearly revealed in this measurement. The technique is based on the formation of interference fringes between the component of ordinary ray and extra-ordinary ray when they pass through the birefringence sample. For this measurement a [100]-oriented polished sample of grown crystal of 1 mm thickness was prepared. A schematic of the measurement setup is shown in Figure 2.24.

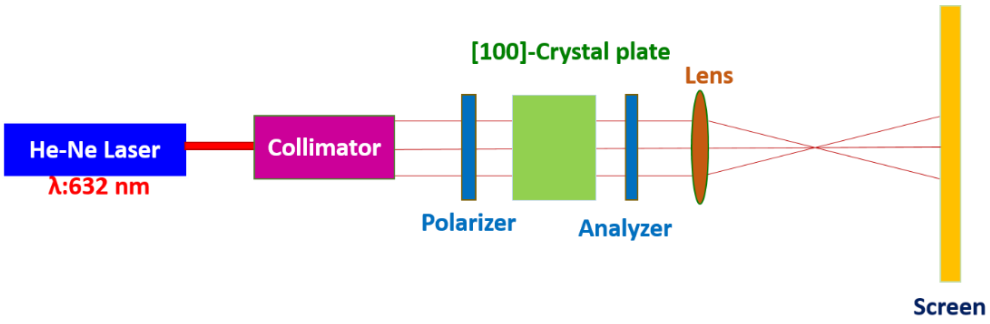

Figure 2.24 Schematic of birefringence interferometry set up

A collimated linearly polarized light (45° with respect to c-axis of the sample) of He-Ne laser (632.8 nm) incident normally on the sample and passes through the cross-polarizer (at 90° to the incident light polarization) and lens. The interference fringes form due to superposition and delay (birefringence induced path difference) between the component of extra-ordinary ray (n_e) and ordinary ray (n_o) is observed on the screen and recorded [131,132].

2.5.7 Judd- Ofelt analysis

Judd-Ofelt theory describes the intensities of lanthanide and actinide transitions in solids and solutions. The utility of the Judd-Ofelt theory is that it provides a theoretical expression for the line strength. The 4f-4f intra-band (mostly) electric dipole (ED) transitions of rare earth ion which are generally not allowed because of the same parity of initial and final states (ED operator is of odd parity) but become allowed due to resultant mixed parity in D_{2d} non-centrosymmetric crystal field of YVO_4 /$GdVO_4$/ $LuVO_4$. However, shielding by outer shells of completely filled $5s^2$ and $5p^6$ is enough to makes the f-f transitions sharp and distinct. The f-f transitions strength of rare earth ion can be analyzed by using Judd-Ofelt theory [14]. According to this theory the line strength of force electric dipole transition between an initial J manifold $|4f^9[L, S]\ J\rangle$ and final J' manifold $|4f^9[L', S']\ J'\rangle$ is given as the relation:

$$S(J \to J') = \sum_{i=2,4,6} \Omega_i \left|\langle [S\ L], J \left\| U^i \right\| [S'\ L'], J' \rangle\right|^2 \quad \ldots\ldots\ldots\ldots\ldots\ldots\ldots\ldots\ldots\ldots\ldots (2.34)$$

$\langle \| U_i \| \rangle$ are the doubly reduced matrix elements of the unit-tensor operators for the transitions from the ground-state to the excited-state manifold, and the coefficients Ω_2, Ω_4 and Ω_6 are phenomenological Judd-Ofelt (J-O) intensity parameters [2]. These matrix elements, especially for the rare earth elements, are calculated in the intermediate coupling approximation [133]. The numerical values of the doubly reduced matrix elements for rare earth ion are computed by *Carnall et al.* [134]. The matrix elements are invariant irrespective of the environment of the ion and used for the present calculations. The experimental line strength of forced electric dipole transition S is calculated using [2,53]:

$$S_{J\to J'} = \frac{\int \alpha(\lambda)d\lambda}{\frac{8\pi^3\rho\bar{\lambda}e^2}{9ch(2J+1)}\left[\frac{(n^2+2)^2}{3n}\right]} \quad \ldots\ldots\ldots\ldots\ldots\ldots\ldots\ldots\ldots\ldots\ldots\ldots\ldots\ldots\ldots\ldots (2.35)$$

where c is the velocity of light, h is the Planck's constant, e is the charge of electron, ρ is the number density of RE ions per cc, J and J′ are the total angular momentum of initial and final states, $\bar{\lambda}$ is the mean wavelength and α(λ) is the absorption coefficient of absorption band, n is the refractive index of the material obtained using Sellmeier's equation and the integral in the numerator is the area under the absorption band [53].

The line strengths (S_{exp}) for all the transitions can be calculated from the absorption spectra using the above equation. Subsequently the JO parameters are calculated using the equation (2.34) and (2.35) by least mean-square fitting for all the transitions. As the number of the absorption lines are more than three it was possible to obtain over-deterministic solutions. Spectroscopic quality factor X = Ω_4/Ω_6 is an important parameter for predicting the stimulated emission for the laser active media.

Further, the emission characteristic can be evaluated using JO theory. Einstein's A coefficient (radiative transition rate) of emission can be estimated as:

$$A(J \to J') = \frac{64\pi^4 e^2}{3h(2J+1)\bar{\lambda}^3}\left[\frac{n(n^2+2)^2}{9}\right]\sum_{i=2,4,6}\Omega_i \left|\langle [S\,L], J \| U^i \| [S'L'], J' \rangle\right|^2 \quad .(2.36)$$

The Einstein A coefficient , can be estimated by using JO parameters calculated for the absorption spectra. However, the matrix values of ⟨‖Ui‖⟩ for emission are different as the transitions are reversed. The radiative lifetime of an excited state J is calculated as $\tau = 1/\Sigma A(J \to J')$.

The fluorescence branching ratio are given by $\beta(J \to J') = A(J \to J')/\sum A(J \to J')$ where the sum is taken over all possible terminal states. The life-time and branching ratio of emission transitions can be calculated. From the PL spectra the emission cross-section of the transition can be calculated by the following relation:

$$\sigma_e(\lambda) = \frac{\bar{\lambda}^4}{8\pi n^2 c \Delta\lambda_{eff}} A(J \to J') \qquad \ldots\ldots\ldots\ldots\ldots\ldots\ldots\ldots\ldots (2.37)$$

where λ is the mean wavelength of emission band and $\Delta\lambda_{eff}$ is the effective line-width of the transition [133–137]. Detail of Judd-Ofelt theory is given in the Annexure-I.

2.5.8 Measurement of laser performance of grown crystals

To check the laser performance of the grown single crystals, a laser testing experimental setup has been developed [Figure 2.25].

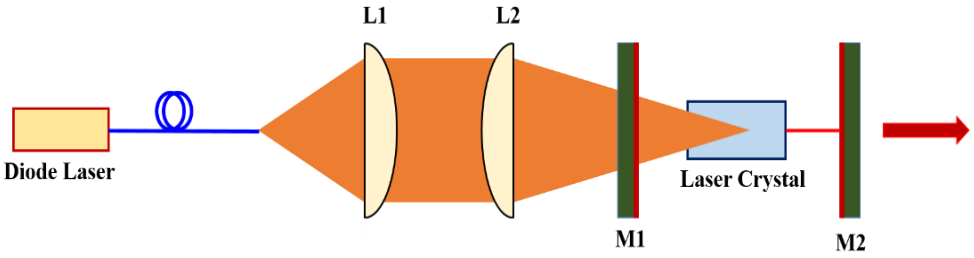

Figure 2.25 Schematic of experimental setup for CW laser operation

Some of the grown crystals, which have been oriented using Laue diffraction method, are used for the measurement. A plane-parallel resonator cavity has been designed for evaluating lasing characteristic of the oriented Nd:$GdVO_4$ and Nd:$LuVO_4$ laser element. The length of the designed cavity is kept ~ 50 mm. Reflectivity of the output coupler is varied and optimized at ~ 89% for maximum power output. The testing

of lasing has been carried out using 808 nm diode laser in end pumped configurations. The CW laser emission of the grown crystals has been demonstrated. The schematic diagram of laser cavity setup is shown in the Figure 2.25.

Chapter-3 Growth of Orthovanadate Single Crystals

The complete growth process of doped orthovanadate single crystals by using optical floating zone technique (OFZ) can be divided into three steps namely (1) synthesis of starting charge, (2) feed rod preparation, and (3) growth of single crystals.

3.1 Synthesis of starting charge

The synthesis and formation of proper phase of any material especially having volatile components are important for the growth of single crystals. The synthesis of orthovanadate materials, such as YVO_4, $GdVO_4$ and $LuVO_4$, requires careful attention because these materials have tendency to form secondary phase due to the volatility of V_2O_5, which is one of the starting precursors of orthovanadate.

3.1.1 Starting precursors for doped YVO_4

For growth of Yb doped YVO_4 single crystals, starting chemical was synthesized using AR grade Y_2O_3, V_2O_5 and Yb_2O_3 with purity level of 99.99% [Make:Alfa aesar] [Table 3.1]. The reaction equation of $Yb_xY_{(1-x)}VO_4$ is formulized as below:

$$\mathbf{xYb_2O_3 + (1\text{-}x)Y_2O_3 + V_2O_5 \longrightarrow 2Yb_xY_{(1-x)}VO_4}$$

Table 3.1 List of molecular weights in g/mol for Yb:YVO_4

Yb_2O_3	Y_2O_3	V_2O_5	$Yb_{0.008}Y_{0.992}VO_4$
394.078	225.781	181.833	204.480

Calculation of required materials:

For 1mole of Yb doped YVO_4 ($Yb_{0.008}Y_{0.992}VO_4$)

$0.008Yb_2O_3$ + $0.992Y_2O_3$ + V_2O_5 ⟶ $2Yb_{0.008}Y_{0.992}VO_4$

3.152 gm + 223.975 gm + 181.833 gm ➔ 408.960 gm

For one gram charge of $Yb_{0.008}Y_{0.992}VO_4$

0.0077 gm + 0.5476+ 0.4447 gm ⟶ 1gm

In the similar manner the chemicals required for 1.5, 3.0, 5.0, 8.0 and 15.0 at.% doping were calculated. Further, according to the our earlier report on the synthesis of YVO_4 materials [43], around 3% of amount of V_2O_5 extra has been be added for complete phase formation of YVO_4 to the compensate the loss of V_2O_5. For each concentration of Yb doping, a batch of 30 gm of total charge was calculated and synthesized as listed in Table 3.2. The accuracy of the measurement of weight of chemical by weighing machine is 1 mg.

Table 3.2 Calculated weight of the precursors for synthesis of Yb:YVO_4

Yb (at.%)	**Yb_2O_3 (gm)**	**Y_2O_3 (gm)**	**V_2O_5 (gm)**
0.8%	0.231	16.429	13.339
1.5%	0.432	16.266	13.301
3.0%	0.859	15.920	13.220
5.0%	1.420	15.466	13.113
8.0%	2.245	14.798	12.955
15.0%	4.096	13.300	12.603

Further, for growth of co-doped YVO_4 single crystals, primary Yb co-doped Er:YVO_4 materials were synthesized. In this the required chemicals for synthesis were

calculated as per the solid-state reaction equation for 30 gm batch and tabulated in the Table 3.3.

$$xYb_2O_3 + (1\text{-}x\text{-}z)Y_2O_3 + zEr_2O_3 + V_2O_5 \longrightarrow 2Yb_xEr_zY_{(1-x-z)}VO_4$$

Table 3.3 Calculated weight of the precursors for synthesis of Er co-doped Yb:YVO_4

Yb (at.%)	Er (at.%)	Yb_2O_3 (gm)	Y_2O_3 (gm)	V_2O_5 (gm)	Er_2O_3 (gm)
1.5	0.7	0.431	16.107	13.265	0.195
3.0	0.7	0.857	15.763	13.184	0.194
8.0	0.7	2.239	14.647	12.922	0.190
12.0	0.7	3.307	13.786	12.719	0.187

Similarly, for the growth of Nd co-doped Yb:YVO_4 single crystals, starting chemical were taken for synthesis of the materials. Required amount of chemicals were calculated according to the solid-state reaction equation for 30 gm charge. The table for required amount of chemicals are given in the Table 3.4.

$$xYb_2O_3 + (1\text{-}x\text{-}z)Y_2O_3 + zNd_2O_3 + V_2O_5 \longrightarrow 2Yb_xNd_zY_{(1-x-z)}VO_4$$

Table 3.4 Calculated weight of the precursors for synthesis of Nd co-doped Yb:YVO_4

Yb (at.%)	Nd (at.%)	Yb_2O_3 (gm)	Y_2O_3 (gm)	V_2O_5 (gm)	Nd_2O_3 (gm)
1.5	0.8	0.431	16.099	13.272	0.196
3.0	0.8	0.857	15.755	13.192	0.195

3.1.2 Starting precursors for doped $GdVO_4$

In case of Nd doped $GdVO_4$ materials, the starting precursors such as Gd_2O_3, V_2O_5 and Nd_2O_3 powder with purity of 99.99% [Make:Alfa aesar] are needed for synthesis. The 30 gm of charges for each doping concentration of Nd were calculated using solid-state reaction equations [Table 3.5]. Additional 2% of amount of V_2O_5 were added during the synthesis to compensate for the loss of V_2O_5 as it is volatile in nature.

$$\mathbf{0.008\ Nd_2O_3 + 0.992Gd_2O_3 + V_2O_5 \longrightarrow 2Nd_{0.008}Gd_{0.992}\ VO_4}$$

Table 3.5 Calculated weight of the precursors for synthesis of Nd:$GdVO_4$

Nd (at.%)	**Nd_2O_3 (gm)**	**Gd_2O_3 (gm)**	**V_2O_5 (gm)**
0.2%	0.037	19.939	10.024
0.6%	0.111	19.863	10.026
0.8%	0.148	19.825	10.027
1.0%	0.186	19.787	10.028
1.2%	0.223	19.748	10.029
1.6%	0.297	19.672	10.031

Further, for the growth of Cr co-doped Nd:$GdVO_4$ single crystals, the chemicals such as Cr_2O_3, Gd_2O_3, V_2O_5 and Nd_2O_3 are required for synthesis and their required amount were calculated for 30 gm batch as per the solid-state reaction equation and given in the Table 3.6.

$$0.005Nd_2O_3 + 0.995Gd_2O_3 + 0.01\ Cr_2O_3 + 0.99V_2O_5 \longrightarrow 2Nd_{0.005}Gd_{0.995}\ Cr_{0.01}V_{0.99}O_4$$

Table 3.6 Calculated weight of the precursors for synthesis of Nd:Cr:$GdVO_4$

Nd (at.%)	Cr (at.%)	Nd_2O_3 (gm)	Gd_2O_3 (gm)	V_2O_5 (gm)	Cr_2O_3 (gm)
0.5	1.0	0.093	19.893	9.931	0.084
0.5	1.2	0.093	19.895	9.912	0.101
0.5	1.5	0.093	19.899	9.883	0.126

3.1.3 Starting precursors for Nd doped $LuVO_4$

For the synthesis of Nd doped $LuVO_4$ materials, the initial precursors such as Nd_2O_3, V_2O_5 and Lu_2O_3 powder with purity of 99.99% [Make:Alfa aesar] were calculated by using solid-state reaction equation. The 30 gm of charge for each doping concentration of Nd were taken as per the equation [Table 3.7]. The 3% extra amount of V_2O_5 were added during the synthesis to compensate the loss of V_2O_5 due to its volatility.

$$0.005\ Nd_2O_3 + 0.995Lu_2O_3 + V_2O_5 \longrightarrow 2Nd_{0.005}Y0.995\ VO_4$$

Table 3.7 Calculated weight of the precursors for synthesis of Nd:$LuVO_4$

Nd (at.%)	Nd_2O_3 (gm)	Lu_2O_3 (gm)	V_2O_5 (gm)
0.25%	0.044	20.543	9.413
0.50%	0.087	20.497	9.416

3.1.4 Ball milling

The required amount of chemicals for each orthovanadate materials were taken for synthesis and subsequently for mixing of the powders, the 30 gm chemicals for each orthovanadate were kept inside the polystyrene bottle along with 15 zirconia balls. The bottle was clamped in the Tarbula ball-milling machine [Figure 3.1] and chemicals were mixed homogeneously using Turbula 3D rotation mixer. The chemicals were mixed for 5-6 hours at a rotational speed of 72 rpm for proper and homogeneous mixing of powders.

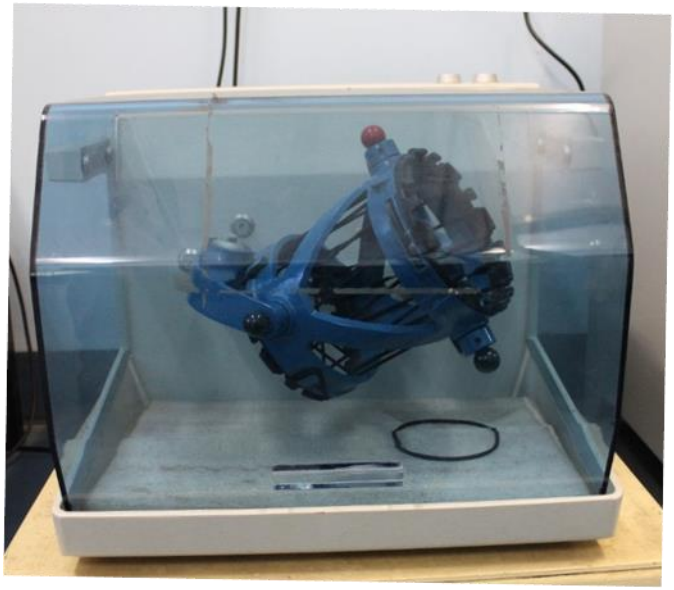

Figure 3.1 Turbula mixer

3.1.5 Solid-state reaction

The homogenous mixed powders for each orthovanadate were taken out form bottle and put inside the platinum crucible. The platinum crucible having 30gm of chemicals was kept inside the muffle furnace for solid-state reaction. The solid-state reaction was done in two steps. In the first step, the charge was kept at 650°C for the 10

hours and in the second step, it was put for 750 °C for 10 hours after the grinding and mixing of the powders. The temperature profile for the solid-state reaction for orthovanadate is shown in Figure 3.2.

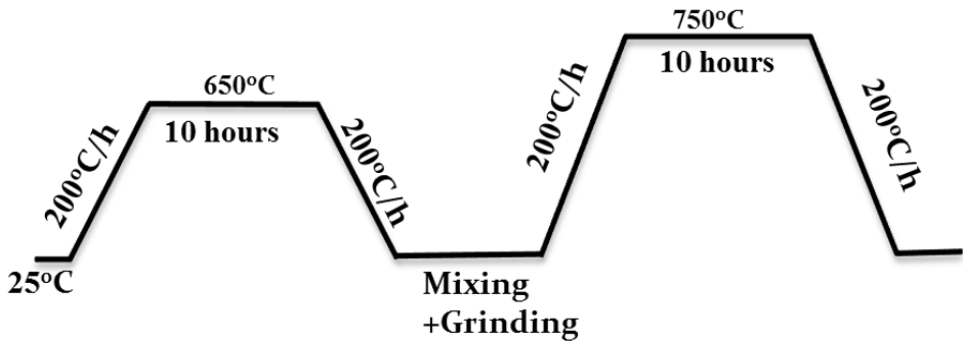

Figure 3.2 Temperature profile of solid-state reaction

3.1.6 Confirmation of phase of orthovanadate by powder XRD

The powder X-ray diffraction (XRD) pattern was measured for synthesized charge of each orthovanadate for confirmation of formation of desired phase. The XRD patterns were recorded using Rigaku Ultrax-18 powder diffractometer in the range 20-70°.

3.1.6.1 Powder XRD measurement of synthesized powder of doped and co-doped YVO_4

Powder X-ray diffraction (XRD) pattern of YVO_4 was measured for synthesized powders and compared with the corresponding JCPDS file. Peak positions of the diffraction pattern for each doped and co-doped synthesized powders of YVO_4 were matched with the reference JCPDS file.76-1649. The peaks matched well and there was no additional peak, thus confirming the formation of single desired phase. The XRD pattern of Yb doped and Er co-doped Yb:YVO_4 & Nd co-doped Yb:YVO_4 with JCPDS file are shown in the Figure 3.3 (a-c).

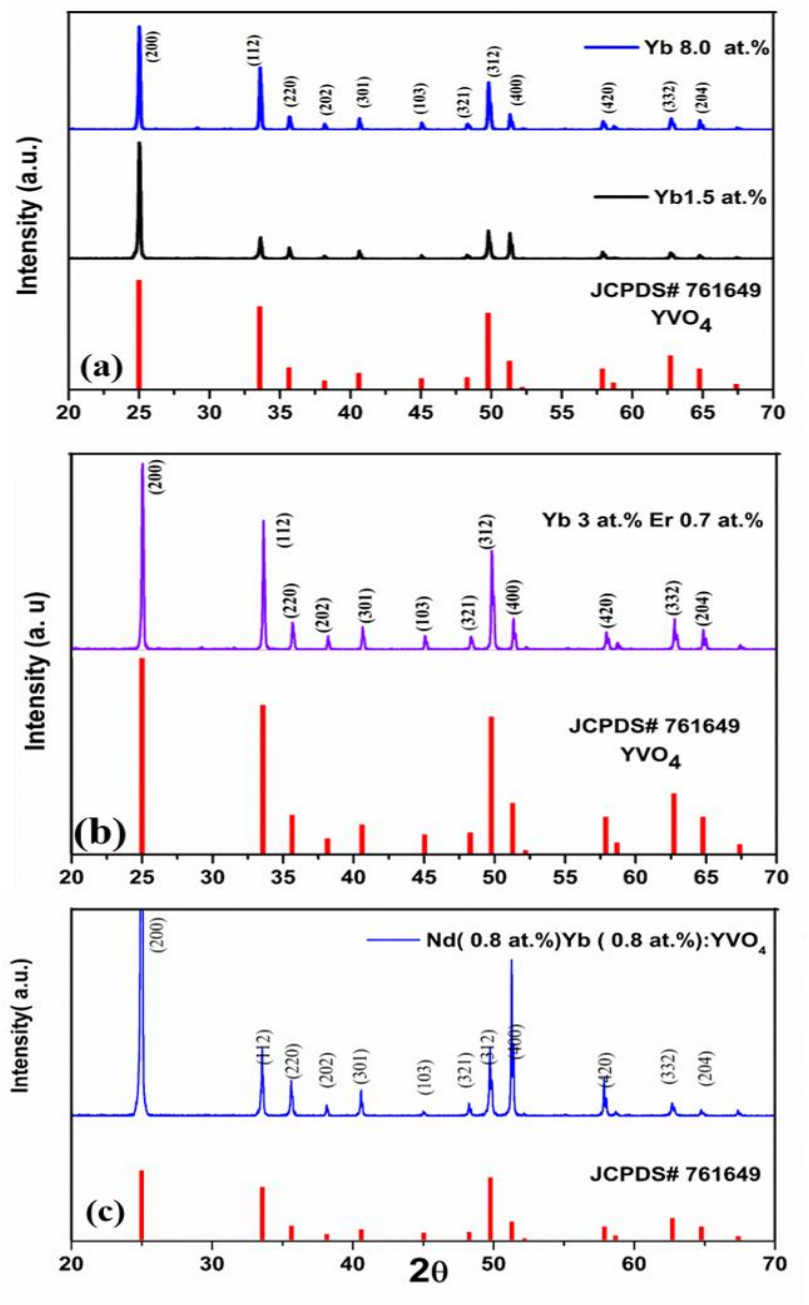

Figure 3.3 Powder XRD patterns of synthesized charge of YVO_4 with different dopants

During the synthesis of chemicals, the phase formation of YVO_4 was the major issue due to the volatile nature of V_2O_5. The problem in the synthesis was optimized by adding 3% extra of V_2O_5 in the chemicals for exact phase of YVO_4. Figure 3.4 shows XRD pattern of YVO_4 with extra 3% and without adding extra of V_2O_5.

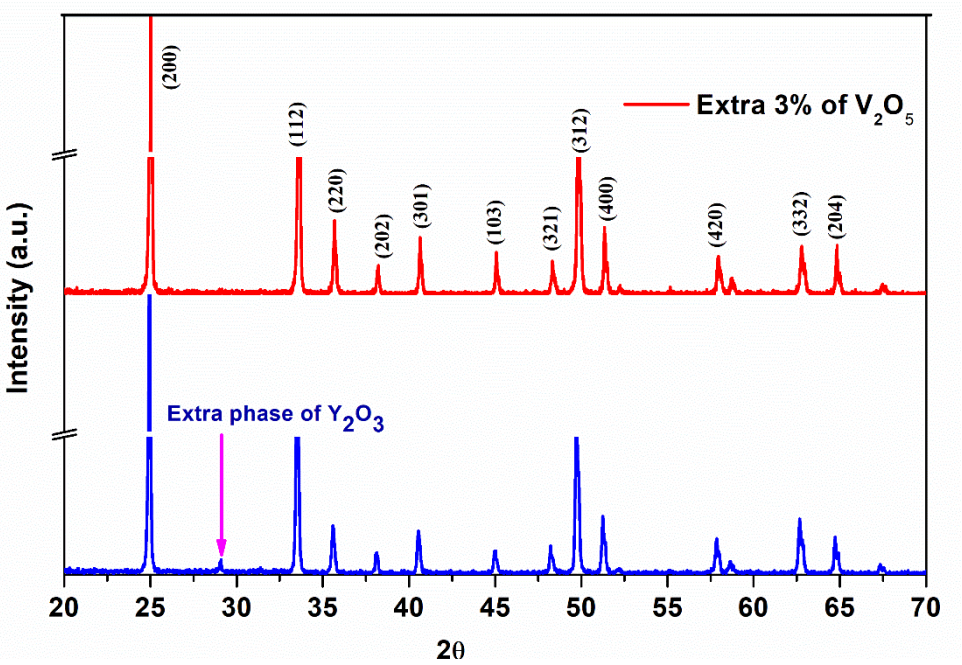

Figure 3.4 Powder XRD patterns of YVO_4 after adding 3% extra of V_2O_5

3.1.6.2 Powder XRD measurement of synthesized powder of doped & co-doped $GdVO_4$

The powder X-ray diffraction (XRD) patterns of doped and co-doped GVO_4 were recorded for confirming the desire phase of $GdVO_4$ materials. These XRD patterns were compared with relevant JCPDS file # 170260. The pattern exactly matched with the reference file that results the phase of $GdVO_4$ materials. The XRD pattern was plotted along with reference file as shown in the Figure 3.5.

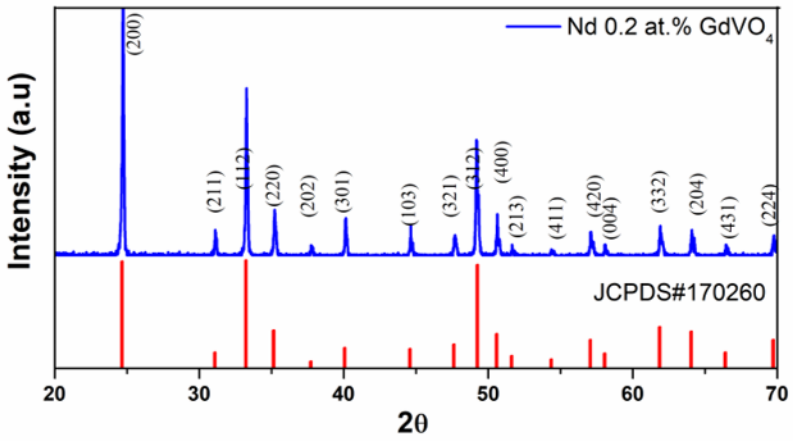

Figure 3.5 Powder XRD patterns of synthesized chemicals of $GdVO_4$

Due to the volatile nature of V_2O_5 the phase formation of $GdVO_4$ was the main problem at time of the synthesis of chemicals. The problem in the synthesis was solved by adding 2% extra of V_2O_5 in the chemicals for exact phase of $GdVO_4$.

3.1.6.3 Powder XRD measurement of synthesized powder of Nd doped $LuVO_4$

For confirming the desire phase of Nd doped $LuVO_4$ materials, the powder X-ray diffraction (XRD) patterns were recorded for both synthesized powders (0.25 and 0.50 at.% of Nd doping). The recorded XRD patterns exactly matched well with the corresponding JCPDS file # 821917, hence, this confirming the desired phase of $LuVO_4$ materials. The XRD patterns and reference file is shown in Figure 3.6. During the synthesis of $LuVO_4$. The 3% extra of V_2O_5 was added for the complete phase formation of $LuVO_4$ material. As already mentioned, the problem of phase arise due to the volatile characteristics and lesser melting point of V_2O_5.

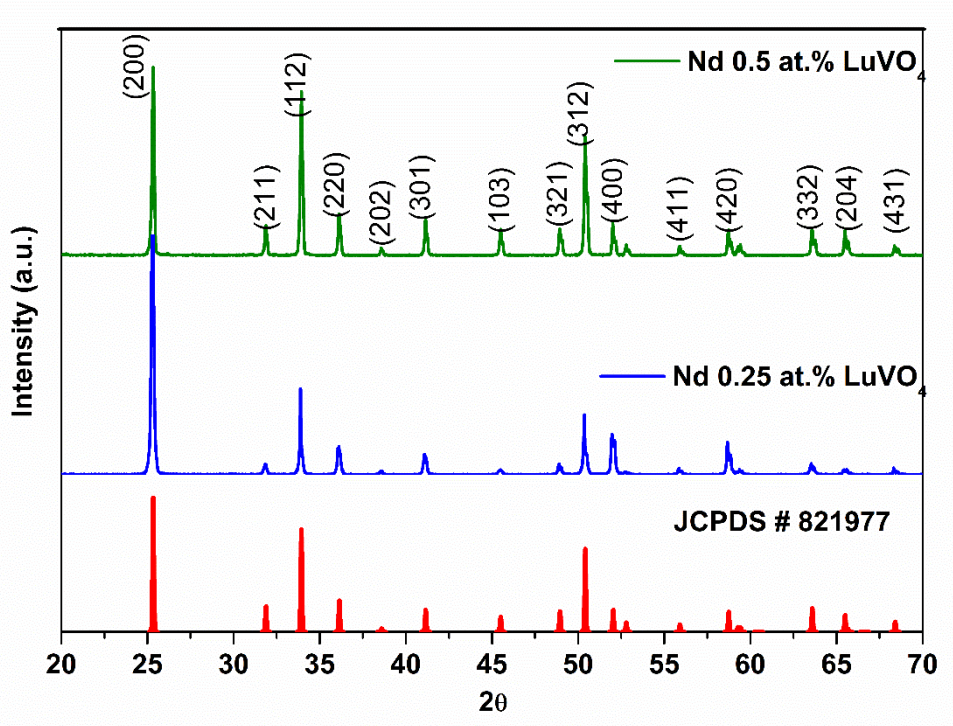

Figure 3.6 Powder XRD patterns of synthesized charge of $LuVO_4$

3.2 Feed rod preparation

3.2.1 Packing of rod

A polycrystalline cylindrical shaped feed-rod is required for the growth of the single crystals by OFZ technique and the feed rod was prepared from the synthesized powders of different orthovanadate. The crystalline quality of crystal depends on the quality of the feed rods. For making the feed rods, the nozzle of a glass funnel was inserted into the long rubber tube as shown in the Figure 3.7. The grinded synthesized powder was filled inside the rubber tube using spatula. The powder was continuously filled and moved towards the bottom of the rubber tube and subsequently it was pressed by long ceramic rod. The powder was packed homogenously upto the desired length nearly 40-70 mm and diameter around 5-7 mm. The trapped air inside the packed powder rod was sucked by rotary pump after removing the funnel and inserting the cotton inside the rubber tube. [Figure 3.8].

Figure 3.7 Packing of synthesized powder

Figure 3.8 Rotary pump sucking the air from the packed rod

Further, the packed rod was pressed to 70 MPa by using the hydrostatic system for 3-5 minutes for the densification [Figure 3.9]. The rubber tube was cut carefully and feed rod was removed as shown in Figure 3.10. A hole on the feed rod was made for hanging the feed rod for sintering.

Figure 3.9 Pressing of rod by hydrostatic press system

Figure 3.10 Cutting of rubber tube

3.2.2 Sintering of feed rod

Sintering is a process for densification of feed rod. In this process, the atoms diffuses across the grains boundaries and fuses the grains for forming the larger grain, which results in the formation of densified polycrystalline feed rod. For sintering, the feed rod was heated to the temperature around ¾th of melting point of the material for the faster rate of diffusion of atoms through grains. In the present work, the sintering of feed rod was done in the Vertical Molisili furnace as shown in Figure 3.11.

The desired temperature profile for sintering was set using temperature programmer attached with Molisili furnace [Figure 3.12 and Figure 3.13]. The present feed rods were sintered in the range of 1250-1400˚C for 10 hours depending on the orthovanadate material.

The up down motion and rotation of feed-rod was done inside the furnace for proper densification and homogeneous sintering of rod. The up down translational speed and rotation was kept at 10 mm/min and 10 rpm respectively during the entire sintering process. Figure 3.14 shows photograph of one of sintered feed rods. A range of dimensions of the sintered feed-rods for all three orthovanadate are listed in Table 3.8.

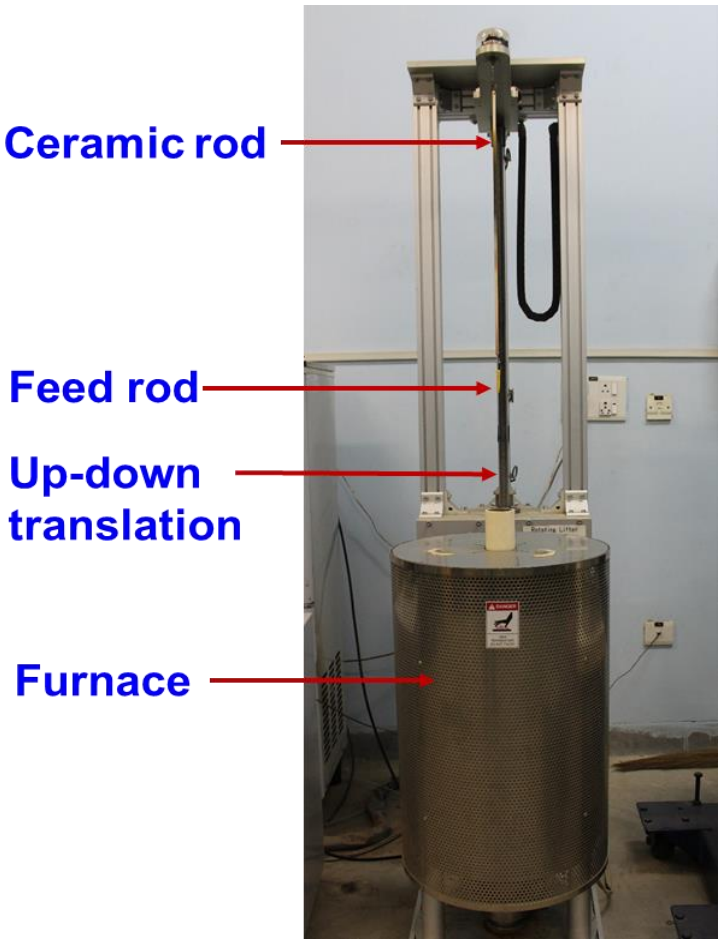

Figure 3.11 Vertical molisili furnace along with rotating lifter

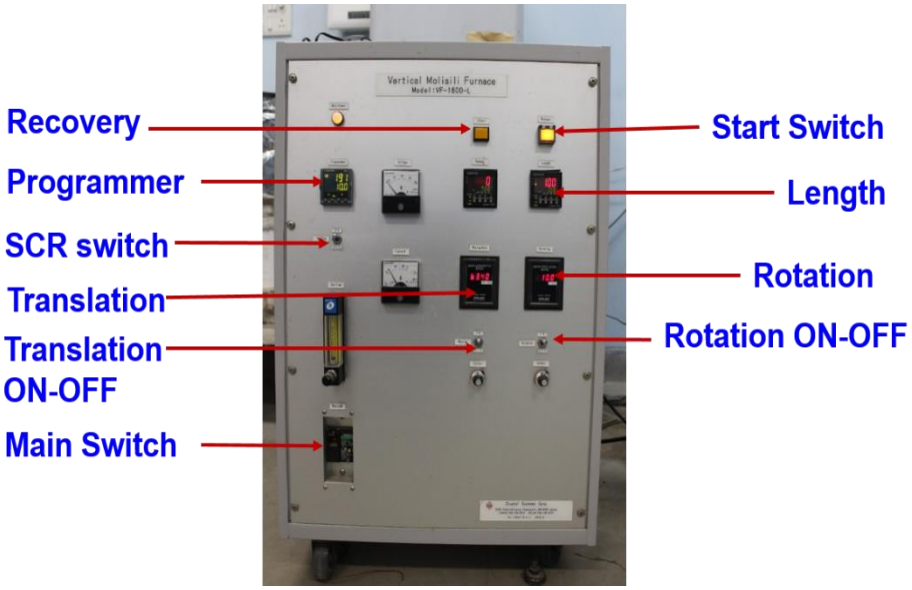

Figure 3.12 Control unit of vertical molisili furnace

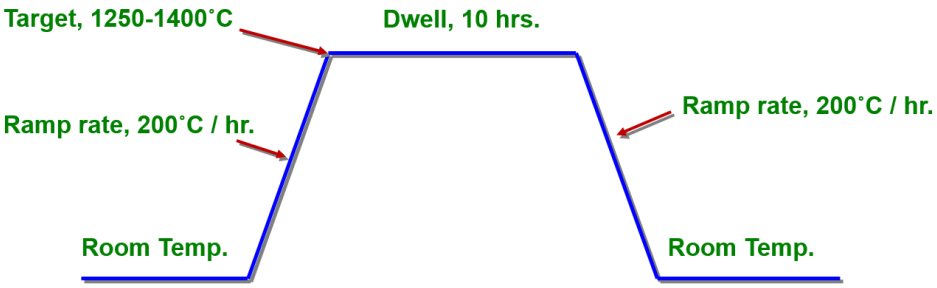

Figure 3.13 Sintering profile of feed-rod

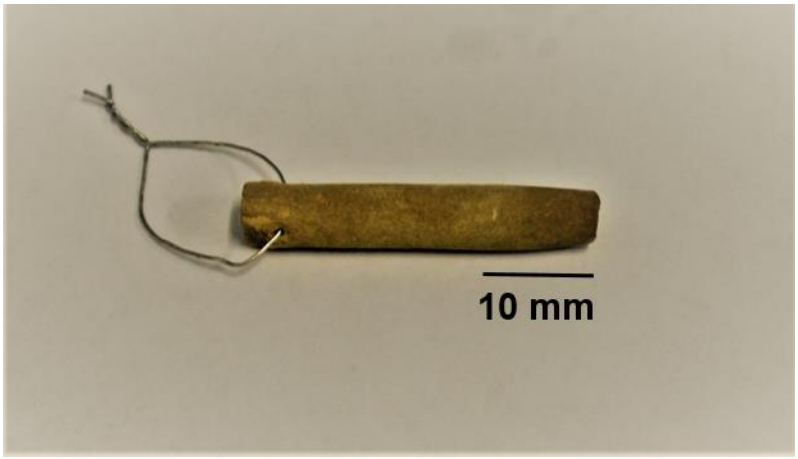

Figure 3.14 Sintered feed rod

Table 3.8 Length and diameter of prepared feed-rod

Feed rods	Rod	Length	Diameter
$YVO_4/GdVO_4/LuVO_4$	Feed rod	~30- 65 mm	~4-7 mm

3.3 Growth of single crystal by OFZ technique

3.3.1 Assembling of feed-rod and seed crystal

For the growth of the single crystals, an important and necessary step is alignment and assemble of the feed rod and seed crystal inside the optical floating zone machine. The oriented seed crystal is tightened to seed holder and put into the lower shaft. The feed rod is hanged into the upper shaft and aligned properly [Figure 3.15]. It is important to make the alignment of the feed rod and seed crystal such that, the vertical axis of both is perfectly matched. The alignment is important steps for achieving stability of the molten zone and preventing the melt overflow for obtaining the good quality crystal. Further, the quartz tube is inserted inside the OFZ machine after moving upwards and downwards to upper and lower shafts respectively. Finally, the tip of the feed rod and seed crystal separated by a few mm were placed at the focal point of the mirrors as shown in the Figure 3.15 and 3.16.

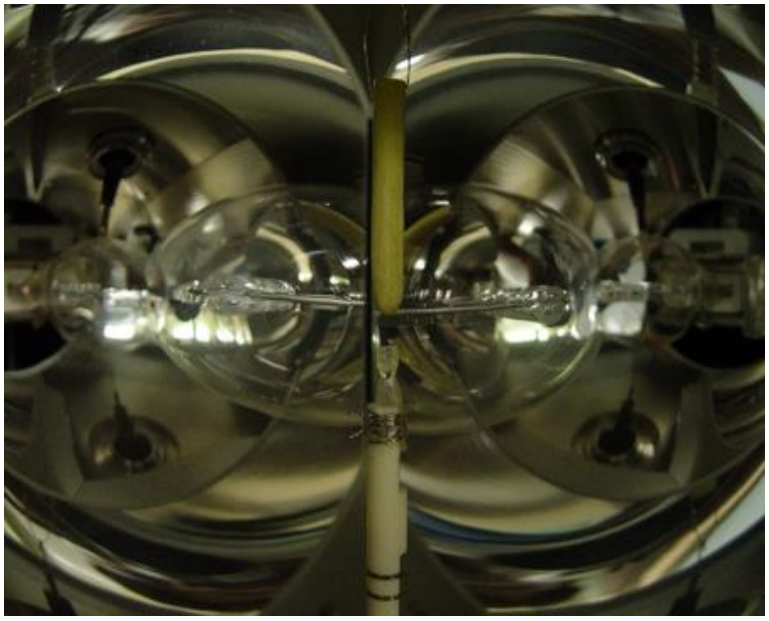

Figure 3.15 Mounting of seed and feed rod

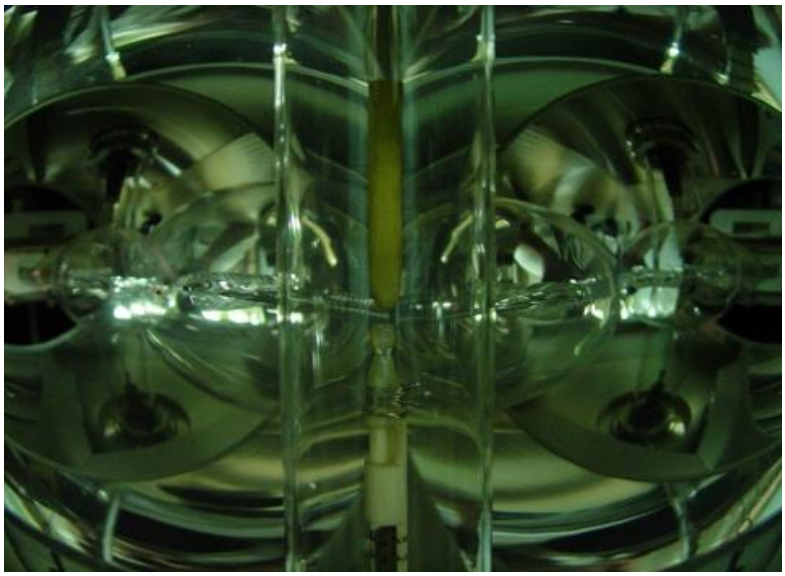

Figure 3.16 Complete assembly after mounting of the seed and feed rod

3.3.2 Crystal growth process

For the growth of orthovanadate single crystals, the heating of the lamps was started with help of the control panel attached with OFZ machine. The power of halogen lamps was initially set at 67% of the maximum power (4 kW). The program was pre-set in such a way that the power reaches to 67% in one hour with a linear slope. Subsequently power of lamps was increased manually to control the melting of the orthovanadate. The rotation of the feed rod and seed crystal was set in counter directions as per the optimized parameters of respective orthovanadate. The ambience flow (air or O_2+N_2) inside the growth chamber were normally put around at 1-2 lpm. When the power of lamps reaches to the melting point of orthovanadate (melting point: 1810°C for YVO_4, 1780°C for $GdVO_4$ and 1800°C for $LuVO_4$), the tip of feed rod started melting as shown in the Figure 3.17. Further, when the tip of the feed-rod was completely melted, the lower shaft holding the seed crystals was attached with molten

feed rod by moving seed crystals upward in a control manner [Figure 3.18] and the growth of the single crystal was started after the given optimized downward translation of both the shafts [Figure 3.18]. We had to monitor and adjust the power of the lamps according to the condition of the molten zone during the growth process. As the desired length of the crystals of the particular material was grown, the feed rod was detached from the growing crystal by stopping the feeding of the material [Figure 3.19]. Further, the power of the halogen lamps was decreased to 0% in 1 hour using power software controller.

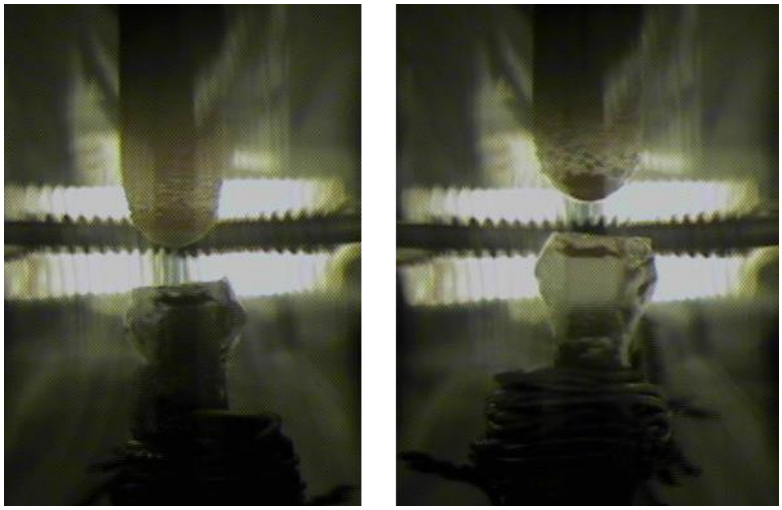

Figure 3.17 Melting of feed rod

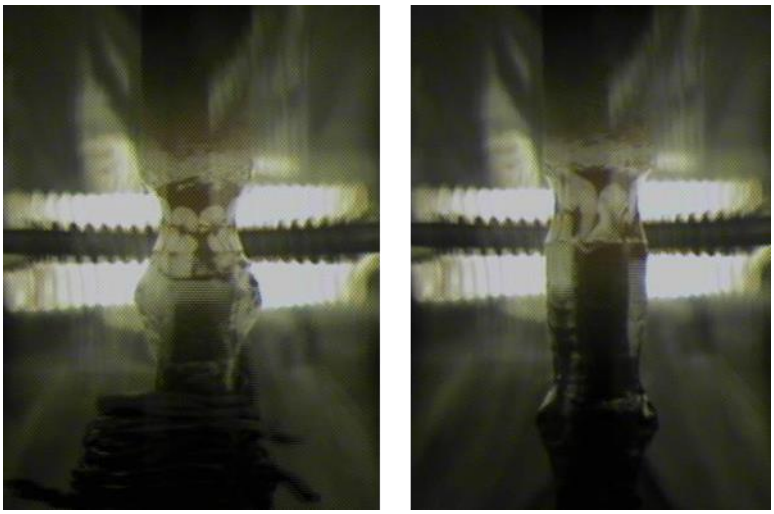

Figure 3.18 Attachment of molten tip to the seed and subsequent crystal growth process

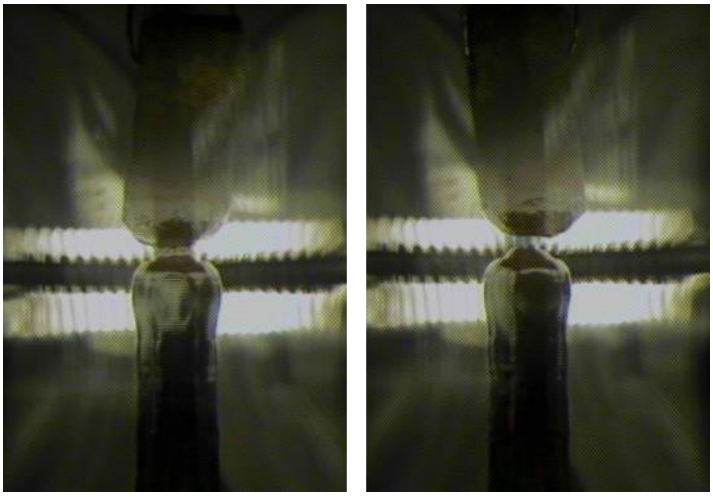

Figure 3.19 Detachment of feed rod

In the present work, all the crystals were grown by optical floating zone technique and there are various parameters such as quality of feed rod, growth ambience, gas flow rate, power of lamps, and feed & growth rate as well as rotation, which were optimized by performing several growth experiments. The major issues faced during the growth of the crystals are described in the individual growth of particular materials. The major issues faced during the growth of the crystals are described in the individual growth section corresponding to the particular material. However, the general description of optimization of the process parameters for growing good quality crystals are given below.

The good quality feed rod is characterized by uniform densification. A poor quality feed rod results into abrupt change in the melt volume during the growth experiment leading to instability in the molten zone. To ensure uniform densification of a polycrystalline rod, the powder was properly grinded, homogenously packed and sintered in the vertical Molisili furnace with simultaneous rotation as well as translations motion.

The growth ambience and gas flow rate inside the growth chamber are also important for obtaining good quality crystals. During the growth of some crystals ($GdVO_4$) when oxygen contents in the growth ambience is high then a problem of melting of the feed rod was experienced. Hence, the optimized amount of oxygen in the growth ambience is in the range of 10-50%. The gas flow rate influences the melting as well as freezing of the rod. If the flow rate is high then the freezing of feed rod and improper melting of feed rod occurs. On the other hand, if the flow rate is low then solidification does not take place properly and melt overflow occurs. Therefore, the gas flow rate were kept around 1-2 lpm inside the growth chamber.

The power of lamp is also an important factor for the growth of good quality crystals. If the power of lamp is lower than the optimized span of lamp power (72-74% for YVO_4) then freezing and shaking as well as improper melting of feed rod are experienced. If the power of lamp is higher then overflow of melt takes place, which spoils the growth experiment. Power of the lamps depends on the melting point of materials.

Rotation rate of feed-rod and seed crystal has a significant influence on the crystalline quality of the grown crystal. The rotation of feed rod and seed crystal are kept counter clockwise to maintain temperature homogenous and mixing of melt. The rotation rate is kept in the range of 30-40 rpm. If the rotation rate is higher than the optimized value wobbling of feed rod and overflow of melt occur, and if the rotation is lower than the optimized value then thermal inhomogeniety at the interface as well as in the molten zone is introduced that result poor crystalline quality in the grown crystal.

The crystalline quality also highly depends on the growth rate. If growth rate is higher than the optimized growth rate (10-15 mm/hours for YVO_4), the grown crystals may contain low angle grain boundaries, strain and hairline cracks. If growth rate is lower than the optimized value, the grown crystal is exposed to high thermal gradient for longer time, therefore it results strains and defects in crystals. The pulling rate depends on the surface tension, thermal conductivity and viscosity of the melt of the material.

3.4 Growth of Yb doped and co-doped YVO_4 single crystals

Single crystals of doped and co-doped (Yb and Yb;Er & Yb;Nd) YVO_4 were grown by using optical floating zone method [119,127,138–141]. The doping concertation of Yb in YVO_4 was 0.8, 1.5, 3.0, 5.0, 8.0 and 1.5 at.%. The co-doped YVO_4 samples such as Er (0.7 at.%) co-doped Yb:YVO_4 with Yb concentration, 1.5, 3.0, 8.0 & 12.0 at.% and Nd (0.8 at.%) co-doped Yb:YVO_4, with Yb concentration 0.8 & 3.0 at.% were grown. For the growth of doped and co-doped ytterbium orthovanadate (YVO_4), [100]-oriented seeds were used for all the crystal growth experiments. During the growth the rotation of feed-rod and seed crystal was optimized to be 60-30 rpm, but in the mutually opposite directions. The growth and feed rate was kept ~10-15 mm/h for obtaining good quality crystal. The rate of gas flow (Air or 80% of N_2 +20% of O_2) inside the quartz growth encloser was kept as 1-2 liter per minute. The optimized parameters resulted a stable growth condition with no overflow of the molten zone. The size of the grown crystals is typical in the range of diameter 4-6 mm and length 10-45 mm. Photographs of as-grown crystals are shown in Figure 3.20-3.22.

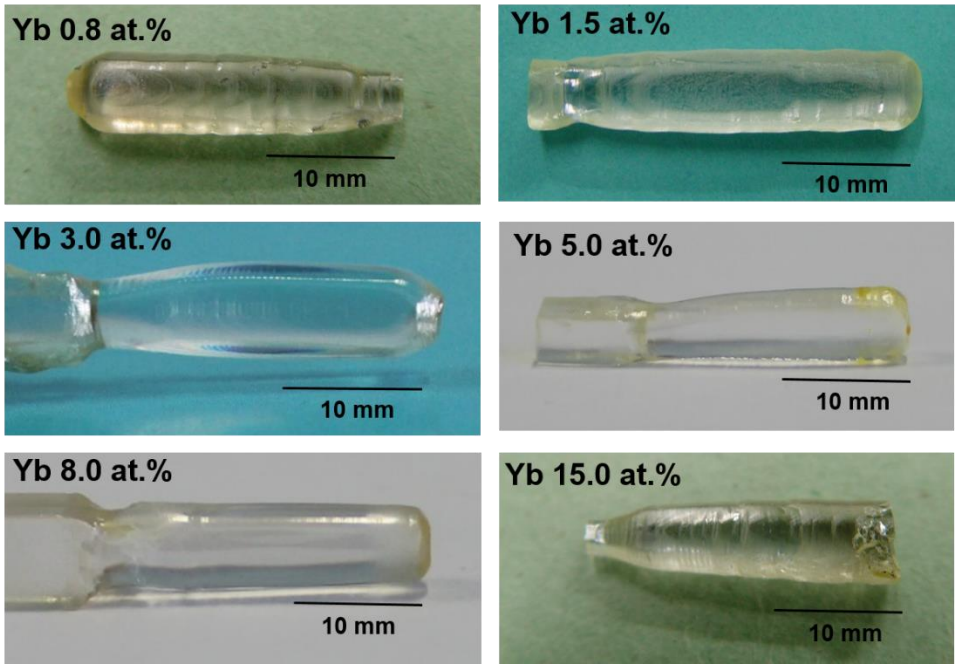

Figure 3.20 Photograph of as-grown single crystals of Yb:YVO_4

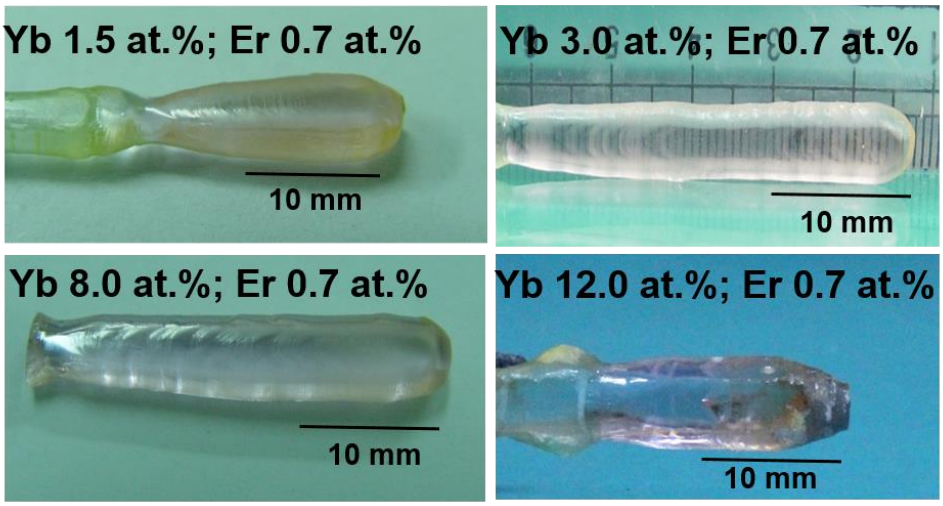

Figure 3.21 Photograph of as-grown single crystals of Er:Yb:YVO_4

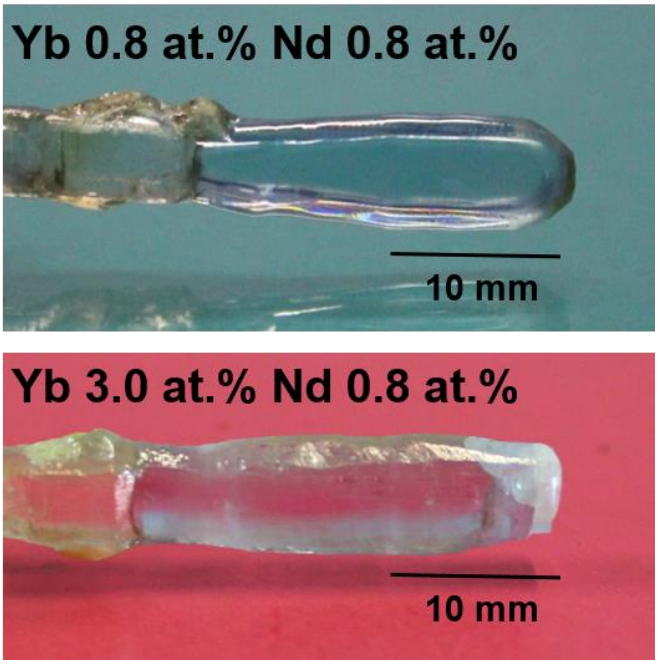

Figure 3.22 Photograph of as-grown single crystals of Nd:Yb:YVO_4

During the growth of single crystals of YVO_4 by OFZ method, there are various growth challenges such as overflow problems, bubble formation, cracking of the crystal, and core formation, etc. These growth problems have been resolved by the optimizing the various growth parameters such as quality of feed rod, rotation rate of feed rod and seed crystal, power of lamp, gas flow rate and growth ambience. Good crystalline quality of single crystals were grown as per optimized parameters [Figure 3.20-3.22]. Figure 3.23 shows the growth problems such as overflow, cracking and core formation when growth parameters are not optimized.

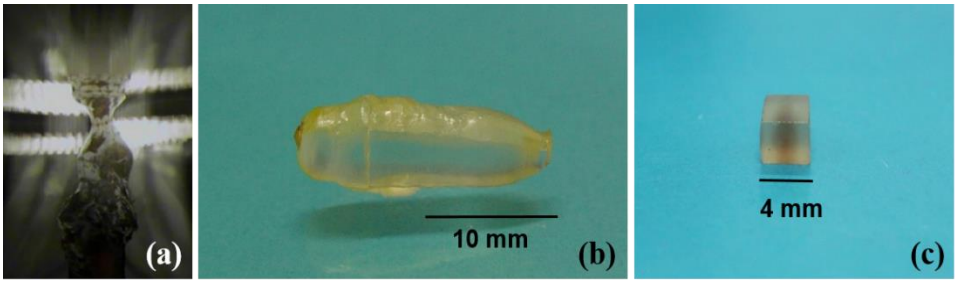

Figure 3.23 Photograph of (a) overflow of melt (b) cracking of crystal (c) core-formation

3.5 Growth of Nd doped and co-doped $GdVO_4$ single crystals

Nd doped $GdVO_4$ single crystals with different doping concentrations of Nd ion in $GdVO_4$ were grown by using optical floating zone method [61,142–144]. In the present work Nd doping of 0.0, 0.2, 0.6, 0.8, 1.0, 1.2 and 1.6 at.% was chosen for growth and subsequently for the investigation. For growing single crystals of Nd:$GdVO_4$, [100]-oriented seed was used. Growth parameters for the growth of $GdVO_4$ crystals were optimized in the initial growth experiments. Growth atmosphere was kept same in all the growth experiments. Crystals of length ~ 15-25 mm and diameter 4-6 mm were grown. Figure 3.24 shows photographs of as-grown crystals.

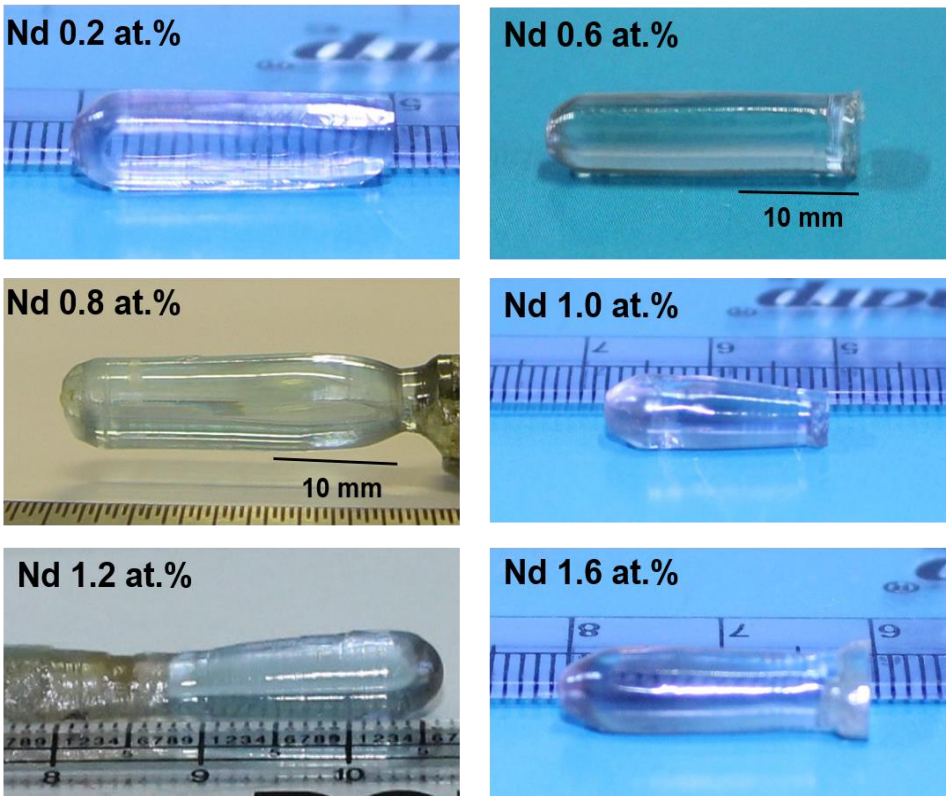

Figure 3.24 Photograph of as-grown single crystals of Nd:$GdVO_4$

The optimized growth rate and rotation of feed/seed was 12 mm/h and 40/30 rpm respectively for obtaining good quality crystal. During the growth of all the single crystals, a mixture of 50% of O_2 and 50% of N_2 was used at a flow rate of 1 liter per minute.

Further, the single crystals of Cr co-doped Nd:$GdVO_4$ single crystals with different doping concentrations were grown by optical floating zone method. In this work, Nd doping was kept as 0.5 at.%, and Cr concentration was varied to be 1.0, 1.2 and 1.5 at.%. Each of the Cr co-doped Nd:$GdVO_4$ crystals were grown with varied mixed ambiance: 10% O_2+90% N_2, 20% O_2+80% N_2 and 25% O_2+75% N_2 [Figure 3.25]. The flow rate of the mixed ambience was 1 lpm. The single crystals were grown

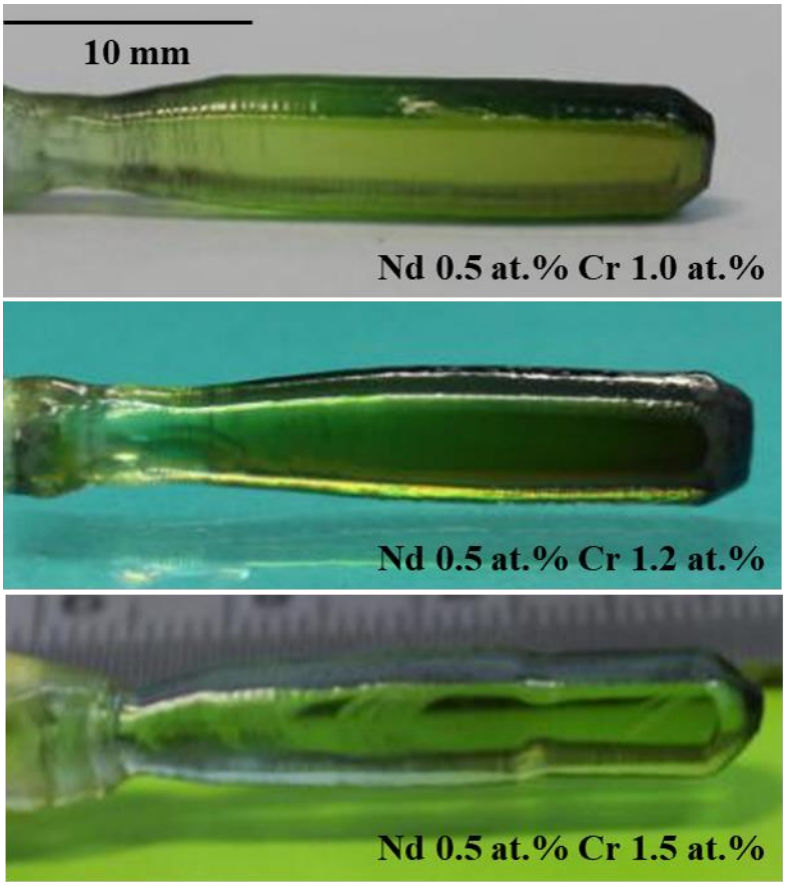

Figure 3.25 Photograph of as-grown single crystals of Cr co-doped Nd:$GdVO_4$

along [100]-direction. Growth rate and rotation rate used were in the range of 12-15 mm/h and 30-40 rpm, respectively for obtaining good quality crystals.

All the growth parameters were kept nearly same except growth ambience, which was varies to see the effect of oxygen on the growth and optical properties. Crystals of length ~10-30 mm and diameter 4-6 mm were grown. Figure 3.25 shows the photograph of some of the grown crystals.

Initially lot of problems during the growth of $GdVO_4$ have been faced for the growing the Nd doped $GdVO_4$ crystals. Melt overflow and feed rod melting was the major issues in the growth of $GdVO_4$ crystals [Figure 3.26].

Many runs for crystal growth were conducted to overcome the problems and subsequently optimized the quality of feed rod, growth ambience, power of lamp and growth pulling rate as well as the rotations. After the optimization, the good crystals were obtained as shown in the Figure 3.24-3.25.

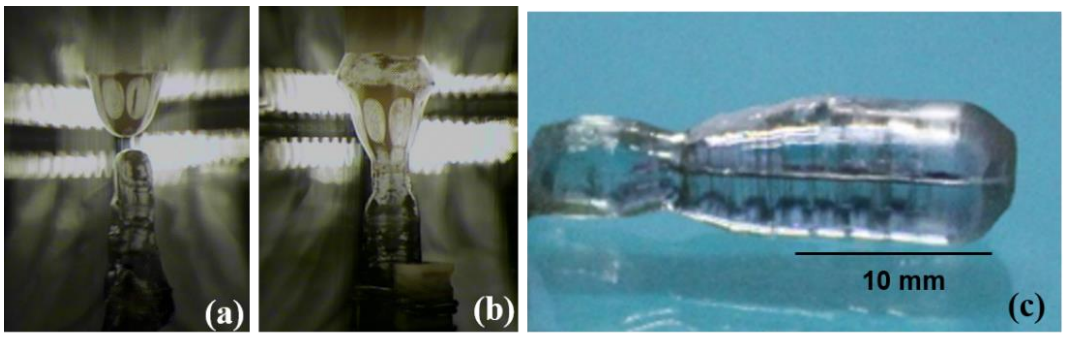

Figure 3.26 Photograph of (a) overflow of melt (b) melting problem of feed rod (c) cracking of the crystals.

3.6 Growth of Nd doped $LuVO_4$ single crystals

The single crystals of Nd doped $LuVO_4$ were grown by using optical floating zone method with different doping concentrations Nd ion in $LuVO_4$. In the present work Nd doping of 0.25 and 0.5 at.% was chosen for the investigation. The single crystals of Nd doped $LuVO_4$ were grown by using the [100]-oriented seed. Growth rate was optimized and kept 12-16 mm/h for obtaining good quality crystal. During the growth of the single crystals, a mixture of 20% of O_2 and 80% of N_2 was used at a flow rate of 1 liter per minute. During growth process all the growth parameters including the growth atmosphere was kept same for the sake of conformity in the subsequent measurement. Crystals of length ~ 10-25 mm and diameter 4-5 mm were grown. Figure 3.27 shows the photographs of some of the as grown crystals.

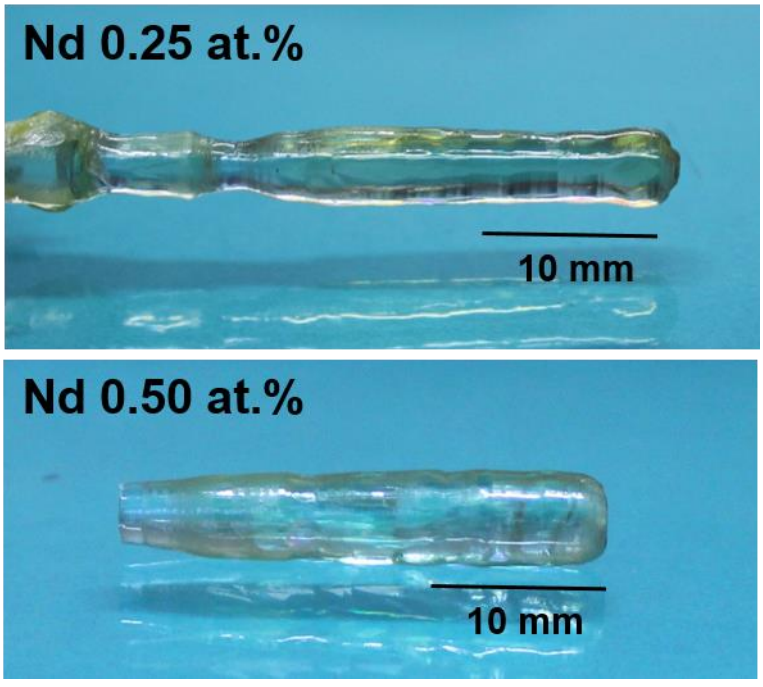

Figure 3.27 Photograph of as-grown single crystals of Nd:$LuVO_4$

During the growth of Nd doped $LuVO_4$ crystals, initially the melting of feed rod, pulling rate for growth and overflow problems have been faced. To overcome these major issues for the growth of $LuVO_4$ crystals, growth runs of $LuVO_4$ crystals were conducted so many times and then optimized power of lamp and growth pulling rate, etc. After the optimization, the good crystals were grown as shown in the Figure 3.27. The problems like overflow, cracking of crystal, bubble formation are shown in the Figure 3.28.

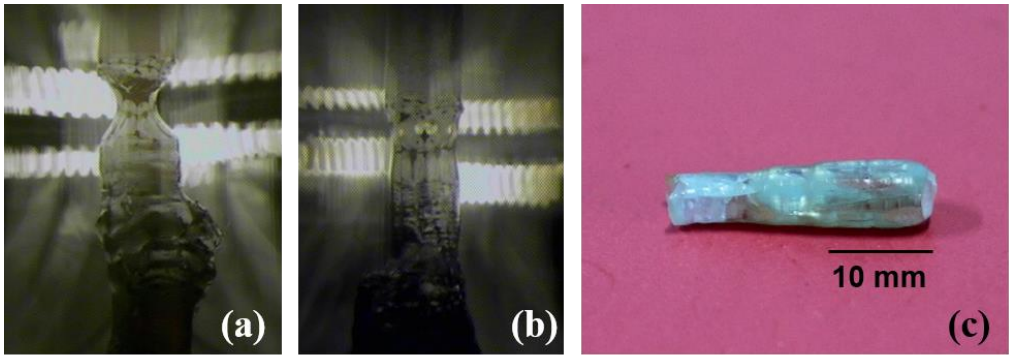

Figure 3.28 Photograph of (a) overflow of melt (b) bubble formation (c) cracking of the crystals.

3.7 Fabrication and polishing of elements for characterization

After the completion of the growth of orthovanadate, the grown crystals were oriented using Proto-make Laue machine for cutting the crystal in the particular direction such as [100] and [001]. Figure 3.29 shows the Laue pattern of [100]-oriented crystal.

Further, the oriented crystals were cut using the diamond blade as shown in Figure 3.30. The samples and elements were cut of dimension ~ 1.0 mm and 3x3x5-6 & 4x4x5-6 mm^3 respectively and subsequently subjected for polishing using polisher machine as shown in Figure 3.31.

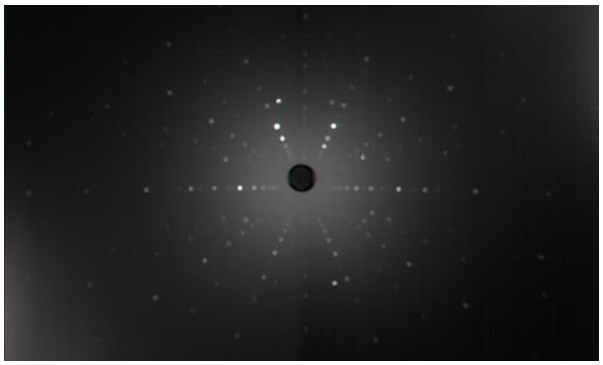

Figure 3.29 Laue pattern of [100]-oriented crystals

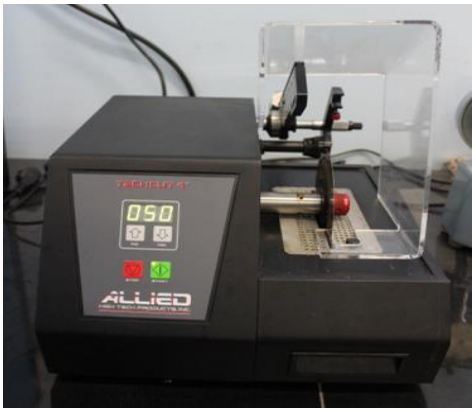

Figure 3.30 Cutting machine

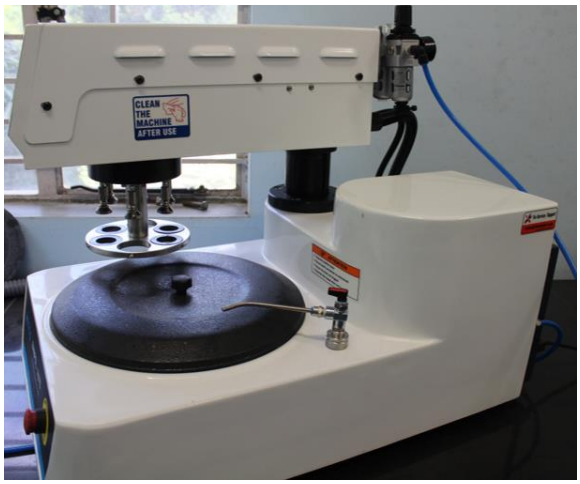

Figure 3.31 Polishing machine

The samples of thickness ~ 1 mm and laser elements of dimension 3x3x5-6 and 4x4x5-6 mm^3 of three orthovanadate are shown in the Fig 3.32 for various characterizations.

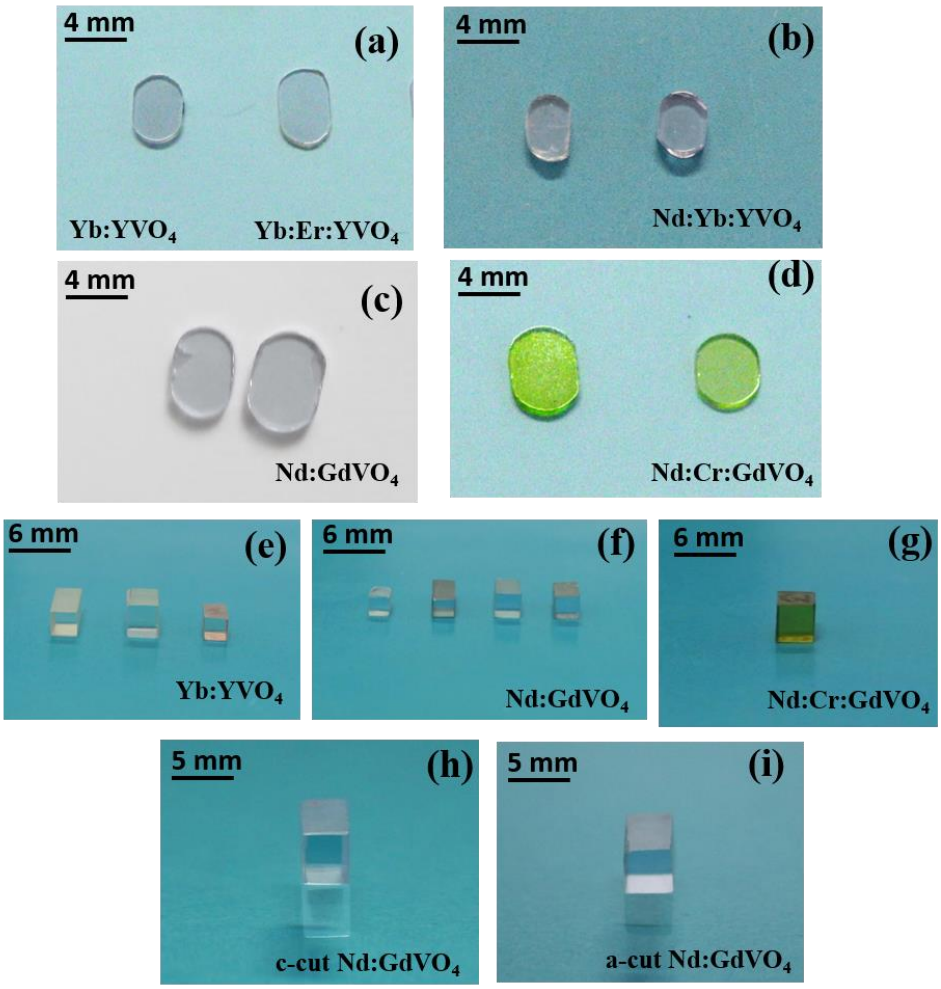

Figure 3.32 Photograph of fabricated elements of orthovanadate crystals

Chapter-4 Optical and Structural Investigations of Yb Doped and Co-doped YVO_4 crystals

4.1 Characterization of Yb doped YVO_4 crystals

The importance of Yb doped and co-doped YVO_4 single crystals and their growth have been described in the chapter 1 and chapter 3 respectively. This chapter deals with the characterization of their optical and structural properties. For characterization of the crystals, the sample plates of ~1-1.5 mm thickness were cut from the grown crystals after orientating the crystal along [100]-direction. Further, the sample plates were polished using alumina powder of different particle size.

4.1.1 Rocking curves measurement

The optical properties of single crystals depend on the crystalline quality of the grown crystals and quality of grown crystal can be checked by HRXRD. Hence, the assessment of crystalline quality of the grown crystals was carried out by the rocking curve measurements on [100]-oriented sample for the (200) diffraction peak in the ADXRD beam-line (BL-12) [112] of the Indus-2 synchrotron facility [112]. The wavelength of the X-ray used was 0.857Å (14.43 keV). Figure 4.1 shows a rocking curve of the plate of 3.0 at.% Yb doped crystal. The presence of single and symmetrical diffraction peak corresponding to (200) planes confirms the orientation of the plate. Occurrence of single diffraction peak confirms these crystals are free from internal sub-grain structures and low-angle grain boundary.

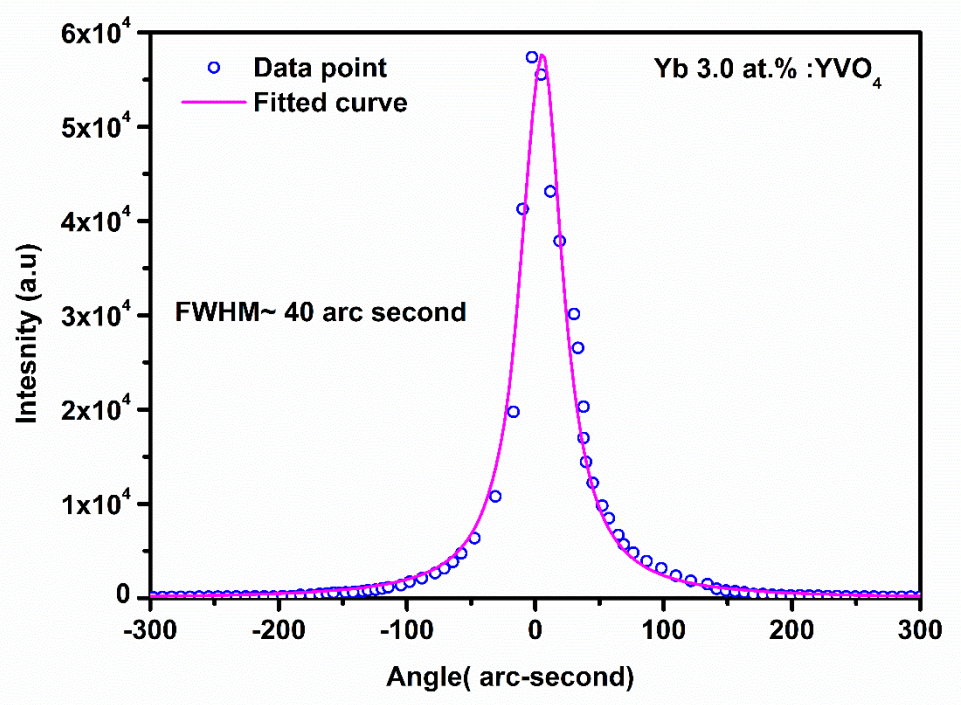

Figure 4.1 Rocking curve of (200)-peak of Yb doped crystals

The FWHM of the diffraction peak was evaluated by Lorentz fitting. The value of the FWHM for the samples of different doping of Yb are ~40-55 arc-second. The lower value of the FWHM reveals good crystalline quality of the grown crystals [141].

4.1.2 Estimation of Yb doping concentration in the grown crystals

The evaluation of the actual concentration of Yb in the grown crystals is useful for laser pumping point of view. Therefore, the X-ray fluorescence (XRF) measurements were carried out on the samples of different Yb concentrations and the standard samples. The standard samples in the form of pellets with known Yb concentrations (1.0, 5.0, 10.0 and 15.0 at. %) in YVO_4 matrix were prepared by applying the 3-ton pressure for 200 second for quantitative estimation of Yb in the grown crystals. The experiments were performed in the Microprobe X-ray Fluorescence Beam-line (BL-16) of the Indus-2 synchrotron facility. The crystal and standard samples were

excited at 12 keV for 300 seconds and corresponding to the XRF spectra for all Yb doping concentrations were measured. The XRF intensity pattern of Yb doped single crystals are shown in the Figure 4.2. The XRF spectra are characterized by the K emission lines of vanadium and the L emission lines of Yb. The strongest lines of Yb i.e L_α emission at 7.4 keV was used for the quantitative analysis. It was observed that the intensity of Yb-L_α peak increased as the doping of Yb was increased. The ratio of the area of V-K_α and Yb-L_α peaks of XRF was calculated by fitting Gaussian peak. The ratio was plotted with respect to the doping concentration of Yb of pellets (standards) and fitted with linear fit and generated the standard plot. Further, the Yb concentration in the grown crystals was estimated using the standard curve and tabulated in the Table 4.1.

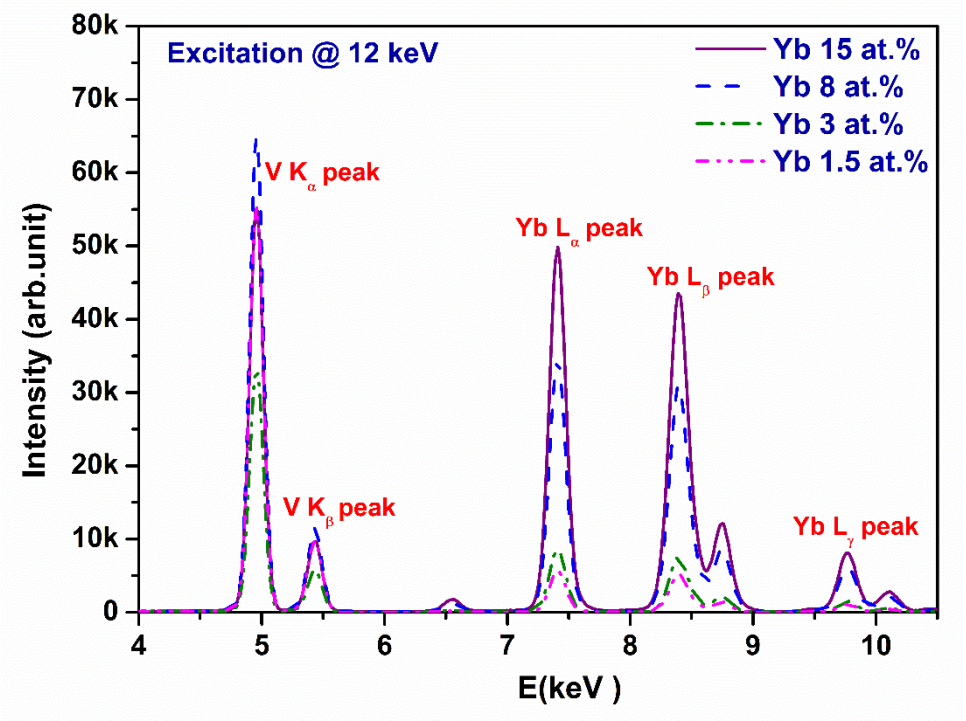

Figure 4.2 X-Ray fluorescence of Yb doped crystals, excitation at 12 keV

It was found that the doping concentration of Yb in the grown crystals is slightly less than the doping concentration added in the synthesized powder used for the growth. The results signify the value of the effective segregation coefficient to be close but not equals to one. The estimated effective segregation coefficient of the grown crystals was ~ 0.95 [119,141].

Table 4.1 Concentration of Yb in the grown crystals estimated by XRF

Sr. No.	Doped Yb Conc. (at.%)	Actual Yb conc. (at.%) evaluated by XRF	Yb/Y
1	1.5	1.48	0.015022
2	3.0	2.94	0.030291
3	8.0	7.88	0.085541
4	15.0	14.3	0.166861

4.1.3 Effect of Yb doping on lattice parameters of YVO_4

To investigate the effect of Yb doping on the lattice parameters of YVO_4, X–rays diffraction patterns were recorded from crystal powders of undoped and Yb doped YVO_4 using Rigaku Ultrax-18 powder diffractometer, Cu-Kα in the range 20-70^o as shown in the Figure 4.3. The lattice parameters for different Yb doped crystals were calculated from the diffraction pattern using Le bail fitting to reduce the systematic error. The calculated values of the lattice parameters for 0.75 at.% doped sample are: a= 7.12(6) Å and c= 6.29(1) Å. It was observed that the lattice volume showed a small but systematic decrease above 2.94 at.% of Yb doping [Table 4.2]. For 14.3 at.% Yb doped sample the lattice parameters are a= 7.11(8) Å and c= 6.28(2) Å. As per the study by Zhong et al. [38] on 0.11 and 0.26 at% Yb doped sample, it exhibited the contraction of lattice. On the other hand study by Chen et al. [21] on the higher Yb doped sample i.e., for 4.8, 9.5 and 18.1 at.% Yb, has shown that the lattice shows shrinkage at doping

concentration of 9.5 and 18.1 at.%. Our systematic study on the whole range of the doping concentration clearly revealed that the lattice volume is indeed not affected at lower doping concentrations but exhibits slight systematic decrease only at higher doping concentration above 2.94 at.%. It is to be noted that the ionic radii of Yb (1.01 Å) [145] and Y (1.04 Å)[140] are close and both are trivalent ion. Hence, it is expected that the substitution will result no change in the lattice parameters at lower concentration and a significant change can only be observed at higher concentrations [119,127].

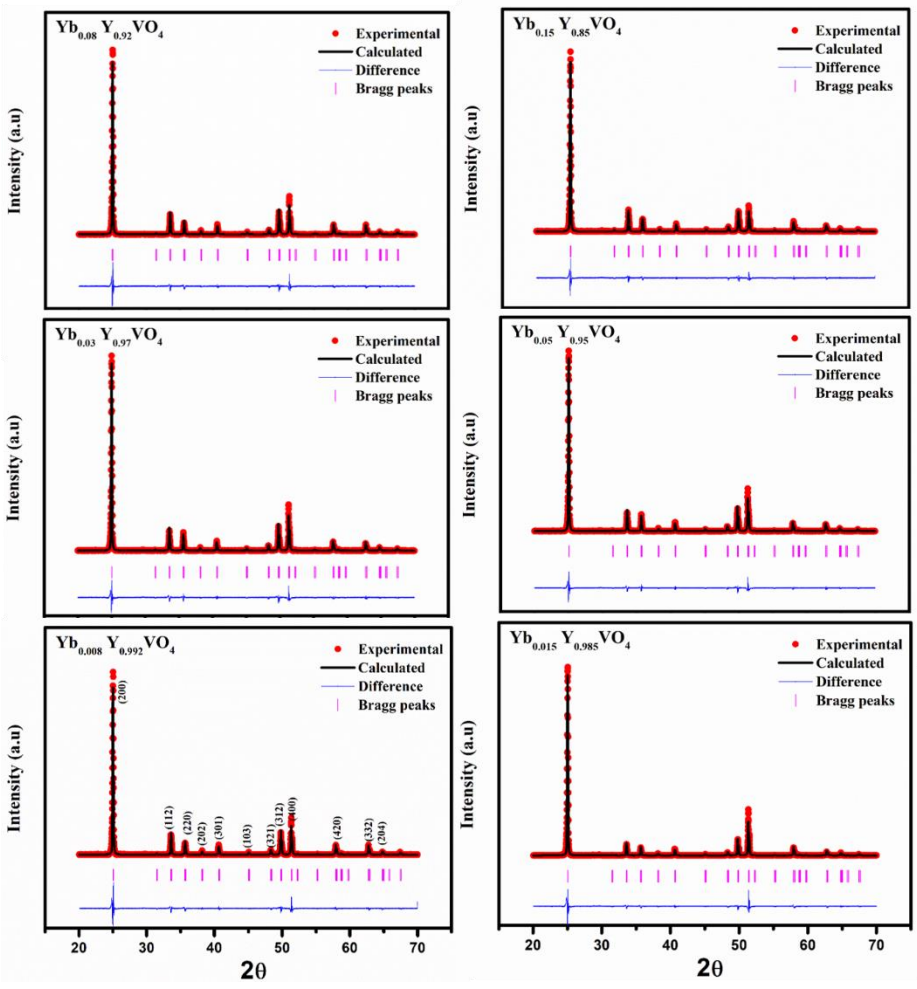

Figure 4.3 Powder X-Ray diffraction pattern of Yb doped crystals

Table 4.2 Lattice parameters and volume of Yb doped YVO_4 crystals

Lattice parameter	Yb conc. (at.%) *Actual Yb concentrations evaluated by XRF are shown in the bracket*						
	Undoped YVO_4	0.8 (0.75)	1.5 (1.48)	3.0 (2.94)	5.0 (4.79)	8.0 (7.88)	15.0 (14.3)
a(Å) & b (Å)	7.12 (5)	7.12(6)	7.12(4)	7.12(0)	7.12(0)	7.12(1)	7.11(8)
c(Å)	6.29 (2)	6.29(1)	6.29(6)	6.28(8)	6.28(6)	6.28(3)	6.28(2)
Volume ($Å^3$)	319.41(7)	319.45(6)	319.53(1)	318.76(6)	318.66(4)	318.60(2)	318.28(3)

4.1.4 Effect of Yb doping on optical absorption of YVO_4 crystals

The absorption of light by the molecule/ion depends on the angle between the polarization of electric field (E) of the incident light and the electric dipole moment (μ) of the molecule/ion in the lattice. The line-strength equations of different polarization of light for an electric dipole (ED) transition from initial |i⟩ multiplet to final ⟨f| multiplet is expressed as [146][147]:

$$S_{FI,q}^{ED} \sim e^2 \left|\left\langle f\left|D_q^{(1)}\right|i\right\rangle\right|^2 \ldots\ldots(4.1)$$

$$S_{FI,\pi}^{ED} = S_{FI,0}^{ED} \ldots\ldots(4.2)$$

$$S_{FI,\sigma}^{ED} = \frac{1}{2}\left(S_{FI,+1}^{ED} + S_{FI,-1}^{ED}\right) \ldots\ldots\ldots(4.3)$$

q (q=0 for π and ±1 for σ) represents the polarization of the incident light and |Dq| represents the polarization dependent irreducible matrix. The absorption for a particular polarization for a specific transition depends on the strength of the |Dq|. From the projection along a-[100] direction [Figure 4.4] it is evident that the symmetry of the

atomic arrangement are different for both the polarization direction resulting in different line strength and absorption characteristics.

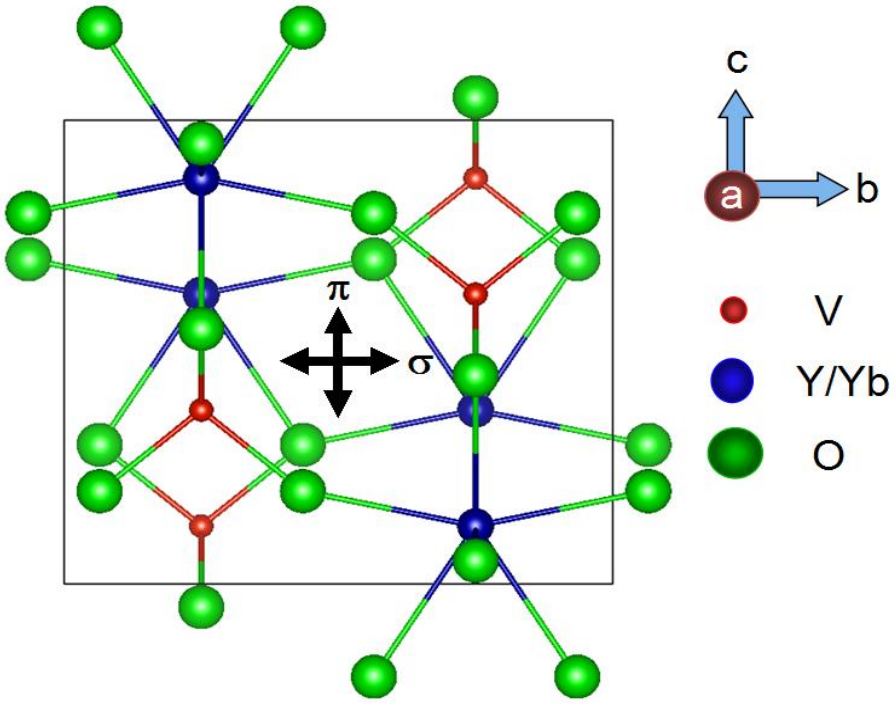

Figure 4.4 a-cut projection of YVO_4 crystal structure

Hence, the optical transmission spectra of [100] oriented polished plates of ~1 mm thickness were recorded at room temperature using polarized light from 200 to 1200 nm. The absorption coefficient was calculated from the transmission spectra at room temperature, using the following relation [128]:

$$T \approx (1 - R)^2 \, exp(-\alpha d) \qquad \ldots\ldots\ldots\ldots\ldots\ldots\ldots\ldots (4.4)$$

where, T is transmittance, R is reflectivity (calculated from Sellmeier's equation using $R \sim [(n-1)^2/(n+1)^2]$ and d is the sample thickness.

The significant polarization dependence is observed in the absorption spectra of YVO_4, because it possesses tetragonal crystal structure [Figure 4.4]. So the absorption spectra of [100] plate was measured with two different polarized light having E || to c-axis (π-polarization) and E⊥c to c-axis (σ-polarization).

Figure 4.5 shows the measured absorption spectra for different doping concentration of Yb crystals. The absorption for π-polarization is higher compared to the absorption for σ-polarization. Both the intensities of the absorption increases as the Yb concentration is increased in the sample for both the polarization. The spectra for the σ-polarization are characterized by strong absorption around 972 and 985 nm whereas the spectra for π-polarization are dominated by the absorption at ~985 nm as shown in the Figure 4.5.

In the literature report, the Yb ion has quasi three level energy. Hence, on analyzing the energy level diagram of Yb in YVO_4 matrix [2], it was observed that the energy difference between the ground state and the second Stark level of $^2F_{7/2}$ (~12 meV) is less than the thermal energy at room temperature (around 25 meV). In the present measurement the optical absorption spectra was measured at room temperature, the second Stark level should have non-zero population, which may cause transition between the second Stark level of $^2F_{7/2}$ to the higher Stark levels of $^2F_{5/2}$ [Figure 4.6].

Therefore, for evaluating the actual absorption cross-section for each transition of Yb ion, the absorption spectra were fitted with four peak corresponding to the Yb transitions. The value of R^2 >0.999 of the fit confirmed goodness of fit. The absorption from the second stark level of ground state of $^2F_{7/2}$ to highest Stark level of $^2F_{5/2}$ corresponds to the ~ 962 nm wavelength. Also, as expected, the absorption

corresponding to each peak increases individually as the doping of Yb is increased. The absorption band of Yb in YVO_4 at 985 nm comprises of four transitions. Therefore, the absorption cross-section for each transition was estimated and tabulated in the Table 4.3.

From the table of the absorption cross-section, it is evident that the cross-section is maximum for the doping concentration around 2.94 at.%. At higher doping concentration the Yb ions in the lattice comes close to each other resulting into interaction among themselves. This leads to concentration quenching which consequently decreases the absorption cross-section [119].

Table 4.3 Absorption cross-section of different Yb transitions

Yb (at.%)	Absorption cross-section (x 10^{-20} cm^2)							
	π polarization				σ polarization			
	985 nm	972 nm	962 nm	952 nm	985 nm	972 nm	962 nm	952 nm
0.75	4.528	0.868	0.469	0.451	1.071	0.951	0.976	0.785
1.48	4.572	0.916	0.555	0.436	1.138	1.063	0.953	0.804
2.94	5.088	1.249	0.683	0.585	1.512	1.493	1.043	1.011
4.79	4.086	0.997	0.492	0.419	1.092	1.094	0.967	0.769
7.88	2.402	1.223	0.526	0.468	1.071	1.241	0.891	0.881
14.3	1.860	1.263	0.415	0.429	1.007	1.138	0.795	0.741

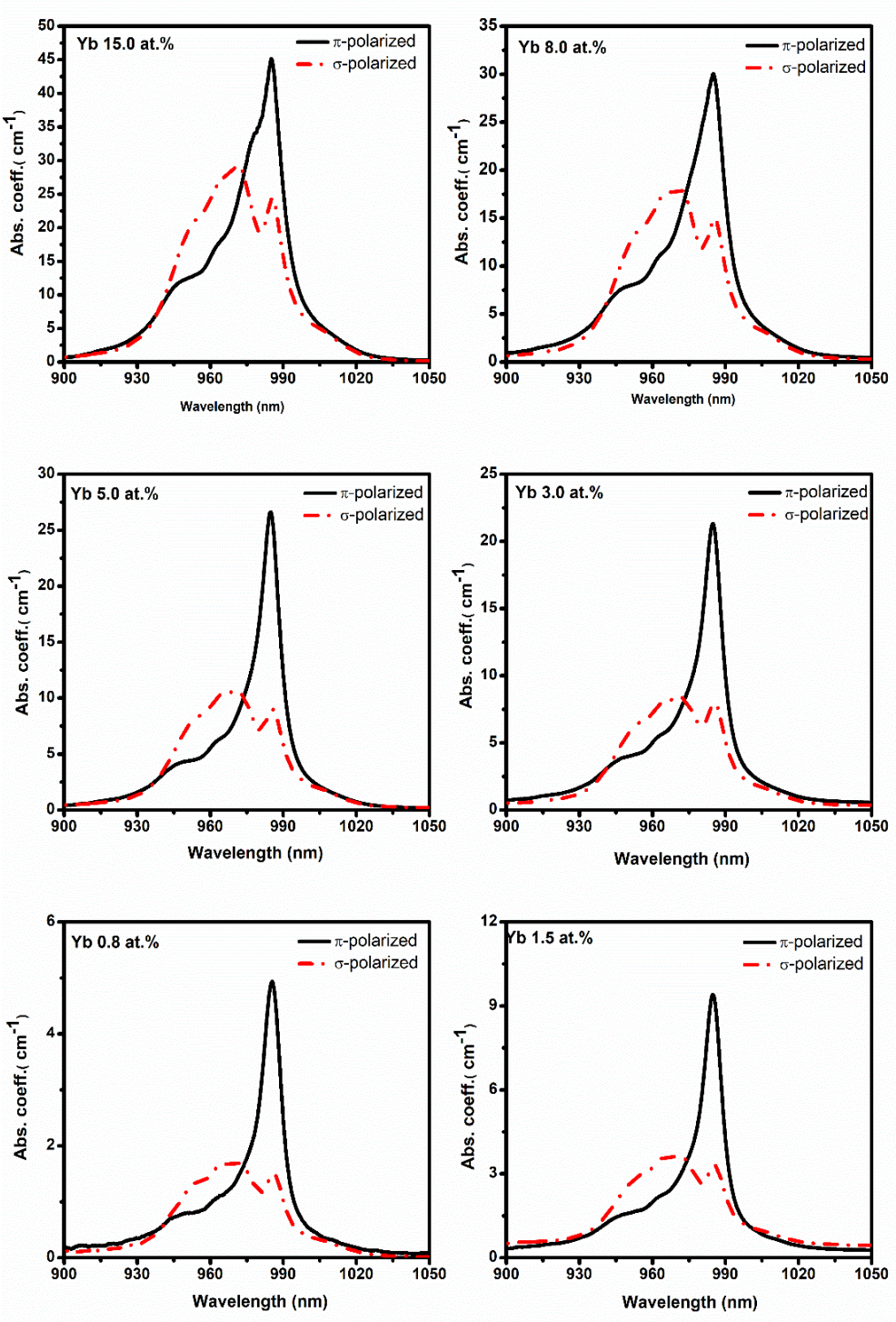

Figure 4.5 Absorption spectra of Yb doped crystals in π and σ-polarized light

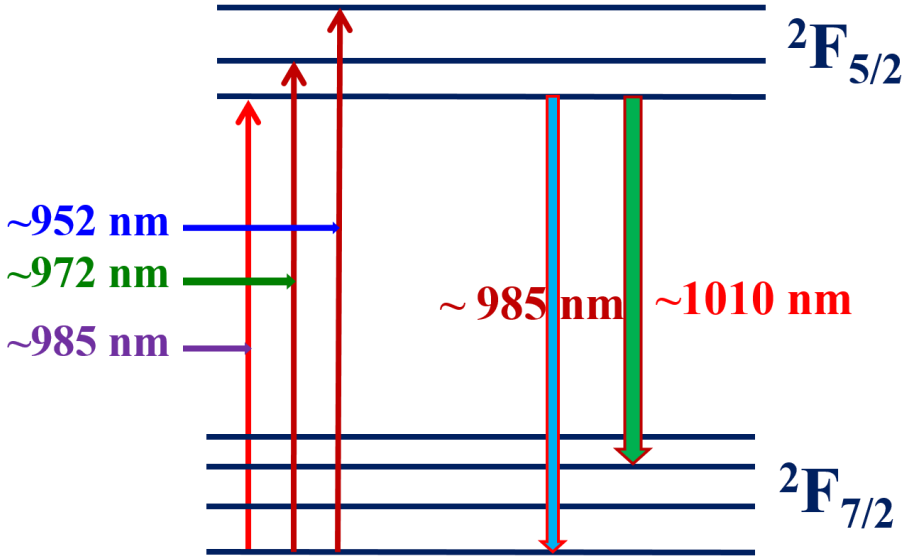

Figure 4.6 Energy level diagram of Yb ion

4.1.5 Effect of Yb concentration on the emission characteristics

The absorption study reveals that there are three prominent absorption transitions of Yb ion at 952, 972 and 985 nm. Therefore, to investigate the emission characteristics of Yb doped samples, the photoluminescence (PL) was measured on the [100] oriented plates of the Yb doped crystals using Edinburgh FL-FS90-s PL spectrometer. All Yb doped samples were excited at 952, 972 and 985 nm and the corresponding PL spectra were recorded in the range of 950-1100 nm. The emission spectra are characterized by two overlapped broad emission bands centered around 985 and 1010 nm [Figure 4.7], which are due to the transitions among different manifolds [Figure 4.6] of the involving energy levels arising due to the $\bar{4}2m$ (D_{2d}) site symmetric crystal field of YVO_4 crystal matrix and the Wyckoff's position of ions like Y, V and O in YVO_4 are such as (0; 3/4; 1/8) (0; 1/4; 3/8) and (0.0; 0.43510; 0.20280) respectively [2]. The PL intensity of Yb ion corresponding to 952 nm and 972 nm excitation is higher as compared to 985 nm excitation.

The emission at 985 nm dominates over 1010 nm at lower doping concentration. As the doping concentration of Yb is increased, the relative intensity of the fluorescence peak at 1010 nm with respect to the intensity at 985 nm increases. The PL intensity of 1010 nm crosses over the PL intensity of 985 nm as Yb doping increased beyond 4.79 at.%. The PL intensity corresponding to 952 nm and 972 nm excitation are of same order whereas the PL intensity corresponding to 985 nm excitation are very less as compared to 952 and 985 nm excitations [Figure 4.7].

Hence, for Yb doped YVO_4 laser gain medium, pumping with the 952 and 972 nm diode laser would be more efficient for YVO_4 laser gain medium [119].

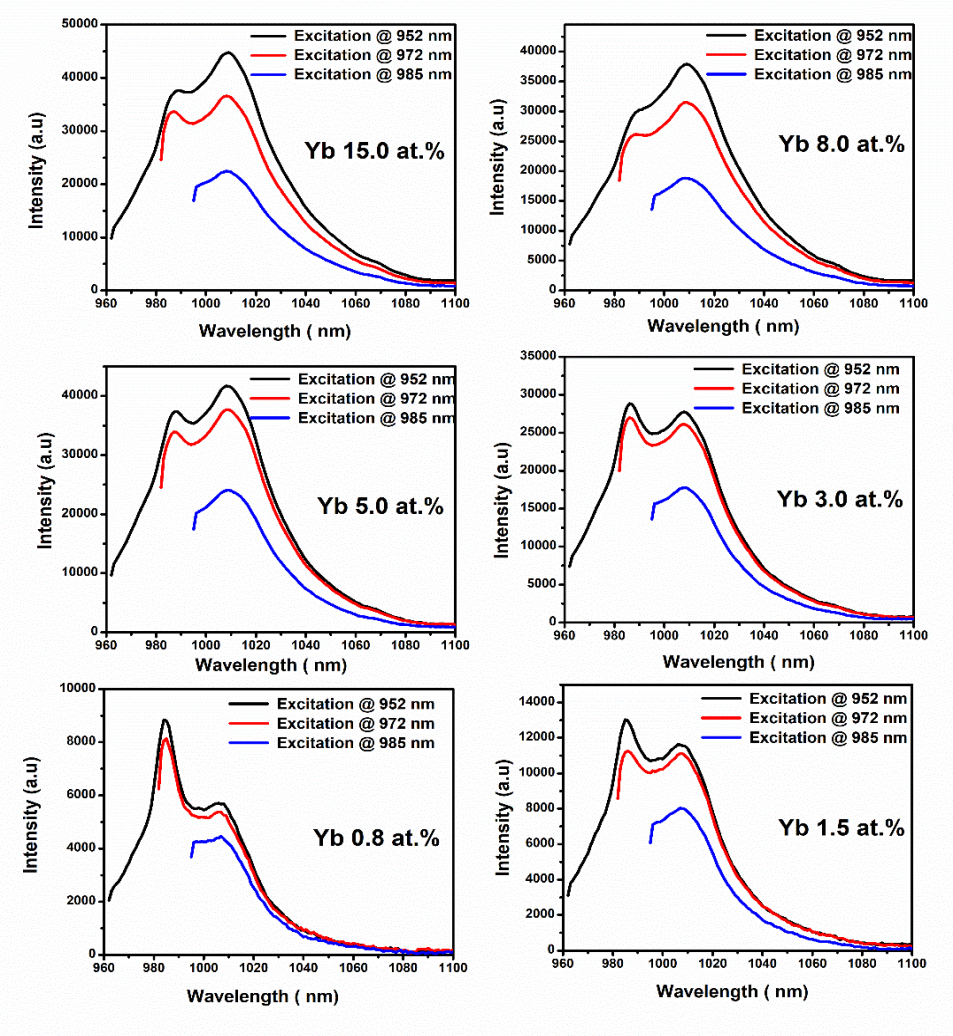

Figure 4.7 Emission spectra of Yb doped YVO_4 crystals with excitation @ 952, 972 and 985 nm

4.1.6 Effect of Yb doping on refractive index of YVO_4

Refractive index and thermo-optic coefficient of Yb:YVO_4 single crystal are important parameters for designing high power laser system. Therefore, the refractive index of Yb doped YVO_4 for Yb doping concentrations 1.5, 3.0, 8.0 and 15.0 at.% was measured using the prism coupling technique equipped with a monochromatic laser beam with orthogonal polarization of light such as TE(s-polarized) and TM(p-polarized) modes. The refractive index of the specimen of interest (n_s) is estimated by detecting the critical angle for both the TE and TM modes of incident light. From the measured θ_c for TM mode one gets the value of n_x and for the TE mode one gets n_y using the relation $n = n_p \sin\theta_c$ [117,120,121,148–150].

Measurement was carried out on [100] oriented polished plate for both the orthogonal polarization. As YVO_4 belongs to tetragonal crystal structure, for the a-cut plate, used in the measurement, b[010] and c[001] directions are on the plane of the sample and a[100] direction along the thickness of the sample [Figure 4.4]. During the measurement contact with the prism was made such a way that TE polarization would give refractive index values along crystallographic c[001] direction (n_e) whereas TM polarization would give value of refractive index along a[100] ($n_o = n_a = n_b$). Refractive indices of Yb doped YVO_4 along c[001] and a[100] were measured at room temperature (30°C) for four different wavelengths i.e., 532, 828, 1064 and 1551 nm and have been tabulated in Table 4.4. On referring to Table 4.4, it can be observed that Yb doping in general increases the refractive index (both n_e & n_o) of YVO_4. However, the variation of n_o is relatively larger in comparison to n_e. Also, n_o increases for all the concentration of Yb whereas n_e increases up to 8.0 at.% of Yb doping and thereafter decreases at 15 at. % of the doping. It is interesting to note that our earlier measurement of lattice

parameters of Yb doped sample [119] show that the lattice volume was almost independent of the doping concentration of Yb upto a doping concentration of 8 at.%, but for doping of 15 at. % of Yb the lattice parameters decrease, which influence the macroscopic polarizability which can be explained by the Classius-Mossotte relation.

The birefringence present in YVO_4 facilitates the generation of direct polarized laser output unlike for the case of YAG (which is isotropic). Also due to high birefringence, proper parallelism and axis matching of laser system during the designing of laser become crucial as it adversely influences the output beam quality and decreases of output power of laser. It is evident from Table 4.4 and Figure 4.8 that the birefringence was found to be maximum for 2.94 at.% of doping. So, a special care should be taken in terms of parallelism and axis matching during fabrication of laser element.

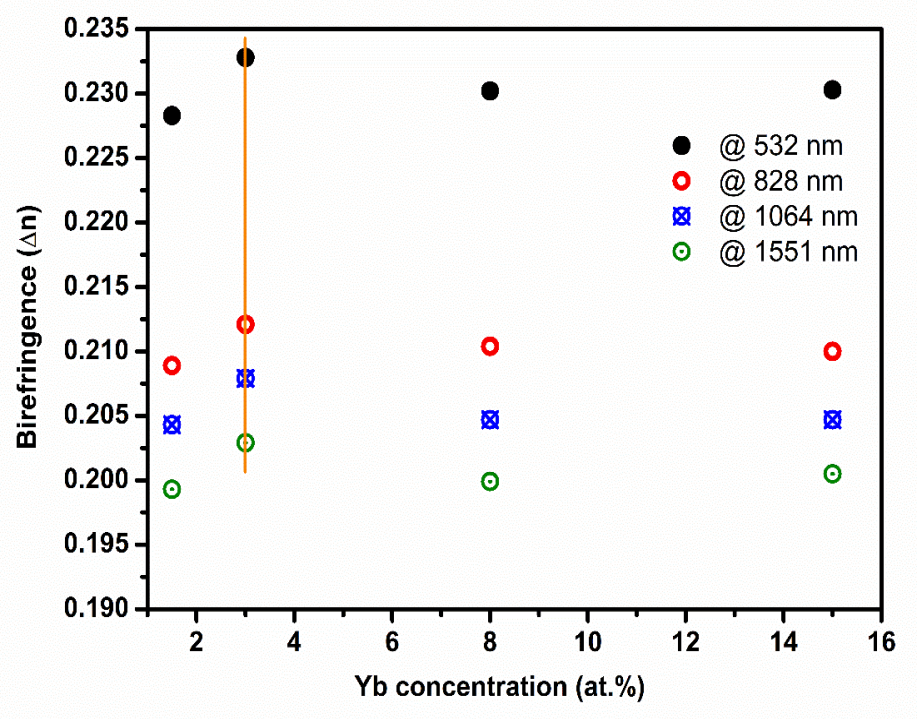

Figure 4.8 Birefringence of Yb doped YVO_4 single crystals

Further, the measured refractive index data were fitted to the Sellmeier equation [122][123]:

$$n^2(\lambda, T) = A_0(T) + \frac{B_0(T)}{\lambda^2 - C_0(T)} - D_0(T)\lambda^2 \ldots\ldots\ldots\ldots\ldots\ldots\ldots\ldots (4.5)$$

where *$A_0(T)$, $B_0(T)$, $C_0(T)$ and $D_0(T)$* are Sellmeier coefficients at temperature T (in °C) and λ is the wavelength (in μm). The plots for Sellmeier fitting for all the samples for n_o and n_e are shown in Figure 4.9.

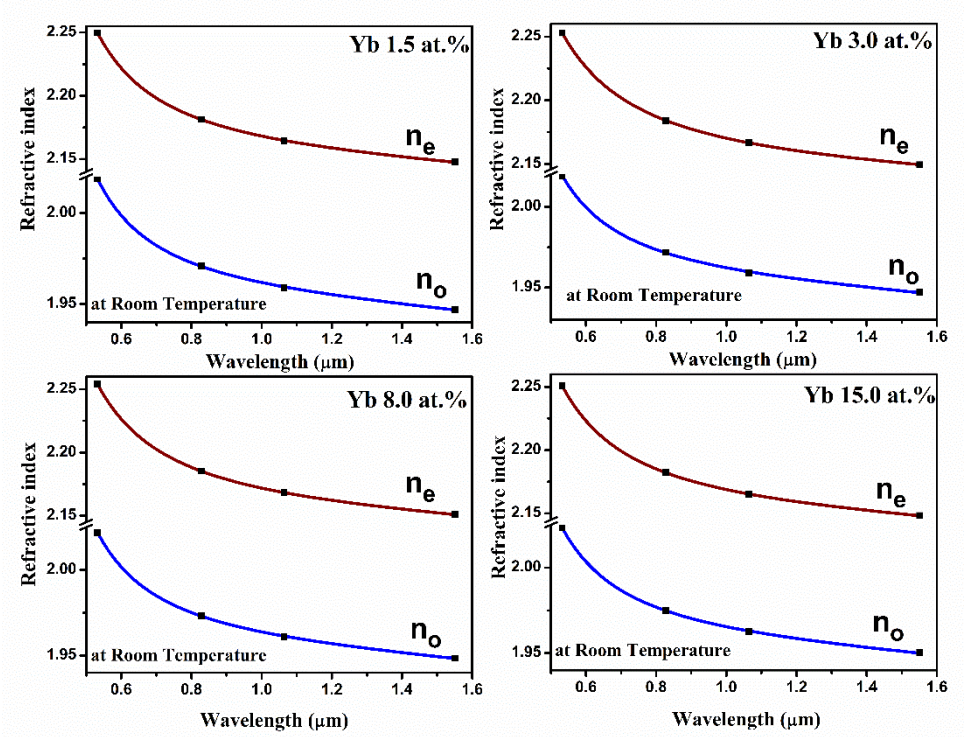

Figure 4.9 Fitting of Sellmeier equation for 1.5, 3.0, 8.0 and 15.0 at.% Yb doped YVO_4 single crystal

Table 4.4 Refractive index for different doping of Yb concentration in YVO_4

λ(nm)	Yb 1.5 at.%		Yb 3.0 at.%		Yb 8.0 at.%		Yb 15 at.%	
	(n_e)	(n_o)	(n_e)	(n_o)	(n_e)	(n_o)	(n_e)	(n_o)
532	2.249(8)	2.018(9)	2.252(8)	2.019(2)	2.253(9)	2.021(9)	2.250(7)	2.023(2)
828	2.181(4)	1.971(0)	2.184(9)	1.971(7)	2.185(3)	1.973(2)	2.182(2)	1.975(0)
1064	2.164(4)	1.958(8)	2.167(0)	1.959(1)	2.168(3)	1.961(0)	2.165(2)	1.962(5)
1551	2.147(6)	1.946(9)	2.149(5)	1.947(0)	2.151(0)	1.948(4)	2.148(2)	1.950(2)

The values of Sellmeier coefficients for different wavelengths have been listed in Table 4.5. It was observed that the Sellmeier coefficients of YVO_4 for TM (n_o) mode increase as the doping of Yb increases [141].

Table 4.5 Sellmeier coefficients at different temperature for YVO_4 crystals doped with different Yb concentrations

Sellmeier coefficients	Temperature (°C)					
	30 (RT)	50	75	100	125	150
Yb 1.5 at.%: n_e						
A_0	4.58303	4.58931	4.59885	4.60829	4.61737	4.62223
B_0	0.11596	0.1171	0.11592	0.11719	0.11631	0.11942
C_0	0.03689	0.03756	0.04177	0.04078	0.04421	0.04099
D_0	0.01191	0.01219	0.0119	0.01229	0.0127	0.01253
Yb 1.5 at.%: n_o						
A_0	3.77555	3.78687	3.79529	3.79895	3.80554	3.81086
B_0	0.07525	0.07152	0.0698	0.07104	0.07187	0.07373
C_0	0.03514	0.04496	0.05639	0.05331	0.04852	0.04293
D_0	0.00823	0.01015	0.01077	0.00949	0.0102	0.0112
Yb 3.0 at.%: n_e						
A_0	4.61202	4.61422	4.62576	**4.62898**	4.63572	4.64512
B_0	0.10807	0.11267	0.111	0.1152	0.11657	0.11679
C_0	0.05125	0.04536	0.04903	0.04517	0.04521	0.04554
D_0	0.01634	0.01497	0.01549	0.01403	0.01368	0.01427
Yb 3.0 at.% : n_o						
A_0	3.78117	3.78655	3.79332	3.79549	3.80262	3.82101
B_0	0.07472	0.07606	0.07512	0.07948	0.07863	0.06925
C_0	0.03474	0.03159	0.03668	0.02799	0.03055	0.05325
D_0	0.01057	0.01095	0.01049	0.01036	0.01035	0.01408
Yb 8.0 at.% : n_e						
A_0	4.59192	4.6052	4.61671	4.61833	4.62756	4.64035
B_0	0.12247	0.11856	0.11694	0.12212	0.12227	0.1214
C_0	0.02893	0.03604	0.03939	0.03541	0.03597	0.03749
D_0	0.01184	0.01366	0.01439	0.0124	0.01284	0.01478
Yb 8.0 at.% : n_o						
A_0	3.79196	3.79531	3.80035	3.80916	3.81818	3.81943
B_0	0.07107	0.07337	0.07375	0.06993	0.06866	0.0738
C_0	0.0445	0.04053	0.04252	0.05513	0.05865	0.04415
D_0	0.01083	0.01037	0.00967	0.00995	0.01178	0.01059
Yb 15 at.% : n_e						
A_0	4.61244	4.6209	4.63126	4.63985	4.6411	4.65072
B_0	0.11162	0.11157	0.11168	0.1115	0.11763	0.11519
C_0	0.04585	0.04786	0.04863	0.05171	0.04442	0.04949
D_0	0.01395	0.01437	0.01498	0.01559	0.01393	0.01348
Yb 15 at.% : n_o						
A_0	3.80704	3.80941	3.81304	**3.83008**	3.82777	3.83714
B_0	0.06646	0.0691	0.072	0.06268	0.06796	0.06627
C_0	0.05446	0.04986	0.04384	0.06995	0.05896	0.06406
D_0	0.01307	0.01251	0.0118	0.0148	0.01159	0.01372

4.1.7 Temperature dependence of refractive index

Thermal coefficient of refractive index is a useful parameter for designing and fabrication of laser. Measurement of temperature dependent refractive index was carried out in the range 30-150 °C in the interval of 25 °C. Accuracy in the temperature control is ±1 °C [116]. Measurement was carried out for the samples with different doping concentrations of Yb i.e., for 1.5, 3.0, 8.0 and 15.0 at. % doped samples. Temperature dependent Sellmeier coefficients for all the doping concentrations of Yb were calculated by fitting Sellmeier equation. For all the doping concentrations of Yb, the Sellmeier fitting is shown in Figure 4.10 and Sellmeier coefficients for all the dopants were tabulated in Table 4.5. It was observed that as the temperature increases the refractive index also increases for all the doping concentrations.

It was found that the "A_0" coefficient increases significantly, (which is in-line with the variation of n with respect to the temperature) in comparison to other Sellmeier coefficients with increasing temperature. In the Sellmeier equation the dimensionless parameter A_0 (the first term) predominantly influence the value of the refractive index whereas the second and third term signifies the wavelength dependence of the refractive index. Hence, the change in the refractive index with temperature is primarily the depiction of the variation of A_0 with respect to the temperature.

Further, the temperature coefficient of the refractive index (the thermo-optic coefficient) was calculated. Figure 4.11 shows the measured refractive indices with different doping concentrations of Yb as a function of temperature for different wavelengths. The temperature dependent refractive index data was found to be linear on fitting (standard deviation ~10^{-6}, R^2-value ~0.9997) as per the following relation for all the doping concentrations:

$$n(\lambda, T) = n_0(\lambda) + \left[\frac{dn(\lambda)}{dT}\right] T \quad \ldots\ldots\ldots\ldots\ldots\ldots\ldots\ldots (4.6)$$

where T is temperature in °C, $n_o(\lambda)$ refers to the refractive index (RI) at 0°C for a specific wavelength and dn/dT is the temperature coefficient of RI.

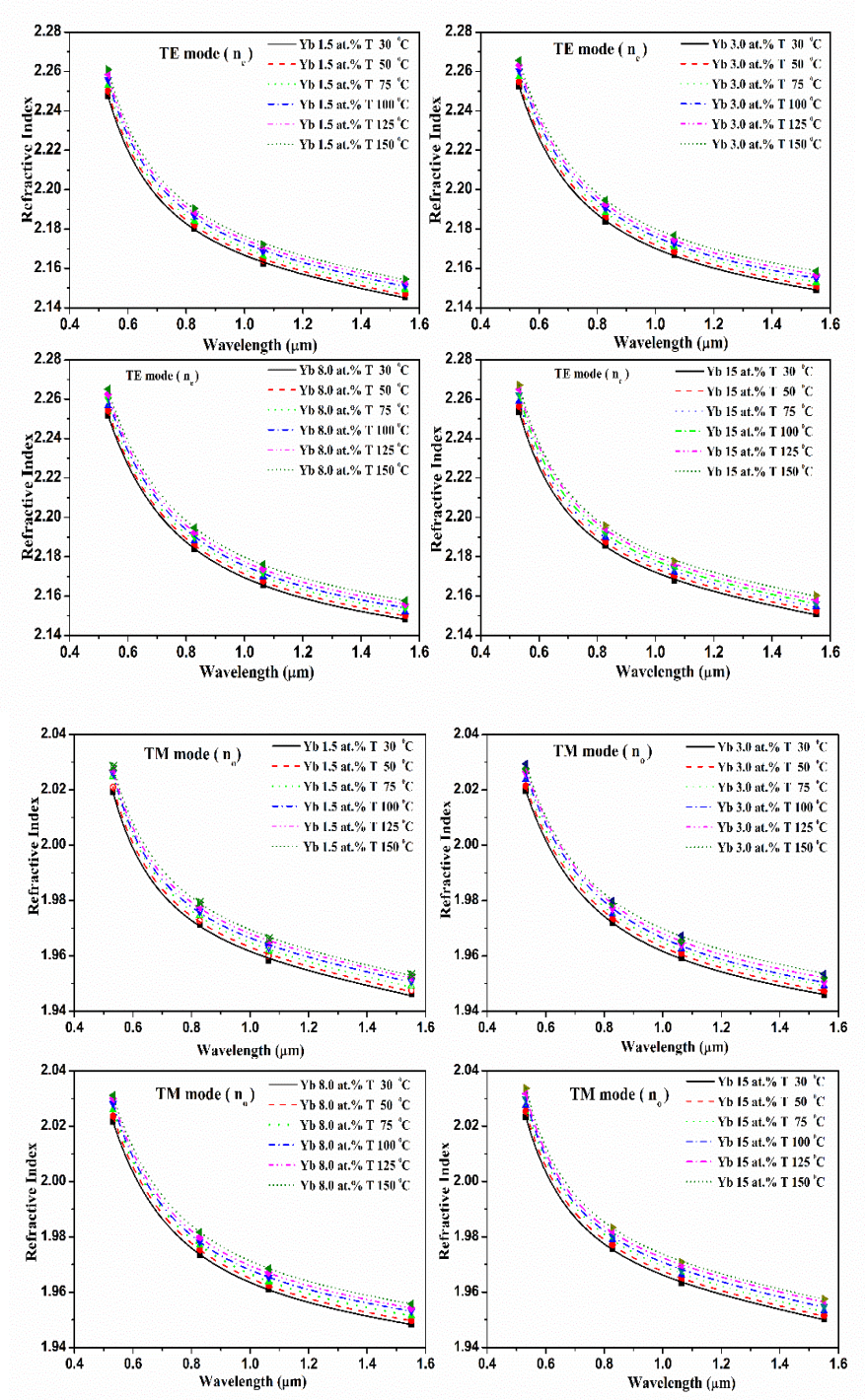

Figure 4.10 Fitting of Sellmeier equation of n_e and n_o of YVO_4 single crystal for all the doping concentrations of Yb

The thermal coefficient of RI was order of 10^{-5}/°C. The values of the thermo-optic coefficient for all the Yb doped YVO_4 crystals are provided in the Table 4.6 It shows that thermo-optic coefficient for extraordinary RI is always higher than that of ordinary RI. Also, significant variation in the thermo-optic coefficients for n_o of Yb:YVO_4 was observed with increasing concentration of Yb in the crystal.

Refractive index depends on the polarizability of the constituent ions and governed by the Clausius-Mossotti equation (also known as Lorentz-Lorenz relation when used in optics). It relates the atomic polarizability of a linear dielectric to the permittivity (dielectric constant) and hence to the refractive index. The variation of dn/dT can be explained on the basis of macroscopic Clausius-Mossotti relation given by:

$$\frac{(\varepsilon - 1)}{(\varepsilon + 2)} = \frac{(n^2 - 1)}{(n^2 + 2)} = \frac{4\pi}{3}\frac{\alpha_m}{V} \ldots\ldots\ldots\ldots\ldots\ldots\ldots\ldots\ldots \quad (4.7)$$

where, ε is the permittivity and α_m is the polarizability of the macroscopic sphere of volume *V*. The macroscopic polarizability is proportional to the number of unit cell in the sphere and depends on the polarizabilities of the particles and structure of the lattice. This macroscopic equation is valid for non-cubic symmetry as well. In the Clausius-Mossotti formalism the long-range influence of the material outside the sphere, due to dipole-dipole interactions is taken into account. Also, the polarizability being a macroscopic quantity, is highly sensitive to the short-range ordering and perturbations.

For example, the internal fields due to the non-cubic environments are sensitive over short distances [151]. Differentiation of equation (4.7) with respect to temperature at constant pressure results [151]:

$$\frac{1}{(\varepsilon+2)(\varepsilon-1)}\left(\frac{\partial\varepsilon}{\partial T}\right)_P = -\beta + \left[\beta\frac{V}{\alpha_m}\left(\frac{\partial\alpha_m}{\partial V}\right)_T\right] + \frac{1}{3\alpha_m}\left(\frac{\partial\alpha_m}{\partial T}\right)_V \ldots\ldots\ldots \quad (4.8)$$

where, β is the thermal expansion coefficient.

If the thermal expansion coefficient is large compared to the other two positive terms, the slope *dn/dT* is negative. In general, the material with high melting point and mechanical hardness leads to low thermal expansion [can be understood through Grüneisen parameter] [152].

Yb:YVO_4 being a material with high melting point and mechanical hardness, the contribution of the first term is expected to be low resulting into the observed positive thermo-optic coefficient.

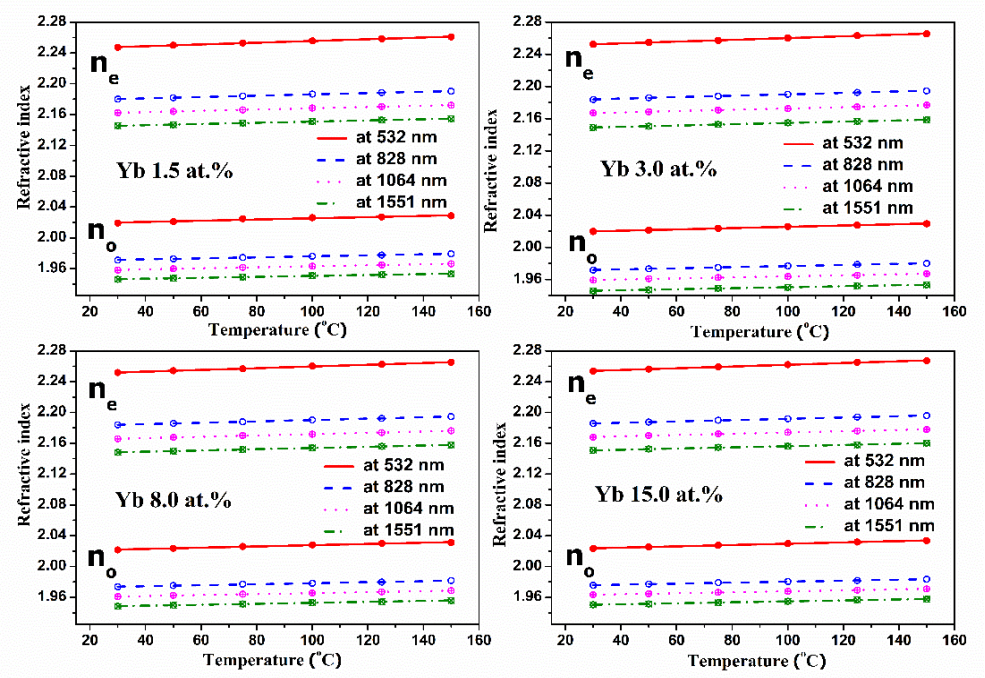

Figure 4.11 dn/dT for all the Yb doped YVO_4 crystals

Table 4.6 Thermo-optic coefficient of Yb doped YVO_4 single crystals

		Thermo-optic coefficient (x10^{-5}/°C)	
		For n_e	For n_o
Yb 1.5 at.%	532 nm	11.27	7.79
	828 nm	8.64	6.65
	1064 nm	8.25	6.70
	1551 nm	7.78	6.02
Yb 3.0 at.%	532 nm	11.02	8.14
	828 nm	8.84	6.88
	1064 nm	8.13	6.53
	1551 nm	8.08	6.26
Yb 8.0 at.%	532 nm	11.1	8.08
	828 nm	8.85	6.44
	1064 nm	8.56	6.30
	1551 nm	7.93	6.19
Yb 15 at.%	532 nm	11.3	8.54
	828 nm	8.60	6.41
	1064 nm	8.10	6.31
	1551 nm	7.71	6.31

Further, the wavelength dependence of the thermo-optic coefficient was obtained by fitting the dn/dT vs wavelength data in cubic polynomial [141]:

$$\left(\frac{dn}{dT}\right)_{n_e}^{1.5\ at.\%} = \left(4.905 + \frac{7.852}{\lambda} - \frac{6.752}{\lambda^2} + \frac{2.329}{\lambda^3}\right) \times 10^{-5}/°C \ldots\ldots\ldots\ldots\ldots\ldots\ldots\ldots (4.9)$$

$$\left(\frac{dn}{dT}\right)_{n_o}^{1.5\ at.\%} = \left(-1.894 + \frac{22.279}{\lambda} - \frac{18.834}{\lambda^2} + \frac{5.173}{\lambda^3}\right) \times 10^{-5}/°C \ldots\ldots\ldots\ldots\ldots (4.10)$$

$$\left(\frac{dn}{dT}\right)_{n_e}^{3.0\ at.\%} = \left(12.966 - \frac{14.761}{\lambda} + \frac{13.164}{\lambda^2} - \frac{3.118}{\lambda^3}\right) \times 10^{-5}/°C \ldots\ldots\ldots\ldots (4.11)$$

$$\left(\frac{dn}{dT}\right)_{n_o}^{3.0\ at.\%} = \left(6.288 - \frac{0.764}{\lambda} + \frac{1.244}{\lambda^2} - \frac{0.166}{\lambda^3}\right) \times 10^{-5}/°C \ldots\ldots\ldots\ldots\ldots\ldots (4.12)$$

$$\left(\frac{dn}{dT}\right)_{n_e}^{8.0\ at.\%} = \left(2.853 + \frac{13.949}{\lambda} - \frac{11.669}{\lambda^2} + \frac{3.510}{\lambda^3}\right) \times 10^{-5}/℃ \ldots\ldots\ldots\ldots\ldots (4.13)$$

$$\left(\frac{dn}{dT}\right)_{n_o}^{8.0\ at.\%} = \left(5.087 + \frac{3.475}{\lambda} - \frac{3.641}{\lambda^2} + \frac{1.405}{\lambda^3}\right) \times 10^{-5}/℃ \ldots\ldots\ldots\ldots\ldots\ldots (4.14)$$

$$\left(\frac{dn}{dT}\right)_{n_e}^{15.0\ at.\%} = \left(6.639 + \frac{2.570}{\lambda} - \frac{2.112}{\lambda^2} + \frac{1.103}{\lambda^3}\right) \times 10^{-5}/℃ \ldots\ldots\ldots\ldots\ldots\ldots (4.15)$$

$$\left(\frac{dn}{dT}\right)_{n_o}^{15.0\ at.\%} = \left(5.377 + \frac{3.588}{\lambda} - \frac{4.504}{\lambda^2} + \frac{1.858}{\lambda^3}\right) \times 10^{-5}/℃ \ldots\ldots\ldots\ldots\ldots (4.16)$$

These relations are useful for calculating the thermo-optic coefficient at any temperature and wavelength in the range of the measurement. The estimation of the value of thermo-optic coefficient will be useful to determine the criticality of the requirement of cooling of the gain medium [1].

4.2 Characterization of Er co-doped Yb:YVO_4 single crystals

To investigate the effect of doping concentration of Yb on the optical and spectral properties of Er (0.7 at.%) dopedYVO_4, the different concentrations of Yb i.e., 1.5, 3.0, 8.0 and 12.0 at% were chosen for the present investigation.

4.2.1 Effect of Yb doping on lattice parameters of Er:YVO_4 crystals

The powder X–rays diffraction patterns were recorded using a Rigaku Ultrax-18 powder diffractometer in the range of 20-70°. The lattice parameters of the crystals were calculated using Le Bail fitting. It was observed that the lattice parameters increase in the both direction (a and c) as the Yb concentration in the crystal was increased which signifies the expansion in the lattice volume [138].

4.2.2 Effect of Yb doping on the spectroscopic properties of Er:YVO_4

To investigate the spectroscopic properties of Yb co-doped Er:YVO_4 single crystals, the transmission spectra of [100] oriented polished plates of ~1 mm thickness were recorded at room temperature using unpolarized and polarized light from 300 to 1200 nm [Figure 4.12-4.14].

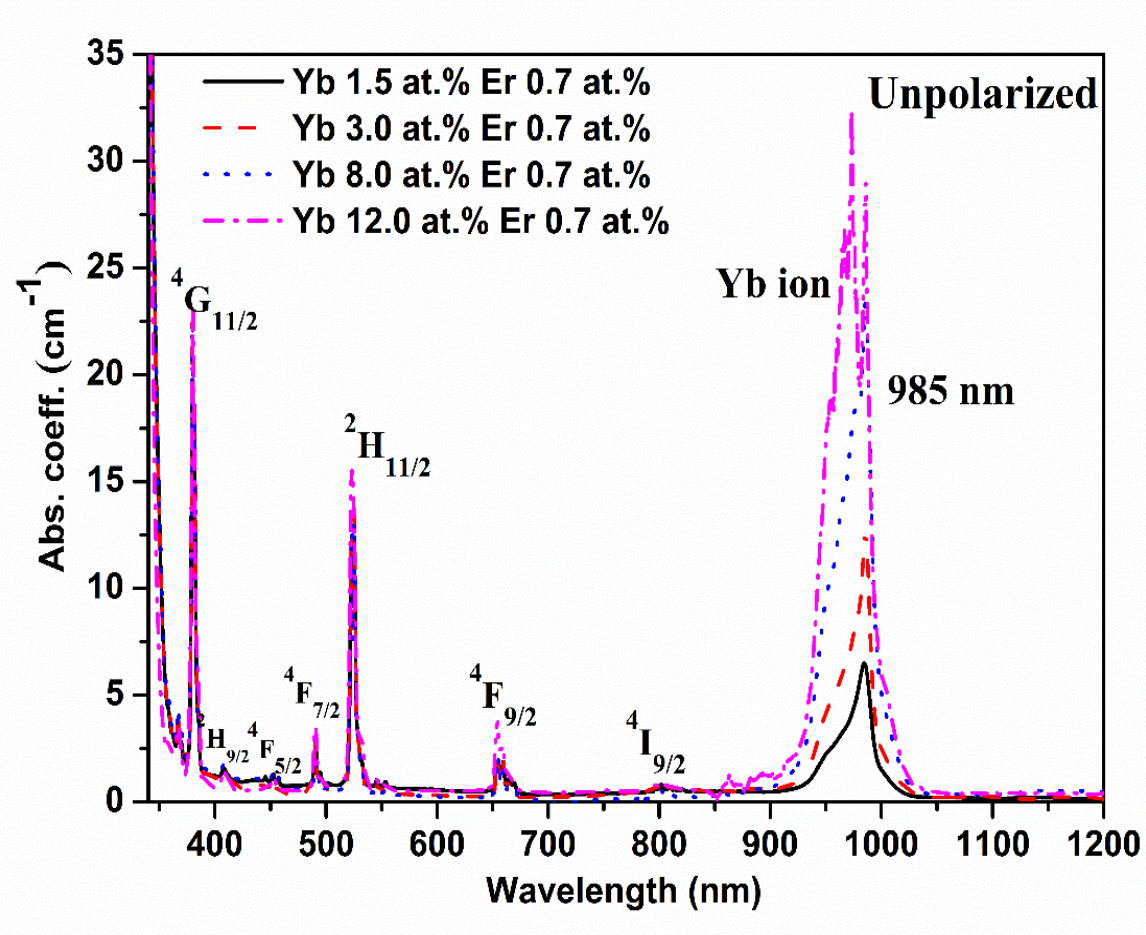

Figure 4.12 Absorption spectra of Yb:Er:YVO_4 crystal using unpolarized light

The absorption coefficient was calculated from the transmission spectra using the equation (4.4).

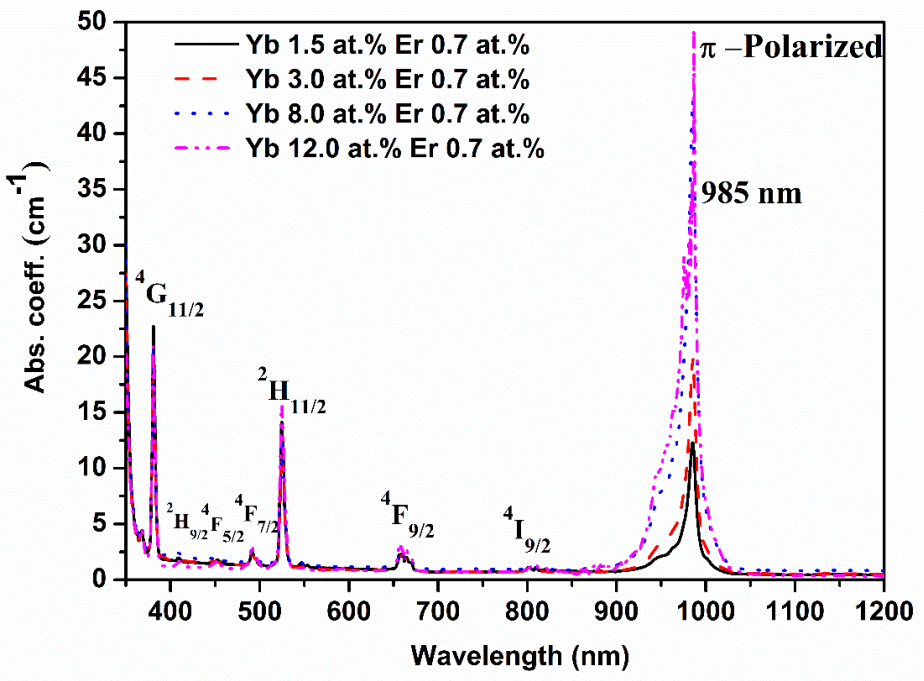

Figure 4.13 Absorption spectra of Yb co-doped Er:YVO_4 crystal for π-polarization

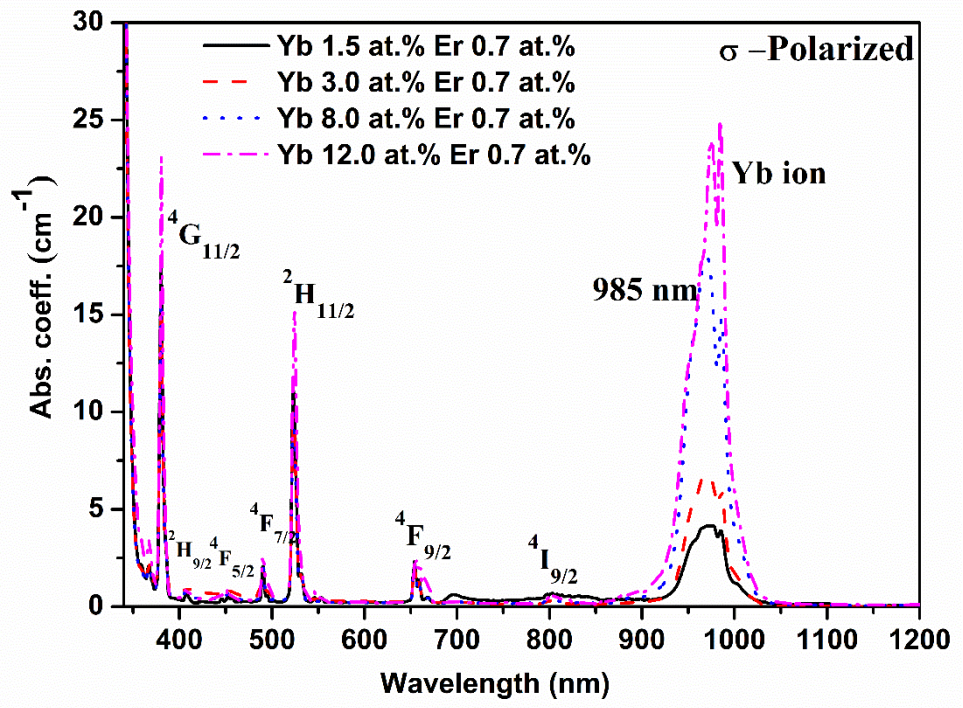

Figure 4.14 Absorption spectra of Yb co-doped Er:YVO_4 crystal for σ-polarization

The absorption spectra exhibit several sharp peaks corresponding to electric dipole (ED) transitions between 4f-4f intra-band of Er ion in both unpolarized and polarized measurement. These transitions are generally not allowed as they violate the parity conservation (ED operator is of odd parity) because of the same parity of initial and final states but become allowed due to resultant mixed parity of the states in D_{2d} non-centrosymmetric crystal field of YVO_4. However, the shielding effect of the outer $5s^2$ and $5p^6$ shells is enough to makes the f-f transitions sharp and distinct. In addition, the spectra are also characterized by the prominent absorption at 985 nm due to Yb ion for all the Yb co-doped samples.

Further, in the absorption spectra, it was also found that the absorption corresponding to all the transitions in the Er ions, including the transition at 808 nm, decreases as the doping concentration of Yb was increased. This is because both Er and Yb ion replace the yttrium ions in the lattice and as a result as the doping concentration of Yb increases, it may inhibit the occupation of Er at the same site. This is attributed to higher ionic radii of Er (1.03 A) than that of Yb (1.00 A) and lesser that of Y (1.04 A) favouring preferential occupation of Yb at Y site. It is evident that the absorption corresponding to the 808 nm, used for pumping in Er laser, is very weak in unpolarized as well as polarized spectra and also as the doping concentration of Yb increases, the absorption of Er ions decreases. However, as it is apparent from the absorption plot, in the Yb co-doped Er:YVO_4 crystals, pumping can be done using the stronger absorption band of Yb ion at 985 nm for emission of Er ions at 1.55 and 2.9 μm. Here, Yb ion acts as sensitizer for Er doped YVO_4 laser gain medium. Therefore, optimization of Yb concentration in this gain medium is important for efficient laser performance.

Therefore, for a better insight, spectroscopic analysis of Er ion having f–f transitions are evaluated by the Judd–Ofelt theory [43,129,135] with respect to varied doping concentration of Yb. Further, Judd-Ofelt parameters calculated from unpolarized and polarized absorption spectra, were used for obtaining the emission parameters of Yb co-doped Er:YVO_4 were compared with the parameters of the Er doped YVO_4.

4.2.2.1 The spectroscopic properties of Er in Yb:YVO_4 using unpolarized light

The absorption characteristics of the f-f transitions of Er^{3+} ion were investigated using Judd-Ofelt (JO) theory [134–136] for unpolarized incident light. According to JO theory the line strength of force electric dipole transition between an initial manifold $|4f^9[L, S]\ J\rangle$ and final manifold $4f^9[L', S']\ J'\rangle$ is

$$S(J \to J') = \sum_{i=2,4,6} \Omega_i \left|\langle [S\ L], J \| U^i \| [S'\ L'], J' \rangle\right|^2 \quad \ldots\ldots\ldots\ldots\ldots\ldots\ldots\ldots (4.17)$$

where $\langle \| U_i \| \rangle$ are the doubly reduced matrix elements of the unit-tensor operators for the transitions from the ground-state to the excited-state manifold, and the coefficients Ω_2, Ω_4 and Ω_6 are phenomenological JO intensity parameters [134]. These matrix elements, especially for the rare earth elements, are calculated with in the intermediate coupling approximation [134][133][135]. The numerical values of the doubly reduced matrix elements for Er [Table 4.7] were computed by Carnall et al. [134]. As the matrix elements do not depend on the environment of the ion, these were used in the present calculations [134]. The experimental line strength of forced electric dipole transition S was calculated from the absorption spectra using following equation [134][135].

$$S_{J\to J'} = \frac{\int \alpha(\lambda)d\lambda}{\frac{8\pi^3\rho\bar{\lambda}e^2}{9ch(2J+1)}\left[\frac{(n^2+2)^2}{3n}\right]} \quad \ldots\ldots\ldots\ldots\ldots\ldots\ldots\ldots\ldots\ldots\ldots\ldots\ldots\ldots (4.18)$$

where *c* is the velocity of light, *h* is the Planck's constant, *e* is the charge of electron, ρ is the number density of Er^{3+} ions per cc, *J* and *J′* are the total angular momentum of initial and final states, $\bar{\lambda}$ is the mean wavelength and *α(λ)* is the absorption coefficient of absorption band, *n* is the refractive index of the material obtained using Sellmeier's equation and the integral in the numerator is the area under the absorption band [43].

Table 4.7 Doubly reduced matrix elements for transition of Er [134]

$[SL]J_i \rightarrow [SL]J_f$	$[U_2]^2$	$[U_4]^2$	$[U_6]^2$
$^4G_{11/2} \rightarrow {}^4I_{15/2}$	0.9183	0.5262	0.1172
$^2H_{9/2} \rightarrow {}^4I_{15/2}$	0.0	0.0189	0.2256
$^4F_{5/2} \rightarrow {}^4I_{15/2}$	0.0	0.0	0.2232
$^4F_{7/2} \rightarrow {}^4I_{15/2}$	0.0	0.1469	0.6266
$^2H_{11/2} \rightarrow {}^4I_{15/2}$	0.7125	0.4125	0.0925
$^4F_{9/2} \rightarrow {}^4I_{15/2}$	0.0	0.5354	0.4618
$^4I_{9/2} \rightarrow {}^4I_{15/2}$	0.0	0.1733	0.0099

The line strengths (S_{exp}) for all the transitions were calculated for Yb 1.5, 3.0, 8.0 and 12.0 at.% in Er 0.7 at.%:YVO_4 from the absorption spectra using the equation (4.18) [Table 4.8]. Subsequently the JO parameters were calculated using equation (4.17) by least mean-square fitting and tabulated in Table 4.9. As the number of the

absorption lines are more than three, it was possible to obtain over-deterministic solutions.

From absorption spectra, the calculated line strength of all absorption transition of Er ions decreases as the doping concentration of Yb increases as shown in Table 4.8 and this is because of Er and Yb both replace the yttrium ions in the lattice. Further, for investigating, the emission characteristics, photoluminescence (PL) was recorded for the [100] oriented plates using excitation at wavelength at 808, 952, 972 and 985 nm and the corresponding PL spectra were recorded in the range of 1000-1700 nm under the similar conditions [Figure 4.15].

Table 4.8 Line strength of Er transition line in doped Yb:YVO_4

$\bar{\lambda}$ (nm)	[SL]J_f	Line strength Sexp. (x10^{-20}) cm^2			
		Yb 1.5 at.%	Yb 3.0 at.%	Yb 8.0 at.%	Yb 12.0 at.%
381	$^4G_{11/2}$	15.0325	14.9013	14.7524	14.6604
410	$^2H_{9/2}$	0.4442	0.5389	0.531	0.5294
452	$^4F_{5/2}$	0.4626	0.6202	0.4974	0.6873
491	$^4F_{7/2}$	1.1017	1.1703	1.4081	1.4073
525	$^2H_{11/2}$	10.4399	10.6221	10.6891	10.8376
658	$^4F_{9/2}$	1.9302	2.1921	2.4592	2.6067
803	$^4I_{9/2}$	0.488	0.615	0.5816	0.5815

Table 4.9 Judd-Ofelt parameters for Er doped Yb:YVO_4

Er (0.7 at.%) Yb concentration	JO parameters (x10^{-20}) cm^2			X= Ω_4/Ω_6
	Ω_2	Ω_4	Ω_6	
Yb 1.5 at.%	14.1597	2.4188	1.3495	1.7924
Yb 3.0 at.%	13.9262	2.8094	1.4727	1.9076
Yb 8.0 at.%	13.6541	3.1255	1.6621	1.8805
Yb 12.0 at.%	13.5723	3.2771	1.7436	1.8796

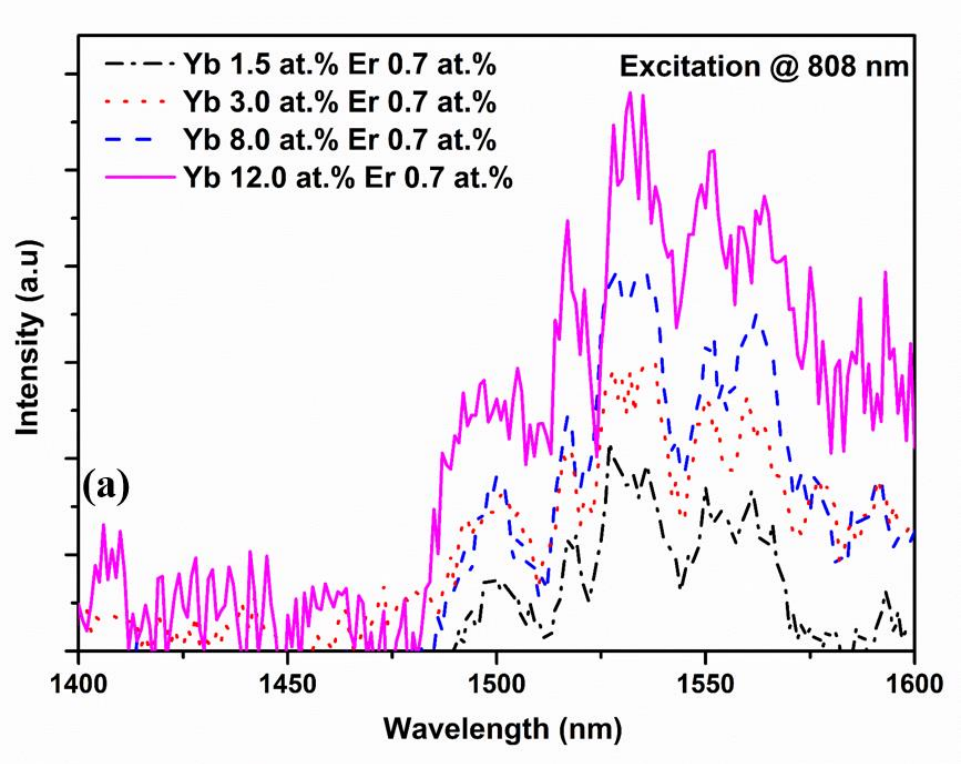
Yb 1.5 at.% Er 0.7 at.%
Yb 3.0 at.% Er 0.7 at.%
Yb 8.0 at.% Er 0.7 at.%
Yb 12.0 at.% Er 0.7 at.%
Excitation @ 808 nm
Intensity (a.u)
(a)
1400
1450
1500
1550
1600
Wavelength (nm)

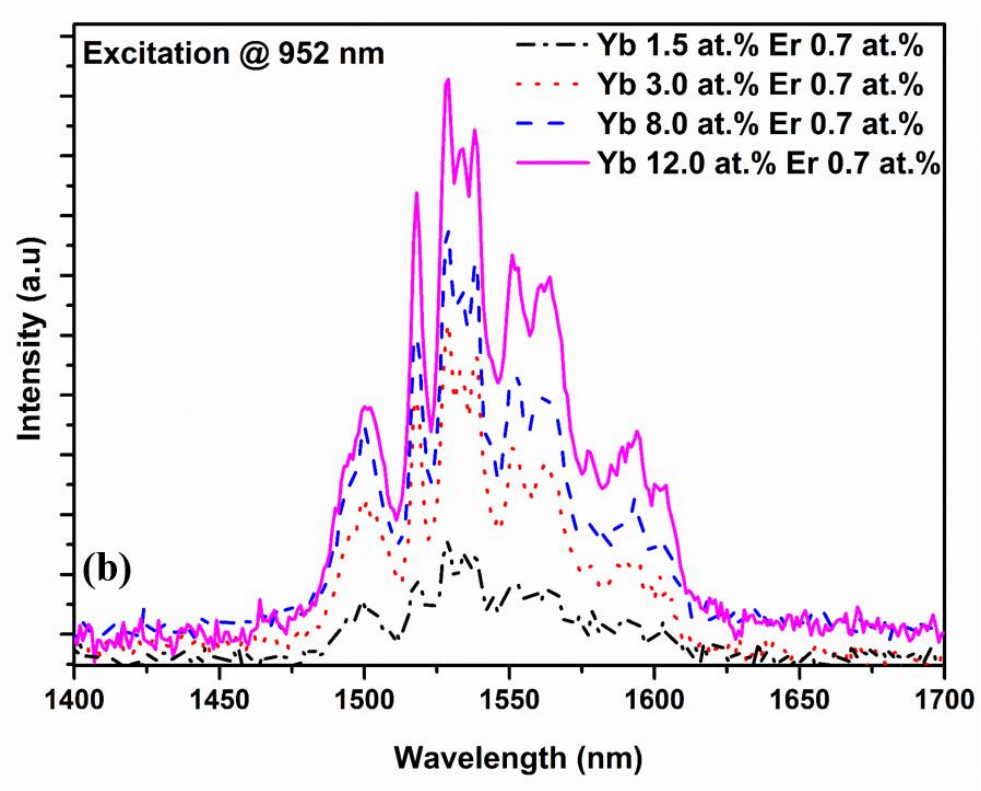
Excitation @ 952 nm
Yb 1.5 at.% Er 0.7 at.%
Yb 3.0 at.% Er 0.7 at.%
Yb 8.0 at.% Er 0.7 at.%
Yb 12.0 at.% Er 0.7 at.%
Intensity (a.u)
(b)
1400
1450
1500
1550
1600
1650
1700
Wavelength (nm)

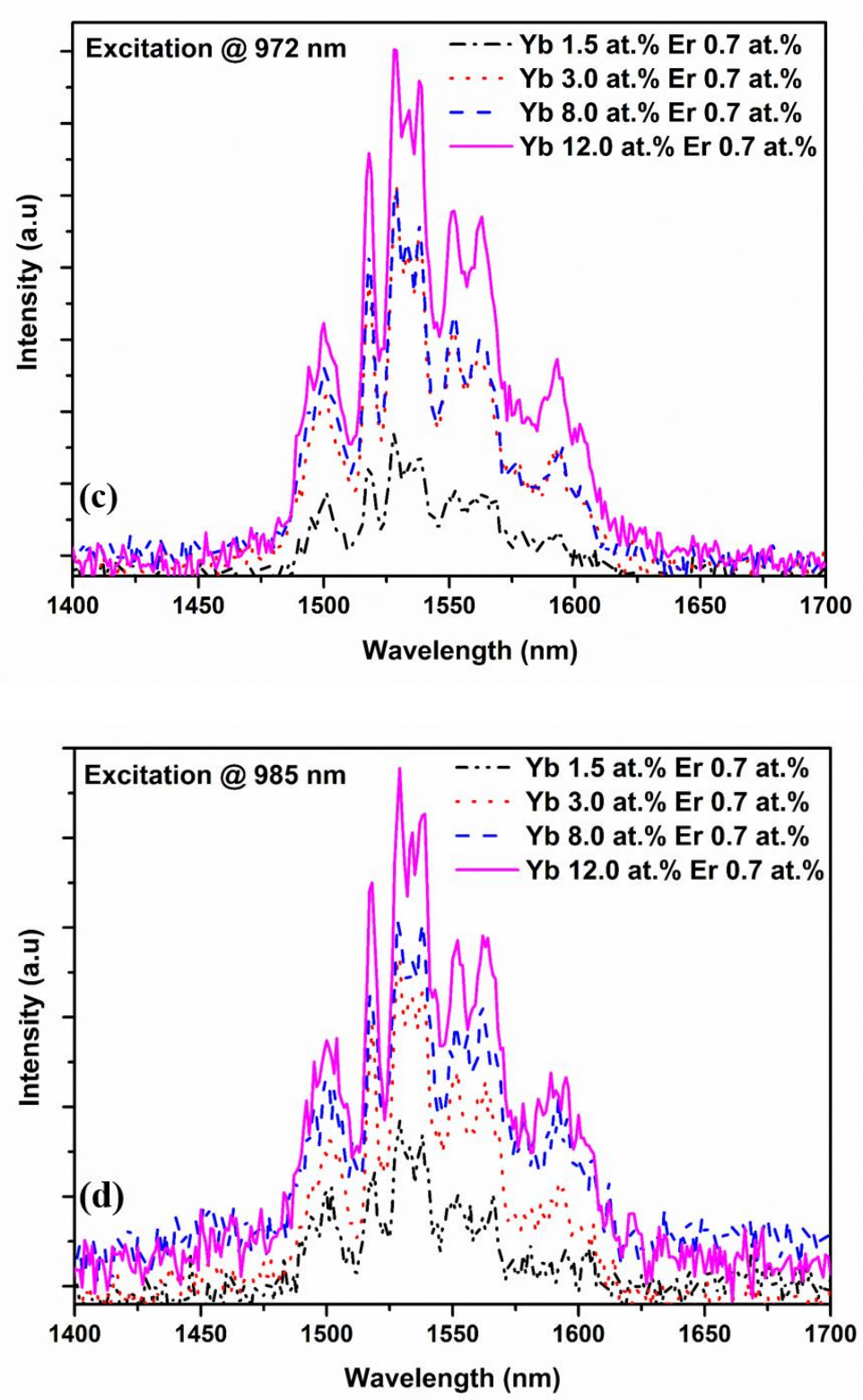

Figure 4.15 Relative PL intensity for Er with 1.5, 3.0, 8.0 and 12.0 at.% Yb when excited at (a) 808 nm and (b) 952 nm (c) 972 nm (d) 985 nm

The emission spectra exhibits a broad band centered around 1550 nm which is associated with $^4I_{13/2} \rightarrow {}^4I_{15/2}$ transition. The band is characterized by multiple peaks caused by transitions among the multiplets of $^4I_{13/2}$ and $^4I_{15/2}$ levels due to D_{2d} site symmetric crystal field of YVO_4 crystal matrix. From the spectra, it is evident that when samples were excited at 952, 972 and 985 nm, the PL intensity is stronger as compared to that for excited at 808 nm. Hence, Yb sensitized excitation of Yb co-doped Er:YVO_4 crystal may help in creating efficient population inversion in the upper state of Er ion [138].

Table 4.10 Emission transition strength of Er ions in the Yb co-doped 0.7 at.% of Er: YVO_4 for some important emission lines (* includes magnetic dipole transition)

Yb conc. (at.%)	$[SL]J_i \rightarrow [SL]J_f$	$\bar{\lambda}$ (nm)	$S_{cal.}$ ($x10^{-20}$) cm^2	A (s^{-1})	Life time τ (ms)	Branching ratio (β)
1.5	$^4I_{13/2} \rightarrow {}^4I_{15/2}{}^*$	1550	2.85	446.2	2.24	1.0
	$^4I_{11/2} \rightarrow {}^4I_{15/2}$	976	0.97	638.1	1.46	0.068
	$^4I_{11/2} \rightarrow {}^4I_{13/2}$	2940	2.21	46.6		
3.0	$^4I_{13/2} \rightarrow {}^4I_{15/2}{}^*$	1550	2.66	478.3	2.09	1.0
	$^4I_{11/2} \rightarrow {}^4I_{15/2}$	976	0.9	668.6	1.39	0.070
	$^4I_{11/2} \rightarrow {}^4I_{13/2}$	2940	2.06	50.6		
8.0	$^4I_{13/2} \rightarrow {}^4I_{15/2}{}^*$	1550	2.74	523.0	1.92	1.0
	$^4I_{11/2} \rightarrow {}^4I_{15/2}$	976	0.91	716.9	1.29	0.072
	$^4I_{11/2} \rightarrow {}^4I_{13/2}$	2940	2.11	55.9		
Yb 12.0	$^4I_{13/2} \rightarrow {}^4I_{15/2}{}^*$	1550	3.1892	542.8	1.81	1.0
	$^4I_{11/2} \rightarrow {}^4I_{15/2}$	976	1.0482	738.1	1.25	0.073
	$^4I_{11/2} \rightarrow {}^4I_{13/2}$	1550	2.4588	58.3		

Further, the emission characteristic was investigated using JO theory. Einstein's A coefficient (radiative transition rate) of emission in Er-ion can be evaluated using following relation:

$$A(J \to J') = \frac{64\pi^4 e^2}{3h(2J+1)\bar{\lambda}^3}\left[\frac{n(n^2+2)^2}{9}\right]\sum_{i=2,4,6}\Omega_i \left|\langle [S\ L], J \| U^i \| [S'L'], J' \rangle\right|^2 \quad \ldots (4.19)$$

Here, for the calculation of '*A*' the JO parameters calculated for the absorption lines were used. The values of $\langle \| U_i \| \rangle$ used in this case are different as the transitions are reversed and taken from ref. [137]. For Er^{+3} ion, the magnetic dipole (MD) transitions are insignificant or not allowed except for the $^4I_{13/2} \rightarrow {}^4I_{15/2}$ transition. Radiative transition rate of MD for $^4I_{13/2} \rightarrow {}^4I_{15/2}$ transition was calculated as described in ref. [43].

The radiative lifetime of an excited state J was calculated as $\tau = 1/\Sigma A(J \to J')$ and the fluorescence branching ratio are $\beta(J \to J') = A(J \to J')/\sum A(J \to J')$ given by where the sum is taken over all the possible terminal states. The life-time and branching ratio of three prominent emission transitions of Er with different Yb concentrations is tabulated in Table 4.11. From the PL spectra [Figure 4.15], the emission cross-section of the transition was calculated by using the following relations

$$\sigma_e(\lambda) = \frac{\bar{\lambda}^4}{8\pi n^2 c \Delta\lambda_{eff}} A(J \to J') \quad \ldots\ldots\ldots\ldots\ldots\ldots\ldots\ldots\ldots\ldots\ldots\ldots\ldots\ldots\ldots (4.20)$$

where $\bar{\lambda}$ is the mean wavelength of emission band and $\Delta\lambda_{eff}$ is the effective line-width of the transition.

$$\Delta\lambda_{eff} = \frac{\int I(\lambda) d\lambda}{I_{max}} \quad \ldots\ldots\ldots\ldots\ldots\ldots\ldots\ldots\ldots\ldots\ldots\ldots (4.21)$$

The emission cross-section of $^4I_{13/2} \rightarrow {}^4I_{15/2}$ line for excitation at 952, 972 and 985 nm is calculated for Yb doping concentration of 1.5, 3.0, 8.0 and 12.0 at.% and the values free from the excitations wavelengths are ~2.29x10^{-20} cm^2, 2.43x10^{-20} cm^2, 2.59x10^{-20} and 2.70x10^{-20} cm^2 respectively.

4.2.2.2 The spectroscopic properties of Er in Yb:YVO$_4$ using polarized light

In an anisotropic media, the absorption depend on the polarization of the incident light. The effect of polarization on the spectroscopic, especially the line strengths and Judd-Ofelt parameters were also investigated. The effective JO parameter was calculated. The effective JO parameters was calculated using the relation $\Omega_{eff} = (\Omega_\pi + 2\Omega_\sigma)/3$ [137] and the values are summarized in Table 4.13.

Table 4.11 Line strength of forced electric dipole transition of Yb co-doped 0.7 at.% Er:YVO$_4$ samples for π and σ polarization for all Yb doped samples (initial state for all the transition is $^4I_{15/2}$).

$\bar{\lambda}$ (nm)	[SL]J_f	Line strength $S_{exp.}$ (x10^{-20}) cm^2							
		Yb 1.5 at.%		Yb 3.0 at.%		Yb 8.0 at.%		Yb 12.0 at.%	
		π pol.	σ pol.	π pol.	π pol.	π pol.	σ pol.	π pol.	σ pol.
381	$^4G_{11/2}$	15.5	14.5	13.9	12.9	13.4	12.7	14.894	13.802
410	$^2H_{9/2}$	0.288	0.369	0.297	0.382	0.325	0.404	0.4923	0.5027
452	$^4F_{5/2}$	0.475	0.478	0.457	0.46	0.439	0.462	0.4898	0.4898
491	$^4F_{7/2}$	1.41	1.38	1.304	1.21	1.29	1.27	1.5739	1.2610
525	$^2H_{11/2}$	11.1	10.4	11.01	9.35	9.97	9.32	10.454	10.157
658	$^4F_{9/2}$	2.75	1.97	2.61	1.81	2.81	1.86	2.4896	2.2437
803	$^4I_{9/2}$	0.641	0.647	0.598	0.418	0.595	0.359	0.6128	0.5101

Table 4.12 Judd-Ofelt parameters of Yb co-doped 0.7 at.% Er:YVO_4 samples for π and σ polarization

Yb concentration	JO parameters (x10^{-20}) cm^2								
	Ω_2			Ω_4			Ω_6		
	π Pol. (Ω_π)	σ Pol. (Ω_σ)	Ω_{eff}	π Pol. (Ω_π)	σ Pol. (Ω_σ)	Ω_{eff}	π Pol. (Ω_π)	σ Pol. (Ω_σ)	Ω_{eff}
Yb 1.5 at.%	13.991	13.742	13.825	3.856	2.423	2.901	1.413	1.603	1.540
Yb 3.0 at.%	12.971	12.314	12.533	3.679	2.071	2.607	1.312	1.516	1.448
Yb 8.0 at.%	11.881	12.169	12.073	4.042	2.036	2.705	1.256	1.626	1.503
Yb 12.0 at.%	13.632	12.919	13.156	3.0780	2.8225	2.927	1.837	1.526	1.629

Further, the emission characteristic was investigated using effective JO theory. Einstein's A coefficient (radiative transition rate) of emission in Er-ion can be evaluated using above relations:

The effective JO parameters estimated for absorption transitions were used for the calculation of '*A*' coefficient. For the emission, characteristics the values of matrix $\langle \| U_i \| \rangle$ are different as the transitions are reversed. In the case of Er^{+3} ion, the magnetic dipole (MD) transitions for the $^4I_{13/2} \rightarrow {}^4I_{15/2}$ transition are significant or allowed. Radiative transition rate of magnetic dipole for $^4I_{13/2} \rightarrow {}^4I_{15/2}$ transition was calculated and described in ref. [43].

The radiative lifetime of an excited state J and the fluorescence branching ratio was also calculated for three prominent emission transitions of Er with different Yb concentrations is tabulated in Table 4.14. From the photoluminescence (PL) spectra [Figure 4.15], the emission cross-section of the transition was calculated by using the above equations (4.20-4.21). The emission cross-section of $^4I_{13/2} \rightarrow {}^4I_{15/2}$ line for excitation at 952, 972 and 985 nm is calculated for Yb doping concentration of 1.5, 3.0, 8.0 and 12.0 at.% and the values are ~ 2.33x10^{-20} cm^2, ~2.25x10^{-20} cm^2, ~2.33x10^{-20} cm^2 and ~2.55x10^{-20} cm^2 respectively. The emission cross-section does not depend on the excitation wavelengths [138].

Table 4.13 Emission line strength of Yb co-doped 0.7 at.% of Er doped YVO_4 for some important emission lines (* includes magnetic dipole transition)

Yb conc. (at.%)	$[SL]J_i \rightarrow [SL]J_f$	$\bar{\lambda}$ (nm)	$S_{cal.}$ ($x10^{-20}$) cm^2	A (s^{-1})	Life time τ (ms)	Branching ratio (β)
1.5	$^4I_{13/2} \rightarrow {}^4I_{15/2}{}^*$	1550	2.85	510.38(5)	1.96	1.0
	$^4I_{11/2} \rightarrow {}^4I_{15/2}$	976	0.97	683.21(9)	1.34	0.071
	$^4I_{11/2} \rightarrow {}^4I_{13/2}$	2940	2.21	52.37(3)		
3.0	$^4I_{13/2} \rightarrow {}^4I_{15/2}{}^*$	1550	2.66	481.69(3)	2.08	1.0
	$^4I_{11/2} \rightarrow {}^4I_{15/2}$	976	0.9	633.91(4)	1.36	0.071
	$^4I_{11/2} \rightarrow {}^4I_{13/2}$	2940	2.06	48.81(8)		
8.0	$^4I_{13/2} \rightarrow {}^4I_{15/2}{}^*$	1550	2.74	493.77(4)	2.03	1.0
	$^4I_{11/2} \rightarrow {}^4I_{15/2}$	976	0.91	640.95(8)	1.45	0.072
	$^4I_{11/2} \rightarrow {}^4I_{13/2}$	2940	2.11	50.00(3)		
	$^4I_{13/2} \rightarrow {}^4I_{15/2}{}^*$	1550	2.9727	511.40	1.95	1.0
12.0	$^4I_{11/2} \rightarrow {}^4I_{15/2}$	976	0.9917	698.50	1.32	
	$^4I_{11/2} \rightarrow {}^4I_{13/2}$	2940	2.2924	54.32		0.072

Further, it was found that the value of Ω_2, which strongly depends on the environment of ligand (i.e. the value of Ω_2 is related to the symmetry of the hosts), decreases as doping of Yb is increased. The value of Ω_2 signifying the dependence of co-valency between the rare earth ions and ligand anions clearly reflects the presence of asymmetry of the local environment in the proximity of RE ion site. The characteristic feature of Ω_2 parameter is therefore related to asymmetry of coordinate structure, bonding nature and polarizability of the ligand ions or molecule and is sensitive to the local environment of the RE ions. The smaller value of Ω_4 and larger Ω_6 are favorable for the luminescence transition. The Ω_4 and Ω_6 two parameters are important for calculating spectroscopic quality factor, which predicts the dominance of stimulated emission for the laser gain medium [2][43].

Spectroscopic quality factor is given as $X = \Omega_4/\Omega_6$ and calculated from values of JO intensity parameters for unpolarized light and polarized absorption spectra. The value of spectroscopic quality factor for 0.7 at.% Er co-doped Yb 1.5, 3.0, 8.0 at.% and 12. at.% in YVO_4 was found be same for all the samples with value around 1.80 for unpolarized and polarized absorption spectra. In general, the trend for the Ω parameters in the crystal system follows $\Omega_2 > \Omega_4 > \Omega_6$. It was found that the value of spectroscopic quality factor (X) is almost constant (around ~ 1.80) for different Yb concentration and better as compared to 1.31 reported for Er (1.0 at.%) doped YVO_4 [43]. A higher value of spectroscopic quality factor indicates that the Yb co-doping in Er:YVO_4 makes it an efficient laser gain medium [153,154].

In the emission characteristics, for $^4I_{13/2} \rightarrow {}^4I_{15/2}$ transition radiative lifetime is ~ 2.00 ms which was calculated from JO parameters for polarized and unpolarized measurement and branching ratio is unity as there is only one possible transition from $^4I_{13/2}$. For Er doped YVO_4, the reported radiative life-time for a $^4I_{13/2} \rightarrow {}^4I_{15/2}$ transitions is 2.45 ms [43]. For emission at 2.9 μm (transition $^4I_{11/2} \rightarrow {}^4I_{13/2}$) the estimated life times were found to be in the range of 1.29-1.45 ms for unpolarized and 134- 1.45 ms for polarized absorption data. The corresponding branching ratio is 0.070, which is independent of doping concentrations and state of polarization.

Hence it was found that the radiative life time of Er ions is almost constant (τ~2.0 ms) for 1550 nm transition with the increasing Yb doping concentration but it is slightly less than the YVO_4 gain medium doping with only Er. Hence the lifetime of Er ions is independent of Yb doping at least upto a concentration of 12 at.% Yb which has been investigated in the present work. This is the biggest advantage of Yb co-doping in

the Er doped YVO_4 laser system that results in high population density in the upper level of Er ions and an efficient pumping of the gain medium [138].

Estimated emission cross-section from JO parameters for polarized and unpolarized measurement is also independent of doping concentration of Yb. For only Er doped YVO_4, the reported emission cross-section for the $^4I_{13/2} \rightarrow {}^4I_{15/2}$ transitions is ~2.59×10^{-20} cm^2 [43]. The estimated values for Yb co-doped crystals are in agreement with the above reported value. Similarly, for all the doping concentrations of Yb, the emission cross-section for 808 nm excitation were calculated for the same transitions and the values were found to be of the same order as for the excitation with 952, 972 and 985 nm. It shows that the emission cross-section does not depend on the excitation wavelength as well as Yb doping concentrations [138].

It, therefore, reflects that Yb as co-dopant in Er gain medium acts as good sensitizer and it does not affect the emission cross-section and lifetime of Er ions. Also, the emission cross-section of Er ions are of the same order for the excitation wavelength at 808 nm (absorption due to Er) and 952, 972 and 985 nm (absorptions due to Yb) [138].

4.3 Characterization of Nd co-doped Yb:YVO_4 single crystals

The growth of Nd (0.8 at.%) co-doped Yb (0.8 and 3.0 at.%):YVO_4 single crystal were carried out in OFZ system. The dimension of grown crystals was ~4- 5 mm in diameter and 10-15 mm in length [139,140].

4.3.1 Effect of doping on the lattice parameters

The effect of Nd doping on the lattice parameters of Yb:YVO_4 crystals were investigated by powder X–rays diffraction (XRD). The diffraction patterns were recorded using Rigaku Ultrax-18 powder diffractometer in the range 20-70°. The recorded XRD pattern is shown in Figure 4.16.

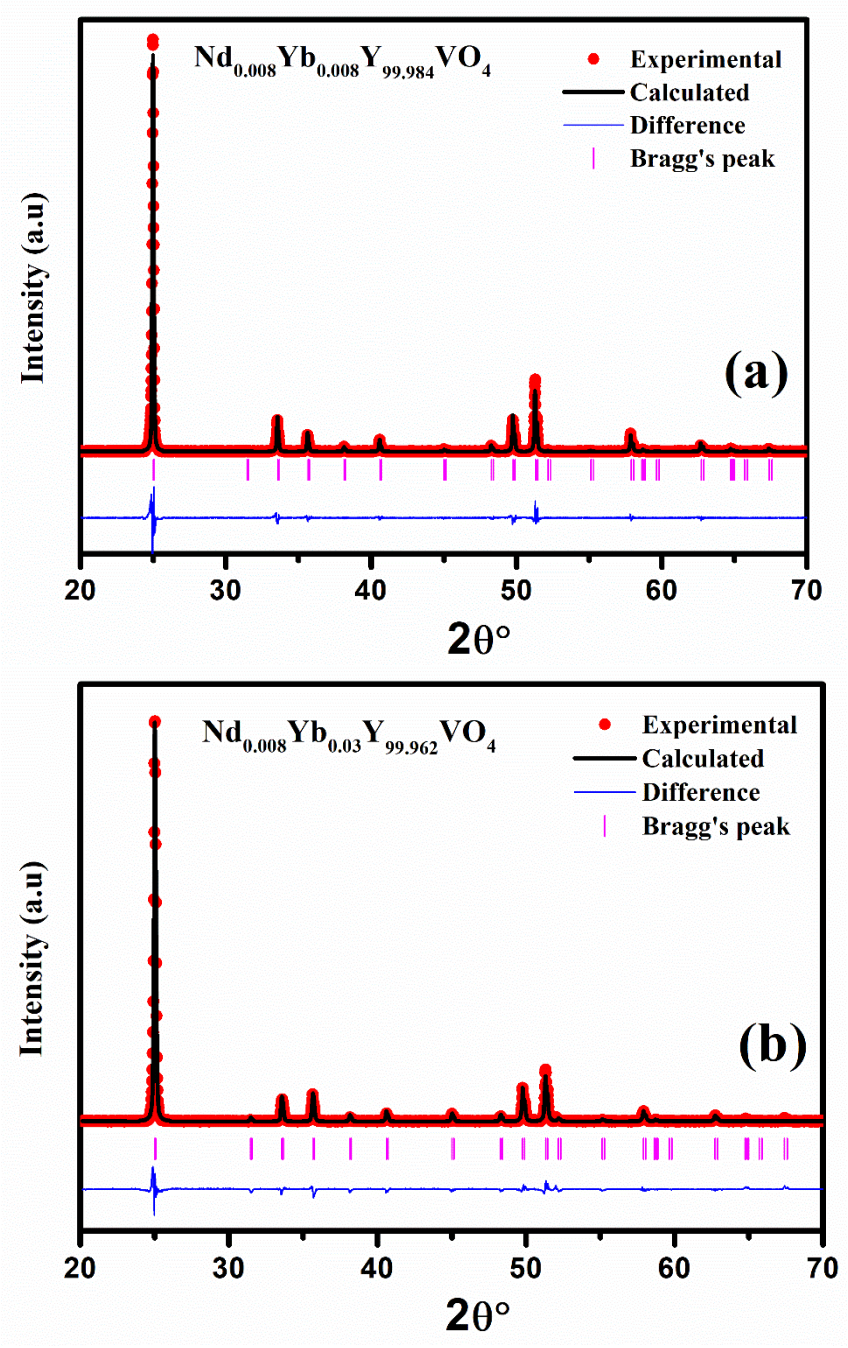

Figure 4.16 XRD pattern of Nd:Yb:YVO_4 crystals

On 0.8 at.% doping of Nd in the Yb (0.8 and 3.0 at.%):YVO_4 crystal it was observed that the peaks exhibit a small shift towards the lower angle signifying expansion of the lattice volume. This is because of the higher ionic radius of Nd (112 pm) in comparison to the ion radii of Y (104 pm) it is substituting. The ionic radii of Yb is 100 pm which is similar to Y. The estimated lattice parameters and unit cell volume of Nd:Yb:YVO_4 crystals are listed in the Table 4.14 [139,140].

Table 4.14 Lattice parameters of Nd:Yb:YVO_4 crystals

Sr.no.	Lattice parameters of YVO_4		
		Yb:0.8 at.%	Nd:0.8 at.%-Yb:0.8 at.%
1.	a and b (Å)	7.125(9)	7.126(8)
2.	c (Å)	6.291(4)	6.291(9)
3.	Volume ($Å^3$)	319.46(7)	319.57(3)

4.3.2 Evaluation of crystalline quality by rocking curve measurement

Investigation of defect or crystalline perfection in a laser host crystal is important as it influences the laser performance. The evaluation of the crystalline quality of the grown crystals was carried out by rocking curve measurement at angle dispersive X-rays diffraction (ADXRD) beamline (BL-12) of Indus-2 synchrotron radiation source [116]. For this, sample was cut perpendicular to [100] direction from the grown crystals and then it was polished using alumina powder. The rocking curve measurement was performed for (200) diffraction peak is shown in Figure 4.17. The diffraction peak is symmetric and consisting of single peak which signifies that the crystals have single grain. Further, the peak was analyzed by Lorentz fitting and the full width at half maxima of (200) diffraction peak was found to be around 200±3 arc-

second which confirms good crystalline quality of Nd co-doped Yb:YVO_4 single crystals grown by OFZ technique [139,140].

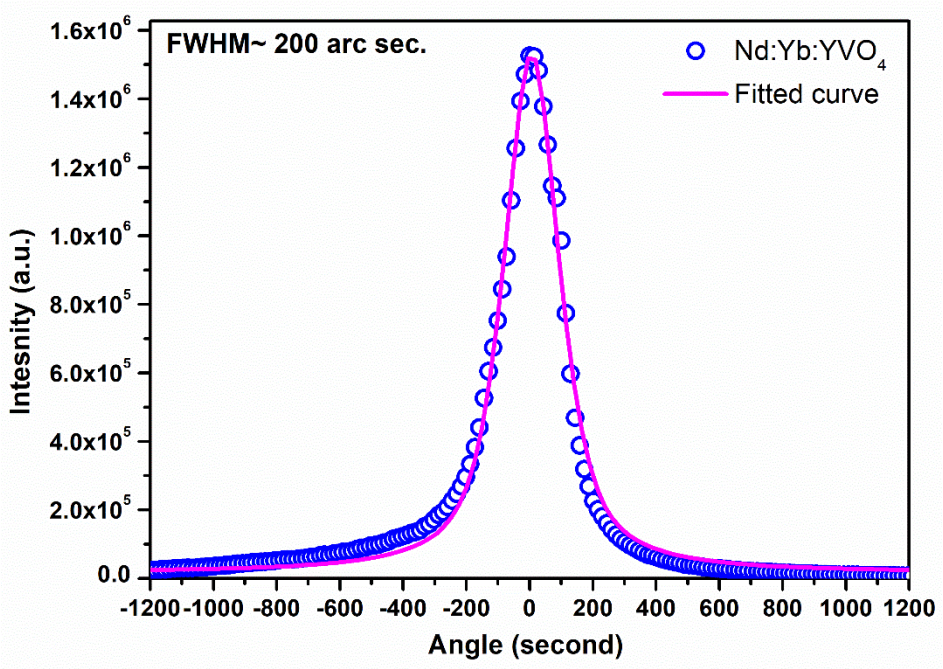

Figure 4.17 Rocking curve of Nd:Yb:YVO_4 crystal

4.3.3 X-ray photoelectron spectroscopy (XPS) measurement

X-ray photoelectron spectroscopy measurements were carried using hard x-ray photoelectron spectroscopy (HAXPES) beamline (BL-14) at synchrotron radiation facility Indus-2 [113]. The X-rays from double crystal monochromator [Si(111)] of energy 4.311 keV was used for excitation. To explore the oxidation state of vanadium in the host of YVO_4 crystal, XPS measurement was carried out and the recorded XPS spectrum is shown in Figure 4.18.

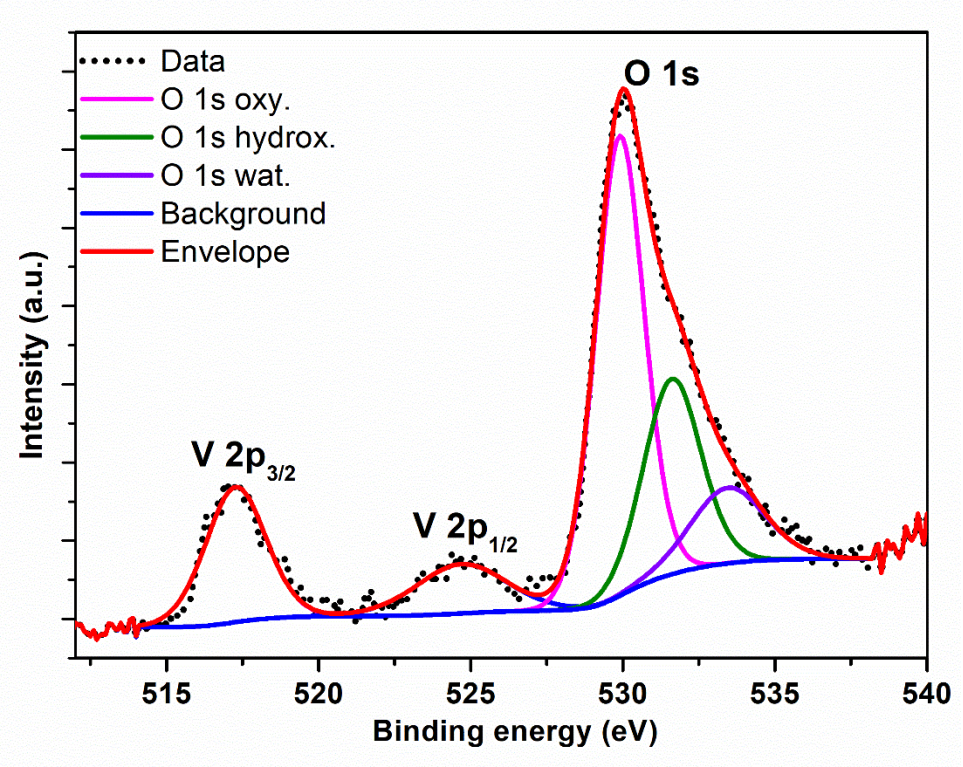

Figure 4.18 XPS spectrum of the Nd-Yb co-doped YVO_4 crystal

Initially, a survey spectrum was recorded over a range of 0 to 1000 eV and the energy calibration was done for all the edges with respect to the reference (C 1s peak at a binding energy value of 284.8 eV of adventitious carbon). From the XPS spectrum it was observed that the V-2p peaks consist of two spin-splitted peaks for S = 3/2 and 1/2. Both the spin-splitted peaks of V-2p could be fitted with single peak. The peak position of these vanadium lines are at around 517.22 and 524.81 eV respectively, which is attributed due to V^{5+} ions [155]. Hence, this confirms that the V in the grown crystal is in the pentavalent state. As the crystals are grown in oxygen rich environment, unlike Cz technique [156], the concentration of oxygen vacancy is relatively less in the OFZ grown crystal [20], which further promotes the pentavalent state of the vanadium ion in the lattice site [139,140].

4.3.4 Defect study by chemical etch method

High crystalline quality is the essential requirement of a material to be used as laser gain medium. The preferential chemical etching of the crystal surface provides an easier way to explore the crystal defects, particularly the line and surface defects and to determine the quality of crystals. For the evaluation of dislocation or etch pit density, the polished plate of 1 mm thickness was used. For observing the etch pit on the crystal plate the concentration of the etchant hydrochloric acid, temperature and time period of etching were optimized. It was found that the optimized condition for etching to carry out the treatment for 1 h using diluted hydrochloric acid (25 % of H_2O and 75% of HCl) at 100^oC. The etched surface was investigated using OLYMPUS BX60 optical microscope.

Figure 4.19 (a) shows photograph of the pristine sample plate as viewed under the optical microscope before chemical etching. Finally under the optimized conditions, the proper etch pits were formed on the crystals as shown in Figure 4.19 (b). The dislocation etch pit density were calculated by observing the pits on the plate of crystal. The dislocation etch pit density was estimated to be ~$1.25x10^4/cm^2$ [139,140].

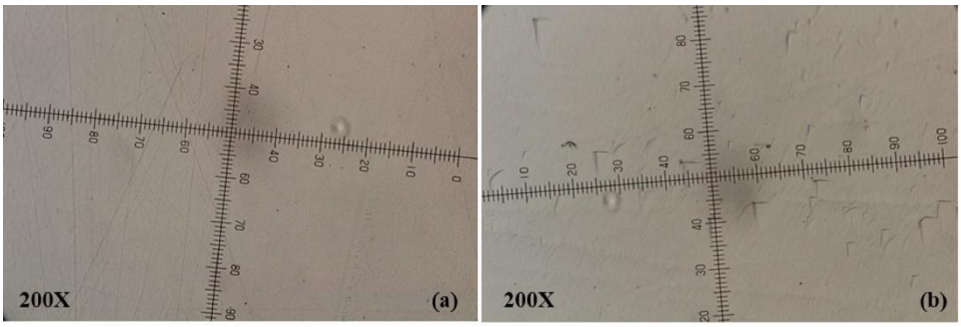

Figure 4.19 Sample surface as seen under optical microscope: (a) before etching and (b) after etching

4.3.5 Optical homogeneity measurement

Optically homogeneous crystal is an important requirement for laser application. As a part of checking the quality of the grown crystal, the optical homogeneity of the crystal was further investigated by birefringence interferometry. The technique is based on the formation of interference fringes between the component of ordinary ray and extra-ordinary ray when they pass through the birefringence sample. For this the measurement a [100]-oriented polished sample of Nd:Yb:YVO_4 crystal of 1 mm thickness was prepared. A collimated linearly polarized light (45° with respect to sample c-axis) of He-Ne laser (632.8 nm) incident normally on the sample and passes through the cross-polarizer (at 90° to the incident light polarization) and lens. The interference fringes form due to superposition and delay (birefringence induced path difference) between the component of extra-ordinary ray (n_e) and ordinary ray (n_o) is observed on the screen and recorded.

The birefringence patterns recorded in the present experiment are characterized by a sharp, distinguished and closely spaced nearly straight fringes as shown in Figure 4.20. The straightness of the fringes is the characteristic of the high optical homogeneity of the crystal and depicts uniform dopant distribution in the crystal under investigation. The observed fringes of nearly uniform thickness and spacing indicates the optical uniformity of the crystal across the cross-section and having a small wedge across the length. Also, the uniform periodic nature of the fringes depicts that the crystal is free from local residual stresses [139,140].

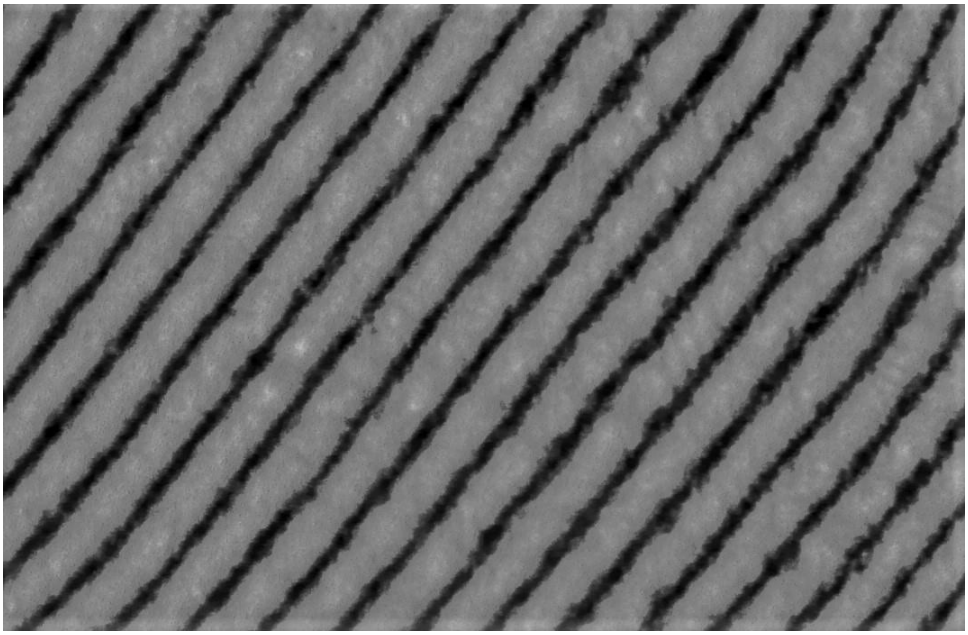

Figure 4.20 Nearly straight fringes of Nd:Yb:YVO_4 plate as seen by birefringence interferometry

Further, on close examination of the fringes, a very small distortion in the shape of the fringes i.e. a slight deviation from the straightness and variation in the fringe spacing was observed. This indicates the presence of small optical inhomogeneities associated with local compositional (doping/impurities) fluctuations which are very commonly observed particularly, in case of growth from high temperature melt and melts with added dopants [131,132]. Such compositional fluctuations or other growth defects are primarily arising because of unavoidable random temperature fluctuations at the growth interface during the growth and hence give rise to small variation in birefringence (Δn).

The order of optical homogeneity i.e. variation in the refractive index $\delta(\Delta n)$ associated with the observed fringe distortion can be analyzed by estimating the per fringe variation in $\delta(\Delta n)$ across the sample aperture. The formation of fringes is

attributed to the variation in refractive index/birefringence and variation in the sample thickness due to the presence of wedge in the sample, which is given by: $\delta(\Delta n)(L+\delta L) \approx \lambda$, where λ is wavelength of the laser, L is sample thickness, δL is change in sample thickness due to the presence of finite wedge in the sample. The parallel and equidistant fringes can be assigned to the variation in the thickness (wedge of the sample) and the distortion in the fringe i.e. the deviation from the linearity can be correlated to the $\delta(\Delta n)$. Practically $\delta L << L$, and so the variation in Δn associated with the fringes across the aperture is given by $\delta(\Delta n) \approx \lambda/L \approx 5.64\times10^{-4}$. On referring to Figure 4.20, the observed fringe distortion is appreciably lesser than the spacing between two subsequent fringes. So the order of optical homogeneity [$\delta(\Delta n)$] of the test sample should be $< 5.64\times10^{-4}$. It is therefore inferred that the observed nearly straight fringes depict the overall good optical and compositional homogeneity of the crystals [139,140].

4.3.6 Refractive index measurement

Refractive index (RI) of Nd co-doped in Yb:YVO_4 single crystals were measured by prism coupling technique (Metricon 2010/M system) at wavelength 532, 828, 1064 and 1551 nm with polarization TE (s) or TM (p). Figure 4.21 shows the ordinary and extra-ordinary refractive indices measured for Nd(0.8 at.%)Yb(0.8 at.%) :YVO_4 at room temperature. The measured data were fitted using Sellmeier's equation and the Sellemeier coefficients were determined. The fitted Sellemeier equations for the ordinary and extraordinary refractive index are given below:

$$n_e^2 = 4.6229 + \frac{0.0973}{(\lambda^2 - 0.0678)} - 0.0205\lambda^2 \ldots\ldots\ldots\ldots\ldots (4.22)$$

$$n_o^2 = 3.7867 + \frac{0.0687}{(\lambda^2 - 0.0479)} - 0.0124\lambda^2 \ldots\ldots\ldots\ldots\ldots\ldots (4.23)$$

The estimated Sellemeier coefficients for Nd co-doped Yb:YVO_4 were in agreement with the reported for Yb:YVO_4 crystal [119]. These relations can be used to the calculate the refractive index in the wavelength range of 532- 1551 nm [139,140].

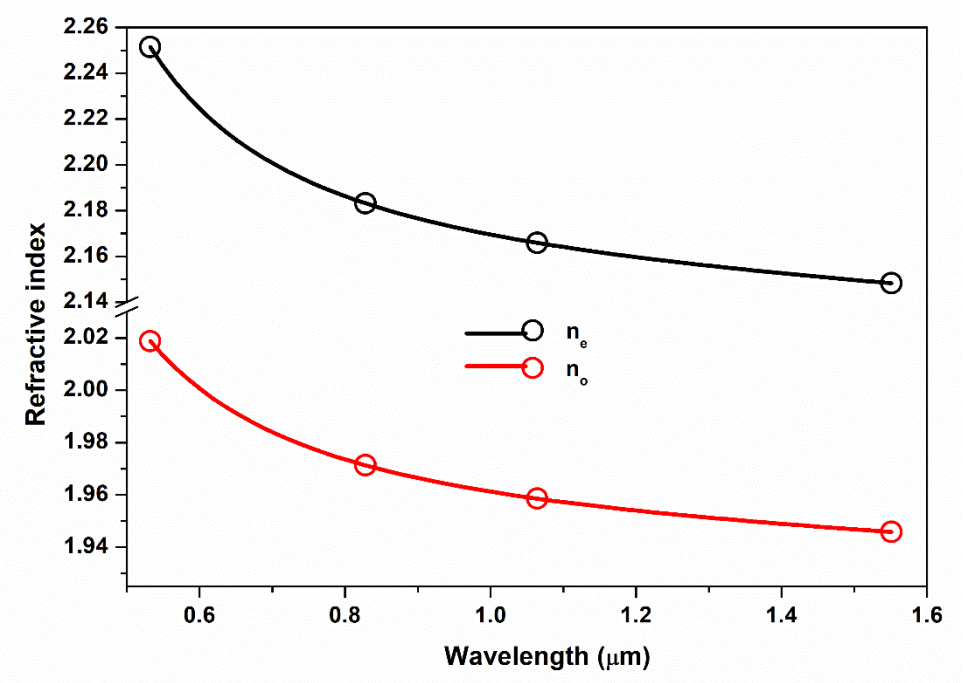

Figure 4.21 Sellmeier fitting on measured refractive index with different wavelengths

4.3.7 Fluorescence lifetime measurement

To investigate the energy transfer from Nd ion to Yb ion in YVO_4 host, the fluorescence lifetime measurements were carried out using ultrafast technique. The Nd co-doped Yb:YVO_4 sample was excited using a Ti:Sapphire femto-second laser operating at 808 nm wavelength. Figure 4.22 shows the fluorescence decay of Nd co-doped Yb:YVO_4 sample. The emission profile consists of emission due to Nd ion as well as Yb ion. The total emission decay profile, which is combination of the rise time, decay of Nd ion and Yb ion, was fitted by exponential function. Therefore, the decay profile was fitted by the following equation:

$$Y = Y_0 + A_1 e^{-t/t_1} + A_2 e^{-t/t_2} + A_3 e^{-t/t_3} \ldots\ldots\ldots\ldots\ldots\ldots (4.24)$$

where Y_0 is constant and τ_1, τ_2 and τ_3 is the rise time for excitation, decay of Nd ion and Yb ion, respectively.

The measured fluorescence lifetime of Nd ion and Yb ion in Nd,Yb:YVO_4 sample ~66 and 581 μs respectively. The reported fluorescence life-time of Nd in the Nd:YVO_4 is around 101 μs [157] whereas in our study the measured fluorescence life-time of Nd, co-doped in theYb:YVO_4 is 66 μs. Hence, the measurement shows that the Nd ion transferred sufficient energy to the Yb ion. The energy transfer efficiency can be calculated by measuring the fluorescence lifetime of Nd ion present in the lattice of YVO_4 and Yb:YVO_4 crystal. The fluorescence life-time of Nd ion is around 101 μs (τ_p) reported by Bhaumik et al. [157]. In the present investigation it was observed that the fluorescence lifetime of Nd ion in Yb (0.8 and 3.0 at.%):YVO_4 is ~ 66μs (τ_m). The efficiency of energy transfer from Nd ion to Yb ion is given by [2]:

$$\eta = \left(1 - \frac{\tau_m}{\tau_p}\right) \quad \ldots\ldots\ldots\ldots\ldots\ldots\ldots\ldots\ldots\ldots\ldots\ldots\ldots\ldots\ldots\ldots (4.25)$$

where τ_p is the fluorescence lifetime of Nd in YVO_4 and τ_m is fluorescence life time of Nd in Yb:YVO_4.

The calculated energy transfer efficiency is around ~35%. This efficient energy transfer confirms that the Nd ion, used as co-dopant, acts as sensitizer and will enable efficient pumping as the transfers of energy from the Nd to Yb ion provides a powerful channel for pumping. The Nd^{3+}co-doped and Yb^{3+} doped combination laser crystals provide the multiple pump possibilities in the gain medium [50,54,56]. The lifetime of

Nd transition measured on the OFZ grown crystal is similar to that of the Cz grown crystal [50].

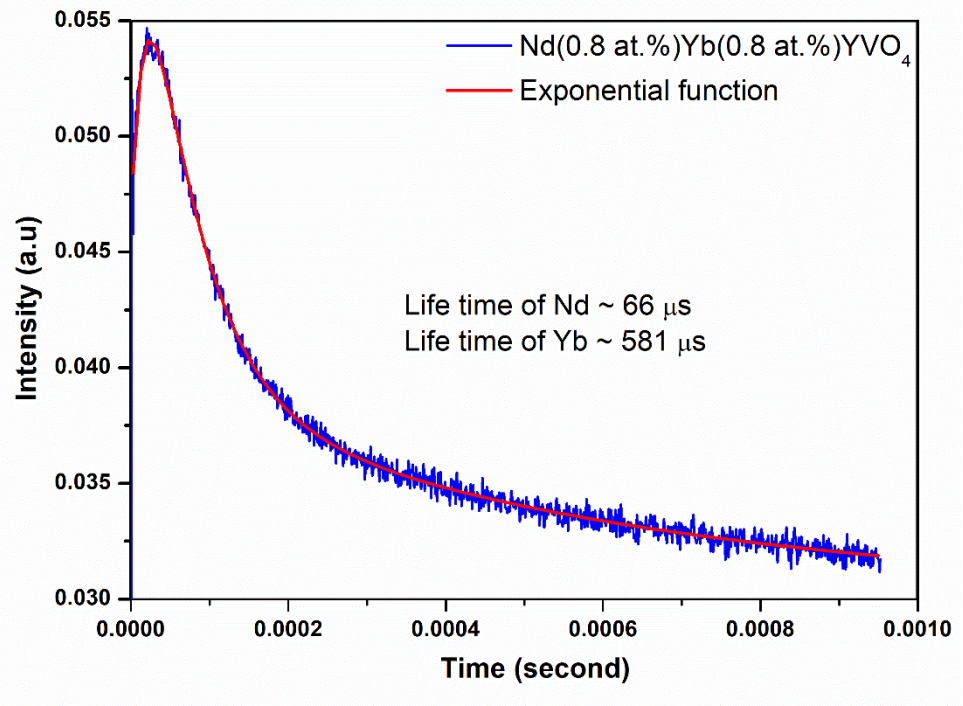

Figure 4.22 Fluorescence decay of Nd 0.8 at. % co-doped Yb(0.8at.%):YVO_4 crystal

4.4 Optical absorption measurement of Nd co-doped Yb:YVO_4

[100]-oriented polished plates of Nd co-doped Yb:YVO_4 crystal with thickness ~1.5 mm were used to investigate the optical transmission of the co-doped crystal. The transmission spectra were measured by spectrophotometer (JASCO V670) for polarized incident light [π-polarization (E||c) and σ-polarization ($E^{\perp}$ c)]. All the measurements were carried out in the range 300-1200 nm. Using the equation (4.4) the absorption coefficient was calculated from the transmission spectra. The polarized optical absorption characteristics of [100]-oriented Nd co-doped Yb:YVO_4 crystal plates are shown in the Figure 4.23-4.24.

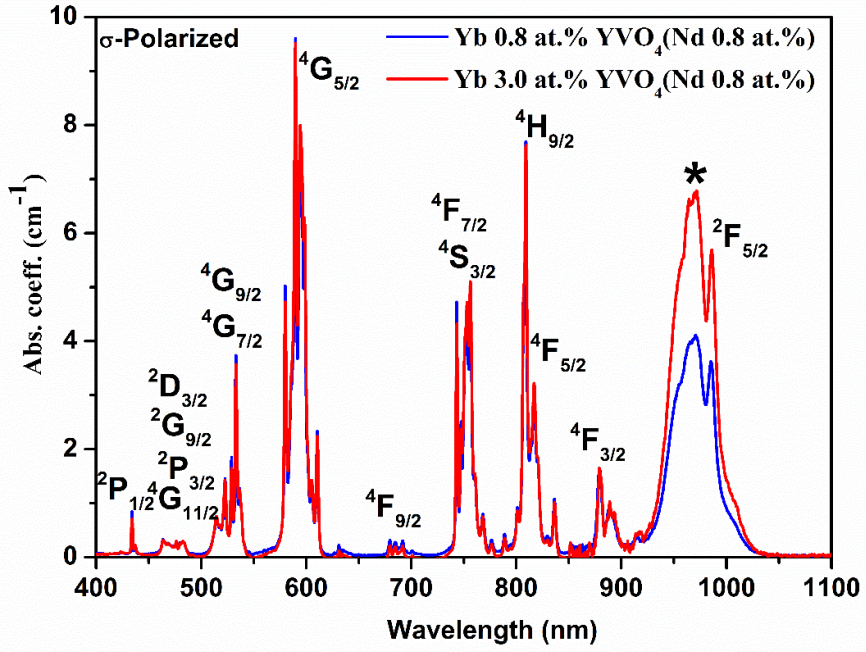

Figure 4.23 Absorption spectra of Nd co-doped Yb:YVO_4 crystal for σ-polarization

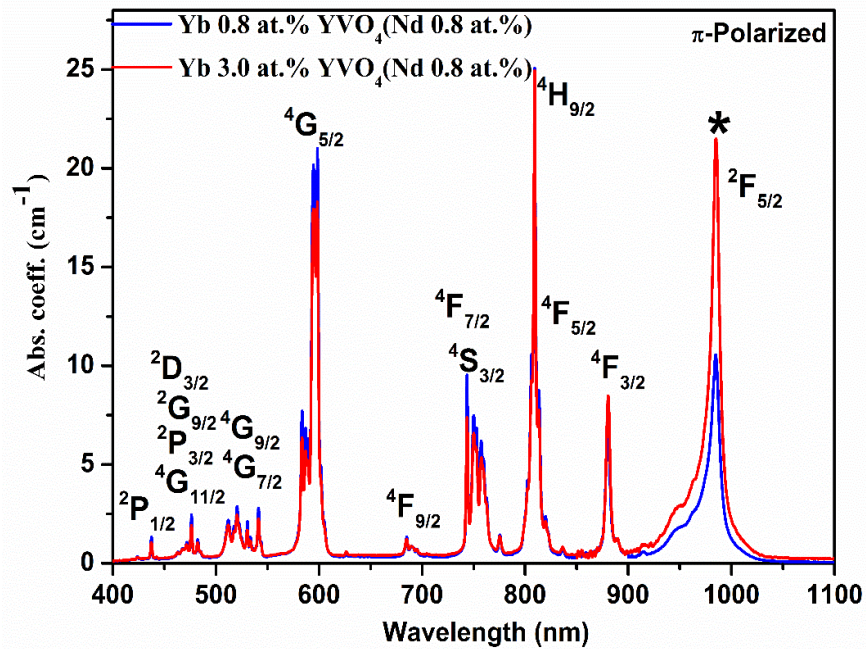

Figure 4.24 Absorption spectra of Nd co-doped Yb:YVO_4 crystal for π- polarization

4.5 Spectroscopy parameters of Nd:Yb:YVO_4 by Judd-Ofelt theory

The absorption spectra for polarized light exhibit several sharp absorption peaks due to Nd ion and a broad peak around 985 nm due to Yb ion. Theses absorption peaks are because of forced electric dipole (ED) transitions between 4f-4f intra-band of Nd and Yb ion. The absorption spectra are characterized by different features in the different polarization of light. According to Laporte rule, the f-f transitions are not allowed because of the same parity of the initial and final states, as this violates the selection rule of the conservation of parity (ED operator is of odd parity). However, due to the presence of D_{2d} non-centrosymmetric crystal field of YVO_4, the states are characterized by mixed parity and these transitions become allowed [146]. These f-to-f transitions are sharp and distinct due to the shielding effect of outer shells ($5s^2$ and $5p^6$) of Nd ion [2,43,135,138].

The detail investigation reveals that the absorption spectra of Nd co-doped Yb:YVO_4 crystals are polarized sensitive. The overall absorption spectra for π-polarization (E || to c-axis) is observed to be stronger than σ-polarization (E $\perp$ to c-axis) as shown in Figure 4.23 and 4.24.

It is important to note that the absorption coefficients are same (within the range of experimental error) for the Nd related absorption for both the samples having different Yb concentrations. The absorption coefficient corresponding to Nd (0.8 at.%) ion at 808 nm in both the crystals is ~26 cm^{-1} for π-polarization (E||c) and ~8 cm^{-1} for σ-polarization (E$\perp$c), whereas the absorption coefficient of Yb at 985 nm for 0.8 at.% and 3.0 at.% Yb are ~10.6 and ~22 cm^{-1} for π-polarization (E||c) and ~4 and ~7.0 cm^{-1} for σ-polarization (E$\perp$c) respectively. These values are significant as the absorption

band of Nd ion at 808 nm can be used for pumping the gain medium for emission of Yb. The relative values of the absorption coefficient suggest that π-polarized (E||c) absorption line of Nd ion at 808 nm can be used for efficient pumping of the Yb:YVO_4 laser gain medium [139,140].

Further, on the comparison of Cz and OFZ grown crystals, it was noted that Xia et al. [158] had reported the occurrence of wide absorption band near the band edge of Yb doped YVO_4 crystal grown by Cz method due to presence of the oxygen vacancies in the grown crystal. However, in the present experiment there is no evidence of such an absorption corresponding to the oxygen vacancy in the absorption spectra. Also they have reported that the band gap due to the valence-conduction band transition for the YVO_4 crystal is ~3.44 eV (~360 nm) whereas in present work the estimated band gap of the OFZ grown crystal (ambience of 20% O_2) Nd:Yb:YVO_4 depicts a blue shift with the value around 3.49 eV for π-polarization and 3.56 eV for σ-polarization. This also reflects the presence of lesser defect density states close to the bands in the OFZ grown crystal. The absorption cross-sections of the Yb transitions in Nd-Yb co-doped YVO_4 crystals and only Yb doped YVO_4 crystal, grown by OFZ method, are of the same order [25,119]. However, there is a significant enhancement in the absorption characteristics corresponding to the Yb ions in comparison to the values reported in the literature for only Yb doped YVO_4 crystals that are grown by Cz method: (a) Kisel et al. [37] reported the absorption coefficient at 985 nm for 2.0-3.0 at.% Yb is 14.7 cm^{-1} for π-polarization; (b) Zhang et al. [10] showed that the absorption coefficient at 985 nm is 14.9 cm^{-1} for 2.0 at.% Yb (estimated from the absorbance data); (c) Su-Mei et al. [50] showed that the absorption coefficient at 985 nm is 6 cm^{-1} for π-polarization for a doping concentration of 1.0 at.% Yb. Hence, in the present report the OFZ grown crystals show

better properties in context of the Yb absorption characteristics compared the Cz grown Yb doped YVO_4 crystals, possibly because of the lesser oxygen vacancy as these are grown in oxygen rich ambience unlike the Cz method.

For a detailed insight of the absorption characteristics of Nd ion in the lattice of YVO_4 in the presence of Yb as the second dopant, the spectroscopic properties of Nd ion having f–f transitions were estimated by the Judd–Ofelt theory [2,43,135,138]. Judd-Ofelt parameters were determined from the absorption spectra of Nd co-doped Yb:YVO_4 crystals for both the polarization of light, and then those were used for obtaining the characteristic emission properties of the Nd ion as discussed in the subsequent sections.

4.5.1 Absorption characteristic of Nd:Yb:YVO_4 crystals

Judd-Ofelt parameters were estimated for both the Nd-Yb co-doped samples from the absorption spectra using Judd-Ofelt (JO) theory [2,43,135,138]. The experimental line strengths of the forced electric dipole transition S for various transitions of Nd ion were calculated using the above equation (4.8) [2,43,135,138]. Ω_2, Ω_4 and Ω_6 are the Judd-Ofelt intensity parameters [2,135]. The matrix elements for the rare earth ions are computed within the intermediate coupling approximation [2,135]. In the present investigation, the values of the doubly reduced matrix elements computed by Carnall et al. [133] for Nd ion (Table 4.17) were used. These the matrix elements do not depend on the surroundings of the ion [146].

As the absorption coefficients (Figure 4.23 and 4.24) for all the transitions of Nd ions are same (within the range of the experimental error) for both the samples having different Yb doping concentrations, all the parameters related to JO analysis

calculated for both the samples were found to be same. So, henceforth the result has been discussed for only one sample (0.8% Yb doped sample). The line strengths (S_{exp}) for all the absorption transitions having Nd concentrations $0.992x10^{20}$/cc (0.8 at.% Nd) in 0.8 at.%Yb:YVO_4 crystals are tabulated in Table 4.16.

Table 4.15 Line strength of Nd ion in Yb (0.8 at.%):YVO_4 crystals

			Pi polarized		sigma polarized	
Initial transition state $[SL]J_i$	Final transition level $[SL]J_f$	Central wavelength (nm)	S_{exp} ($x10^{-20}$ cm^2)	S_{cal} ($x10^{-20}$ cm^2)	S_{exp} ($x10^{-20}$ cm^2)	S_{cal} ($x10^{-20}$ cm^2)
$^4I_{9/2}$	$^2P_{1/2}$	437	0.1732	0.3237	0.2247	0.1329
$^4I_{9/2}$	$^4G_{11/2}$,$^2P_{3/2}$,$^2D_{3/2}$,$^2G_{9/2}$	476	0.9466	0.6494	0.6222	0.4259
$^4I_{9/2}$	$^4G_{9/2}$, $^4G_{7/2}$	520	3.1134	3.2827	2.2594	2.1634
$^4I_{9/2}$	$^4G_{5/2}$	598	14.4383	14.4286	12.2677	12.2751
$^4I_{9/2}$	$^4F_{9/2}$	685	0.5116	0.3798	0.2677	0.3237
$^4I_{9/2}$	$^4S_{3/2}$,$^4F_{7/2}$	743	5.2663	5.3530	4.9293	4.9922
$^4I_{9/2}$	$^2H_{9/2,}$$^4F_{5/2}$	808	6.1853	6.0751	4.8204	4.7463
$^4I_{9/2}$	$^4F_{3/2}$	879	2.3717	2.3643	1.0075	1.2017

The line strength of the force electric dipole transition from an initial manifold $|4f^9[L', S'] J'\rangle$, to a final manifold $|4f^9[L', S'] J'\rangle$, according to JO theory, is given by the equation (4.17) in the above section.

The line strength of absorption transition of Nd ions, particularly the absorption at 808 nm which is used as pumping wavelength, depends on the polarization of light [Table 4.17]. The line strength or oscillator strength of the transitions depends on the site symmetry of rare earth (RE) ion present in the lattice. The smaller value of the oscillator strength indicates higher site symmetry of the RE ion whereas the higher value of the line strength corresponds to the lower symmetry around the ion [138] [43].

Further, Judd-Ofelt parameters Ω_2, Ω_4 and Ω_6 were evaluated using all the line strengths of the absorption spectra by least square method for both the polarization of incident light. As YVO_4 is polarization sensitive, the Judd-Ofelt parameters are different for both the polarization namely sigma and pi polarization of absorption spectra. From the Judd-Ofelt parameters for sigma and pi polarization the effective value of Judd-Ofelt parameter were estimated using the relation $\Omega_{eff} = (\Omega_\pi + 2*\Omega_\sigma)/3$ and listed in Table 4.18 [137].

The Ω_4 and Ω_6 parameters are important for calculating the spectroscopic quality factor (X) which is given by $X = \Omega_4/\Omega_6$ [2,146]. The higher spectroscopic quality factor is correlated to the degree of dominance of the stimulated emission for the laser gain medium. The value of X for Nd doped 0.8 at.%Yb:YVO_4 is 0.70. It is important to note that the spectroscopic quality factor of this co-doped crystal is lower than the spectroscopic quality factor (0.97) of Nd (1.0 at.%) doped YVO_4 [157]. This suggests that there is energy transfer from Nd ion to Yb ion, which are shown in emission spectra of the sample when excited at 808 nm.

The process can be understood from the schematic of energy level of Nd and Yb ion as shown in the Figure 4.24 [50]. When Nd ion is excited by 808 nm pumped wavelength (absorption line of Nd ion), it goes to the upper level $^4F_{5/2}$+ $^2H_{9/2}$ from ground state $^4I_{9/2}$. The excited Nd ions come down to the energy level of $^4F_{3/2}$ via non-radiative decay. Then some of the excited Nd atoms transfer their energy to nearby state $^2F_{5/2}$ of Yb ions before undergoing radiative transition to its own state $^4I_{11/2}$ as shown in the Figure 4.25.

This clearly shows that there is transfer of energy from Nd to Yb ion in the Nd co-doped Yb:YVO_4 single crystals and moreover the lower spectroscopic quality factor indicates an efficient energy conversion from Nd to Yb ion that can ease the lasing action in Yb:YVO_4 laser gain medium [139,140].

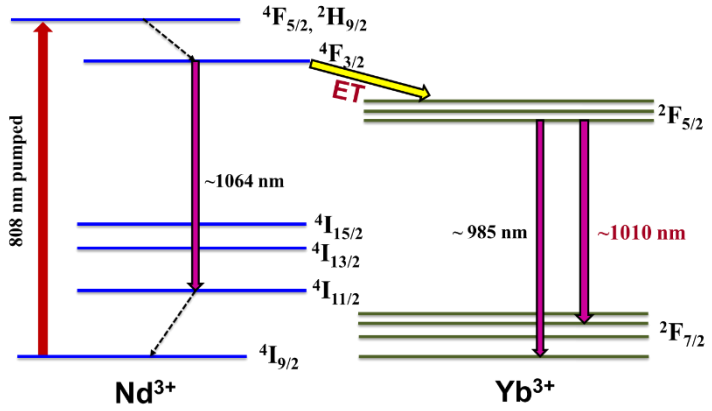

Figure 4.25 Schematic of energy level of Nd and Yb [50]

Table 4.16 Doubly reduced matrix elements for transition of Nd [134]

Final transition level $[SL]J_f$	Wavelength	$\|U_2\|$	$\|U_4\|$	$\|U_6\|$
	nm			
$^2P_{1/2}$	432	0	0.0381	0
$^4G_{11/2}$,$^2P_{3/2}$,$^2D_{3/2}$,$^2G_{9/2}$	475	0.010	0.0431	0.0361
$^4G_{9/2}$, $^4G_{7/2}$	532	0.0597	0.2180	0.0954
$^4G_{5/2}$	594	0.8968	0.4049	0.0355
$^4F_{9/2}$	685	0.0010	0.0096	0.0381
$^4S_{3/2}$,$^4F_{7/2}$	751	0.0010	0.0447	0.6603
$^2H_{9/2}$,$^4F_{5/2}$	808	0.0101	0.2437	0.5169
$^4F_{3/2}$	879	0	0.2299	0.0547

Table 4.17 Judd Ofelt parameters of Nd:Yb:YVO_4 samples for π and σ polarization

JO parameters (x10^{-20}) cm^2			
	π pol. (Ω_π)	σ pol. (Ω_σ)	Ω_{eff}
Ω_2	11.9556	11.8234	11.8675
Ω_4	8.4962	3.4885	5.1577
Ω_6	7.5137	7.3064	7.3755

4.5.2 Emission characteristic of Nd:Yb:YVO_4 crystals

In order to investigate the effect of Nd concentration on the emission characteristics of Yb (0.8 and 3.0 at.%):YVO_4, photo-luminescence (PL) spectra were recorded for ~1 mm [100] oriented sample by exciting the samples at 808 nm. The PL emission spectra were recorded in the range of 900 to 1150 nm (Figure 4.26). The emission spectra were characterized by one broad emission around 1010 nm due to Yb ion and sharp emission lines at 914, 1064, 1072 and 1085 nm due to Nd ion. From the plot it is evident that as the Yb concentration increases in the lattice the PL intensity around 1010 nm due to Yb significantly increases. Further the relative emission intensity of the ~1010 nm peak is nearly 2.3 times less compared to the emission of Nd ion at ~1064 nm for 0.8 at.% Yb. It is to be noted that according to the report by Su-Mei et al. [50] the relative emission intensity of Yb emission peak is 4.5 times smaller compared to the emission of Nd ion at 1064 nm even for 1.0 at.% (higher than 0.8 at.%) Nd co-doped 1.0 at.% Yb:YVO_4 [50]. Therefore, the efficacy of energy transfer is higher in the present case. As can be seen in Figure 4.26, as the Yb concentration becomes 3.0 at.% the relative intensity of the Yb emission becomes almost same as the Nd emission intensity for the same Nd doping level (0.8 at.%). This is because the Nd ion more effectively excites the Yb ion in the upper state. This can be understood from Figure 4.25. As the Nd ion has higher absorption cross-section compared to Yb ion, when the Yb concentration is increased in the lattice more number of Yb ions are in the excited state because of energy transfer from Nd. Hence, Nd ions transfer their energy efficiently to Yb ion and act as good sensitizer. Therefore using Nd excitation peak 808 nm one can easily achieve laser action in Yb:YVO_4 gain medium. Also the lasing

wavelength can be tuned due to the inherent characteristics of broad emission peak of Yb ion.

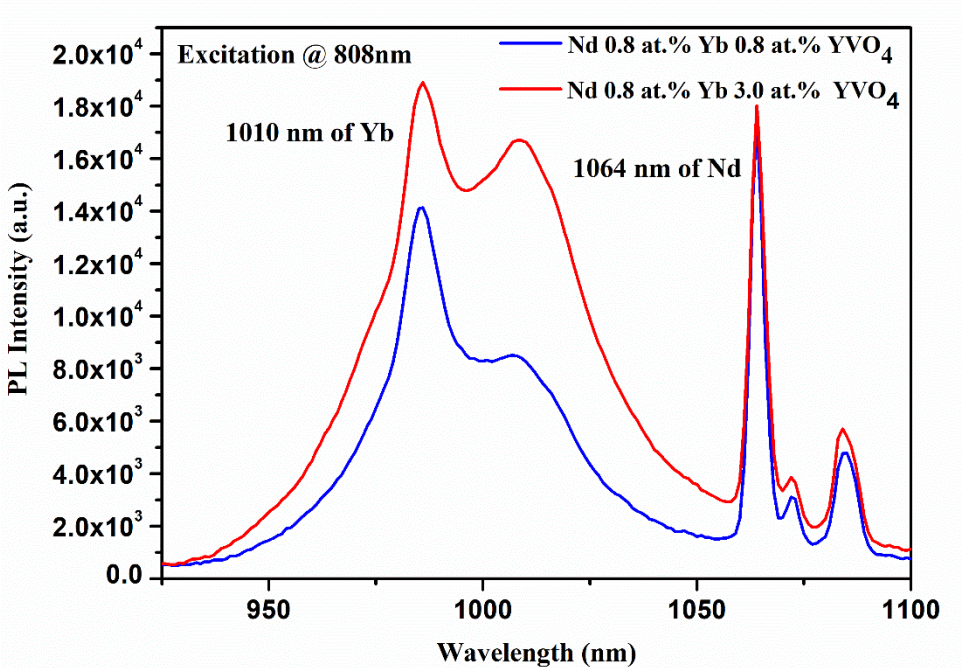

Figure 4.26 PL intensity of Nd:Yb:YVO_4 with excitation 808 nm

Further, the emission properties of Nd co-doped Yb (0.8 at.%):YVO_4 single crystals were investigated using the JO theory. The luminescence line strength of different transitions were calculated using the effective Judd-Ofelt parameters given in Table 4.18. Further the radiative transition rate i.e. the Einstein's A coefficient of emission of Nd-ion was estimated using the above equations (4.19) [2,43,135,138]:

In calculation for different luminescence transitions of Nd ion in Yb:YVO_4, the values of matrix elements $\langle \| U_i \| \rangle$for emission lines used are different from that for the absorption lines and obtained from ref. [43].

$$\tau = \frac{1}{\sum A(J \rightarrow J')} \quad \ldots\ldots\ldots\ldots\ldots\ldots\ldots\ldots\ldots\ldots\ldots\ldots\ldots\ldots\ldots\ldots\ldots\ldots\ldots\ldots\ldots\ldots \quad (4.26)$$

$$\beta(J \to J') = \frac{A(J \to J')}{\sum A(J \to J')} \quad \ldots\ldots\ldots\ldots\ldots\ldots\ldots\ldots\ldots\ldots\ldots\ldots\ldots\ldots\ldots\ldots\ldots\ldots\ldots\ldots\ldots\ldots. (4.27)$$

The radiative lifetime (τ_R) of $^4F_{3/2}$ energy level of Nd ion was calculated using the equation (4.26) and then the fluorescence branching ratio (β) were estimated using equation (4.27). In both the equations, the sum is over all possible final states:

The estimated radiative life-time ($^4F_{3/2}$ level) and branching ratio are given in Table 4.18 for four prominent emission transitions of Nd. The calculated radiative life time of $^4F_{3/2}$ level of Nd ion is ~111 µs [Table 4.18]. The calculated branching ratio of different transitions of Nd ion is maximum for $^4F_{3/2} \to {}^4I_{11/2}$ transition and it is ~51% of all the transitions of Nd ion. Now using the Einstein's A coefficient of $^4F_{3/2} \to {}^4I_{11/2}$ transition of Nd-ion and the photoluminescence (PL) spectra [Figure 4.26] of Nd co-doped Yb:YVO_4 samples, the emission cross-section was calculated by using the equations (4.20) and (4.21) [2,43,134–136,138].

Table 4.18 Luminescence spectral parameters for Nd (0.8 at.%):Yb(0.8 at.%):YVO_4 crystals

Transition final state	Central wavelength (nm)	S_{cal} (x10^{-20} cm^2)	A(J-J') x10^3	β	Radiative life -time (µs)	Emission cross section for $^4F_{3/2} \to {}^4I_{11/2}$ transition (x10^{-19} cm^2)
$^4I_{9/2}$	914	1.5995	3.2289	0.3728	~111	
$^4I_{11/2}$	1064	3.7358	4.7123	0.5178		4.1
$^4I_{13/2}$	1350	1.5614	0.9700	0.1046		
$^4I_{15/2}$	1880	0.2028	0.0447	0.0048		

The estimated emission cross-section of $^4F_{3/2} \to {}^4I_{11/2}$ transition line with an excitation at 808 nm is 4.1x10^{-19} cm^2 which is almost same as estimated by Bhaumik et

al. ($3.2x10^{-19}$ cm^2) [157] for only Nd doped sample. Hence emission cross-section of $^4F_{3/2} \rightarrow {}^4I_{11/2}$ (Nd) transition is not influenced by the presence of Yb (0.8 and 3.0 at.%) doping in YVO_4. Therefore Nd ion acts as excellent sensitizer for Yb:YVO_4 laser gain medium and make efficient pumping in the gain medium for getting laser action easily.

Therefore, in the Yb:YVO_4 laser gain medium, the strongest absorption band of Yb ion at 985 nm is primarily used for excitation or pumping of the laser gain medium. As seen in the absorption spectra of Nd:Yb:YVO_4 the stronger absorption band of Nd ion at 808 nm can be used for the excitation of Yb ions in YVO_4 that would provide an efficient pumping by avoiding the re-absorption of emission of light due to Yb ion (at 985 nm). The present findings further reveal that the stronger π-polarized (E||c) absorption band of Nd ion at 808 nm can be effectively utilized for pumping Yb:YVO_4 laser gain medium for developing an efficient laser system [139,140].

Chapter-5 Characterization of Nd Doped and Co-doped $GdVO_4$ Crystals

5.1 Characterization of Nd doped $GdVO_4$ crystals

Single crystals of undoped and Nd doped $GdVO_4$ with different Nd concentrations of 0.2, 0.6, 0.8, 1.0, 1.2 and 1.6 at.% were grown by optical floating zone technique. Crystals of length ~ 15-25 mm and diameter 5-6 mm were grown. The details of crystal growth have been presented in the Chapter 3. Further, for characterization of crystals, sample plates of ~1.0-1.5 mm thickness were cut from the grown crystals after orientating crystal in the [100] direction.

5.1.1 Rocking curve measurement

The crystalline quality of the Nd doped $GdVO_4$ single crystals was evaluated by the rocking curve measurements for [100]-oriented sample plate for (200) diffraction peak [Figure 5.1-5.2]. The experiments were done at the ADXRD beam-line (BL-12) [10] of the Indus-2 synchrotron facility [112] [Figure 5.1-5.2].

The wavelength of the X-ray used was 0.857Å (14.43 keV). Figure 5.1 and 5.2 shows a recorded rocking curve of the sample plate of 1.2 and 0.6 at. % Nd doped crystal. The presence of single and symmetrical diffraction peak corresponding to (200) planes confirms the orientation of the plate and these crystals are free from internal sub-grain structures and low-angle grain boundary. The FWHM of the diffraction peak was evaluated by Lorentz fitting. The observed value of the FWHM for the samples of different doping of Nd are ~43-56 arc-sec, which reveals the good crystalline quality of the grown crystals.

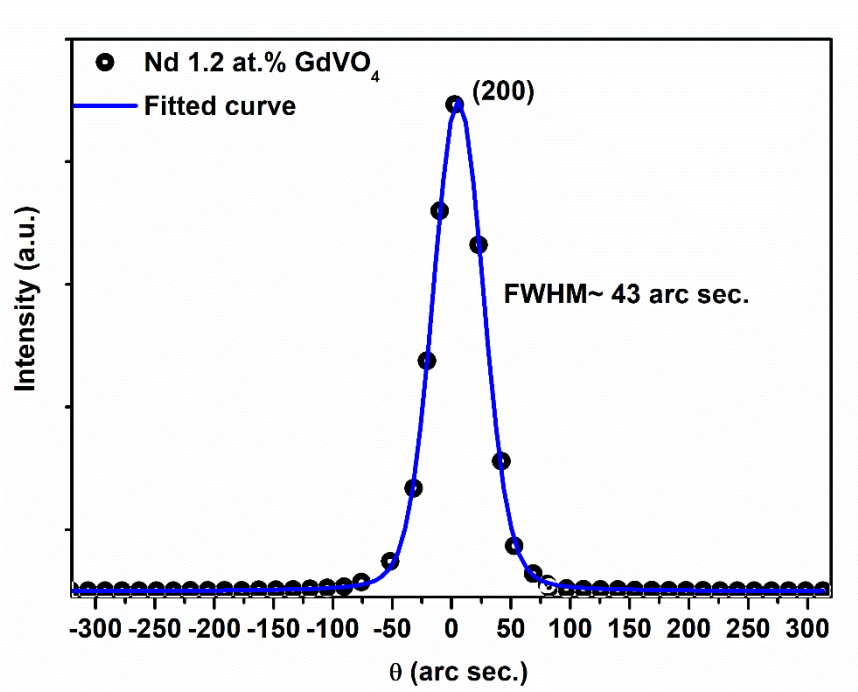

Figure 5.1 Rocking curve of (200)-peak of Nd (1.2 at.%):$GdVO_4$ doped crystal

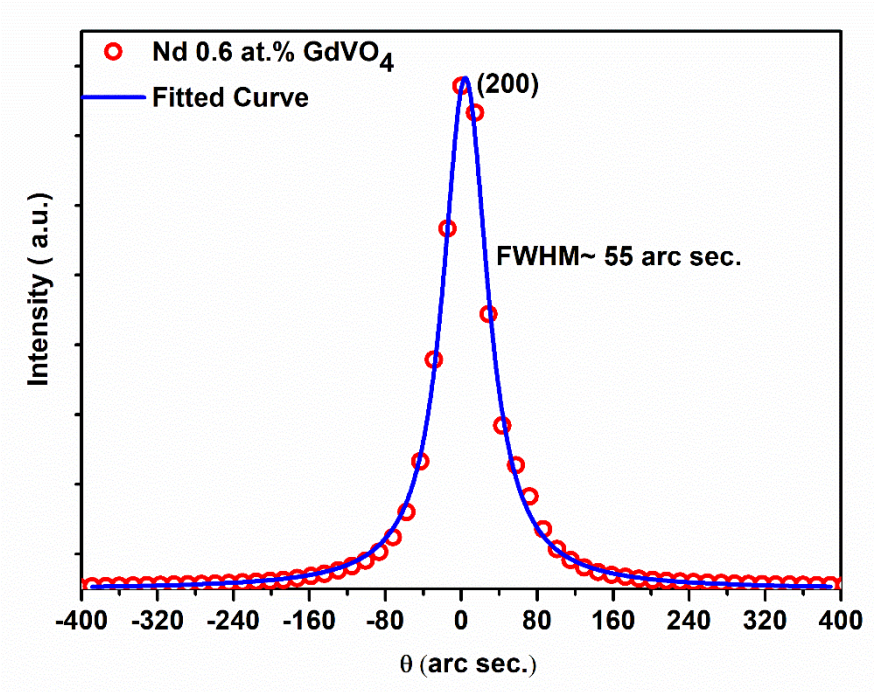

Figure 5.2 Rocking curve of (200)-peak of Nd (0.6 at.%):$GdVO_4$ doped crystal

5.1.2 Estimation of Nd concentration in the grown crystals

To estimate the actual Nd concentration and segregation coefficient of Nd in the grown $GdVO_4$ crystals, X-ray fluorescence measurements were carried out on the samples with different Nd concentrations. The experiments were performed in the Microprobe X-ray Fluorescence Beam-line (BL-16) of the Indus-2 synchrotron facility. For standard, polycrystalline pellets with known doping concentration of 0.2, 0.5, 1.0 & 2.0 at.% Nd in $GdVO_4$ were synthesized for generating the standard fluorescence reference curve and comparing with the fluorescence data of grown crystal samples for quantitative analysis. To ensure accuracy, experiments were performed at similar conditions. The actual Nd concentration in the grown $GdVO_4$ crystals were determined by comparing with standard data and the segregation coefficient of Nd ion in the $GdVO_4$ is found ~ 0.92

5.1.3 Defect study by chemical etching

The dislocation density on [100]-orientated plate of different Nd doped $GdVO_4$ grown crystal was estimated by chemical etching using diluted HCl after optimizing the etching parameters (75% of HCl and 25% of H_2O solution for 60 minutes at 100°C) [Figure 5.3]. The etch pit density is in the range of $10^3 – 10^4$ /cm^2.

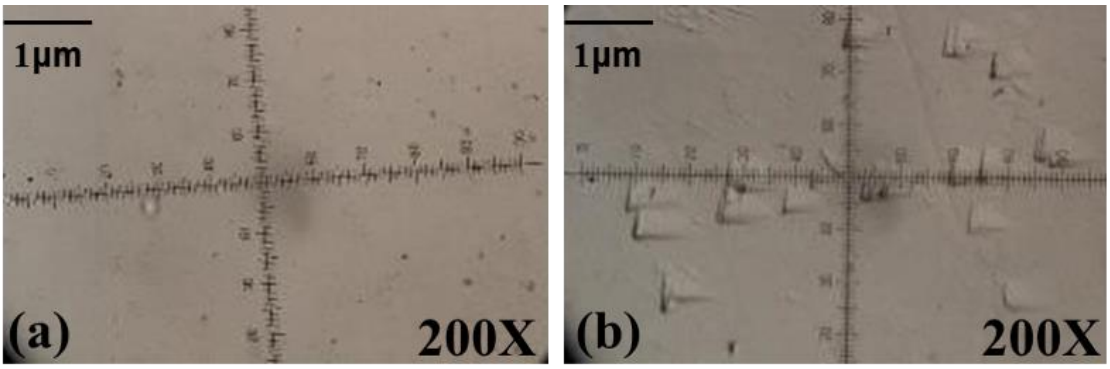

Figure 5.3 Photo-graphs of Nd:$GdVO_4$ plate before and after chemical etching

5.1.4 Effect of Nd doping on structural property of $GdVO_4$ crystals

The powder X–rays diffraction measurement was carried out by Rigaku make Ultrax-18 powder diffractometer using Cu-K_α in the range 20-70° for investigating the effect of Nd doping on the lattice parameters of $GdVO_4$ crystals [Figure 5.4 (a)].

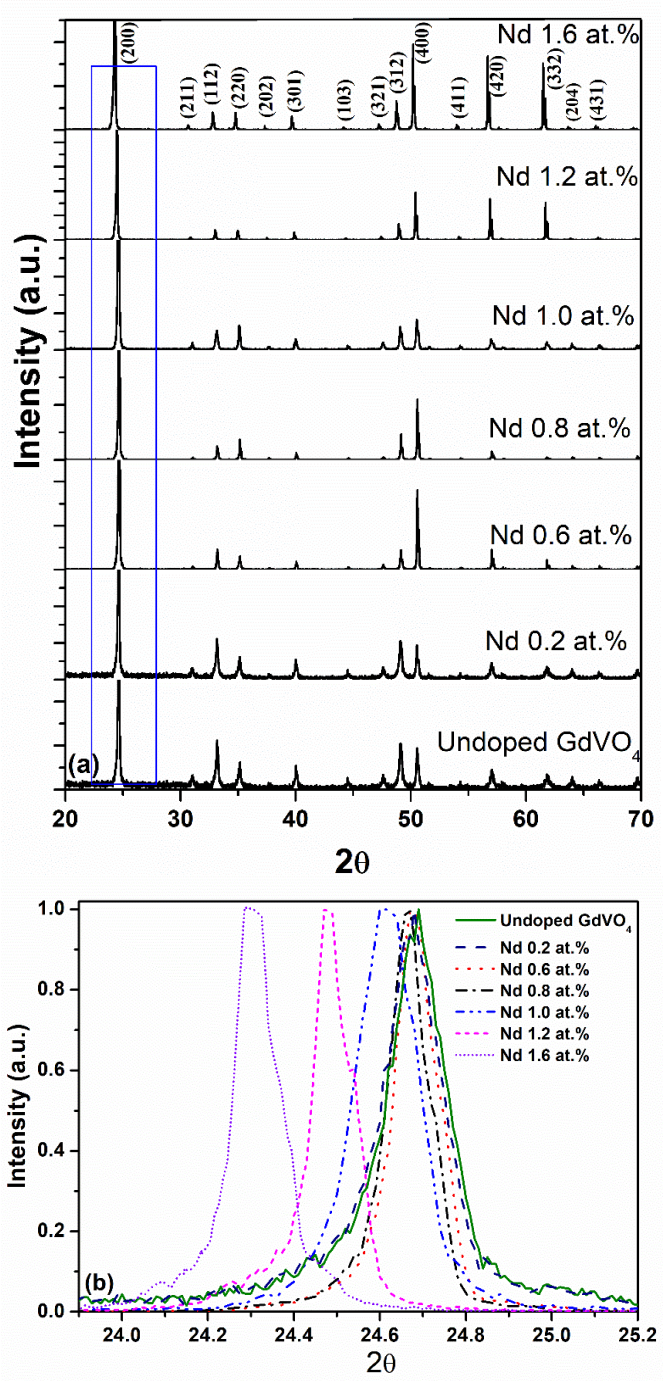

Figure 5.4 (a) Powder X-ray diffraction pattern of Nd doped $GdVO_4$ single crystals, (b) (200) diffraction peak.

The lattice parameters of undoped and doped $GdVO_4$ samples with six different doping concentrations of Nd were evaluated using all the diffraction peaks in the range of 20-70° to minimize the systematic error. It was found that the diffraction peaks shift systematically towards the lower angle as the Nd concentration varies from 0.2 to 1.6 at.% in the crystal signifying expansion of the lattice volume [Figure 5.4 (b)][144].

The observed expansion of lattice on Nd doping in $GdVO_4$ is due to the larger ionic size of Nd^{3+} ion (112.3pm) compared to the Gd^{3+} ion (107.8pm), which it replaces. The change in the lattice parameters and volume is listed in Table 5.1.

Table 5.1 Lattice parameters of Nd:$GdVO_4$ single crystals

Lattice Parameters	*Nd concentration*						
	undoped	*0.2 at.%*	*0.6 at.%*	*0.8 at.%*	*1.0 at.%*	*1.2 at.%*	*1.6 at.%*
a(Å) and b (Å)	7.21(5)	7.22(2)	7.22(4)	7.22(5)	7.22(6)	7.22(6)	7.22(7)
c(Å)	6.36(9)	6.37(1)	6.37(9)	6.38(7)	6.41(3)	6.43 (4)	6.45(8)
Volume (Å^3)	331.53(9)	332.29(4)	332.89(8)	333.36(5)	334.83(3)	335.97(3)	337.29(8)

5.1.5 Effect of Nd doping on the optical properties of $GdVO_4$ crystal

Polished plates of thickness ~1 mm having [100]-orientation were used to study the optical absorption characteristics of the grown crystals. The optical transmission spectra were recorded using UV-VIS-NIR spectrophotometer (JASCO V670) for both the unpolarized and polarized incident light at room temperature. The recorded spectra range was 300 -1000 nm [Figure 5.5]. For investigating the influence of Nd incorporation in $GdVO_4$, the absorption coefficient was evaluated from the recorded transmission spectra using the relation:

$$T \approx (1-R)^2\, exp(-\alpha d) \qquad \ldots\ldots\ldots\ldots\ldots\ldots\ldots\ldots\ldots\ldots\ldots\ldots\ldots\ldots\ldots\ldots\ldots\ldots\ldots\ldots (5.1)$$

where, R, T, d and α stand for reflectance, transmission, thickness of the samples and absorption coefficient respectively. The reflectivity was calculated from the relation

R =$[n(\lambda)-1]^2/[n(\lambda)+1]^2$ using the refractive index n(λ) of Nd doped in $GdVO_4$ single crystals which were measured using the prism coupling technique. The extra-ordinary refractive index and ordinary refractive were measured for all the doping concentration of Nd and given in section 5.1.6.

Figure 5.5 shows the recorded unpolarized absorption spectra of Nd doped $GdVO_4$ single crystals in the range of 300 -1000 nm. The absorption spectra depicts multiple absorption corresponding to different transition of Nd and absorption increases with the increase in the doping concentration of Nd.

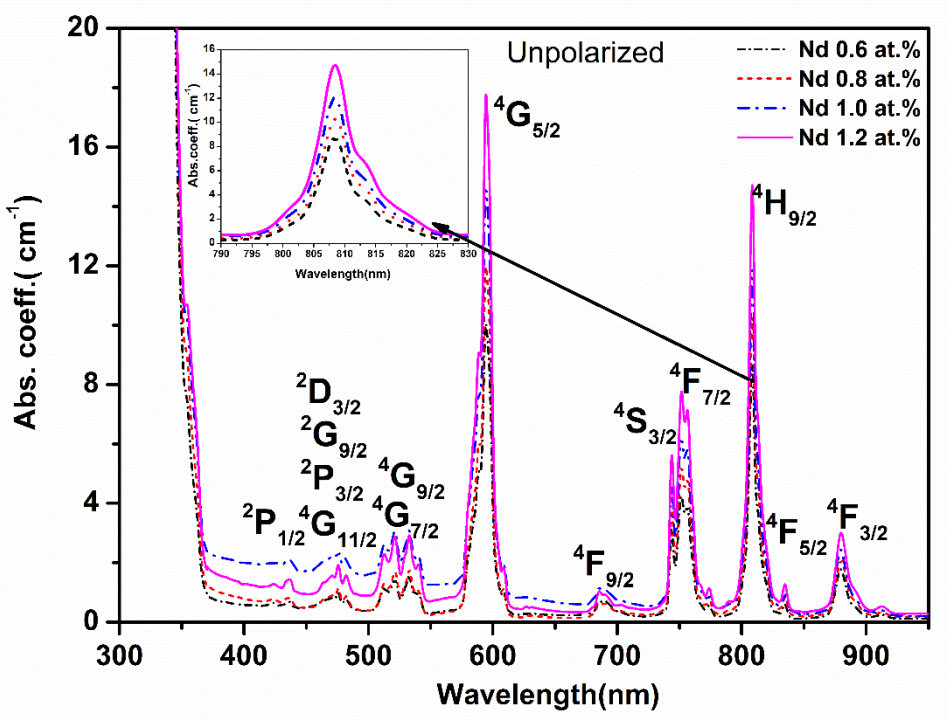

Figure 5.5 Absorption spectra of Nd doped $GdVO_4$ crystals in unpolarized light

The polarized absorption spectra of all the samples for both the polarization are shown in Figure 5.6-5.7. The absorption spectra for unpolarized and polarized light are

characterized by several absorption peaks, which are due to forced electric dipole (ED) intra-band (4f-4f) transitions of Nd ions [146,157].

The absorption spectra exhibit different feature in the polarized and unpolarized light. It is well known that the f-f transitions are forbidden because of the same parity of the initial and final wave function as it violates the conservation of parity (ED operator is of odd parity). But these transitions become allowed in the presence of asymmetric crystal field associated non-centrosymmetric (D_{2d}) site of $GdVO_4$ as the parity of the initial and final states gets modified to the mixed parity. The screening associated with outer $5s^2$ and $5p^6$ shells of Nd ion makes these f-to-f transitions sharp and distinct [2,146,157].

Polarized absorption spectra revealed that the Nd:$GdVO_4$ single crystals are polarization sensitive [119]. The absorption peak for π-polarization is higher than that for the σ-polarization as shown in Figure 5.6 and 5.7. The absorption coefficient of Nd 1.2 at.% corresponding to the 808 and 879 nm are ~38 and 11 cm^{-1} for π-polarization and ~11 and 2 cm^{-1} for σ-polarization respectively. Whereas, in the case of unpolarized light the absorption coefficient corresponding to these 808 and 879 nm transition for Nd 1.2 at.% are ~15 and 3 cm^{-1} which can also be obtained from both polarization data using a proper waiting factor. The strong π-polarized (E||c) absorption band of Nd:$GdVO_4$ laser gain medium centered at 808 nm is usually used to make efficient pumping of Nd:$GdVO_4$ gain medium using an AlGaAs diode laser operating around 808 nm wavelength. Also, the absorption coefficient for all the transitions increases with the increase in the doping concentration of Nd [143]. Further, for any laser gain medium, it is important to optimize the dopant (Nd) concentration for efficient lasing

performance. However, from the absorption spectra, it was observed that the absorption of Nd ions increases with increase in the doping concentration of Nd. But, emission spectra may have different characteristics due to ion - ion interaction at higher doping concentration that leads to an increase in non-radiative transitions probability. Hence, finding an optimum Nd doping concentration is therefore essential. For a proper insight, spectroscopic properties of Nd ion for all the f–f transitions were evaluated using the Judd–Ofelt theory [2,146,157] for different concentration of Nd. Hence, Judd-Ofelt parameters for all the samples for both polarization of light were evaluated from the absorption spectra, and used for calculating the fluorescence spectroscopic parameters of Nd ion [143].

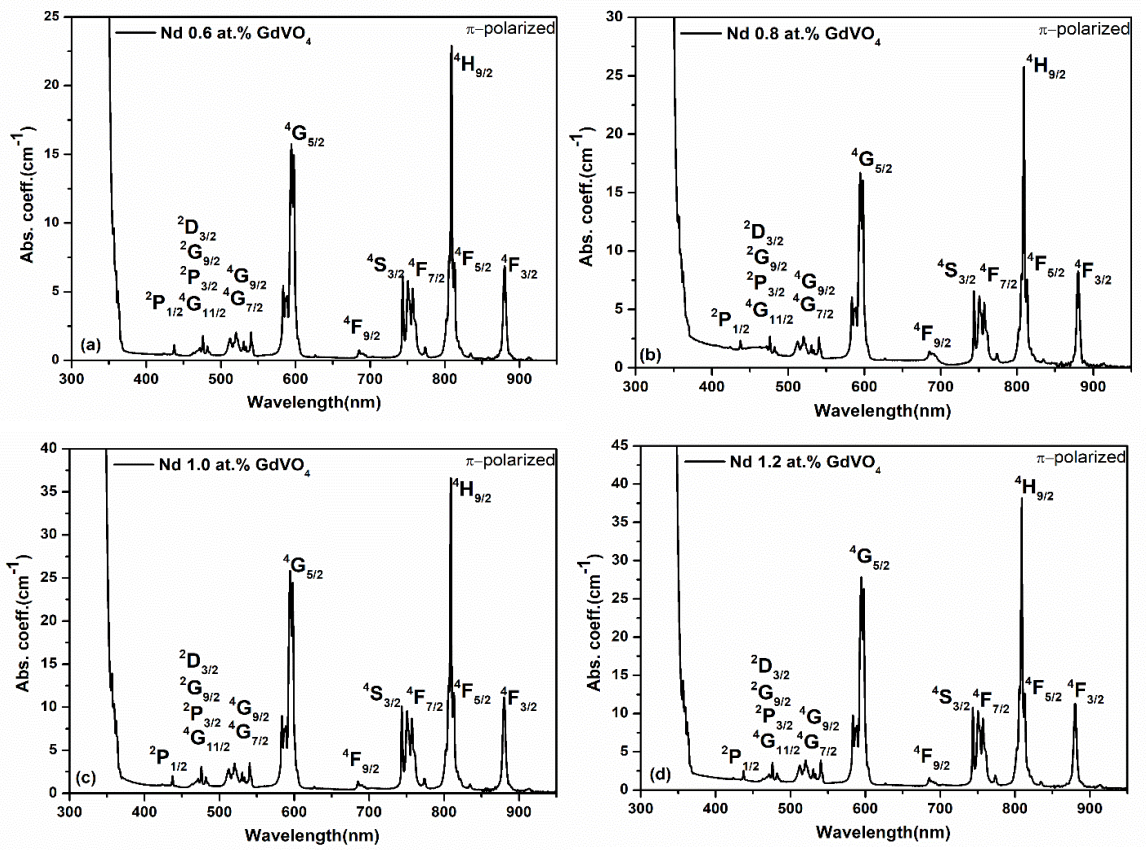

Figure 5.6 Absorption spectra of Nd doped $GdVO_4$ crystals in π- polarized light

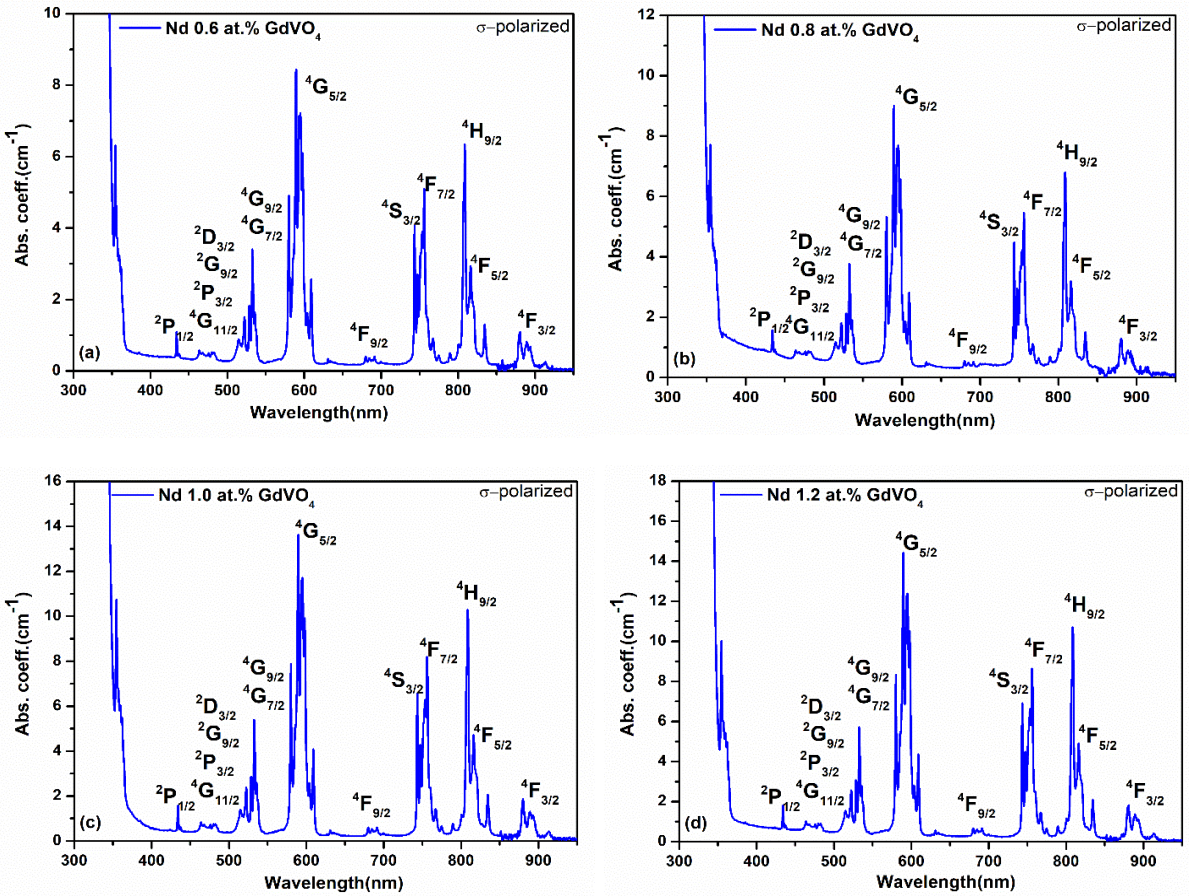

Figure 5.7 Absorption spectra of Nd doped GdVO$_4$ crystals in σ- polarized light

5.1.5.1 Effect of Nd doping on the absorption characteristic of Nd:GdVO$_4$

Judd-Ofelt parameters were estimated from the absorption characteristics of Nd ion having the f to f transitions for both the polarization of light using Judd-Ofelt (JO) theory [2,43,146,157]. The line strengths of forced ED transition ‘S’ were experimentally evaluated from the absorption spectrum by the following relation [2,43,146,157]:

$$S_{J\to J'} = \frac{\int \alpha(\lambda)d\lambda}{\frac{8\pi^3\rho\bar{\lambda}e^2}{9ch(2J+1)}\left[\frac{(n^2+2)^2}{3n}\right]} \quad \ldots\ldots\ldots\ldots\ldots\ldots\ldots\ldots\ldots\ldots\ldots\ldots\ldots\ldots\ldots\ldots\ldots.(5.2)$$

where *e* is charge of electron, *h* is the Planck's constant, ρ is the density of Nd^{3+} ions per cc, *c* is the velocity of light, *J* and *J′* are the total angular momentum of the initial and final state respectively, $\alpha(\lambda)$ is the absorption coefficient of absorption band and $\bar{\lambda}$ is the mean wavelength and n is the refractive index of the host material.

Using the above equation, the line-strengths (S_{exp}) of all the transitions were calculated for different Nd concentrations in GdVO4: 0.727×10^{20}/cc, 0.970×10^{20}/cc, 1.213×10^{20}/cc and 1.456×10^{20}/cc. The value of line strength are summarized in the Table 5.3-5.6.

The line strengths of force ED transitions from an initial manifold $|4f^9[L, S]\ J\rangle$ to a final manifold $|4f^9[L', S']\ J'\rangle$ was calculated according to JO theory by using following relation [2,43,146,157]:

$$S(J \rightarrow J') = \sum_{i=2,4,6} \Omega_i \left|\langle [S\ L], J \| U^i \| [S'\ L'], J' \rangle\right|^2 \quad \ldots\ldots\ldots\ldots\ldots\ldots\ldots\ldots\ldots\ldots\ldots\ldots\ldots (5.3)$$

where $\langle||Ui||\rangle$ represents the doubly-reduced matrix elements of the unit-tensor operator and the coefficients Ω_2, Ω_4 and Ω_6 are phenomenological JO intensity parameters [2,43,146,157]. The matrix elements of rare earth ions were evaluated with the help of the intermediate coupling approximation [2,43,146,157]. In the present calculation, the values of doubly reduced matrix elements for Nd [Table 5.2] used are the ones computed by Carnall et al. [134]. It is to be noted that these matrix elements are independent of the environment of the rare earth ion within a reasonable approximation [2,43,146,157]. The line strengths (oscillator strength) of the transition related to the absorption at 808 and 879 nm, which are used as pumping wavelengths, as well as other the wavelengths were calculated from the absorption spectrum and are

given in Table 5.3-5.6. The line strength of a particular transition depends on the symmetry around rare earth (RE) ion present in the lattice. The stronger oscillator strength implies stronger covalent bonding among the ligands whereas the smaller line strength tells higher symmetry around the rare earth ion [143].

Table 5.2 Doubly reduced matrix elements for different transition of Nd [134]

Final transition state [SL]Jf	Wavelength (nm)	$\|\|U_2\|\|$	$\|\|U_4\|\|$	$\|\|U_6\|\|$
$^2P_{1/2}$	432	0	0.0381	0
$^4G_{11/2}$,$^2P_{3/2}$,$^2D_{3/2}$,$^2G_{9/2}$	475	0.010	0.0431	0.0361
$^4G_{9/2}$,$^4G_{7/2}$	532	0.0597	0.2180	0.0954
$^4G_{5/2}$	594	0.8968	0.4049	0.0355
$^4F_{9/2}$	685	0.0010	0.0096	0.0381
$^4S_{3/2}$,$^4F_{7/2}$	751	0.0010	0.0447	0.6603
$^2H_{9/2}$,$^4F_{5/2}$	808	0.0101	0.2437	0.5169
$^4F_{3/2}$	879	0	0.2299	0.0547

Table 5.3 Line strength of Nd ion for Nd (0.6 at. %):$GdVO_4$

Initial transition state [SL]J_i	Final transition state [SL]J_f	Central wavelength (nm)	Pi polarized		Sigma polarized	
			S_{exp} ($x10^{-20}$ cm^2)	S_{cal} ($x10^{-20}$ cm^2)	S_{exp} ($x10^{-20}$ cm^2)	S_{cal} ($x10^{-20}$ cm^2)
$^4I_{9/2}$	$^2P_{1/2}$	432	0.1876	0.3981	0.1989	0.2076
$^4I_{9/2}$	$^4G_{11/2}$, $^2P_{3/2}$, $^2D_{3/2}$,$^2G_{9/2}$	475	1.0516	0.7954	0.6969	0.5025
$^4I_{9/2}$	$^4G_{9/2}$,$^4G_{7/2}$	532	2.9609	3.8375	3.2709	2.5838
$^4I_{9/2}$	$^4G_{5/2}$	594	14.7906	14.7427	13.2413	13.2846
$^4I_{9/2}$	$^4F_{9/2}$	685	0.3054	0.4639	0.2697	0.3341
$^4I_{9/2}$	$^4S_{3/2}$,$^4F_{7/2}$	751	5.9466	6.5824	5.0442	4.9305
$^4I_{9/2}$	$^2H_{9/2}$,$^4F_{5/2}$	808	8.4225	7.4392	4.8713	5.1092
$^4I_{9/2}$	$^4F_{3/2}$	879	2.7293	2.9076	1.2622	1.6397

Table 5.4 Line strength of Nd ion for Nd (0.8 at. %):$GdVO_4$

Initial transition state [SL]J_i	Final transition state [SL]J_f	Central wavelength (nm)	Pi polarized		Sigma polarized	
			S_{exp} ($x10^{-20}$ cm^2)	S_{cal} ($x10^{-20}$ cm^2)	S_{exp} ($x10^{-20}$ cm^2)	S_{cal} ($x10^{-20}$ cm^2)
$^4I_{9/2}$	$^2P_{1/2}$	432	0.1072	0.3395	0.1825	0.1920
$^4I_{9/2}$	$^4G_{11/2}$, $^2P_{3/2}$, $^2D_{3/2}$,$^2G_{9/2}$	475	0.7912	0.6504	0.5962	0.4370
$^4I_{9/2}$	$^4G_{9/2}$,$^4G_{7/2}$	532	2.3244	3.1263	2.5538	2.3129
$^4I_{9/2}$	$^4G_{5/2}$	594	11.4507	11.4061	12.1838	12.2020
$^4I_{9/2}$	$^4F_{9/2}$	685	0.7146	0.3661	0.2409	0.2798
$^4I_{9/2}$	$^4S_{3/2}$,$^4F_{7/2}$	751	4.6044	5.1240	3.8938	4.0543
$^4I_{9/2}$	$^2H_{9/2}$,$^4F_{5/2}$	808	6.7271	5.9492	4.5247	4.3289
$^4I_{9/2}$	$^4F_{3/2}$	879	2.3951	2.4393	1.0752	1.4747

Table 5.5 Line strength of Nd ion for Nd (1.0 at. %):$GdVO_4$

Initial transition state [SL]J_i	Final transition state [SL]J_f	Central wavelength (nm)	Pi polarized		Sigma polarized	
			S_{exp} ($x10^{-20}$ cm^2)	S_{cal} ($x10^{-20}$ cm^2)	S_{exp} ($x10^{-20}$ cm^2)	S_{cal} ($x10^{-20}$ cm^2)
$^4I_{9/2}$	$^2P_{1/2}$	432	0.1872	0.3840	0.1884	0.2041
$^4I_{9/2}$	$^4G_{11/2}$, $^2P_{3/2}$, $^2D_{3/2}$,$^2G_{9/2}$	475	1.0990	0.7659	0.6320	0.4640
$^4I_{9/2}$	$^4G_{9/2}$,$^4G_{7/2}$	532	2.8217	3.6896	3.1770	2.3923
$^4I_{9/2}$	$^4G_{5/2}$	594	14.1305	14.0837	11.8991	11.9497
$^4I_{9/2}$	$^4F_{9/2}$	685	0.2769	0.4461	0.2953	0.2969
$^4I_{9/2}$	$^4S_{3/2}$,$^4F_{7/2}$	751	5.6580	6.3289	4.3716	4.3187
$^4I_{9/2}$	$^2H_{9/2}$,$^4F_{5/2}$	808	8.1871	7.1583	4.4328	4.5983
$^4I_{9/2}$	$^4F_{3/2}$	879	2.5606	2.8029	1.0503	1.5688

Table 5.6 Line strength of Nd ion for Nd (1.2 at. %):$GdVO_4$

Initial transition state [SL]J_i	Final transition state [SL]J_f	Central wavelength (nm)	Pi polarized		Sigma polarized	
			S_{exp} ($x10^{-20}$ cm^2)	S_{cal} ($x10^{-20}$ cm^2)	S_{exp} ($x10^{-20}$ cm^2)	S_{cal} ($x10^{-20}$ cm^2)
$^4I_{9/2}$	$^2P_{1/2}$	432	0.1676	0.3303	0.1613	0.1755
$^4I_{9/2}$	$^4G_{11/2}$, $^2P_{3/2}$, $^2D_{3/2}$,$^2G_{9/2}$	475	0.8845	0.6709	0.6009	0.4291
$^4I_{9/2}$	$^4G_{9/2}$,$^4G_{7/2}$	532	2.5735	3.2347	2.7805	2.2044
$^4I_{9/2}$	$^4G_{5/2}$	594	12.6203	12.5850	11.3355	11.3720
$^4I_{9/2}$	$^4F_{9/2}$	685	0.2713	0.3964	0.2670	0.2870
$^4I_{9/2}$	$^4S_{3/2}$,$^4F_{7/2}$	751	5.1187	5.6541	4.3309	4.2447
$^4I_{9/2}$	$^2H_{9/2}$,$^4F_{5/2}$	808	7.1468	6.3269	4.1907	4.3805
$^4I_{9/2}$	$^4F_{3/2}$	879	2.2207	2.4286	1.0659	1.3924

Further, Judd-Ofelt parameters Ω_2, Ω_4 and Ω_6 were calculated using the line strength with the help of least square fitting. The Judd-Ofelt parameters are different for sigma and pi polarization of absorption spectra that shows the line strength and Judd-Ofelt parameters depend on the nature of polarization of the incident light [Table 5.7]. The effective Judd- Ofelt parameters (Ω_{eff}) were evaluated using $\Omega_{eff} = (\Omega_\pi + 2\Omega_\sigma)/3$ [137]. The spectroscopic quality factor (X) depends on the Ω_4 and Ω_6 parameters as per the relation $X = \Omega_4/\Omega_6$. The higher value of the parameter X signifies dominant stimulated emission in the gain medium [2,43,146,157]. The calculated spectroscopic quality factor for Nd doped $GdVO_4$ along [100] are 0.91, 1.02, 0.98 and 0.88 for Nd doping concentrations of 0.6, 0.8, 1.0 and 1.2 at.%, respectively. The estimated value of spectroscopic quality factor was found to be maximum for 0.8 at.% Nd doped $GdVO_4$ crystals. It indicates that the optimum doping concentration of Nd in $GdVO_4$ for efficient lasing is around 0.8 at.% [143].

Table 5.7 Effective Judd-Ofelt parameters of Nd:$GdVO_4$ samples

Nd conc.	Judd Ofelt parameters ($x10^{-20}$) cm^2								
	Ω_2			Ω_4			Ω_6		
	π Pol. (Ω_π)	σ Pol. (Ω_σ)	Ω_{eff}	π Pol. (Ω_π)	σ Pol. (Ω_σ)	Ω_{eff}	π Pol. (Ω_π)	σ Pol. (Ω_σ)	Ω_{eff}
0.6 at.%	11.3562	12.0735	11.8344	10.4478	5.4476	7.1143	9.2443	7.0800	7.8014
0.8 at.%	8.4128	11.1023	10.2058	8.9104	5.0388	6.3293	7.1441	5.7822	6.2362
1.0 at.%	10.8027	10.6620	10.7089	10.0775	5.3576	6.9309	8.8863	6.1617	7.0699
1.2 at.%	9.8038	10.3600	10.1746	8.6695	4.6050	5.9598	7.9612	6.1010	6.7211

5.1.5.2 Effect of Nd doping on the emission characteristics

For investigating the effect of Nd doping concentration on the emission properties of $GdVO_4$ the photo-luminescence (PL) spectra of the samples were recorded in the range of 1050 to 1100 nm with an excitation at 808 nm under similar experimental conditions [Figure 5.8]. The emission spectra were characterized by emission at 912

and 1062 nm. It also has other emissions at 1340 and 1880 nm [65]. Among these, the PL intensity at 1062 nm is the highest. This peak is characterized by three sharp peaks at around 1062, 1069 and 1081 nm. The emission intensity at ~1062 nm is the largest for all Nd concentrations (0.6, 0.8 1.0 and 1.2 at. %) at an excitation of 808 nm.

PL intensity at 1062 nm (the lasing wavelength), 1069 and 1081 nm increases as the doping concentration of Nd was increased up to 0.8 at.% of Nd doping, but thereafter it decreases for 1.0 and 1.2 at.% of Nd doping as shown in the Figure 5.8. Therefore, the emission characteristics also revealed that the optimum concentration of Nd in $GdVO_4$ single crystals for lasing application is around 0.8 at.% of Nd [143]. The decrease in PL intensity for 1.0 and 1.2 at.% Nd:$GdVO_4$ is attributed to the concentration quenching [64], which occurs due to ion-to-ion interaction resulting into the reduction of fluorescence life-time [143].

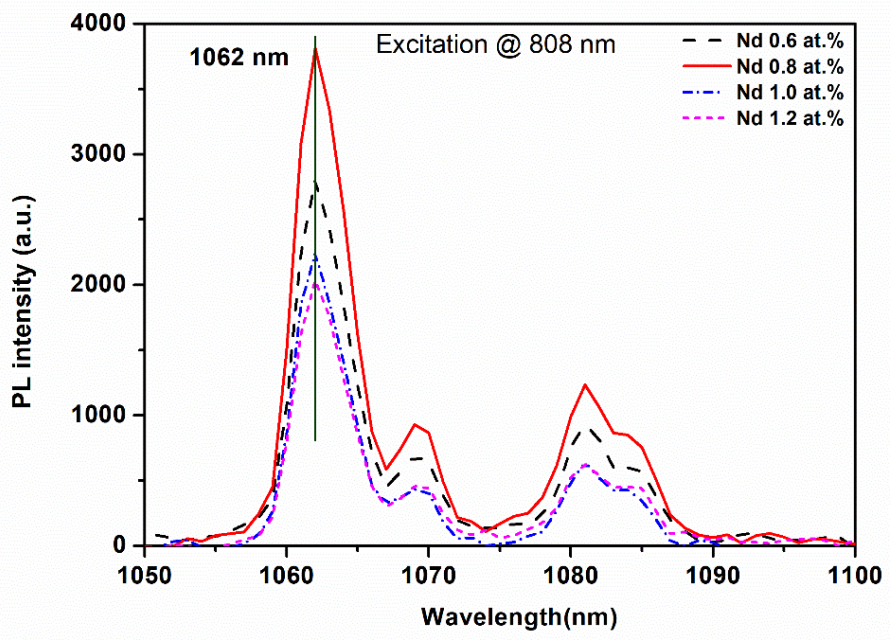

Figure 5.8 Emission spectra of Nd doped $GdVO_4$ single crystals

Further, the emission characteristics of Nd doped $GdVO_4$ single crystals were investigated using the JO theory. Using the effective JO parameters of the luminescence line-strength for different transitions were calculated and tabulated in Table 5.8.

The radiative transition rate of emission in Nd-ion, i.e. Einstein's coefficient (A), are calculated using the relation [2,43,146,157].

$$A(J \rightarrow J') = \frac{64\pi^4 e^2}{3h(2J+1)\bar{\lambda}^3}\left[\frac{n(n^2+2)^2}{9}\right]\sum_{i=2,4,6} \Omega_i \left|\langle [S\,L],J \| U^i \| [S'L'],J'\rangle\right|^2 \quad \ldots .(5.4)$$

The JO parameters obtained for the absorption spectra were used in the calculation. In the calculation of luminescence transition, the values of matrix elements ⟨||Ui||⟩ are different from the ones used for absorption and were taken from ref. [2]. The radiative lifetime was evaluated using the following equation (5.5) and the fluorescence branching ratio are given by equation (5.6).

$$\tau = \frac{1}{\sum A(J \rightarrow J')} \qquad \ldots\ldots\ldots\ldots\ldots\ldots\ldots\ldots\ldots\ldots\ldots\ldots\ldots \quad (5.5)$$

$$\beta(J \rightarrow J') = \frac{A(J \rightarrow J')}{\sum A(J \rightarrow J')} \qquad \ldots\ldots\ldots\ldots\ldots\ldots\ldots\ldots\ldots\ldots\ldots\ldots\ldots (5.6)$$

The summation in both the expressions is over all possible final states or terminal states. The branching ratio for different transitions and radiative life-time of $^4F_{3/2}$ state of Nd ion for all Nd concentrations are given in Table 5.9. The experimentally calculated fluorescence lifetime was ~100 and 101 μs for 0.6 and 0.8 at.% whereas, it decreases to ~92 and ~93 μs for 1.0 and 1.2 at.% of Nd doping respectively. The branching ratio is maximum for $^4F_{3/2} \rightarrow {}^4I_{11/2}$ transition and the total contribution of this

in the all transitions is around ~ 50% , which is almost independent of doping concentrations of Nd ion [143].

Table 5.8 Luminescence parameters of Nd:$GdVO_4$ samples for different transition

Transition from $^4F_{3/2}$ level	Wavelength (nm)	Nd 0.6 at.%	Nd 0.8 at.%	Nd 1.0 at.%	Nd 1.2 at. %
		S_{cal} ($x10^{-20}$ cm^2)	S_{cal} ($x10^{-20}$ cm^2)	S_{cal} ($x10^{-20}$ cm^2)	S_{cal} ($x10^{-20}$ cm^2)
$^4I_{9/2}$	912	2.0727	1.8043	1.9894	1.8468
$^4I_{11/2}$	1062	4.1876	3.4388	3.8637	3.5836
$^4I_{13/2}$	1340[65]	1.6516	1.3202	1.4967	1.6228
$^4I_{15/2}$	1880[65]	0.2145	0.1715	0.1944	0.1848

5.1.5.3 Fluorescence lifetime measurement

Experimentally fluorescence lifetime measurement of Nd doped $GdVO_4$ single crystals were carried out using ultrafast technique. The sample was excited at 808 nm by Ti:Sapphire femto-second laser (Pulse width: 35fs, repetition rate: 1kHz) and corresponding fluorescence decay profile of sample was recorded using IR detector and digital oscilloscope. Figure 5.9 shows the fluorescence decay of 0.6 at.% of Nd doped sample as a representative data. The fluorescence decay plot has rising part as well as decaying part.

Therefore, the fluorescence data for all the samples was analyzed and fitted using the exponential function which has rising as well as decaying part. The decaying part of fluorescence yield results the fluorescence life-time of Nd:$GdVO_4$ samples and found to be ~ 100±0.03, 101±0.03, 92±0.03 and 93±0.03 μs corresponding to the doping concentration 0.6, 0.8, 1.0 and 1.2 at.% of Nd respectively. It shows that the fluorescence life-time of $^4F_{3/2}$ level starts decreasing after 0.8 at.% of Nd doping which implies that the quenching of Nd ion occurs beyond 0.8 at.% of Nd doping [143].

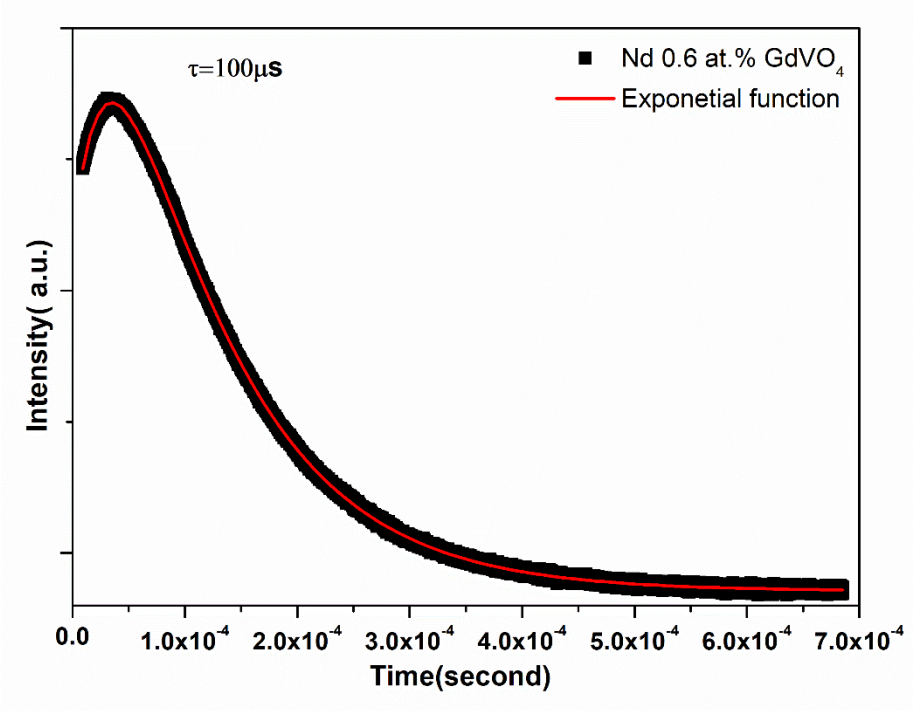

Figure 5.9 Fluorescence decay profile of 0.6 at.% Nd ion

Further using the calculated Einstein's coefficient and the photoluminescence (PL) spectra [Figure 5.8], the emission cross-section of the $^4F_{3/2} \rightarrow {}^4I_{11/2}$ transition for all doping concentration of Nd:$GdVO_4$ samples was evaluated by the following relations [2,43,146,157]:

$$\sigma_e(\lambda) = \frac{\bar{\lambda}^4}{8\pi n^2 c \Delta\lambda_{eff}} A(J \rightarrow J') \quad \ldots\ldots\ldots\ldots\ldots\ldots\ldots\ldots\ldots\ldots\ldots\ldots\ldots\ldots (5.7)$$

$$\Delta\lambda_{eff} = \frac{\int I(\lambda) d\lambda}{I_{max}} \quad \ldots\ldots\ldots\ldots\ldots\ldots\ldots\ldots\ldots\ldots\ldots\ldots\ldots\ldots\ldots\ldots (5.8)$$

where $\bar{\lambda}$ is the mean wavelength and $\Delta\lambda_{eff}$ is the effective line-width of emission band.

The emission cross-section of $^4F_{3/2} \rightarrow {}^4I_{11/2}$ transition for all Nd concentrations for an excitation at 808 nm was estimated and their values are ~ 4.5×10^{-19} cm^2, $4.5 \times 10^{-}$

^{19} cm^2, 4.0x10^{-19} cm^2 and 3.98x10^{-19} cm^2 for 0.6, 0.8, 1.0 and 1.2 at.% of Nd respectively [Table 5.9-5.12].

It shows that the estimated value of emission cross-section for $^4F_{3/2} \rightarrow {}^4I_{11/2}$ transition was found to be nearly same for all Nd doping concentrations. Our finding shows that the emission cross section is independent of Nd doping concentration whereas quenching effect reduces the fluorescence life-time as well as the emission intensity after 0.8 at.% of Nd doping concentration [143].

Table 5.9 Luminescence parameters for Nd (0.6 at.%) :$GdVO_4$ sample

Transition from $^4F_{3/2}$ level	Central wavelength (nm)	S_{cal} (x10^{-20} cm^2)	A(J-J') (x10^3 sec^{-1})	β	τ (μs)	Emission cross section for $^4F_{3/2} \rightarrow {}^4I_{11/2}$ (x10^{-19} cm^2)
$^4I_{9/2}$	912	2.0727	4.3602	0.39745	~91	
$^4I_{11/2}$	1062	4.1876	5.4997	0.50133		~4.5
$^4I_{13/2}$	1340	1.6516	1.0615	0.09676		
$^4I_{15/2}$	1880	0.2145	0.0489	0.00446		

Table 5.10 Luminescence parameters for Nd (0.8 at.%) :$GdVO_4$ sample

Transition from $^4F_{3/2}$ level	Central wavelength (nm)	S_{cal} (x10^{-20} cm^2)	A(J-J') (x10^3 sec^{-1})	β	τ (μs)	Emission cross section for $^4F_{3/2} \rightarrow {}^4I_{11/2}$ (x10^{-19} cm^2)
$^4I_{9/2}$	912	1.8043	3.7956	0.41259	~109	
$^4I_{11/2}$	1062	3.4388	4.5163	0.49093		~4.5
$^4I_{13/2}$	1340	1.3202	0.8485	0.09223		
$^4I_{15/2}$	1880	0.1715	0.0391	0.00425		

Table 5.11 Luminescence parameters for Nd (1.0 at.%) :$GdVO_4$ sample

Transition from $^4F_{3/2}$ level	Central wavelength (nm)	S_{cal} (x10^{-20} cm^2)	A(J-J') (x10^3 sec^{-1})	β	τ (μs)	Emission cross section for $^4F_{3/2} \rightarrow {}^4I_{11/2}$ (x10^{-19} cm^2)
$^4I_{9/2}$	912	1.9894	4.1850	0.40767	~97	
$^4I_{11/2}$	1062	3.8637	5.0743	0.49430		~4.0
$^4I_{13/2}$	1340	1.4967	0.9620	0.09371		
$^4I_{15/2}$	1880	0.1944	0.0443	0.00432		

Table 5.12 Luminescence parameters for Nd (1.2 at.%) :$GdVO_4$ sample

Transition from $^4F_{3/2}$ level	Central wavelength (nm)	S_{cal} ($x10^{-20}$ cm^2)	A(J-J') ($x10^3$ sec^{-1})	β	τ (μs)	Emission cross section for $^4F_{3/2} \rightarrow {}^4I_{11/2}$ ($x10^{-19}$ cm^2)
$^4I_{9/2}$	912	1.8468	3.8850	0.40148	~103	
$^4I_{11/2}$	1062	3.5836	4.7065	0.48638		~3.98
$^4I_{13/2}$	1340	1.6228	1.0430	0.10779		
$^4I_{15/2}$	1880	0.1848	0.0421	0.00435		

Therefore, to summarize, our findings suggest that the optimum concentration of Nd ion in $GdVO_4$ single crystals is around ~ 0.8 at.% at which the best lasing performance can be obtained.

5.1.6 Effect of Nd doping on refractive index of $GdVO_4$ crystals

Refractive index of undoped and Nd doped in $GdVO_4$ single crystals was measured using the prism coupling technique having four lasers (wavelength: 532, 828, 1064 and 1551 nm) by two orthogonal polarization corresponding to TE and TM modes. Figure 5.10 shows the variation of detector intensity with respect to angle of incidence of the laser light recorded in one of the experiments [144].

The refractive index is calculated using the relation $n = n_p \sin\theta_c$ where θ_c is critical angle and n_p is prism refractive index [117,120,141,148]. As $GdVO_4$ is a uniaxial crystal (tetragonal), [100]-oriented sample plate is having b[010] and c[001] directions is on the plane of the sample [Inset of Figure 5.10]. The measurement of refractive index on a [100] plate would provide the value of ordinary refractive index, (n_o) for TM mode of incident laser light, whereas TE mode would give the extra ordinary refractive index (n_e) along any direction perpendicular to [100] depending on the contact made with the prism face.

During the measurement the sample was placed in such a manner that the TE mode would result into n[001] (extra-ordinary refractive index, n_e) [inset of Figure 5.10]. Refractive indices of undoped and Nd doped $GdVO_4$ crystal and doped with different doping concentrations of Nd ion i.e., 0.2, 0.6, 0.8, 1.0, 1.2 and 1.6 at.% were measured for four different wavelengths along c[001] and a[100]-direction at room temperature (30 °C) and the values are tabulated in Table 5.13.

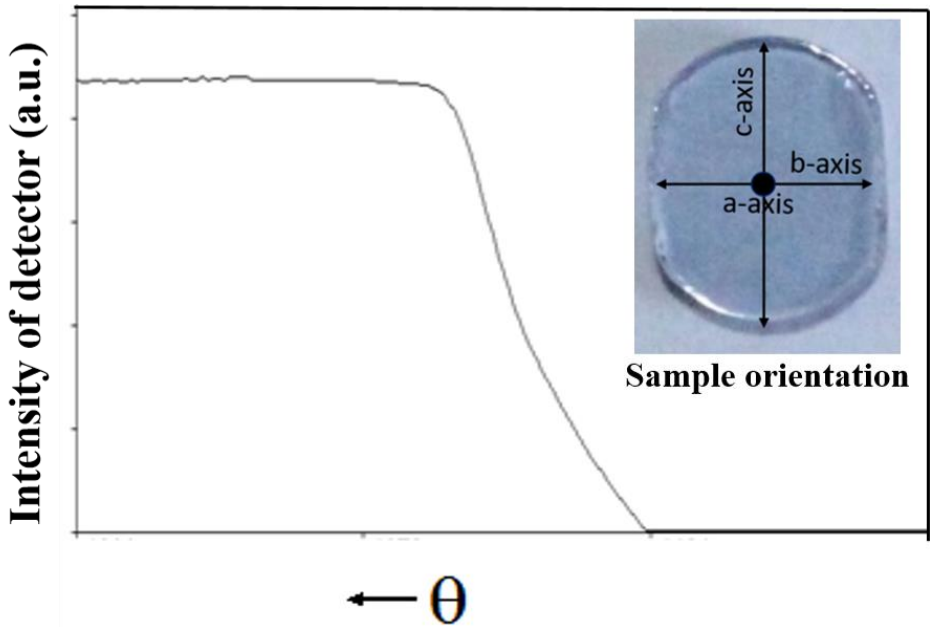

Figure 5.10 Variation of intensity of detector as function of angle of incidence. Inset shows the orientation of the sample

Table 5.13 Refractive index of different Nd doping concentration in $GdVO_4$ crystals

Wavelength →	532 nm		828 nm		1064 nm		1551 nm	
Nd conc.↓	n_e	n_o	n_e	n_o	n_e	n_o	n_e	n_o
undoped	2.279(5)	2.033(0)	2.209(2)	1.984(8)	2.191(1)	1.972(1)	2.173(0)	1.959(1)
0.2 at.%	2.276(1)	2.033(7)	2.205(3)	1.984(8)	2.187(8)	1.972(4)	2.169(7)	1.959(8)
0.6 at.%	2.273(7)	2.033(3)	2.203(9)	1.984(9)	2.186(2)	1.972(1)	2.168(7)	1.959(2)
0.8 at.%	2.277(7)	2.033(5)	2.206(3)	1.984(5)	2.189(1)	1.972(1)	2.171(8)	1.959(4)
1.0 at.%	2.279(4)	2.033(8)	2.208(7)	1.984(2)	2.191(1)	1.971(5)	2.173(0)	1.958(9)
1.2 at.%	2.280(3)	2.033(2)	2.209(9)	1.984(5)	2.191(7)	1.972(0)	2.173(9)	1.959(4)
1.6 at.%	2.281(8)	2.034(4)	2.211(0)	1.984(6)	2.192(9)	1.972(6)	2.175(0)	1.960(0)

Referring to Figure 5.11 (a-d), it was observed that extra-ordinary refractive index initially decreases with increasing Nd doping concentration and thereafter it gradually increases and surpasses the value of undoped $GdVO_4$ for the concentration higher than 1.0 at.% Nd. For 1.2 and 1.6 at.% Nd, the extra-ordinary RI of $GdVO_4$ crystal become higher than that of undoped $GdVO_4$ crystal as shown in Figure 5.11 (a-d) and listed in Table 5.13 [144].

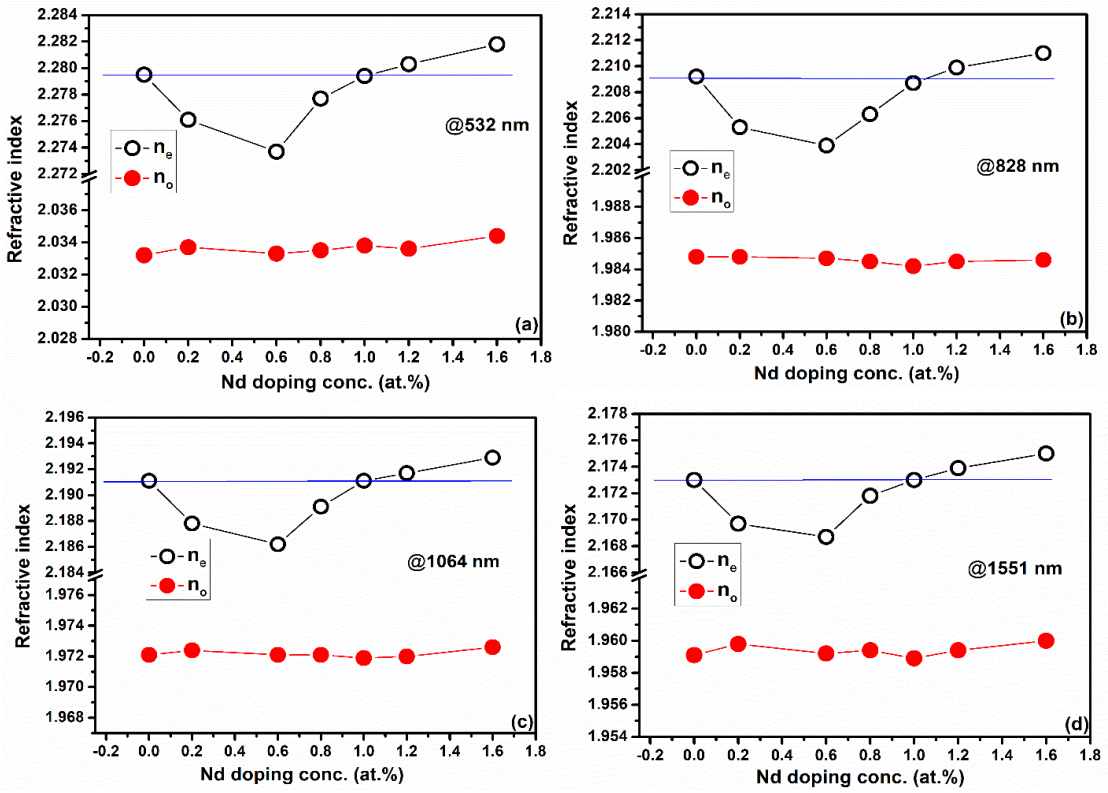

Figure 5.11 Variation of refractive index with different doping concentration of Nd in $GdVO_4$ at different wavelength (joining lines are for guiding the eye).

The refractive index depends on the electron density of the bound valence electron of the constituent atoms in the lattice, lattice parameters and the macroscopic polarizability of the material, which is certainly influenced by doping. The macroscopic polarizability depends on the ease of polarization of the molecules and structure of the

lattice. The variation of refractive index (n) with macroscopic polarizability of a material is given by Classius-Mossotte relation:

$$\frac{(\varepsilon-1)}{(\varepsilon+2)}=\frac{(n^2-1)}{(n^2+2)}=\frac{4\pi}{3}\frac{\alpha_m}{V} \quad \ldots\ldots\ldots\ldots\ldots\ldots \quad (5.9)$$

where, α_m is the polarizability of the macroscopic sphere of volume V.

In the crystal lattice, on doping, the Nd ions replace the Gd ions of the host medium [59,159]. The electron density of Gd^{3+} ion (having seven unpaired valance electrons and ionic radii: 107.8 pm) is higher than Nd^{3+} ion (having three unpaired valance electrons and ionic radii: 112.3 pm) [159,160]. When Nd ion is doped in $GdVO_4$ crystals, the electron density of the material decreases that in turn decreases the extra-ordinary refractive index of the material. On the contrary, the XRD result shows that because of Nd substitution the lattice elongates along the c-direction.

The macroscopic polarizability is, therefore, higher for an electric field parallel to the c-direction that leads to an increase in the extra-ordinary refractive index of the material. The variation of extra-ordinary RI on doping is, therefore, attributed to both these phenomena. As per our findings, at lesser Nd^{3+} doping concentration, the contribution of decrease in electron density sue to Nd^{3+} ions dominates that leads to a decrease in the RI and at higher doping concentration, RI increases due to lattice expansion induced increase in the polarizability. Possibly the effect of the lattice elongation dominates over the reduction in the electron density beyond 0.6 at.% of doping, resulting into the trend observed in the RI. Subsequently the extra-ordinary RI becomes equal to that for the undoped samples when the doping concentration is 1.0 at.% Nd [144].

The ordinary RI remains more or less unaffected on Nd doping within the measurement limit of the present investigation [Table 5.13]. It is to be noted that Nd ion occupies the octahedral site in the lattice [119,159] and also the structural analysis carried out in present investigation shows that the oxygen octahedra elongates only along the c-direction with an increase in Nd doping concentration. Hence doping of Nd only influences the refractive index for extra-ordinary polarization of incident light significantly in comparison to the ordinary polarization [144].

Further the measured refractive index data for undoped and Nd doped crystals was fitted to the Sellmeier equation [116,121,122,141]:

$$n^2(\lambda, T) = A_0(T) + \frac{B_0(T)}{(\lambda^2 - C_0(T))} - D_0(T)\lambda^2 \quad \ldots\ldots\ldots\ldots\ldots (5.10)$$

where $A_0(T)$, $B_0(T)$, $C_0(T)$ *and* $D_0(T)$ are the Sellmeier coefficients at a temperature T (in °C) and λ is the wavelength (in μm). The plots for Sellmeier fitting for n_o and n_e for all the Nd oped and undoped $GdVO_4$ samples are shown in Figure 5.12 (a-g). Sellmeier coefficients of all the samples were estimated and are listed in Table 5.14.

Table 5.14 Sellmeier coefficients for undoped and doped with 0.2, 0.6, 0.8, 1.0, 1.2 and 1.6 at.% Nd in $GdVO_4$ single crystals

Sellmeier coefficients	undoped	Nd 0.2 at.%	Nd 0.6 at.%	Nd 0.8 at.%	Nd 1.0 at.%	Nd 1.2 at.%	Nd 1.6 at.%
	TE mode (n_e) at 30 ºC						
A_0	4.727 (14)	4.721(67)	4.703(84)	4.725(56)	4.734(08)	4.728(00)	4.730(57)
B_0	0.106(23)	0.095(74)	0.103(24)	0.094(45)	0.097(57)	0.105(76)	0.106(67)
C_0	0.060(59)	0.077(32)	0.063(89)	0.081(28)	0.074(52)	0.062(26)	0.061(44)
D_0	0.019(75)	0.022(95)	0.018(57)	0.020(57)	0.022(45)	0.018(83)	0.018(89)
	TM mode (n_o) at 30 ºC						
A_0	3.850(64)	3.845(68)	3.835(77)	3.845(51)	3.837(75)	3.842(17)	3.853(96)
B_0	0.062(58)	0.063(73)	0.072(54)	0.063(13)	0.067(29)	0.065(45)	0.057(15)
C_0	0.065(95)	0.066(29)	0.062(69)	0.067(96)	0.060(21)	0.061(44)	0.085(39)
D_0	0.017(81)	0.013(35)	0.011(64)	0.013(83)	0.012(12)	0.012(82)	0.015(38)

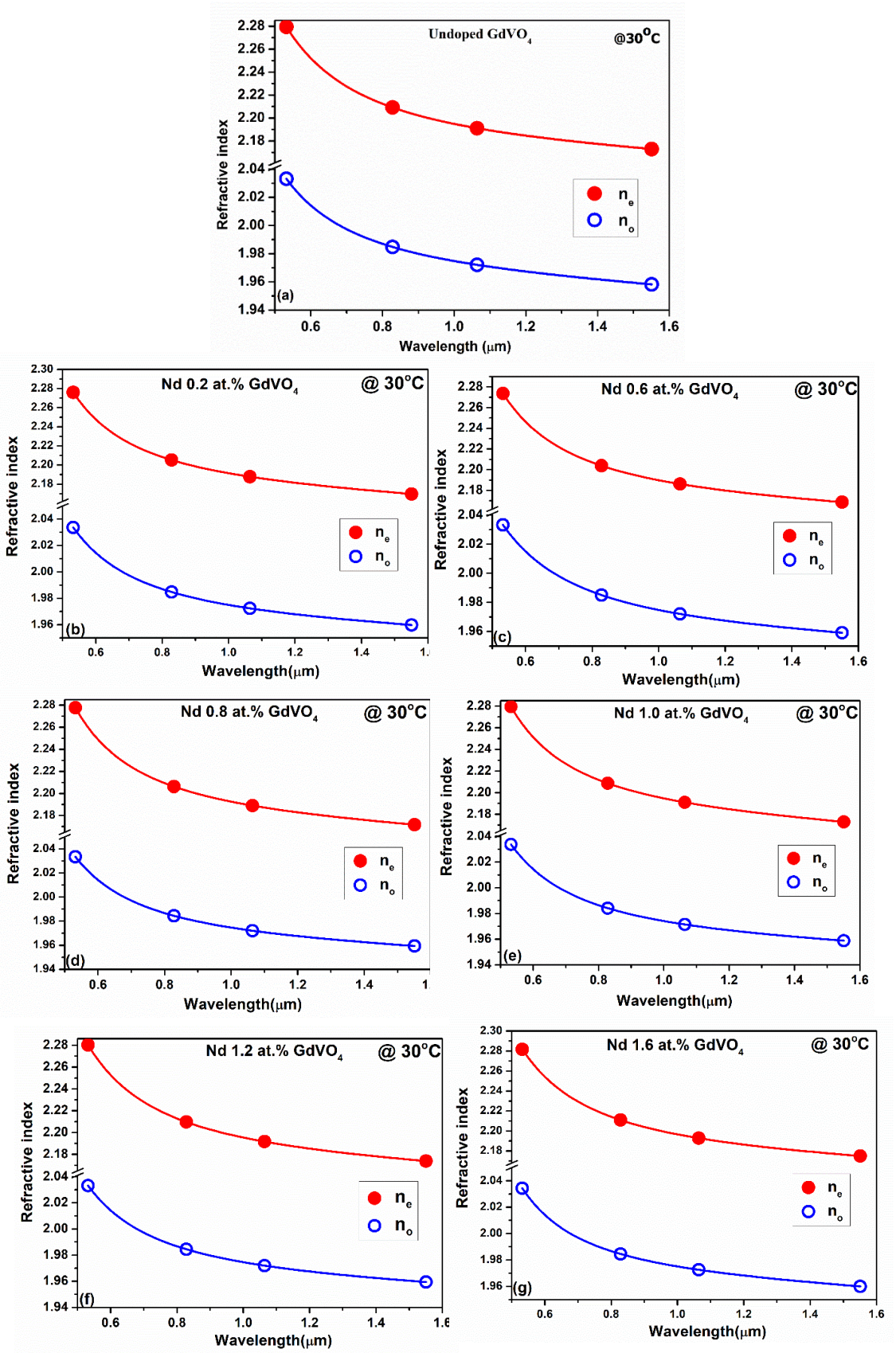

Figure 5.12 Fitting of the Sellmeier equation for (a) undoped $GdVO_4$ (b) 0.2 (c) 0.6 (d) 0.8 (e) 1.0 (f) 1.2 and (g) 1.6 at.% Nd doped $GdVO_4$ single crystals

Table: 5.14 show the variation of the Sellmeier coefficients with respect to the doping concentration of Nd ion. It was found that the Sellmeier coefficients for TE mode (n_e) is higher than the Sellmeier coefficients of TM (n_o) mode for all the Nd doping concentrations.

This is because of higher value of the extra-ordinary refractive index compared to the ordinary refractive index. Also, the Sellmeier coefficients for TM mode (n_o) are nearly unaffected by the Nd doping concentrations which is expected as the n_o does not change appreciably with doping concentration of Nd [144].

5.1.6.1 Temperature dependence of refractive index

The thermo-optic coefficient of laser gain medium is an important thermal parameter for designing and developing a laser system. The temperature dependent refractive index measurement was carried out in the temperature range of 30-150 °C in the interval of 25 °C in the similar geometry.

The temperature of both the sample and the prism could be controlled with an accuracy of around ±1°C. From the measurement, it was observed that as the temperature of all the Nd doped samples was increased, the refractive index of sample also increases that results positive thermo-optic coefficient of $GdVO_4$ crystals. The occurrence of positive or negative of thermo-optic coefficient of any material can be understood from the equation (5.11) in combination with the equation (5.9) [151].

$$\frac{1}{(\varepsilon+2)(\varepsilon-1)}\left(\frac{\partial\varepsilon}{\partial T}\right)_P = -\beta + \left[\beta\frac{V}{\alpha_m}\left(\frac{\partial\alpha_m}{\partial V}\right)_T\right] + \frac{1}{3\alpha_m}\left(\frac{\partial\alpha_m}{\partial T}\right)_V \quad \ldots\ldots (5.11)$$

where, ε is the permittivity and β is the thermal expansion coefficient. Generally the material which has high melting point and mechanical hardness exhibits relatively

low thermal expansion (which can be understood through Grüneisen parameter) [152]. Nd:$GdVO_4$ crystals having high melting point (1780°C) and mechanical hardness (~5 mohs) shows positive thermo-optic coefficient due to the relatively low contribution of the first term in equation (5.3).

Sellmeier coefficients $A_0(T)$, $B_0(T)$, $C_0(T)$ and $D_0(T)$ for all the samples were calculated at different temperature by fitting Sellmeier equation and are tabulated in Table 5.15 and 5.16. In the Sellmeier equation, value of the refractive index is mainly governed by the dimensionless parameter $A_0(T)$. The other terms in the Sellmeier equation signifies the wavelength dependence of the refractive index [144].

Table 5.15 Sellmeier coefficients of n_e for all the doping concentrations of Nd at different temperature

Temp.(↓)/ Nd conc.→		0.0 at.%	0.2 at.%	0.6 at.%	0.8 at.%	1.0 at.%	1.2 at.%	1.6 at.%
@ 50 °C	A_0	4.741(06)	4.722(31)	4.712(37)	4.750(17)	4.737(63)	4.724(73)	4.727(94)
	B_0	0.099(69)	0.100(79)	0.103(62)	0.085(01)	0.100(13)	0.113(24)	0.114(09)
	C_0	0.072(55)	0.070(31)	0.064(85)	0.096(63)	0.072(14)	0.052(49)	0.050(08)
	D_0	0.022(10)	0.020(99)	0.018(76)	0.026(14)	0.020(57)	0.016(83)	0.016(67)
@ 75 °C	A_0	4.741(22)	4.732(79)	4.714(21)	4.760(75)	4.737(65)	4.740(24)	4.773(04)
	B_0	0.107(51)	0.101(78)	0.109(41)	0.085(21)	0.107(25)	0.108(14)	0.090(03)
	C_0	0.061(85)	0.069(18)	0.058(21)	0.097(17)	0.062(89)	0.062(86)	0.087(82)
	D_0	0.019(62)	0.022(08)	0.016(89)	0.026(78)	0.017(61)	0.018(30)	0.026(72)
@ 100 °C	A_0	4.750(97)	4.747(49)	4.731(91)	4.749(22)	4.759(83)	4.746(09)	4.770(84)
	B_0	0.105(81)	0.098(58)	0.104(17)	0.098(88)	0.098(77)	0.111(66)	0.098(19)
	C_0	0.067(52)	0.076(16)	0.066(52)	0.077(65)	0.077(24)	0.058(82)	0.077(24)
	D_0	0.020(03)	0.024(42)	0.019(59)	0.020(50)	0.021(99)	0.017(88)	0.025(01)
@ 125 °C	A_0	4.757(19)	4.754(91)	4.747(11)	4.763(55)	4.764(75)	4.745(92)	4.774(37)
	B_0	0.108(82)	0.099(62)	0.100(52)	0.094(32)	0.103(93)	0.121(15)	0.101(72)
	C_0	0.063(05)	0.075(87)	0.073(82)	0.086(70)	0.069(12)	0.044(87)	0.073(40)
	D_0	0.019(49)	0.024(07)	0.022(42)	0.022(27)	0.021(45)	0.016(10)	0.024(18)
@ 150 °C	A_0	4.776(10)	4.769(18)	4.747(90)	4.762(57)	4.778(70)	4.754(80)	4.789(11)
	B_0	0.102(91)	0.096(33)	0.105(79)	0.101(77)	0.099(42)	0.124(68)	0.096(42)
	C_0	0.072(61)	0.081(40)	0.067(51)	0.076(26)	0.079(32)	0.042(40)	0.084(78)
	D_0	0.022(75)	0.026(20)	0.020(02)	0.019(85)	0.023(44)	0.014(25)	0.025(09)

Table 5.16 Sellmeier coefficients of n_o for all the doping concentrations of Nd at different temperature

Temp.(↓)/ Nd conc.(→)		0.0 at.%	0.2 at.%	0.6 at.%	0.8 at.%	1.0 at.%	1.2 at.%	1.6 at.%
@ 50 °C	A_0	3.843(20)	3.857(61)	3.847(97)	3.840(32)	3.856(50)	3.857(23)	3.875(97)
	B_0	0.072(09)	0.059(44)	0.064(43)	0.071(23)	0.060(29)	0.059(08)	0.048(80)
	C_0	0.045(95)	0.078(35)	0.066(79)	0.049(47)	0.074(73)	0.078(78)	0.106(37)
	D_0	0.014(18)	0.015(32)	0.013(99)	0.010(08)	0.016(62)	0.015(75)	0.021(64)
@ 75 °C	A_0	3.851(06)	3.884(08)	3.848(69)	3.854(10)	3.857(15)	3.853(27)	3.874(35)
	B_0	0.070(04)	0.045(34)	0.070(42)	0.066(45)	0.062(58)	0.067(48)	0.054(88)
	C_0	0.052(21)	0.117(49)	0.053(32)	0.062(26)	0.074(06)	0.059(76)	0.090(19)
	D_0	0.013(86)	0.021(17)	0.012(13)	0.013(07)	0.014(20)	0.013(06)	0.018(09)
@ 100 °C	A_0	3.867(27)	3.866(74)	3.852(41)	3.863(93)	3.862(15)	3.850(44)	3.875(33)
	B_0	0.063(35)	0.061(31)	0.073(01)	0.062(98)	0.066(13)	0.073(03)	0.057(22)
	C_0	0.068(37)	0.077(23)	0.047(84)	0.072(27)	0.062(41)	0.049(31)	0.086(99)
	D_0	0.017(21)	0.013(73)	0.011(66)	0.014(14)	0.015(38)	0.010(36)	0.016(94)
@ 125 °C	A_0	3.863(42)	3.868(53)	3.857(22)	3.860(93)	3.884(78)	3.860(51)	3.885(36)
	B_0	0.069(83)	0.065(47)	0.073(29)	0.070(34)	0.054(02)	0.071(52)	0.054(33)
	C_0	0.055(21)	0.066(43)	0.048(17)	0.055(62)	0.097(91)	0.051(44)	0.095(25)
	D_0	0.013(59)	0.013(69)	0.011(26)	0.011(83)	0.021(32)	0.012(16)	0.018(83)
@ 150 °C	A_0	3.872(36)	3.844(39)	3.858(39)	3.866(05)	3.871(75)	3.869(62)	3.880(09)
	B_0	0.067(46)	0.084(01)	0.083(84)	0.069(81)	0.064(08)	0.067(35)	0.062(30)
	C_0	0.061(72)	0.030(88)	0.026(31)	0.059(77)	0.073(65)	0.065(16)	0.075(05)
	D_0	0.014(63)	0.004(44)	0.006(86)	0.011(60)	0.014(00)	0.013(00)	0.014(70)

Further, the thermo-optic coefficient (temperature coefficient of the refractive index) was estimated from the refractive indices measured as a function of temperature for different wavelength for undoped and all Nd doped samples [Figure 5.13(a)-5.13(e)]. The variation of refractive index with respect temperature for both the n_e and n_o of samples was found to be linear on fitting (standard deviation ~10^{-6}, R^2-value ~0. 0.9977) as per the following relation [151]:

$$n_j(\lambda, T) = n_j{}^o(\lambda) + \left(\frac{dn_j(\lambda)}{dT}\right)T \quad \ldots\ldots\ldots (5.12)$$

where j represents ordinary or extraordinary refractive index (o, e), T is temperature in °C, $n^o(\lambda)$ refers to the refractive index at 0°C for a specific wavelength and dn/dT is the temperature coefficient of RI.

The thermo-optic coefficients for both the n_e and n_o of undoped and Nd doped $GdVO_4$ crystal was found almost independent of doping concentration of Nd which is

favorable in terms of laser designing, whereas in the refractive index measurement we observed that there is a variation in extra-ordinary refractive index with Nd doping concentration. However, the thermo-optic coefficients for both n_e and n_o of all samples decreases as the wavelength was increased. This is because of refractive index is inversely proportional to the wavelength of the light and small variation of refractive index takes place at higher wavelength according the Sellmeier equation. In the present measurement, the values of the thermo-optic coefficient for undoped and all the Nd doped $GdVO_4$ crystal is $\sim 10^{-5}$ /°C [Table 5.17]. In literature, the thermo-optic coefficient of RI for Nd doped $GdVO_4$ samples are characterized by a range of values: in some of the reports, the value is $\sim 10^{-5}$ /°C [123,161,162] whereas in some cases the value is $\sim 10^{-6}$/°C [152,163–165].

One interesting observation of the present investigation is that the thermo-optic coefficient for extraordinary RI is always higher than that of ordinary RI, whereas Mukhopadhyay et al. [163], Shen et al. [123], Sato et al. [164] and Qin et al. [161] reported that the thermo-optic coefficient for ordinary RI is always higher than that of extraordinary RI. However, it is noteworthy that Soulard et al. [165] reported that the dn/dT for n_e is higher than that for n_o, which is in line with the present observation. This can be understood from the fact that thermal expansion in the c-direction is higher compared to the other two directions [164]. As a result easy of change of macroscopic polarization (polarizability) in the c-direction causes the increase in extra-ordinary refractive index with increase in temperature and can be explained using the equation (5.9) and (5.11) on the basis of macroscopic polarizability at constant pressure.

Table 5.17 Thermo-optic coefficient (dn/dT) for undoped and Nd doped $GdVO_4$ crystals for n_e and n_o

Wave-length (nm)	n_j	Nd dopant concentration													
		Undoped $GdVO_4$		**0.2 at.%**		**0.6 at.%**		**0.8 at.%**		**1.0 at.%**		**1.2 at.%**		**1.6 at.%**	
		n°	**dn/dT (x10^{-5}/°C)**	**n°**	**dn/dT (x10^{-5}/°C)**	**n°**	**dn/dT (x10^{-5}/°C)**	**n°**	**dn/dT (x10^{-5}/°C)**	**n°**	**dn/dT (x10^{-5}/°C)**	**n°**	**dn/dT (x10^{-5}/°C)**	**n°**	**dn/dT (x10^{-5}/°C)**
532	n_e	2.276(39)	11.(4)	2.272(81)	10.(9)	2.270(55)	11(.2)	2.274(46)	11.(2)	2.275(98)	11.(5)	2.277(19)	11.(6)	2.277(88)	11.(4)
	n_o	2.031(26)	7.(9)	2.031(46)	8.(1)	2.031(49)	7.(7)	2.0311(9)	8.(1)	2.031(31)	8.(1)	2.031(07)	8.(2)	2.032(37)	7.(6)
828	n_e	2.206(53)	9.(0)	2.202(78)	8.(9)	2.201(43)	9.(0)	2.203(79)	9.(0)	2.206(04)	9.(2)	2.206(96)	9.(4)	2.208(57)	9.(1)
	n_o	1.983(10)	6.(4)	1.982(94)	6.(4)	1.983(02)	6.(5)	1.982(84)	6.(5)	1.982(66)	6.(3)	1.982(71)	6.(6)	1.982(90)	6.(7)
1064	n_e	2.188(64)	8.(6)	2.185(23)	8.(5)	2.183(78)	8.(6)	2.187(17)	8.(2)	2.188(51)	8.(8)	2.189(27)	8.(3)	2.190(49)	8.(3)
	n_o	1.970(15)	6.(3)	1.971(21)	6.(2)	1.970(48)	5.(9)	1.970((46)	6.(1)	1.970(11)	6.(2)	1.970(47)	6.(0)	1.971(23)	6.(3)
1551	n_e	2.170(71)	8.(2)	2.167(51)	7.(6)	2.166(56)	7.(9)	2.169(50)	8.(0)	2.170(92)	8.(2)	2.171(60)	7.(9)	2.172(81)	7.(4)
	n_o	1.956(23)	6.(7)	1.958(27)	6.(0)	1.957(43)	6.(1)	1.957(94)	6.(0)	1.957(39)	5.(9)	1.957(80)	5.(9)	1.958(11)	6.(2)

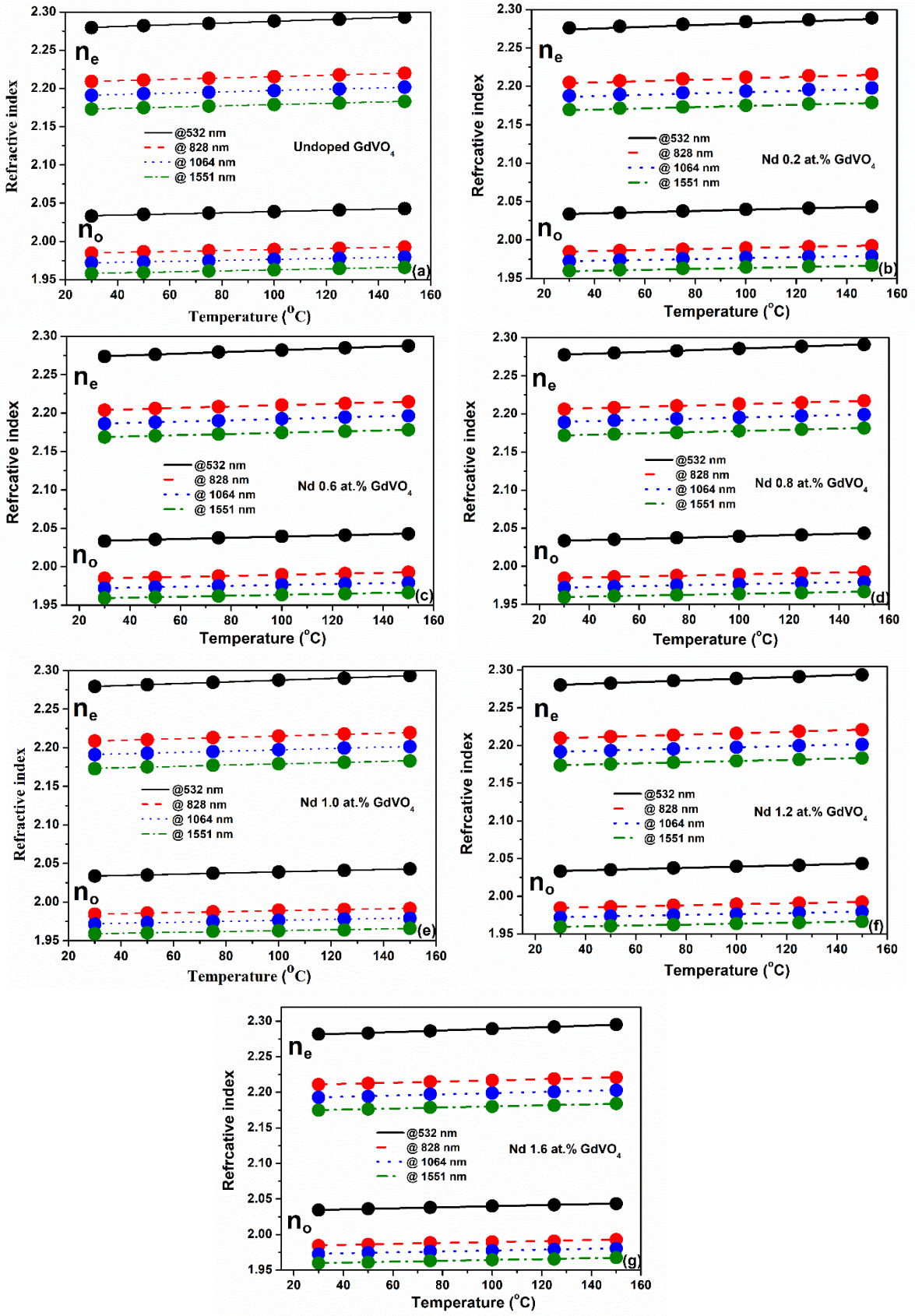

Figure 5.13 Dependence of RI on temperature for different doping concentration of Nd.

An empirical relation is proposed for calculating the thermo-optic coefficient at any desired wavelength in the range of 532 to 1551 nm, the measured thermo-optic coefficients were fitted by employing to cubic polynomial.

The fitted equations for undoped $GdVO_4$ and Nd doped $GdVO_4$ crystals are listed as equation 5.13-5.26 for both orthogonal polarization of light [R^2 value~ 0.9977-0. 9998]. This is an important set of equations, as it will enable the estimation of the thermo-optic coefficient in this wavelength range, which is a critical parameter for designing laser cavity [144].

$$\left(\frac{dn}{dT}\right)_{n_e}^{Undoped} = \left(6.145 + \frac{5.643}{\lambda} - \frac{4.863}{\lambda^2} + \frac{1.777}{\lambda^3}\right) \times 10^{-5}/^oC \ldots\ldots\ldots (5.13)$$

$$\left(\frac{dn}{dT}\right)_{n_o}^{Undoped} = \left(9.638 - \frac{7.045}{\lambda} + \frac{4.328}{\lambda^2} - \frac{5.847}{\lambda^3}\right) \times 10^{-5}/^oC \ldots\ldots\ldots (5.14)$$

$$\left(\frac{dn}{dT}\right)_{n_e}^{0.2\ at.\%} = \left(1.108 + \frac{17.182}{\lambda} - \frac{13.334}{\lambda^2} + \frac{3.721}{\lambda^3}\right) \times 10^{-5}/^oC \ldots\ldots\ldots (5.15)$$

$$\left(\frac{dn}{dT}\right)_{n_o}^{0.2\ at.\%} = \left(5.313 + \frac{1.741}{\lambda} - \frac{1.615}{\lambda^2} + \frac{0.781}{\lambda^3}\right) \times 10^{-5}/^oC \ldots\ldots\ldots (5.16)$$

$$\left(\frac{dn}{dT}\right)_{n_e}^{0.6\ at.\%} = \left(2.784 + \frac{13.678}{\lambda} - \frac{11.065}{\lambda^2} + \frac{3.326}{\lambda^3}\right) \times 10^{-5}/^oC \ldots\ldots\ldots (5.17)$$

$$\left(\frac{dn}{dT}\right)_{n_o}^{0.6\ at.\%} = \left(5.616 - \frac{2.068}{\lambda} + \frac{3.412}{\lambda^2} - \frac{9.115}{\lambda^3}\right) \times 10^{-5}/^oC \ldots\ldots\ldots (5.18)$$

$$\left(\frac{dn}{dT}\right)_{n_e}^{0.8\ at.\%} = \left(13.022 - \frac{15.498}{\lambda} + \frac{14.310}{\lambda^2} - \frac{3.5011}{\lambda^3}\right) \times 10^{-5}/^oC \ldots\ldots\ldots (5.19)$$

$$\left(\frac{dn}{dT}\right)_{n_o}^{0.8\ at.\%} = \left(6.506 - \frac{2.762}{\lambda} + \frac{4.509}{\lambda^2} - \frac{1.282}{\lambda^3}\right) \times 10^{-5}/^oC \ldots\ldots\ldots (5.20)$$

$$\left(\frac{dn}{dT}\right)_{n_e}^{1.0\ at.\%} = \left(5.009 - \frac{5.232}{\lambda} + \frac{6.511}{\lambda^2} - \frac{2.126}{\lambda^3}\right) \times 10^{-5}/^oC \ldots\ldots\ldots (5.21)$$

$$\left(\frac{dn}{dT}\right)_{n_o}^{1.0\ at.\%} = \left(9.017 - \frac{8.297}{\lambda} + \frac{6.443}{\lambda^2} - \frac{1.217}{\lambda^3}\right) \times 10^{-5}/^oC \ldots\ldots\ldots (5.22)$$

$$\left(\frac{dn}{dT}\right)_{n_e}^{1.2\ at.\%} = \left(13.395 - \frac{18.408}{\lambda} + \frac{18.405}{\lambda^2} - \frac{4.882}{\lambda^3}\right) \times 10^{-5}/^{o}C \quad \ldots\ldots\ldots (5.23)$$

$$\left(\frac{dn}{dT}\right)_{n_o}^{1.2\ at.\%} = \left(8.960 - \frac{9.894}{\lambda} + \frac{9.368}{\lambda^2} - \frac{2.297}{\lambda^3}\right) \times 10^{-5}/^{o}C \quad \ldots\ldots\ldots (5.24)$$

$$\left(\frac{dn}{dT}\right)_{n_e}^{1.6\ at.\%} = \left(4.943 + \frac{4.630}{\lambda} + \frac{1.604}{\lambda^2} - \frac{5.181}{\lambda^3}\right) \times 10^{-5}/^{o}C \quad \ldots\ldots\ldots (5.25)$$

$$\left(\frac{dn}{dT}\right)_{n_o}^{1.6\ at.\%} = \left(10.049 - \frac{11.694}{\lambda} + \frac{10.895}{\lambda^2} - \frac{2.864}{\lambda^3}\right) \times 10^{-5}/^{o}C \quad \ldots\ldots\ldots (5.26)$$

Further, the effect of Nd doping on the birefringence of $GdVO_4$ crystals was estimated at different temperature and wavelength. It was found that the birefringence increases with respect to the temperature of the sample and decreases with the increase in wavelength as shown in Figure 5.14(a)-5.14(g).

It was observed that the birefringence of undoped $GdVO_4$ crystal was higher than the Nd doped $GdVO_4$ crystals. As the doping of Nd ion in $GdVO_4$ crystal was increased, the birefringence of $GdVO_4$ increases for full temperature range due to the increase of extra-ordinary refractive index with increase in Nd doping concentration.

The birefringence of Nd (1.2 and 1.6 at.%) doped $GdVO_4$ crystals crosses over the undoped $GdVO_4$ crystal at all the wavelength. The refractive index analysis therefore concludes that a lesser concentration of Nd ions exhibit lesser birefringence, which is an important laser design parameters [144].

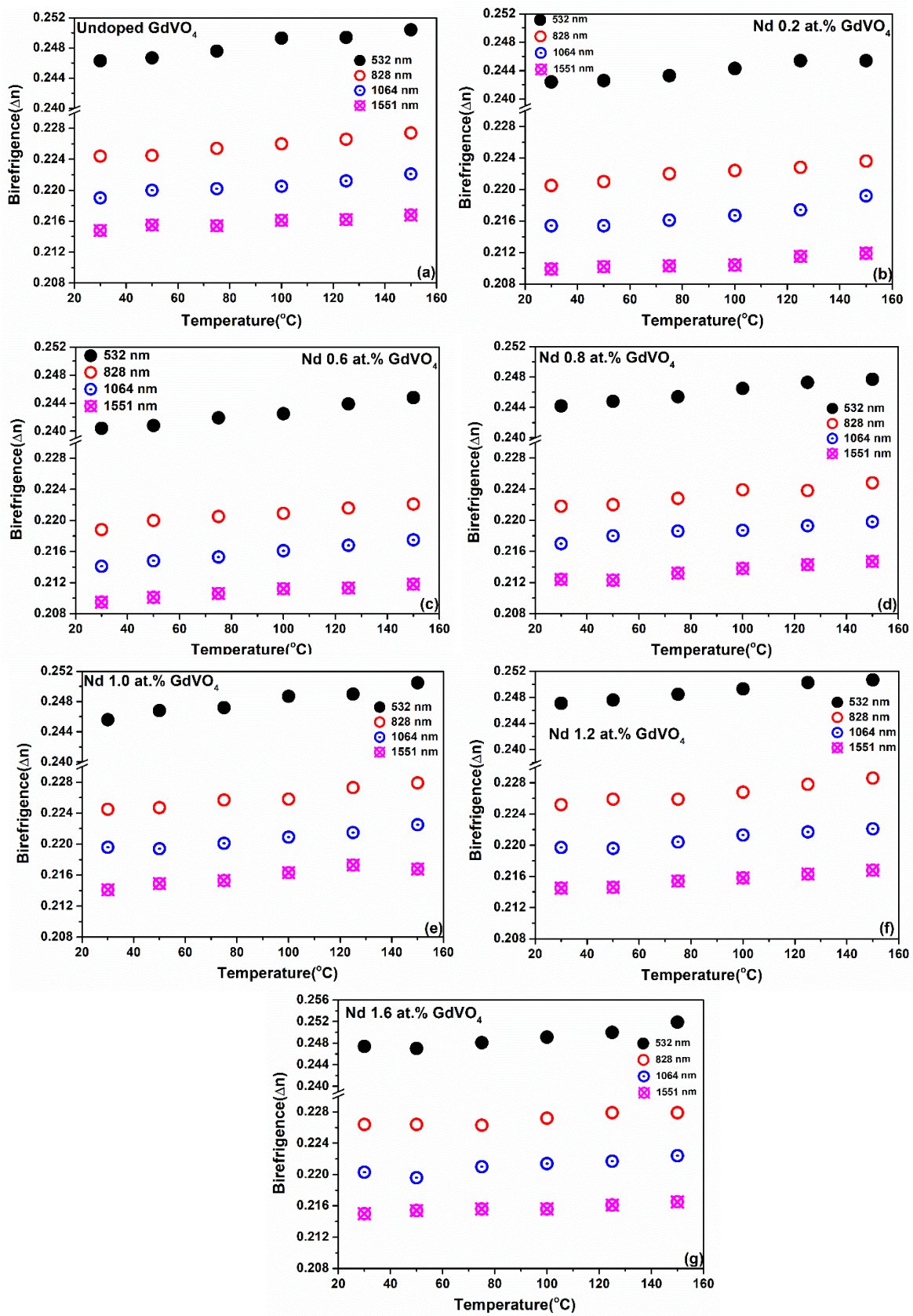

Figure 5.14 Dependence of birefringence on temperature for different Nd doping concentrations

The thermo-optic coefficient of birefringence of crystals were estimated by the linear fitting using the equation (5.27).

$$\Delta n(\lambda, T) = \Delta n(\lambda)_o + \left(\frac{d\Delta n(\lambda)}{dT}\right) T \quad \ldots\ldots\ldots\ldots\ldots \quad (5.27)$$

where $\Delta n(\lambda)_o$ is the birefringence at 0 °C.

The value of thermo-optic coefficient of birefringence is ~10^{-5}/ºC. It decreases with the increase in wavelength. Also $\Delta n(\lambda)_o$ is higher for undoped $GdVO_4$ compared to the Nd doped $GdVO_4$. The value $\Delta n(\lambda)_o$ of Nd doped $GdVO_4$ crystal increases as the doping of Nd concentration increases and it became equal at 1.0 at .% of Nd to undoped $GdVO_4$ and then crosses over to it. Also $\Delta n(\lambda)_o$ decreases as the wavelength increases [Table 5.18]. The TOC of birefringence is nearly three time lesser than that of RI of the crystal [144]. Therefore, the uniaxial $GdVO_4$ crystal has favourable birefringence properties and can be used in the field of generating polarized light, optical isolator and in the measurement of optical transmission system as a passive fiber-optic component [123].

Table 5.18 Thermo-optic coefficient of birefringence

	Undoped $GdVO_4$		**Nd 0.2 at.%**		**Nd 0.6 at.%**		**Nd 0.8 at.%**		**Nd 1.0 at.%**		**Nd 1.2 at.%**		**Nd 1.6 at.%**	
Wavelength (μm)	$\Delta n(\lambda)_o$	$d\Delta n/dT$ 10^{-5}/ºC	$\Delta n(\lambda)_o$	$d\Delta n/dT$ 10^{-5}/ºC	$\Delta n(\lambda)_o$	$d\Delta n/dT$ 10^{-5}/ºC	$\Delta n(\lambda)_o$	$d\Delta n/dT$ 10^{-5}/ºC	$\Delta n(\lambda)_o$	$d\Delta n/dT$ 10^{-5}/ºC	$\Delta n(\lambda)_o$	$d\Delta n/dT$ 10^{-5}/ºC	$\Delta n(\lambda)_o$	$d\Delta n/dT$ 10^{-5}/ºC
0.532	0.245(1)	3.(6)	0.241(4)	3.(0)	0.239(1)	3.(8)	0.243(3)	3.(1)	0.244(6)	3.(8)	0.246(1)	3.(2)	0.246(5)	3.(8)
0.828	0.223(4)	2.(3)	0.219(8)	2.(2)	0.218(4)	2.(7)	0.221(0)	2.(5)	0.223(4)	2.(9)	0.224(2)	2.(9)	0.225(7)	2.(8)
1.064	0.218(5)	2.(5)	0.214(0)	2.(5)	0.213(3)	2.(6)	0.216(7)	2.(1)	0.218(4)	2.(6)	0.218(8)	2.(3)	0.219(3)	2.(2)
1.551	0.214(5)	1.(5)	0.209(2)	1.(7)	0.209(1)	1.(8)	0.211(6)	2.(1)	0.213(5)	2.(5)	0.213(8)	2.(0)	0.214(7)	1.(9)

5.2 Laser testing of Nd doped $GdVO_4$ elements

Finally, the laser testing of the elements fabricated from grown Nd doped $GdVO_4$ crystals has been carried out for the two different orientation of crystal.

5.2.1 Orientation of crystal and fabrication of element

One of the grown crystals of Nd doped $GdVO_4$ crystals were oriented using Proto make X-rays Laue diffraction setup working in the back-reflection geometry. The crystal was mounted in a 3-axis goniometer and X-ray Laue diffraction pattern was recorded at 30kV tube voltage and 30mA current. Laue pattern of the (100) plane is shown in Figure 5.15.

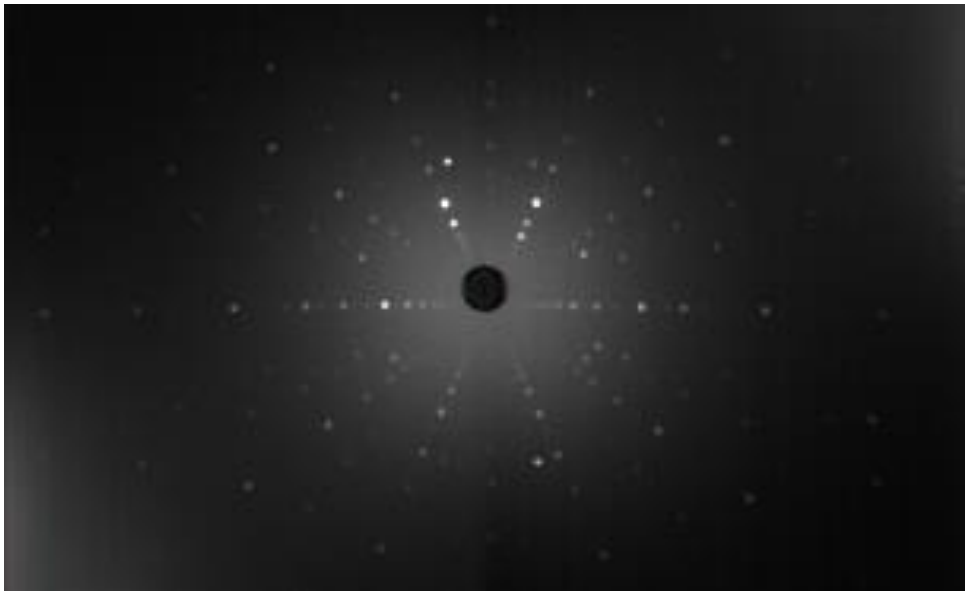

Figure 5.15 Laue pattern of the (100) plane of Nd:$GdVO_4$ crystal

The observed sharp and symmetrical diffraction spots depicts the two-fold symmetry of the (100) face of the crystal, which is slightly off-axis, but having good crystalline perfection [61,142]. The grown crystal was oriented based on the recorded Laue pattern and cut using the diamond wheel crystal cutter. [100] and [001] oriented

elements of dimension 4x4x5-6 and 3x3x5-6 mm^3 were prepared as shown in Figure 5.16. The fabricated element was lapped and polished.

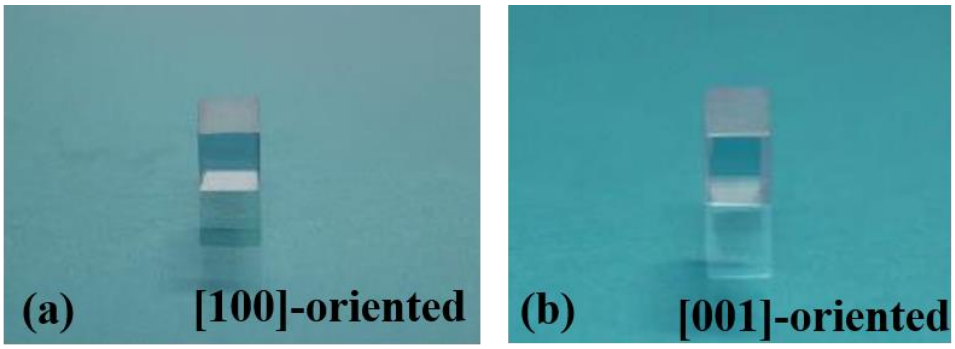

Figure 5.16 (100) and (001)-oriented laser elements of Nd:$GdVO_4$ crystals

5.2.2 Deposition of Anti-reflection coating on Nd:$GdVO_4$ elements

The anti-reflection (AR) coating on the [100]-and [001]-oriented Nd doped $GdVO_4$ laser element was done on both the entrance and exit faces of the element to minimize the cavity reflection losses and improve the lasing output power. For the deposition of AR coating ion-assisted electron beam evaporation was used. To improve the uniformity of the thickness, the element was rotated at 5rpm during deposition. SiO_2 (purity 99.99%) granules were evaporated for deposition. Chamber base pressure was kept at 2×10^{-7} mbar. Deposition temperature was maintained at 150±1ºC. Ion assisted deposition was carried out using a grid less end hall ion source (90 eV, 3.0 A, gases: 20 sccm O_2 & 10 sccm Ar) and neutralizer combination. High purity (99.995%) O_2 and Ar were injected in the ion source and hollow cathode electron source respectively. The deposition rate was maintained at 0.5±0.01 nm/s, controlled by quartz crystal monitor providing a feedback to the e-beam gun. The optical thicknesses monitoring was used for in-situ transmission measurement. Deposited AR coating on dummy substrate was

characterized using spectrophotometer (CARY5000 & CARY50) and found as per design and in-situ measured values [142].

5.2.3 Laser performance of AR coated Nd:$GdVO_4$ single crystal

Lasing characteristic of the AR coated [001]-oriented element was evaluated using plane-plane mirror geometry with 808 nm pumping. The details of the experimental setup and measurement is presented in section 2.10. For the AR coated element maximum output power ~2.7 W at 11.2 W of incident pump power with slope efficiency ~39% was obtained for 95% reflectivity of the output coupler [Figure 5.17]. Also the laser threshold was found to 3.1 W.

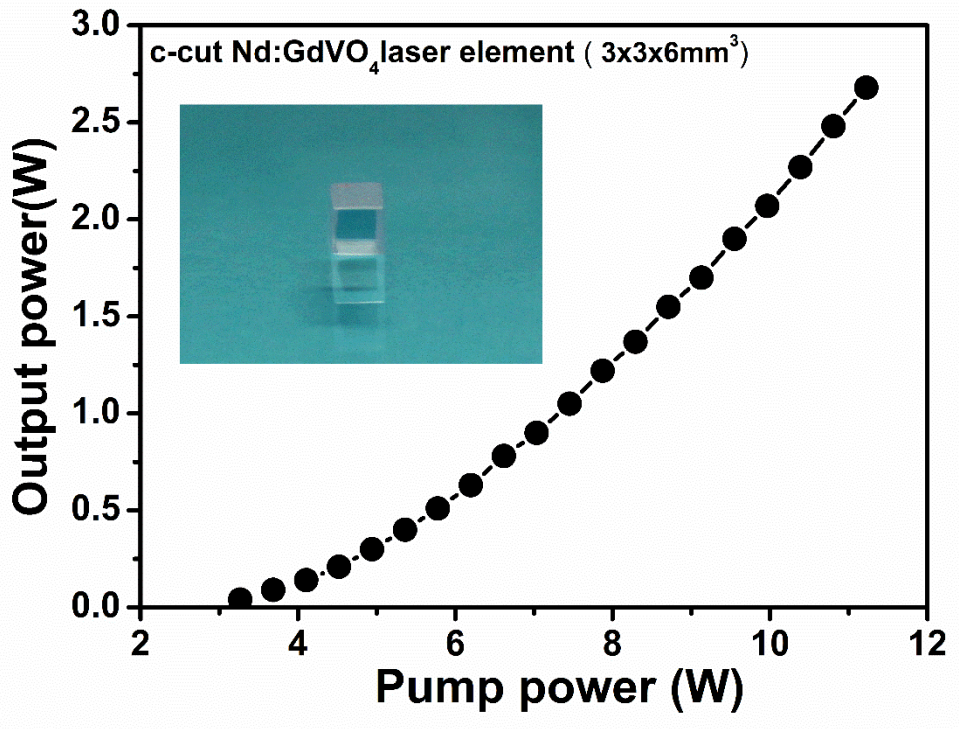

Figure 5.17 Laser performance of [001]-cut Nd:$GdVO_4$ crystal

The testing of lasing for [100]-oriented element carried out using plane-plane resonator geometry (output coupler reflectivity =89%) with 808 nm pumping. The length of the cavity was 50 mm. CW laser emission at 1064 nm was demonstrated. The laser output power of 4.57 W at 1064 nm was achieved for 11.94 W of incident pump power as shown in Figure 5.18. The slope efficiency was around 49.7%. The laser emission profile was recorded by beam profiler and it was nearly Gaussians as shown Figure 5.19 [142].

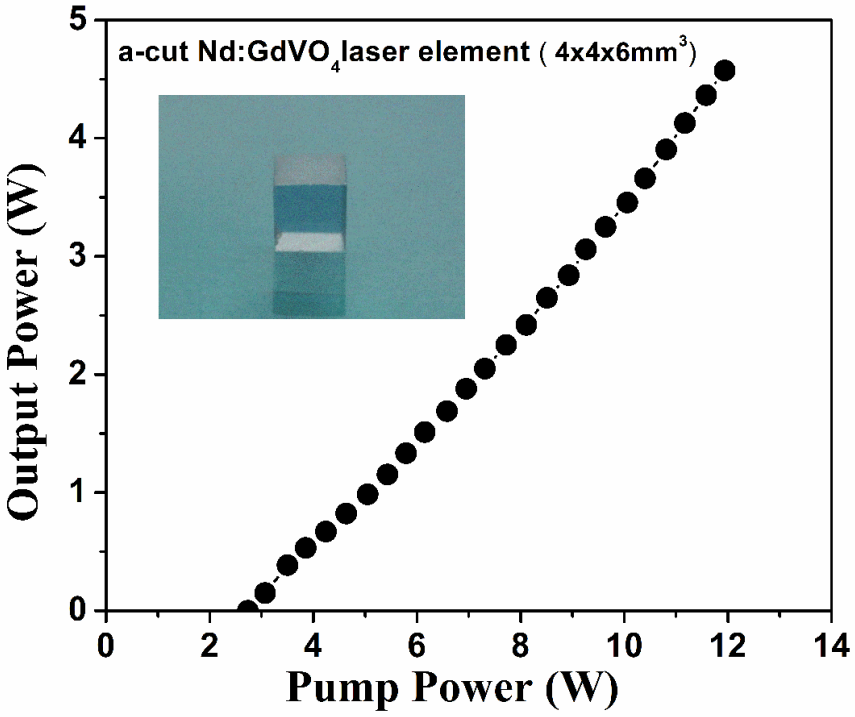

Figure 5.18 Laser performance of [100]-cut Nd:$GdVO_4$ crystal

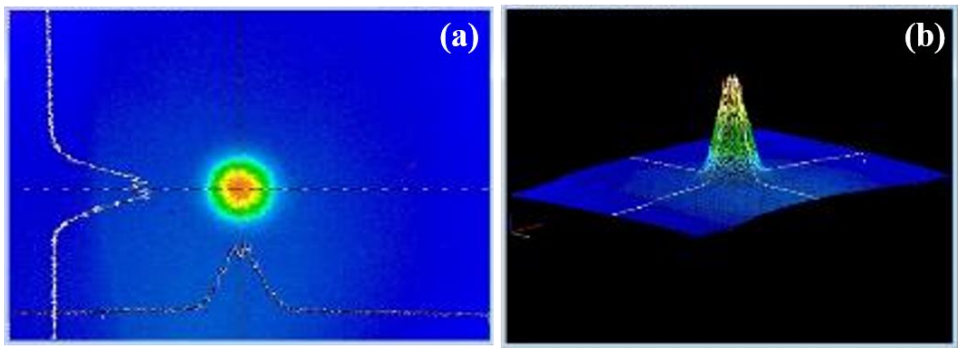

Figure 5.19 Laser beam profile of Nd:$GdVO_4$ elements

5.3 Characterization of Cr co-doped Nd:$GdVO_4$ single crystals

The single crystals with Cr (1.0, 1.2 and 1.5 at.%) co-doped Nd (0.5 at.%):$GdVO_4$ are grown by OFZ method in the varied oxygen ambience such as, 10%, 20% and 25 % O_2. The dimension of grown Cr:Nd:$GdVO_4$ single crystals are 4-5 mm in diameter and 15-30 mm in length [166].

5.3.1 Optical absorption measurement of Cr co-doped Nd:$GdVO_4$ crystals

The transmission spectra for the Cr co-doped Nd (0.5 at.%):$GdVO_4$ crystals were recorded for all the Cr co-doped samples using JASCO spectrophotometer in the two orthogonal polarization of light. The corresponding absorption coefficient were calculated using the equations (5.1) and the recorded absorption spectra are shown in the Figure 5.20-5.22. The absorption spectra are characterized by the multiple peaks at 594, 751, 808 & 879 nm due to Nd^{3+} ion & broad peak at 1100 nm (900-1300nm) and 650 nm due to Cr^{5+} ion. The broad absorption peak at 1100 nm and 650 nm due to Cr^{5+} ion are sensitive to polarization of incident light. The transitions peak of Cr at 1100 nm are allowed for π- polarization of light whereas the transitions at 650 nm are allowed for σ- polarization of light. The broad peak at 1100 nm due to Cr^{5+} ion may used for self Q-switching application in Nd:$GdVO_4$ crystals emitting at 1064 nm. The absorption spectra for π- polarization and σ- polarization are shown in the Figure 5.20-5.22 for three Cr doping concentrations at different oxygen ambience during growth respectively [166].

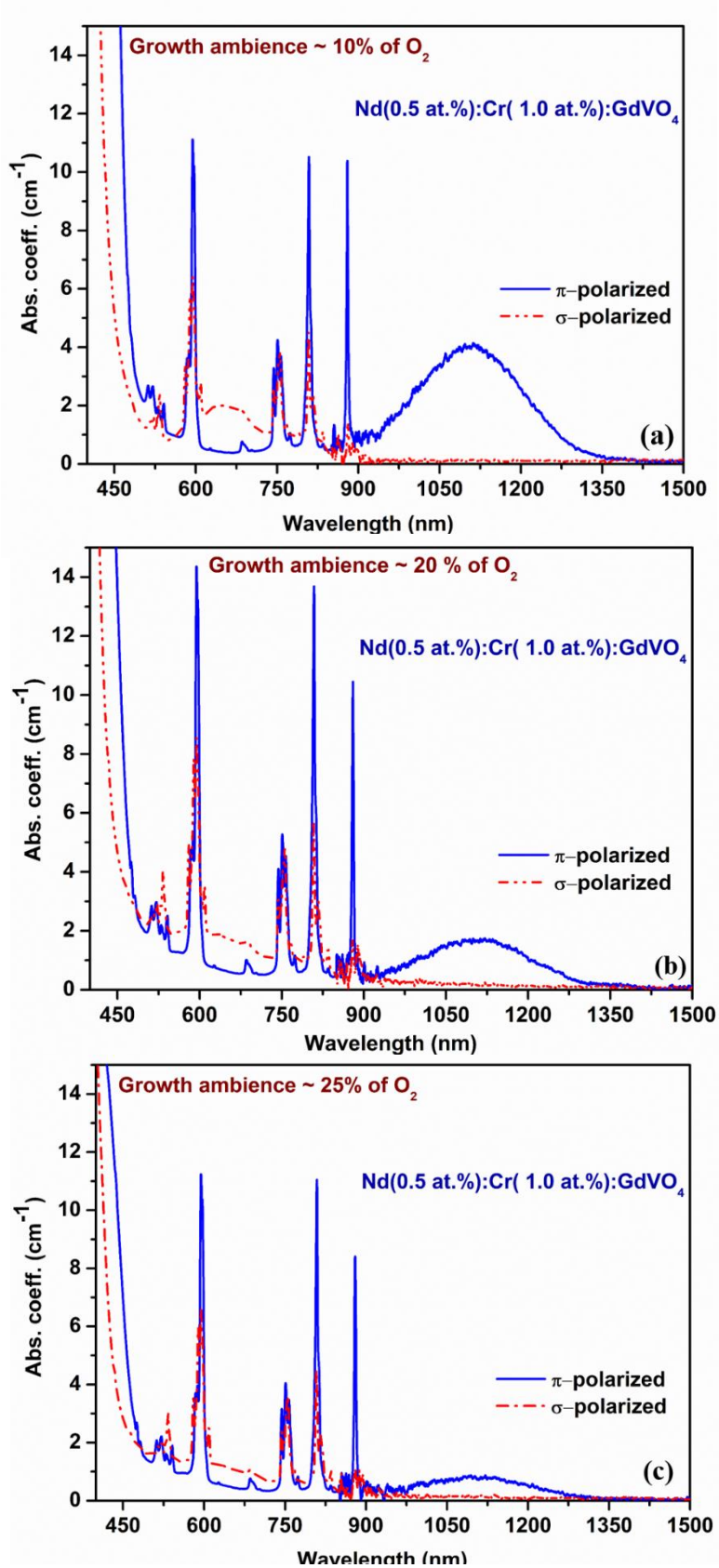

Figure 5.20 Polarized absorption spectra of Cr (1.0 at.%) co-doped Nd (0.5 at.%):$GdVO_4$ crystal at different oxygen level

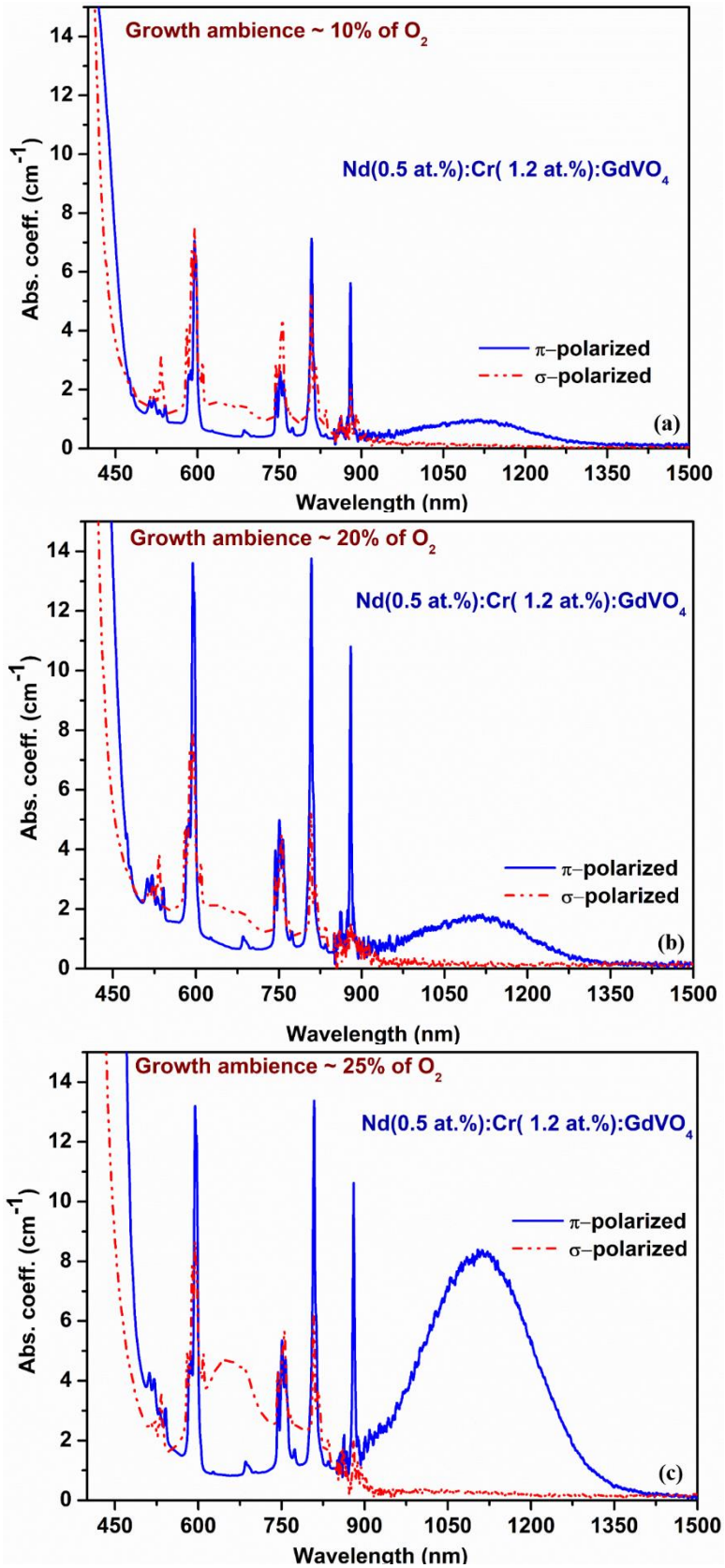

Figure 5.21 Polarized absorption spectra of Cr (1.2 at.%) co-doped Nd (0.5 at.%):$GdVO_4$ crystal at different oxygen level

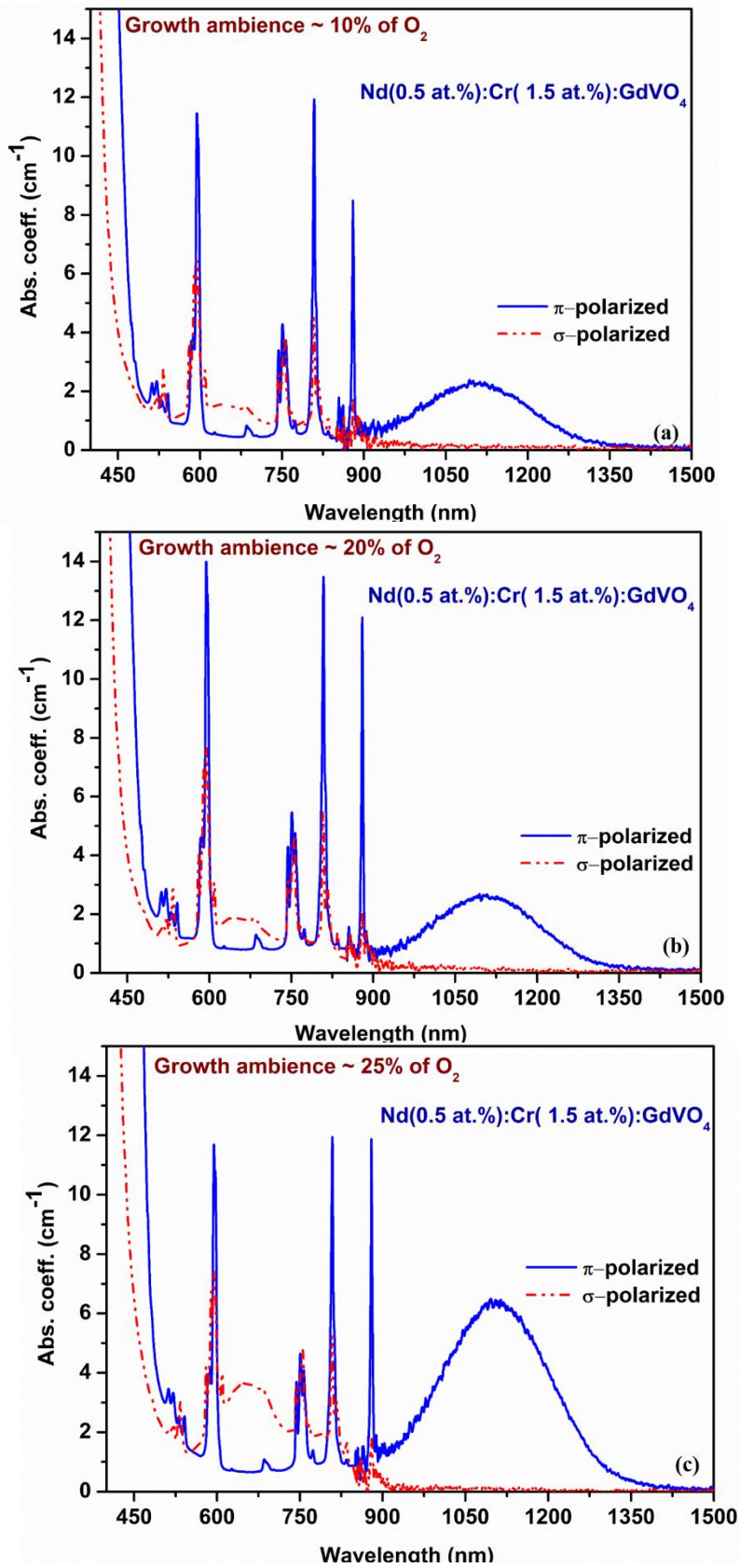

Figure 5.22 Polarized absorption spectra of Cr (1.5 at.%) co-doped Nd (0.5 at.%):$GdVO_4$ crystal at different oxygen level

In addition, the absorption spectra exhibit few interesting facts. When Cr concentration is low, i.e. around 1.0 at.% in the crystals, and the oxygen content is increased in the growth ambience, the absorption of Cr^{5+} ion at 1100 and 650 nm decreases as can be seen in Figure 5.23. On the other hand, when the Cr concentration is high, i.e. around 1.2 and 1.5 at.% in the crystals, as expected, the absorption of Cr^{5+} ion at 1100 and 650 nm increases with increase of the oxygen content in the growth ambience (for 10, 20 and 25 %). This is entirely a different feature or reverse effect to what is observed for low Cr concentration. A similar anomaly had been observed for Cr co-doped Nd:YVO_4 single crystals as well [20]. To have a comparative understanding of lower and higher doping concentration of Cr, the optical absorption spectra for the π- polarization of light are re-plotted in the range of 900 to 1500 nm in Figure 5.23[166].

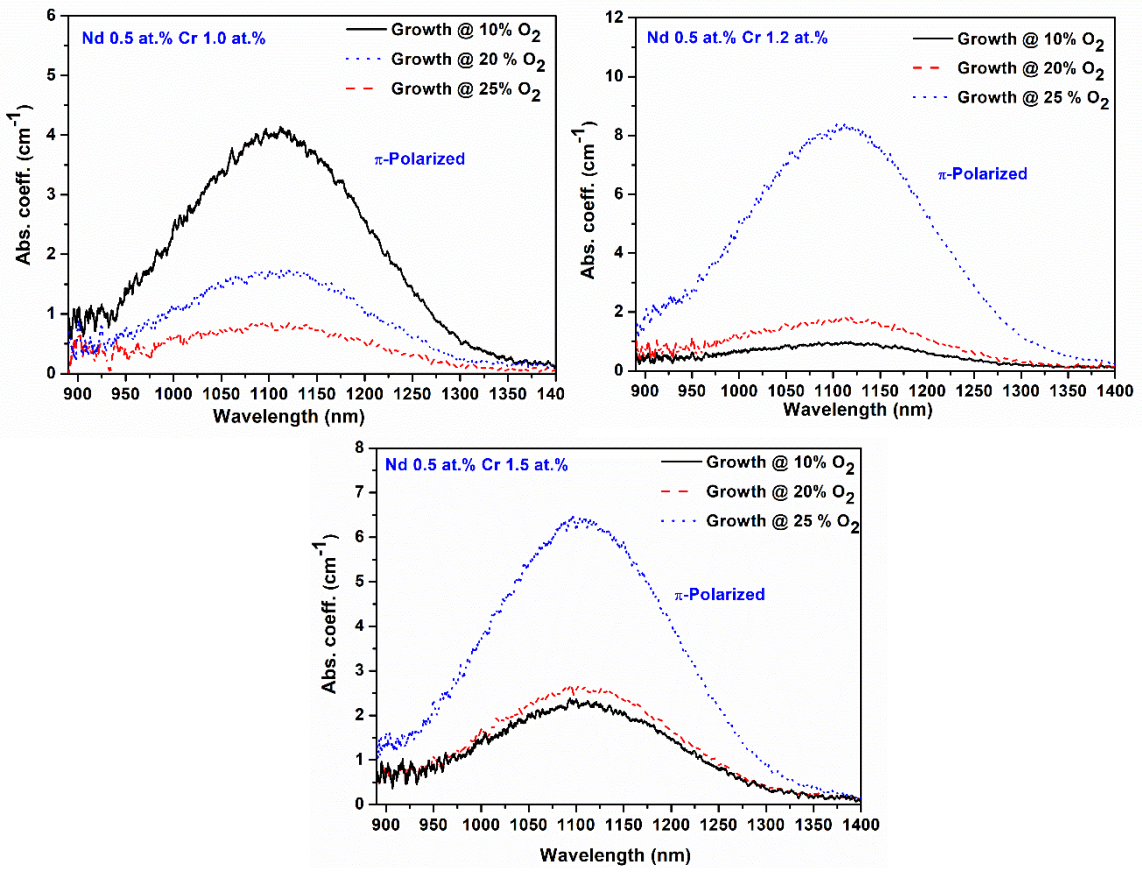

Figure 5.23 π-Polarized absorption spectra for all Cr concentration in the Nd:$GdVO_4$ grown in different ambience

The integrated area of Cr at 1100 nm for all the samples grown in different oxygen containing ambience were calculated after baseline correction and listed in Table 5.19.

Table 5.19 Integrated area of absorption centered at 1100 nm for all the samples

	Integrated area (nm cm-1)		
Oxygen in growth ambience	***10 %***	***20%***	***25%***
Cr 1.0 at.% Nd 0.5 at.% $GdVO_4$	851	346	174
Cr 1.2 at.% Nd 0.5 at.% $GdVO_4$	136	265	1681
Cr 1.5 at.% Nd 0.5 at.% $GdVO_4$	464	532	1368

5.3.2 Comparative absorption study of Cr co-doped Nd:$GdVO_4$ and Nd:YVO_4 crystals

To compare the optical absorption properties of Cr, co-doped Nd:$GdVO_4$ and Nd:YVO_4 single crystals, the optical absorption spectra of lower and higher doping of concentration of Cr for the π- polarization of light are plotted with increasing the oxygen contain in the growth ambience [Figure 5.24-5.25].

It was observed that both the crystals show the similar behavior at lower concentration as well as higher concentration of Cr. At lower concentration of Cr, both crystals show a decrease of absorption at 1100 nm with increase of oxygen concentrations as shown in the Figure 5.24 and for higher concentration of Cr, both crystals show an increase of absorption at 1100 nm with increase of oxygen concentrations as shown in the Figure 5.25.

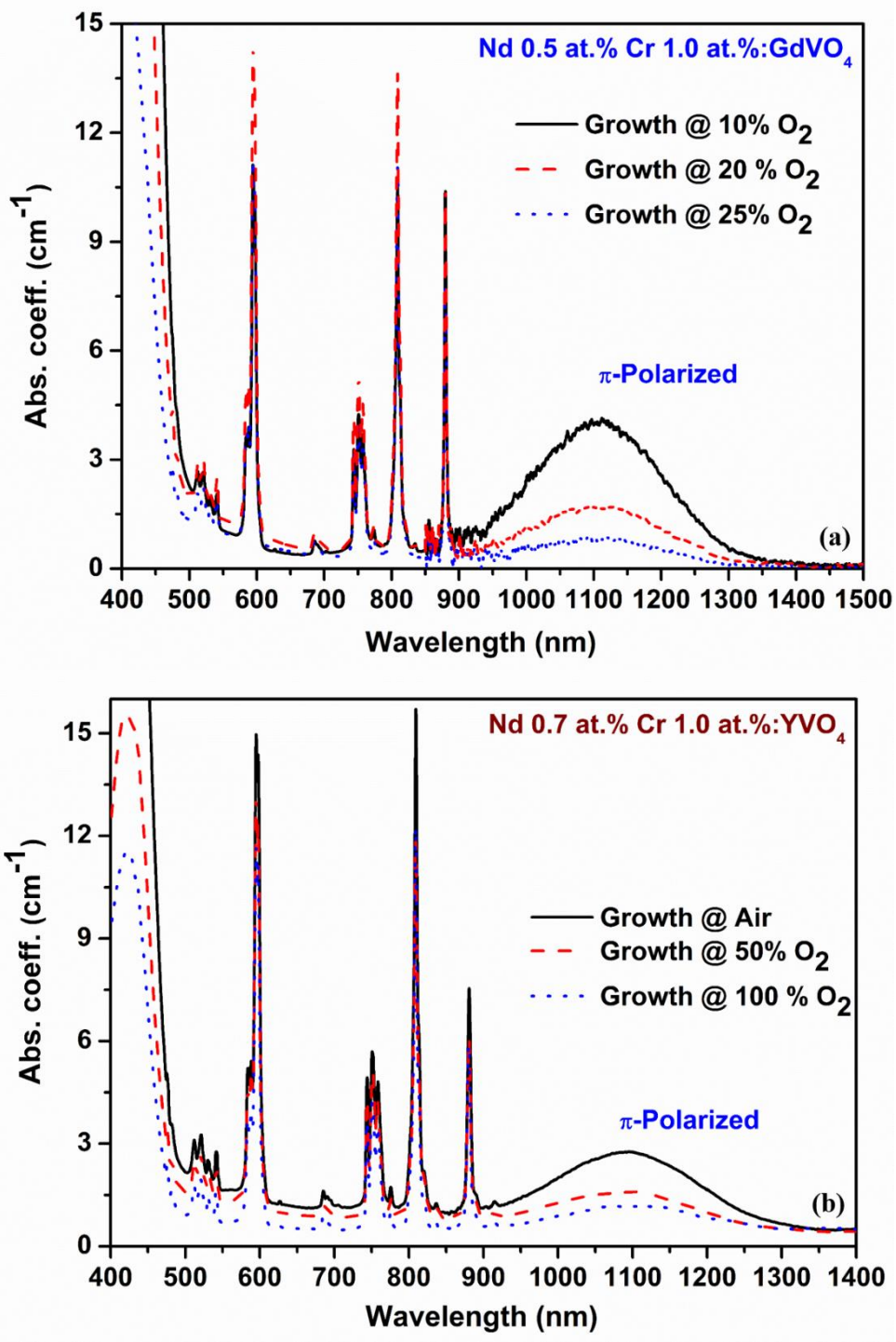

Figure 5.24 π-Polarized absorption spectra for lower Cr concentration in the Nd:$GdVO_4$ and Nd:YVO_4 crystal at different oxygen level

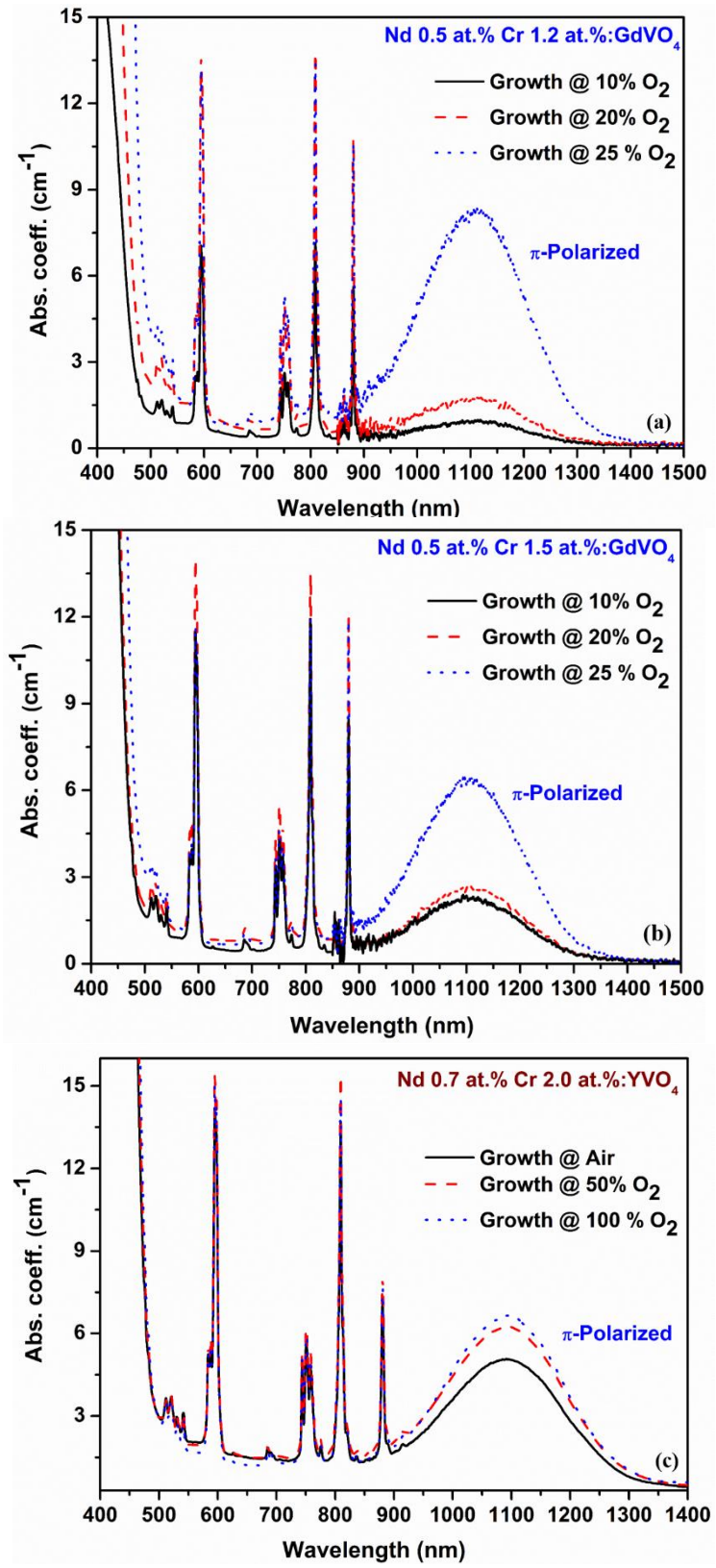

Figure 5.25 π-Polarized absorption spectra for higher Cr concentration in the Nd:$GdVO_4$ and Nd:YVO_4 crystal at different oxygen level

The comparison of absorption data around 1100 nm between the Nd:Cr:$GdVO_4$ and Nd:Cr:YVO_4 [167] crystals grown in oxygen ambience reveals a very interesting fact. For Cr doping concentration of 2.0 at.%, in Nd:YVO_4 and 1.5 at.% in Nd:$GdVO_4$ the absorption is found to increase as the oxygen content in the growth ambience increased [Figure 5.24] [167]. This is expected as reported in Ref [20]. When the crystals are grown in lower oxygen-containing ambience, a higher concentration of oxygen vacancies is generated in the grown crystal, as oxygen tends to escape from the lattice [168]. This in turn reduces the Cr^{5+} present in the lattice to Cr^{3+} to compensate the charge imbalance arising due to the presence of oxygen vacancies [20]:

$O_O \rightarrow 1/2\ O_2 + \ddot{V}_O + 2e$ (generation of oxygen vacancy),

$Cr^{5+} + 2e \rightarrow Cr^{3+}$ (reduction of Cr^{5+}).

Here O_o represents the oxygen occupancy at the oxygen site and $V_{\ddot{o}}$ is the oxygen vacancy. When the oxygen content in the ambience is increased, the number of oxygen vacancies decreases and as a result Cr retains its desired pentavalent state. As the absorption around 1100 nm is a characteristic of Cr in the pentavalent state [74,169], the crystals grown in ambience containing higher oxygen exhibits higher absorption at 1100 nm, as the crystals contain a higher concentration of Cr in the pentavalent state (Figure 5.23 (b-c)).

However, when the comparison was made with the crystals having Cr concentration of 1.0 at.% in the both crystals (Nd:$GdVO_4$ and Nd:YVO_4[167]) a reverse effect was observed. It was found that the absorption around 1100 nm decreases with the increase in the oxygen content in the growth ambience (Figure 5.23 (a)). This implies that at lower concentration of Cr, the presence of oxygen in the growth

ambience inhibits the formation of Cr^{5+}. A possible explanation for this may be as follows: YVO_4 crystal has defects like vanadium and oxygen vacancies as studied in the literature [20,170].

When the crystals with lesser concentration of doping are grown in lower oxygen-containing ambience, for crystals grown with a lower concentration of doping, the Cr gets easily incorporated in the intrinsic vanadium vacancy (V_{Cr}), as there would be sufficient vacant sites promoted by the growth condition. However, as the oxygen content in the ambience is increased, the concentration of oxygen vacancy in the crystal decreases, which in turn decreases the vanadium vacancy for overall charge balancing. Thus, the concentration of Cr incorporated in the lattice decreases in the absence of sufficient vanadium vacancy. The results have been published in Applied physics A [167].

5.3.3 Optical emission characteristics of Cr co-doped Nd:$GdVO_4$ crystals

For investigating the effect of Cr (1.0, 1.2 and 1.5 at.%) doping concentration on the emission properties of Nd (0.5 at.%) $GdVO_4$ the photo-luminescence (PL) spectra of Cr doped Nd:$GdVO_4$ samples were measured in the range of 900 to1500 nm with an excitation at 808 nm. It was observed that the intensity of photo-luminescence at 1064 nm for 1.0 at.% Cr co-doped Nd:$GdVO_4$ crystals is minimum for the crystal grown in 10% of oxygen ambience and PL intensity increases with increasing the oxygen contain in the growth ambience (Figure 5.26).

This is inline with the absorption data, where the absorption of Cr^{5+} at 1064 nm is maximum for the same oxygen level (10%) for 1.0 at.% Cr doping concentration, and the absorption decreased with the increase of oxygen level. Hence, the generated PL is

absorbed more compared to the crystals grown in higher oxygen containing ambience (20 and 25%)[166].

Similarly, the intensity of PL at 1064 nm is minimum for the crystal grown in 25% of oxygen ambience for 1.2 and 1.5 at.% of Cr doping concentrations in the Nd:$GdVO_4$ crystals and the PL intensity further decreases with the increase of the oxygen in the growth ambience (Figure 5.27). This is because the absorption of Cr^{5+} at 1064 nm was found to be maximum for the same oxygen level (25%) and these doping concentrations, thus more PL is absorbed [166].

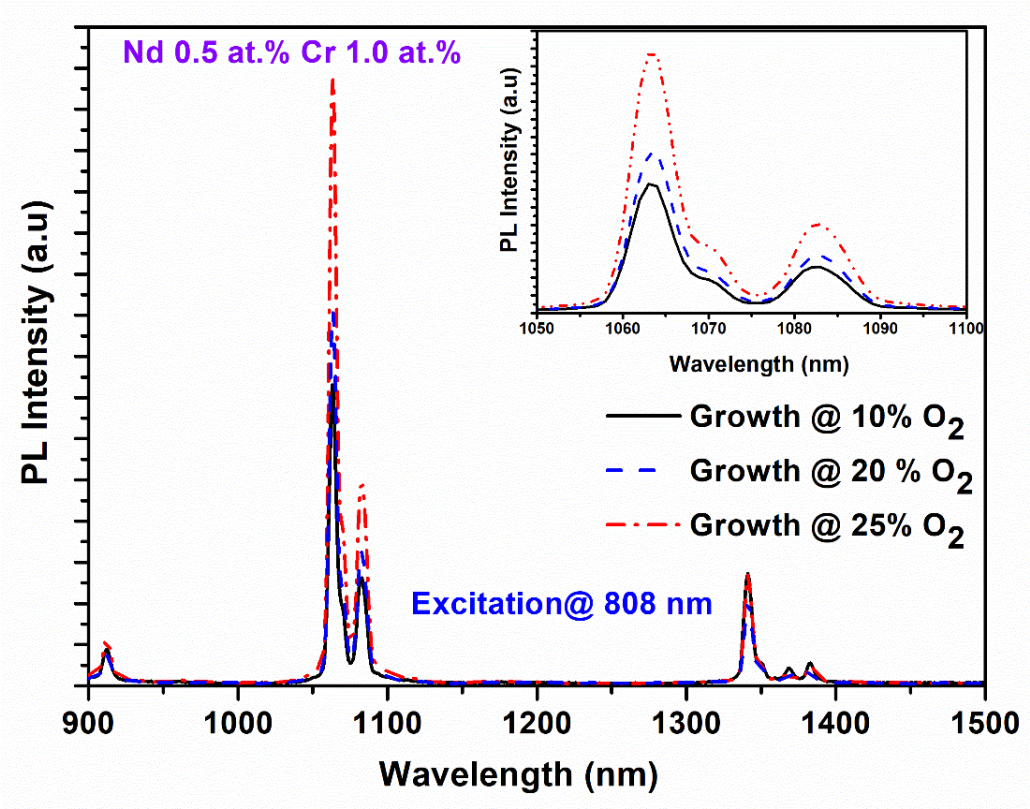

Figure 5.26 Photo-luminescence spectra of Cr (1.0 at.%) co-doped Nd:$GdVO_4$ crystals

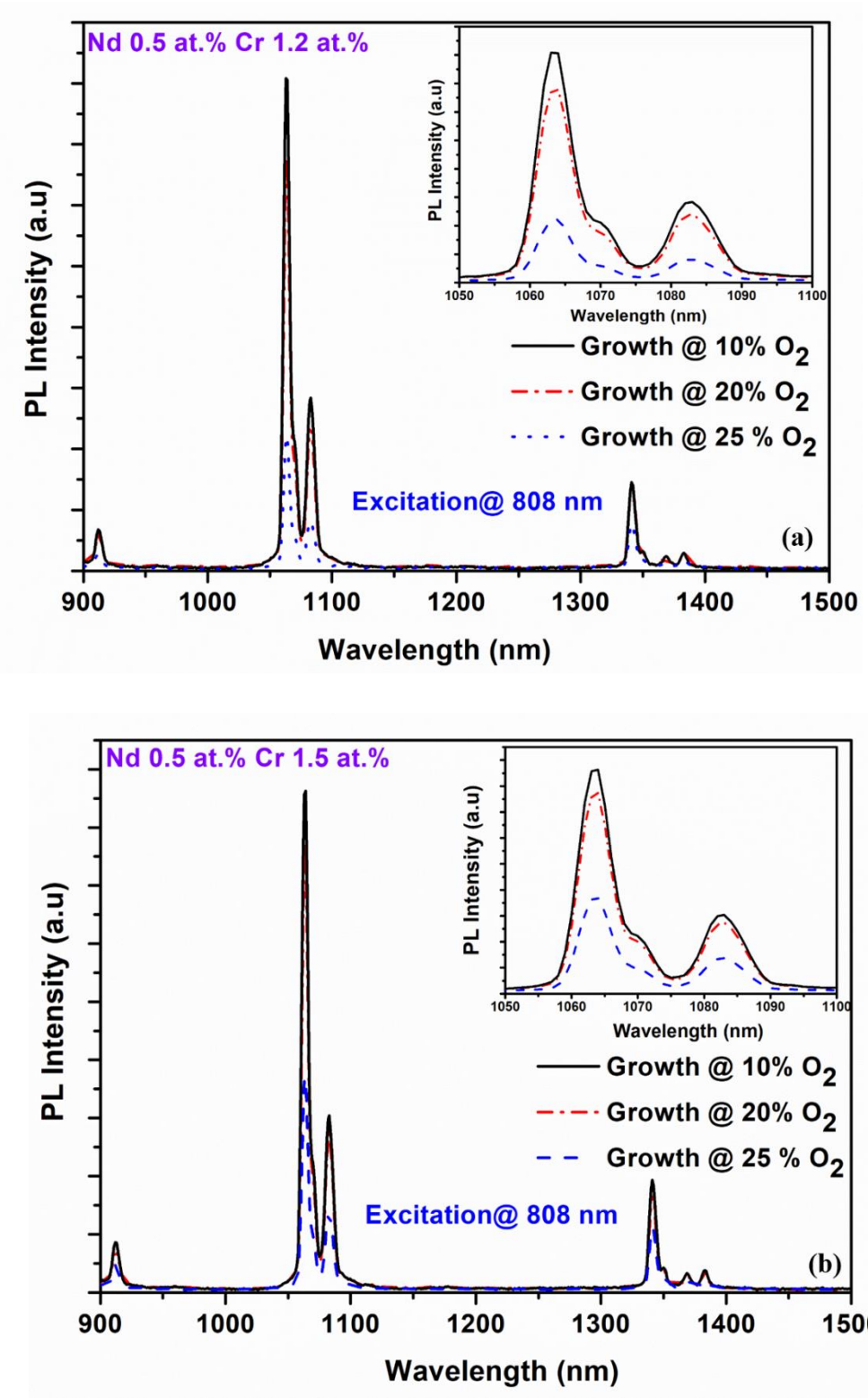

Figure 5.27 Photo-luminescence spectra of Cr (1.2 and 1.5 at.%) co-doped Nd:$GdVO_4$ crystals

5.3.4 Saturable absorption measurement of Cr co-doped Nd:$GdVO_4$ crystal

The saturable absorption characteristics of Cr co-doped Nd:$GdVO_4$ crystal was measured by using Z-scan technique with continuous wave Nd:YVO_4 laser operating at 1064 nm. The a-cut plate of thickness ~1mm of Cr co-doped Nd:$GdVO_4$ crystal was scanned through focused (50 mm) Gaussian beam. An intensity dependent transmittance of the sample was recorded. An increase of transmission from 0.57 to 0.66 (9%) was observed for an incident power of 200 mW as shown in Figure 5.28. The increase in intensity dependent transmittance is attributed to saturation of absorption of the Cr^{5+} ions causing bleaching of the 1064 nm absorption. This decrease of intensity dependent transmission in absorption feature can be utilized for passive self-Q-switching.

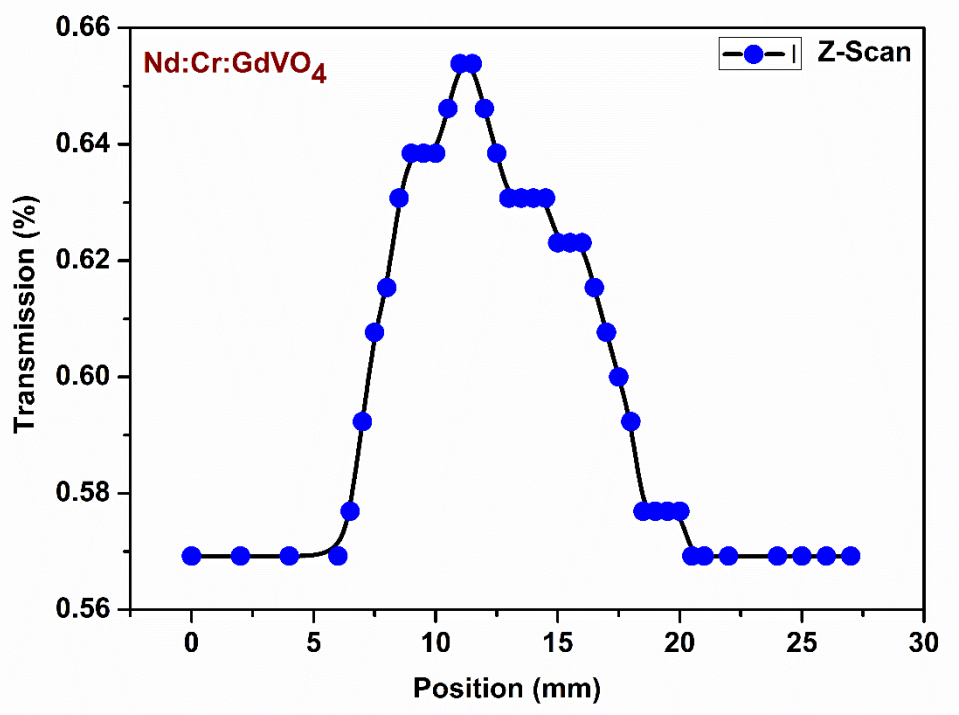

Figure 5.28 Z-scan of Nd:Cr:$GdVO_4$ crystal for saturation absorption

Chapter-6 Optical and Structural Investigations of Nd Doped $LuVO_4$ Crystals

6.1 Structural characterization of Nd doped $LuVO_4$ crystals

Single crystals of Nd doped $LuVO_4$ with 0.25 and 0.5 at.% of Nd concentrations were grown by optical floating zone technique. The dimension of the grown crystals was around 10-25 mm in the length and 4-6 mm in the diameter. Sample plates of ~1mm thickness from grown Nd doped $LuVO_4$ crystals were used for characterization of the crystals.

6.1.1 Rocking curves measurement

The rocking curve measurements of Nd doped $LuVO_4$ crystals were carried out to check the crystalline quality. The measurements were done on [100]-oriented samples for the (200) diffraction peak at the ADXRD beam-line (BL-12) of the Indus-2 synchrotron facility [112]. The X-ray photons of energy 14.43 keV (wavelength 0.857Å) were used for the measurement. Figure 6.1 shows the rocking curve of 0.5 at. % Nd doped $LuVO_4$ crystal.

The FWHM of the diffraction peak was evaluated by Lorenz fitting. The value of the FWHM for the samples of different doping of Nd are ~130 arc-sec and signifies the good crystalline quality of the grown crystals. A single and symmetrical diffraction peak corresponding to (200) planes of $LuVO_4$ crystal confirms the orientation of the sample plate of the grown crystals and also, shows that the grown single crystals are free from low-angle grain boundary and internal sub-grain structures.

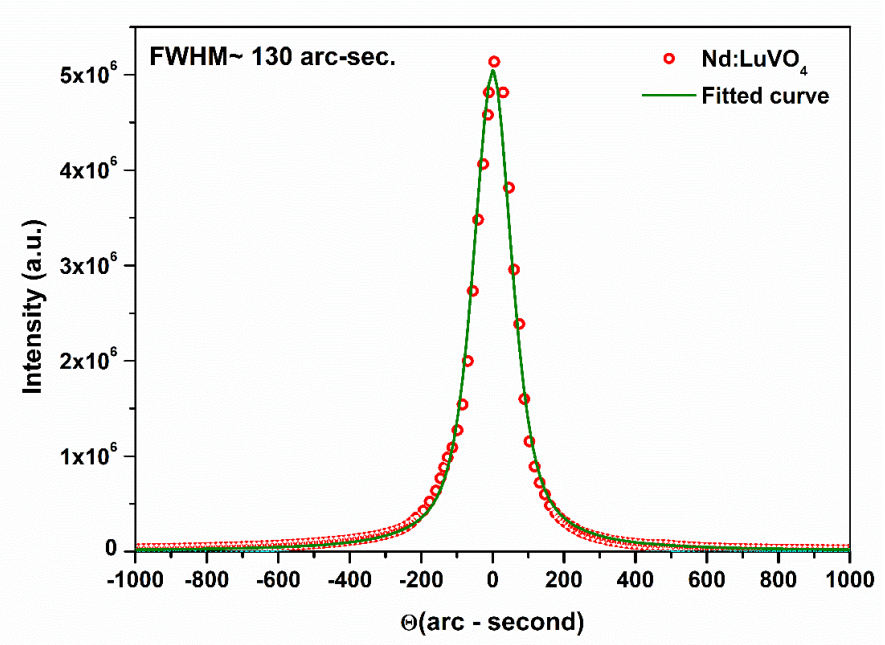

Figure 6.1 Rocking curve of (200)-peak of Nd:$LuVO_4$ crystal

6.1.2 Effect of Nd doping on lattice parameters of $LuVO_4$ crystals

For investigating the effect of Nd doping on the lattice parameters of $LuVO_4$ crystals. The powder XRD data was recorded using Cu-Kα in the range 20-70° [Figure 6.2]. The lattice parameters of Nd doped $LuVO_4$ samples were evaluated using XRD pattern peaks in the range of 20-70° and the XRD pattern profile was fitted by Le Bail fitting to minimize the systematic error.

It was found that the (200) diffraction peaks slightly shift systematically towards the lower angle as the Nd concentration varies from 0.25 to 0.5 at.% in the crystal signifying a small expansion of the lattice volume [Figure 6.2]. The observed slightly expansion of lattice on Nd doping in $LuVO_4$ is due to the larger ionic size of Nd^{3+} ion (112.3pm) compared to the Lu^{3+} ion (100.1pm) which it replaces. The change in the lattice parameters and volume is listed in Table 6.1.

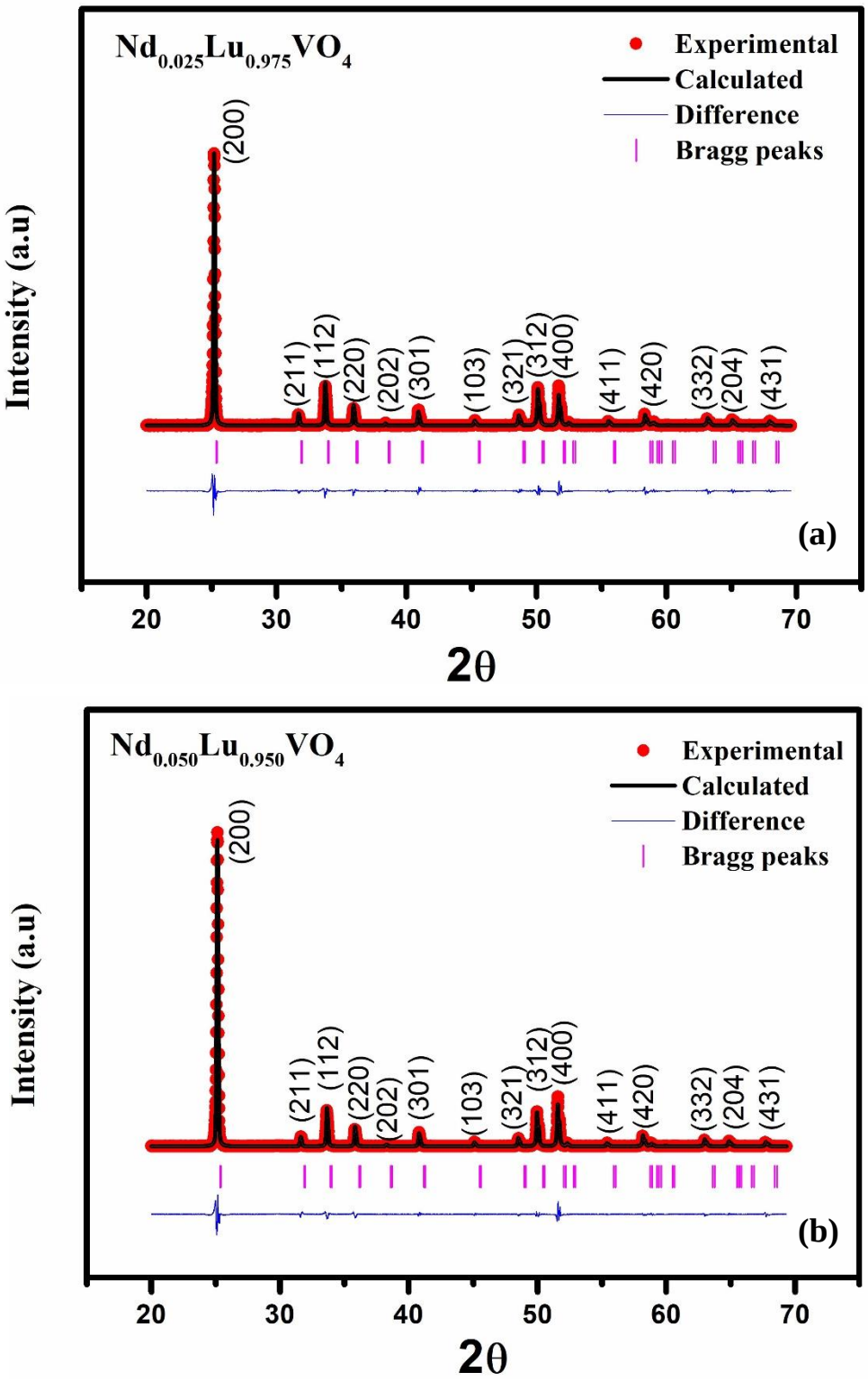

Figure 6.2 Powder X-ray diffraction pattern of Nd doped $LuVO_4$ single crystals

Table 6.1 Lattice parameters of Nd:$LuVO_4$ single crystals

Lattice parameters	Nd 0.25 at.%	Nd 0.50 at.%
a(Å) and b (Å)	7.021(7)	7.023(1)
c(Å)	6.229(1)	6.232(4)
Volume ($Å^3$)	307.12(1)	307.40(6)

6.2 Effect of Nd doping on the optical properties of $LuVO_4$ crystals

6.2.1 Effect of Nd doping on the absorption characteristics

The optical transmission spectra were recorded using spectrophotometer (JASCO V670) for two orthogonal polarized incident light at room temperature. For the investigation of the optical absorption characteristics of the grown crystals, the [100]-orientated polished plate of thickness ~1.0 mm was used for the measurement. The absorption spectra were measured in the wavelength range 300 to 1000 nm for both polarization of light [Figure 6.3-6.4]. Further, the coefficient of absorption of Nd ion doped in the $LuVO_4$ host was evaluated from the recorded transmission spectra using the relation [126]:

$$T \approx (1 - R)^2 \, exp(-\alpha d) \qquad \ldots\ldots\ldots\ldots\ldots\ldots\ldots\ldots\ldots\ldots\ldots\ldots\ldots\ldots\ldots\ldots (6.1)$$

where, R, T, d and α stand for reflectance, transmission, thickness of the samples and absorption coefficient respectively. The reflectivity $R = [n(\lambda)-1]^2/[n(\lambda)+1]^2$ was calculated from the refractive index $n(\lambda)$ of Nd doped $LuVO_4$ single crystals which was measured using the prism coupling technique.

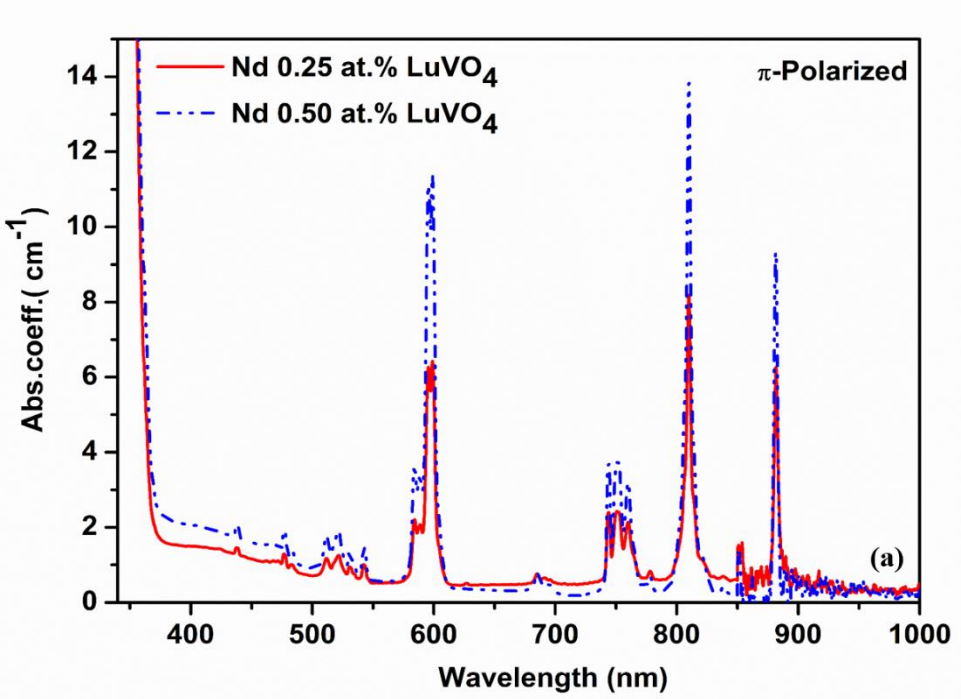

Figure 6.3 Absorption spectra of Nd doped $LuVO_4$ single crystals π- polarized light

The absorption spectra for both the polarization are shown in Figure 6.3 and 6.4. Several absorption peaks of Nd ion were observed in the polarized absorption spectra. The observed absorption peaks are due to forced electric dipole (ED) intra-band (4f-4f) transitions of Nd ion [2]. Due to anisotropic nature of the $LuVO_4$ crystal, the absorption spectra was found to be polarization sensitive. In the rare earth ions, generally the f-f transitions are forbidden due to the same parity of the initial and final states as per Laporte transition rule and it violates the conservation of parity for any optical transitions. The forbidden f-f transitions of Nd ions due to the parity conservation are allowed in the presence of D_{2d} non-centrosymmetric crystal field of $LuVO_4$ host. The

observed sharp and distinct transitions are due to the screening effect of outer shells electrons ($5s^2$ and $5p^6$) [135].

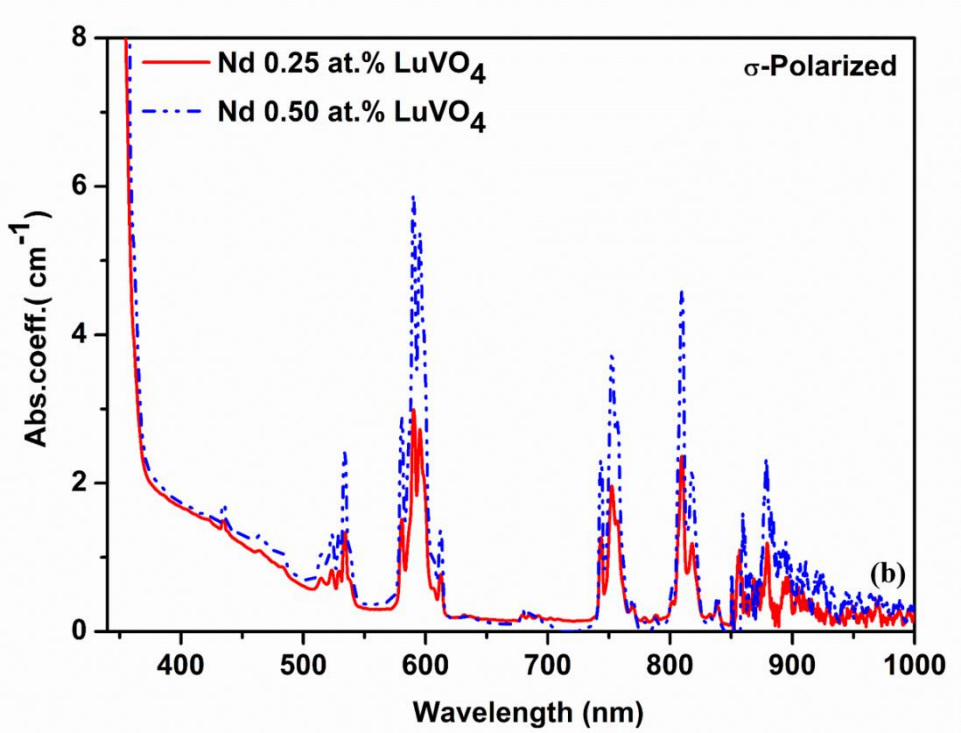

Figure 6.4 Absorption spectra of Nd doped $LuVO_4$ single crystals σ- polarized light

In the polarized absorption spectra of both Nd doped samples, the absorption peak for π-polarization is higher than that for the σ-polarization as shown in the Fig. 6.3. The absorption coefficient for Nd 0.25 and 0.5 at.% corresponding to the 810 nm are ~8.3 and 14 cm^{-1} for π-polarization whereas for σ-polarization are ~ 2.4 and 4.6 cm^{-1} respectively. The strong π-polarized (E||c) absorption band of Nd:$LuVO_4$ laser gain medium for π-polarized (E||c) light is centered at 810 nm and this 810 nm absorption band of Nd can be used for efficient pumping of Nd:$LuVO_4$ laser gain medium by using a diode laser operating at ~ 810 nm wavelength.

Further, the band gap of Nd doped $LuVO_4$ crystals were estimated for both the samples and polarization of light. There is no significant change in the band gap of $LuVO_4$ crystals observed with Nd doping concentration upto 0.5 at.%. The value of

band gap depends on the polarization of incident of light and was found to be ~ 3.50 eV for π-polarized and 3.55eV for σ-polarized.

6.2.2 Effect of Nd doping on the emission characteristics

The photo-luminescence (PL) spectra of the sample plates of Nd doped $LuVO_4$ crystals were measured at two-excitation wavelengths 810 and 880 nm to investigate the effect of Nd doping concentration on the emission properties of $LuVO_4$ single crystals. The photo-luminescence (PL) spectra were recorded in the range of 900 to 1450 nm [Figure 6.5-6.6]. It depicts emission peaks at, 916, 1065, 1087 and at 1342 nm for both excitations. Among these, the PL intensity at 1065 nm is the highest for the both the samples for the both excitation wavelengths.

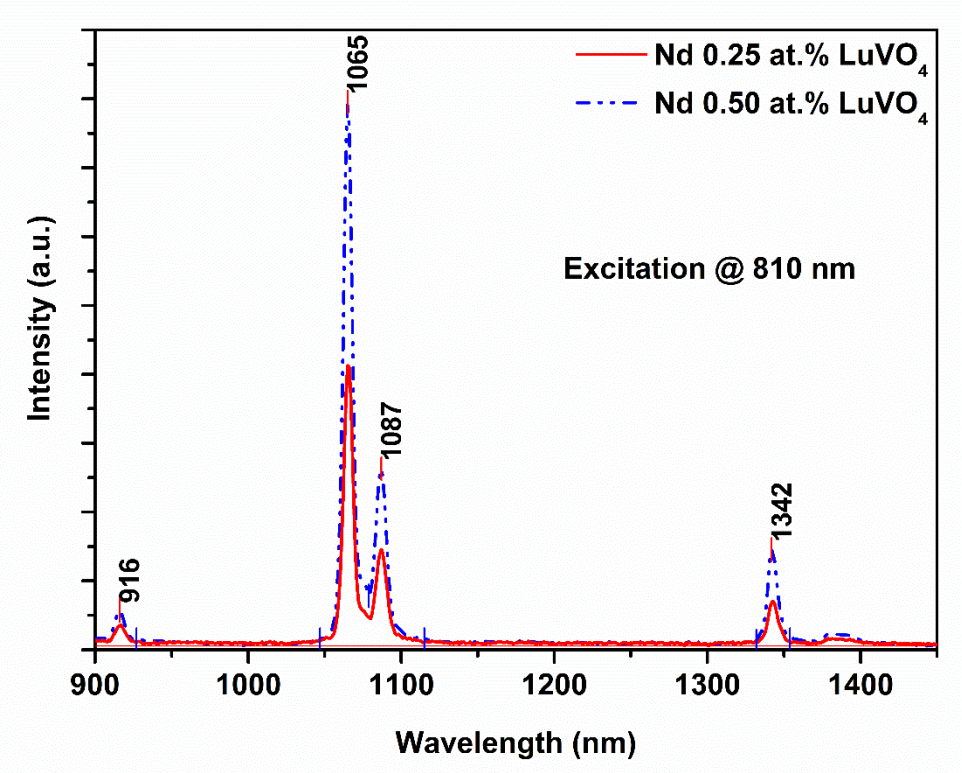

Figure 6.5 PL spectra of Nd doped $LuVO_4$ single crystals at excitation 810 nm

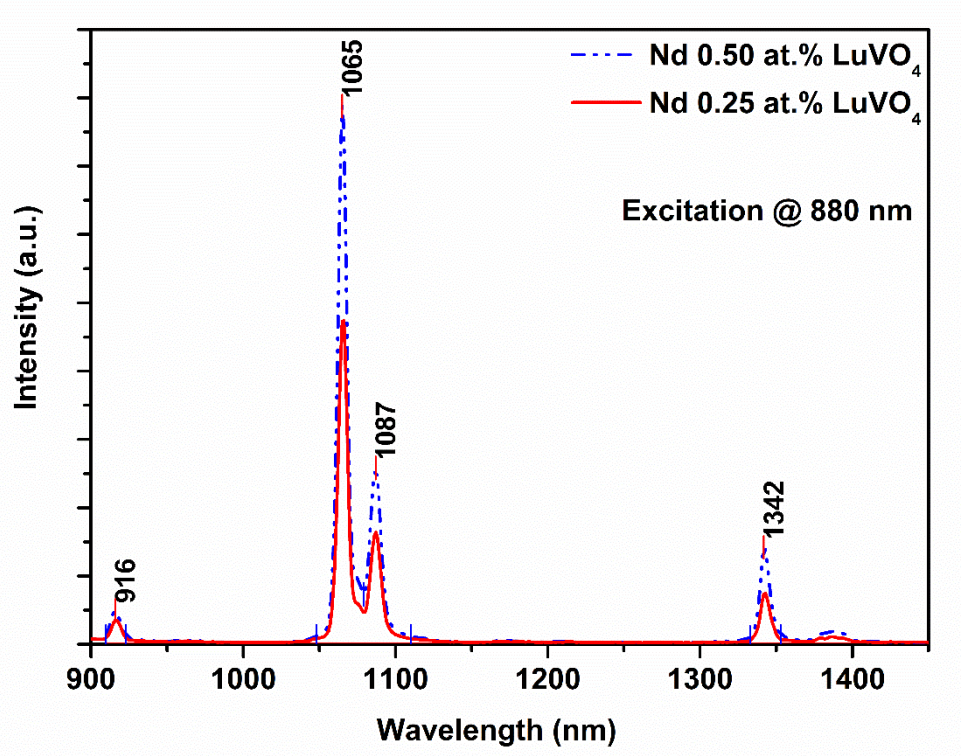

Figure 6.6 PL spectra of Nd doped $LuVO_4$ single crystals at excitation 880 nm

6.2.3 The fluorescence lifetime measurement

For measuring the fluorescence life-time of Nd ion the fluorescence lifetime measurement of Nd doped $LuVO_4$ single crystals samples were carried out with excitation at 810 nm by Ti:Sapphire femto-second (35 fs pulse width) laser and the corresponding fluorescence decay profile of Nd doped $LuVO_4$ single crystals was recorded using IR detector. The fluorescence decay of 0.5 at.% of Nd doped sample is shown in the Figure 6.7. The measured fluorescence decay plot is combination of rising part as well as decaying part. Therefore, the exponential function containing the rising as well as decaying part was fitted to the measured fluorescence decay profile. The decaying part of fluorescence yield results the fluorescence life-time of Nd ion in the $LuVO_4$ sample and it was found to be~ 95±0.02 μs for doping concentration 0.5 at.%

of Nd. The measured fluorescence life-time is in well agreement with the reported value [5].

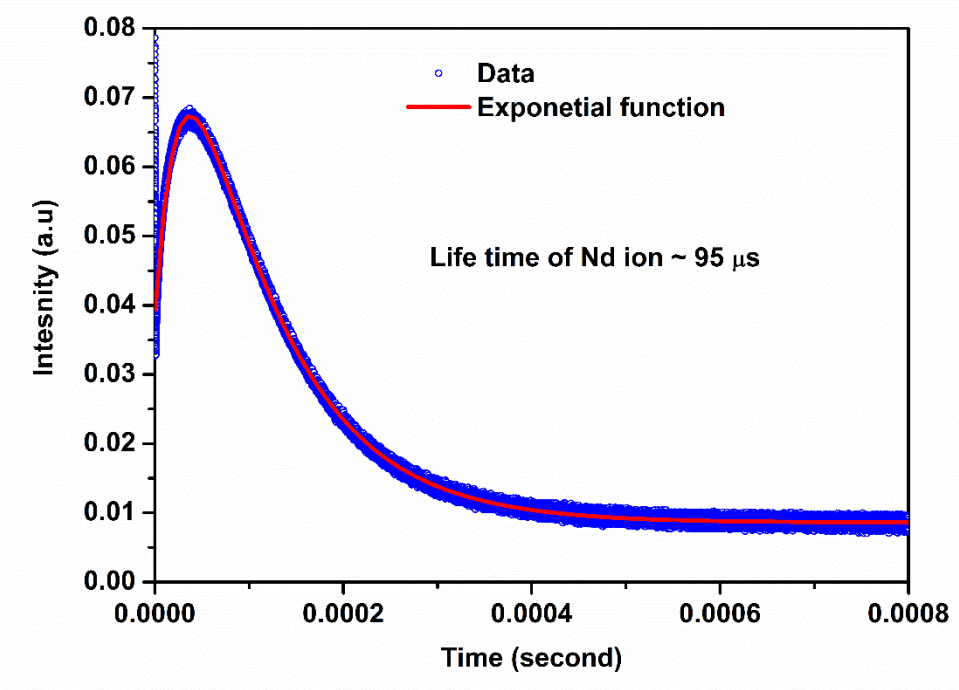

Figure 6.7 Emission decay profile of Nd doped $LuVO_4$ single crystals

6.2.4 Testing of laser performance of Nd doped $LuVO_4$ crystals

For preliminary testing of laser performance of Nd doped $LuVO_4$ crystals, [100]-oriented element was fabricated and polished. The testing of lasing was carried out using plane-plane resonator geometry (output coupler reflectivity =90%) with pumping wavelength around 808 nm. The design cavity length was 45 mm. CW laser emission at 1066 nm was obtained. Laser output power was ~360 mW with absorbed pump power of 13.6 W as shown in Figure 6.8. The slope efficiency of laser crystal was around 3.2 %.

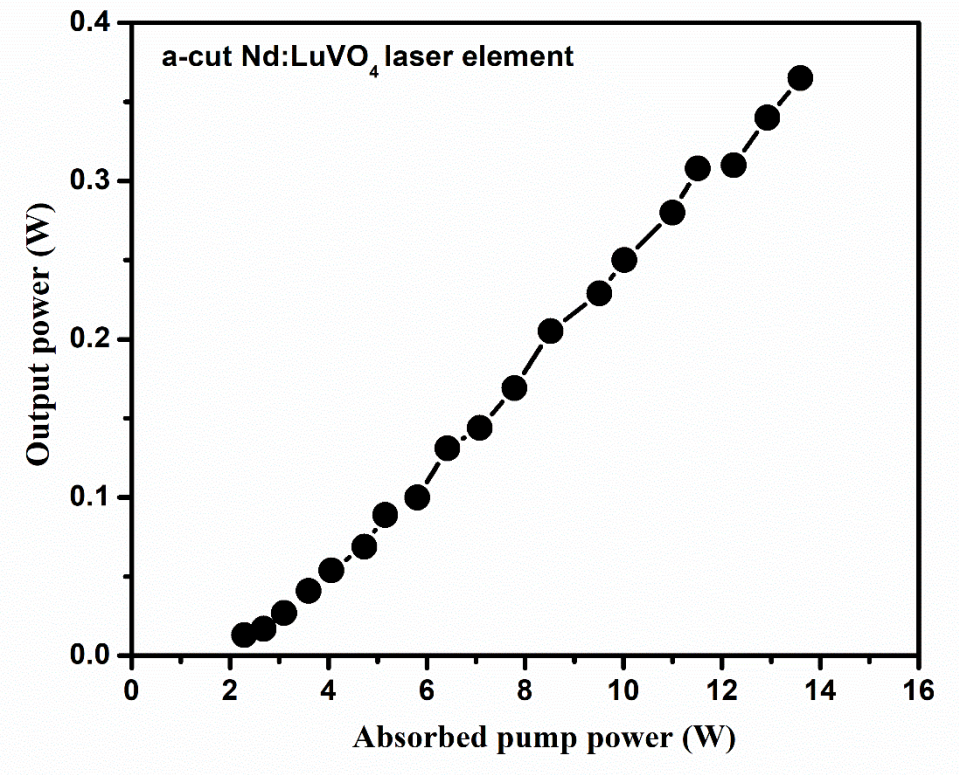

Figure 6.8 Testing of lasing of Nd doped $LuVO_4$ crystals

Chapter-7 General Conclusions and Scope for Future Work

7.1 Summary of works on doped and co-doped YVO_4 crystals

7.1.1 Yb doped YVO_4 crystals

Single crystals of Yb doped YVO_4 with dopant concentration in the range of 0.8 to 15 at.% with good crystalline quality (FWHM ~ 43-55 arc-sec of rocking curve) have been grown by optical floating zone technique. The lattice parameters of YVO_4 remain unaffected up to 2.94 at.% doping of Yb but a contraction in the lattice volume was observed at higher concentrations. Further, the absorption spectra exhibited significant polarization dependence. It was found that for σ-(E⊥c) polarized light, the absorption band at ~ 972 nm and for π- (E||c) polarized light absorption at ~985 nm dominates. The absorption cross-section at 952, 972 and 985 nm was found to be maximum at 2.94 at.% of doping for both the polarization signifying quenching at higher concentration (beyond 2.94 at.%). The emission spectra of Yb doped crystals were characterized by two overlapped broad emissions centered at 985 and 1010 nm. It is interesting to note that the PL intensity at 1010 nm is stronger for excitation at 952 and 972 nm in comparison to that for 985 nm.

Further, the refractive index (RI) measurements were also measured at four wavelengths as a function of temperature for different Yb concentration (1.5, 3.0, 8.0 and 15.0 at.%) doped YVO_4. The measurements show that as the doping concentration of Yb is increased, the refractive index varies marginally for extra-ordinary RI (n_e) whereas there is a significant change in the value of ordinary RI (n_o). The thermo-optic coefficient (dn/dT) was found to be positive with a value ~ 10^{-5}/°C which is one order

higher than that for the undoped YVO_4 crystal. The thermo-optic coefficient is higher for n_e compared to that of n_o. Also, a set of relations describing the wavelength dependence of the thermo-optic coefficient were established (empirically) which are useful for calculating the thermo-optic coefficient at any temperature in the range 30-150°C and at any wavelength in the range 532-1551 nm.

7.1.2 Er co-doped Yb:YVO_4 crystals

Single crystals of Er (0.7 at.%):YVO_4 co-doped with varied concentrations of Yb (1.5, 3.0, 8.0 and 12.0 at.%) have been grown by optical floating zone technique. The absorption spectra of the grown crystal are characterized by the prominent absorption at 985 nm due to Yb ion and multiple absorptions due to Er ions. The overall characteristic absorption for π-polarization (E||c) is stronger than that for σ-polarization ($E\perp c$) due to alignment of dipole moments along c-direction. Judd-Ofelt parameter Ω_2, which strongly depends on the environment of ligand, decreases with increasing Yb concentration in the lattice. The value of spectroscopic quality factor for both polarized and unpolarized absorption data was found to be nearly invariant (~1.80) with respect to the Yb doping concentration but better than that for Er doped YVO_4 (~1.31) [157]. The PL intensity of Er ion at 1550 nm was sufficient enhanced with excitation of three prominent absorption line of Yb ion at 952, 972 and 985 nm. The emission cross-section of $^4I_{13/2} \rightarrow {}^4I_{15/2}$ line for excitation at 808 nm (Er absorption line) and 952, 972 & 985 nm (Yb absorption line) were found to be nearly same order. The radiative lifetime and emission cross-section of $^4I_{13/2} \rightarrow {}^4I_{15/2}$ transition of Er ions was also found to be independent of Yb doping concentration. This is one of the biggest advantages of Yb co-dopant as a good sensitizer in the Er:YVO_4 as it results in high population density in upper level of Er ions.

7.1.3 Nd co-doped Yb:YVO_4 crystals

Nd co-doped Yb:YVO_4 single crystals have been grown for the first time by using optical floating zone method to the best of our knowledge. The dimension of grown crystals were ~4-5 mm in diameter and 10-15 mm in length. Powder crystal XRD shows that there is a small shift of diffraction peaks towards the lower angle with Nd doping in the crystal, signifying slight expansion of the lattice volume. The quality of the crystal was estimated by rocking curve measurement. The observed nearly straight fringes in birefringence interferogram ensured the good optical homogeneity of grown crystals. The variation in birefringence was found to be less than 5.64×10^{-4}. The dislocation etch pit density was estimated by chemical etching and found to be ~$1.2x10^4/cm^2$. The measured fluorescence life-time of Yb (0.8 at.%) and Nd (0.8 at.%) co-doped YVO_4 crystal is around 581 and 66 μs respectively. The polarized absorption spectra depicted an overall higher absorption for π-polarization (E||c) than the σ-polarization (E⊥c). The absorption coefficient at 808 nm & 985 nm corresponding to Nd (0.8 at.%) & Yb (0.8 at.%) ions are ~ 26 & 9.2 cm^{-1} for π-polarization and ~13.7 & 4.6 cm^{-1} for σ-polarization, respectively, which is found to be better than the crystals grown by conventional Cz technique. In the Judd-Ofelt analysis, the estimated effective Judd-Ofelt parameters are 11.8675×10^{-20}, 5.1577×10^{-20} and 7.3755×10^{-20} cm^{-2}. Spectroscopic quality factor of Nd co-doped Yb:YVO_4 is 0.70, which is lower than that for Nd (1.0 at.%) doped YVO_4 (0.97) [157], that indicates the energy transfer from Nd^{3+} ion to Yb^{3+} ion. The estimated emission cross-section of $^4F_{3/2} \rightarrow {}^4I_{11/2}$ Nd transition with an excitation at 808 nm for both the concentrations of Yb is ~4.0×10^{-19} cm^2, which is almost same as estimated by Bhaumik et al. [157]. Hence, emission cross section of $^4F_{3/2} \rightarrow {}^4I_{11/2}$ transition is not influenced by Yb co-doping. Also, the PL intensity of Yb

at 1010 nm enhances with the increase in Yb co-doping for same Nd (0.8 at.%) doping which is because the Nd^{3+} ion more effectively excite the Yb^{3+} ion in the upper state in sample with higher Yb doping concentration. Therefore Nd^{3+} ion acts as excellent sensitizer for Yb:YVO_4 laser gain medium and make efficient pumping in the gain medium.

7.2 Summary of works on doped and co-doped $GdVO_4$ crystals

7.2.1 Nd doped $GdVO_4$ crystals

Undoped and Nd (0.2, 0.6, 0.8, 1.0, 1.2 and 1.6 at.%) doped $GdVO_4$ single crystals have been grown by optical floating zone technique. The value of the FWHM of the (200) diffraction peak for the samples of different Nd doped samples are ~43-56 arc-sec. The low value of FWHM reveals the good crystalline quality of the grown crystals. XRD analysis reveals small lattice expansion especially along c-axis on Nd doping. In the refractive index measurement, it has been observed that the extra-ordinary refractive index (RI) of undoped $GdVO_4$ crystals is higher than that of the doped $GdVO_4$ single crystals upto 1.0 at.% Nd doping, beyond which it surpasses the value of the undoped crystal. This is due to the competing effect of lattice elongation and decrease in electron density on Nd doping. The increase in RI with Nd doping is attributed to macroscopic polarization effects. Moreover, the extra-ordinary refractive index (n_e) only increases on increasing Nd concentration, whereas ordinary refractive index (n_o) remains unaffected within the measurement limits. The temperature dependent RI measurements depicted a positive thermo-optic coefficient (TOC) for RI and birefringence, which is ~10^{-5}/°C and is independent of doping concentration. TOC for n_e is higher than n_o, which has been explained on the basis of anisotropic thermal

expansion. An important set of relations between TOC and wavelength (532-1551 nm) has been established which is useful for estimating TOC in the temperature range 30-150 °C.

Further, in the absorption study, the calculated absorption coefficient for two orthogonal polarization of light is different due to anisotropic structure in both the direction. The evaluated line strengths and Judd-Ofelt parameters from the recorded absorption spectra were also found to be dependent on the polarization of the incident light. Further, the spectroscopic quality factor was estimated by Judd-Ofelt parameters and found to be maximum for 0.8 at.% Nd doped $GdVO_4$ crystals. The emission study shows that photoluminescence (PL) intensity at 1062 (lasing wavelength), 1069 and 1081 nm increases with the doping concentration of Nd up to 0.8 at.% and beyond that the PL intensity decreases. The emission cross-section for the $^4F_{3/2} \rightarrow {}^4I_{11/2}$ transition was estimated by Judd-Ofelt theory and it was found to be independent of doping of Nd in $GdVO_4$. The measured fluorescence life-time of Nd:$GdVO_4$ samples is ~ 100, 101, 92 and 93 μs corresponding to the doping concentration of 0.6, 0.8, 1.0 and 1.2 at.% of Nd respectively. The measured fluorescence life-time exhibits the maximum value for 0.8 at.% of Nd doping. The decrease in the PL intensity as well as fluorescence life-time for higher doping concentration is because of quenching due to ion-to-ion interaction in the crystal. All the spectroscopic investigation presented here suggest that the optimum concentration of Nd ion in $GdVO_4$ single crystals is 0.8 at.%, at which the best lasing performance can be obtained.

The testing of lasing for [001] and [100]-oriented elements was carried out using plane-plane resonator geometry (output coupler reflectivity =89%) with 808 nm pumping. CW laser emission at 1064 nm was demonstrated. The laser output power for

[001]-oriented element was 2.7 W at 11.2 W of incident pump power. The slope efficiency was around 39%. However, the laser output power for [100]-oriented element was 4.57 W at 11.94 W of incident pump power. The slope efficiency was around 49.7%.

7.2.2 Cr co-doped Nd:$GdVO_4$ crystals

The single crystals [diameter ~ 4-5 mm & length: 15-30 mm] with a Cr (1.5 at.%):Nd (0.5 at.%):$GdVO_4$ were grown by OFZ method in the ambience of 10%, 20% and 25 % O_2. The absorption spectra have multiple peaks at 594, 751, 808 & 879 nm due to Nd^{3+} ion & broad peak at 1100 nm (900-1300nm) due to Cr^{5+} ion. The absorption spectra show that when Cr concentration is small around 1.0 at.% in the crystals and the oxygen content increases in the growth ambience, then the absorption of Cr^{5+} ion at 1100 and 650 nm decreases. Further, when Cr concentration is large around 1.2 and 1.5 at.% in the crystals then the revered effect is observed such that the absorption of Cr^{5+} ion at 1100 and 650 nm increases with increase of the oxygen content in the growth ambience (for 10, 20 and 25 %). The comparison of absorption at around 1100 nm between grown crystals of Nd:Cr:$GdVO_4$ and Nd:Cr:YVO_4 in the varied oxygen ambience reveals a similar results. PL intensity increases for Cr 1.0 at.% whereas it decreases for the Cr 1.2 and 1.5 at.% with increase of oxygen percentage in the growth ambience, respectively and these results are inline with the absorption data. These results have important technical significance. In practice, the concentration of Cr required in $GdVO_4$ crystals for application related to saturable absorption might be different for different experimental conditions. Our finding suggests that for the growth of crystal with required concentration of Cr^{5+} in Nd:$GdVO_4$ to achieve a certain

desirable level of saturable absorption, the growth ambience have to be chosen as per the result obtained.

Further, an intensity dependent transmittance was recorded. It was found that an increase of transmission from 0.57 to 0.66 (9%). The increase in the intensity dependent transmittance is attributed to saturation of absorption of the Cr^{5+} ions causing bleaching of the 1064 nm absorption that give rise to passive self Q-switching.

7.3 Summary of works on the Nd doped $LuVO_4$ crystals

Single crystals of Nd doped $LuVO_4$ with 0.25 and 0.5 at.% of Nd concentrations have been grown by optical floating zone technique. The dimension of grown crystals are ~ 10-25 mm in length and 4-6 mm in diameter. The value of the FWHM (rocking curve) of (200) diffraction peak for the samples are ~130 arc-sec which signifies the good crystalline quality of the grown crystals. In XRD analysis, there was slightly expansion of the lattice volume as the Nd concentration varies from 0.25 to 0.5 at.% in the crystal. The absorption coefficients for Nd 0.25 and 0.5 at.% corresponding to the 810 nm are ~8.3 and 14 cm^{-1} for π-polarization whereas for σ-polarization the values are ~ 2.4 and 4.6 cm^{-1} respectively. The strong absorption band of Nd:$LuVO_4$ laser gain medium for π-polarized (E||c) light is centered at 810 nm and this 810 nm absorption band of Nd can be used for efficient pumping to the Nd:$LuVO_4$ laser gain medium by using a diode laser operating ~ 810 nm wavelength. The emission spectra were characterized by emission at 916, 1065, 1087 and at 1342 nm with the excitations at 810 and 880 nm. Among these, the PL intensity at 1065 nm was the highest for the both samples as well both excitation wavelengths. The measured fluorescence life-time of Nd^{3+}ion in the $LuVO_4$ crystals was found to be ~ 95±0.02 μs for doping concentration

0.5 at.% of Nd. Laser output power for Nd:$LuVO_4$ element was 360 mW with absorbed power pump of 13.6W. Lasing wavelength was 1066 nm.

7.4 Scope for future work

This thesis highlights the structural and optical properties of the three excellent orthovanadate single crystals for the laser applications. In this research work the details investigations of effect of doping on the various optical properties of orthovanadate crystals have been reported. However, there are several aspects and investigations that can be further studied as a future scope of the work. The different investigations of the orthovanadate crystals, which can be characterized, are given below.

7.4.1 Future Scope on the rare earth doped YVO_4 crystals

Our investigation shows that the PL intensity at 1010 nm of Yb^{3+}ion is stronger for excitation at 952 and 972 nm in comparison to that for 985 nm for Yb doped YVO_4 laser crystals. Hence, the laser testing of Yb doped YVO_4 crystal with pumped 952 972 and 985 nm diode laser can be investigated for better laser performance. Further, the optical study of Yb co-doped Er:YVO_4 laser crystals shows that Yb is excellent sensitizer for the Er doped crystal. Hence a comparative laser performance of different Yb doped Er:YVO_4 laser crystals can be done for optical communication application as this crystal is used as eye safe laser and further, effect of Yb doping on the reflective index and thermo-optic coefficient of Er doped YVO_4 can be investigated for high power laser designing. In this area, the optimum concentration of Nd^{3+} and Yb^{3+} ion in the YVO_4 laser crystal may be investigated to overcome the problem of Yb doped YVO_4 laser gain medium and better laser characteristics. Further, the detail investigation of powder XRD of Yb doped YVO_4 crystals can be carried out and obtained results can be compared with the some theoretical model.

7.4.2 Future Scope on the rare earth doped $GdVO_4$ crystals

In the present work, Nd doped $GdVO_4$ crystals have been grown by OFZ method with a wide range of solubility of Nd ion and investigated for crystalline quality, defect study by etch pits, and optical properties like RI, absorption and emission. The defect studies like topography and thermal luminescence of Nd doped $GdVO_4$ crystals and oxidation state of Nd, V and Gd ion by XANES method can be carried out. In case of Cr co-doped Nd:$GdVO_4$ crystals, the growth of single crystals by OFZ method and optical investigation such as absorption and emission properties have been carried out. The oxidation state of Cr ion in the lattice is very important for self Q-switching applications and therefore, XANES and EXAFS measurement can be carried out. Further, the optimization of Cr concentration in the Nd doped $GdVO_4$ crystals can be carried out for desired pulse width and laser performance. In addition to this, the effect of Cr co-doping on the refractive index and thermo-optical coefficient can be investigated.

7.4.3 Future Scope on the rare earth doped $LuVO_4$ crystals

This thesis also contains the growth, structural and optical investigation of 0.25 and 0.5 at.% of Nd doped $LuVO_4$ single crystals. Therefore, the growth of Nd doped $LuVO_4$ single crystals with wide range of Nd doping concentrations and investigations for the optimum concentration may be carried out. Also, the comparative laser performance for optimum and other Nd dopant concentrations can be investigated for the better Nd doped laser gain medium.

References

[1] W. Koechner, Solid-State Laser Engineering, Springer, New York, NY, 2006. https://doi.org/https://doi.org/10.1007/0-387-29338-8.

[2] Richard C. Powell, Physics of Solid State Laser Materials, 1st ed., Springer-Verlag New York, 1988. https://www.springer.com/gp/book/9781563966583.

[3] W.T. Silfvast, Laser Fundamentals, 2nd ed., Cambridge, Cambridge University Press, 2004.

[4] O. Svelto, Principles of Lasers, 5th ed., Springer US, 2010. https://doi.org/10.1007/978-1-4419-1302-9.

[5] C. Maunier, J.L. Doualan, R. Moncorgé, A. Speghini, M. Bettinelli, E. Cavalli, Growth, spectroscopic characterization, and laser performance of Nd:$LuVO_4$ a new infrared laser material that is suitable for diode pumping, J. Opt. Soc. Am. B. 19 (2002) 1794–1800. https://doi.org/10.1364/JOSAB.19.001794.

[6] J. Liu, H. Zhang, Z. Wang, J. Wang, Z. Shao, M. Jiang, H. Weber, Continuous-wave and pulsed laser performance of Nd:$LuVO_4$ crystal, Opt. Lett. 29 (2004) 168–170. https://doi.org/10.1364/OL.29.000168.

[7] C. Zhang, L. Zhang, Z. Wei, C. Zhang, Y. Long, Z. Zhang, H. Zhang, J. Wang, Diode-pumped continuous-wave Nd:$LuVO_4$ laser operating at 916nm, Opt. Lett. 31 (2006) 1435–1437. https://doi.org/10.1364/OL.31.001435.

[8] A.W. Tucker, M. Birnbaum, C.L. Fincher, J.W. Erler, Stimulated-emission cross section at 1064 and 1342 nm in Nd : YVO_4, J. Appl. Phys. 48 (1977) 4907–4911. https://doi.org/10.1063/1.323618.

[9] H. Zheng, H. Yang, Y. Zhang, J. Zhou, H. Xia, X. Wu, Y. Jiang, Nd:YVO_4 crystal growth by the floating zone method, J. Cryst. Growth. 160 (1996) 136–140. https://doi.org/https://doi.org/10.1016/0022-0248(95)00901-9.

[10] H. Zhang, X. Meng, L. Zhu, P. Wang, X. Liu, Z. Yang, J. Dawes, P. Dekker, Growth, Morphology and Characterization of Yb : YVO_4 Crystal, Phys. Status Solidi. 175 (1999) 705–710. https://doi.org/10.1002/(SICI)1521-396X(199910)175:2<705::AID-PSSA705>3.0.CO;2-N.

[11] S. Erdei, G.G. Johnson Jr., F.W. Ainger, Growth studies of YVO_4 crystals (II). Changes in Y□V□O-stoichiometry, Cryst. Res. Technol. 29 (1994) 815–828. https://doi.org/10.1002/crat.2170290610.

[12] A.I. Zagumennyĭ, V.G. Ostroumov, I.A. Shcherbakov, T. Jensen, J.P. Meyen, G. Huber, The Nd:$GdVO_4$crystal: a new material for diode-pumped lasers, Sov. J. Quantum Electron. 22 (1992) 1071–1072. https://doi.org/10.1070/qe1992v022n12abeh003672.

[13] T. Jensen, V.G. Ostroumov, J.-P. Meyn, G. Huber, A.I. Zagumennyi, I.A. Shcherbakov, Spectroscopic characterization and laser performance of diode-laser-pumped Nd: $GdVO_4$, Appl. Phys. B. 58 (1994) 373–379. https://doi.org/10.1007/BF01081876.

[14] P.A. Studenikin, A.I. Zagumennyi, Y.D. Zavartsev, P.A. Popov, I.A. Shcherbakov, $GdVO_4$as a new medium for solid-state lasers: some optical and thermal properties of crystals doped with Cd^{3+}, Tm^{3+}, and Er^{3+}ions, Quantum Electron. 25 (1995) 1162–1165. https://doi.org/10.1070/qe1995v025n12abeh000556.

[15] S. Nakamura, T. Agata, T. Ogawa, S. Wada, M. Higuchi, Optical properties and laser performance of Yb-doped vanadates grown by floating zone method, Opt. Rev. 20 (2013) 390–394. https://doi.org/10.1007/s10043-013-0070-x.

[16] Z.B. Pan, B. Yao, H.H. Yu, H.H. Xu, Z.P. Wang, J.Y. Wang, H.J. Zhang, Growth and characterization of self-Q-switched Nd:Cr:YVO_4 crystal, Opt. Express. 20 (2012) 2178–2183. https://doi.org/10.1364/OE.20.002178.

[17] I. Sokólska, E. Heumann, S. Kück, T. Lukasiewicz, Laser oscillation of Er^{3+}:YVO_4 and Er^{3+}, Yb^{3+}:YVO_4 crystals in the spectral range around 1.6 μm, Appl. Phys. B. 71 (2000) 893–896. https://doi.org/10.1007/s003400000458.

[18] N.A. Tolstik, A.E. Troshin, S. V Kurilchik, V.E. Kisel, N. V Kuleshov, V.N. Matrosov, T.A. Matrosova, M.I. Kupchenko, Spectroscopy, continuous-wave and Q-switched diode-pumped laser operation of Er^{3+},Yb^{3+}:YVO_4 crystal, Appl. Phys. B. 86 (2007) 275–278. https://doi.org/10.1007/s00340-006-2427-3.

[19] H. Yu, H. Zhang, Z. Wang, J. Wang, Y. Yu, W. Gao, X. Tao, M. Jiang, Growth and passively self-Q-switched laser output of new Nd^{3+},Cr^{5+}:$GdVO_4$ crystal, Opt. Express. 16 (2008) 3320–3325. https://doi.org/10.1364/OE.16.003320.

[20] I. Bhaumik, S. Ganesamoorthy, R. Bhatt, A. Saxena, A.K. Karnal, P.K. Gupta, Growth of Nd:Cr:YVO_4 Single Crystals by the Optical Floating Zone Technique under Different Oxygen Partial Pressures to Control the Oxidation State of Chromium, Cryst. Growth Des. 13 (2013) 3878–3883. https://doi.org/10.1021/cg400506d.

[21] J. Chen, F. Guo, N. Zhuang, J. Lan, X. Hu, S. Gao, A study on the growth of Yb:YVO_4 single crystal, J. Cryst. Growth. 243 (2002) 450–455. https://doi.org/https://doi.org/10.1016/S0022-0248(02)01537-3.

[22] S. Wu, G. Wang, J. Xie, X. Wu, G. Li, Growth of large birefringent YVO_4 crystal, J. Cryst. Growth. 249 (2003) 176–178. https://doi.org/https://doi.org/10.1016/S0022-0248(02)02067-5.

[23] S. Erdei, F.W. Ainger, Crystal growth of YVO_4 using the LHPG technique, J. Cryst. Growth. 128 (1993) 1025–1030. https://doi.org/https://doi.org/10.1016/S0022-0248(07)80091-1.

[24] Y. Sato, T. Taira, N. Pavel, V. Lupei, Laser operation with near quantum-defect slope efficiency in Nd:YVO_4 under direct pumping into the emitting level, Appl. Phys. Lett. 82 (2003) 844–846. https://doi.org/10.1063/1.1544659.

[25] C. Kränkel, D. Fagundes-Peters, S.T. Fredrich, J. Johannsen, M. Mond, G. Huber, M. Bernhagen, R. Uecker, Continuous wave laser operation of Yb^{3+}:YVO_4, Appl. Phys. B. 79 (2004) 543–546. https://doi.org/10.1007/s00340-004-1635-y.

[26] E.M. LEVIN, The System Y_2O_3-V_2O_5, J. Am. Ceram. Soc. 50 (1967) 381–382.

https://doi.org/10.1111/j.1151-2916.1967.tb15136.x.

[27] S. Erdei, B.M. Jin, F.W. Ainger, B. Keszei, J. Vandlik, A. Süveges, Possible trends for the growth of low scattering Nd:YVO_4 laser crystals; phase relations — growth techniques, J. Cryst. Growth. 172 (1997) 466–472. https://doi.org/https://doi.org/10.1016/S0022-0248(96)00765-8.

[28] S. Erdei, Growth of oxygen deficiency-free YVO_4 single crystal by top-seeded solution growth technique, J. Cryst. Growth. 134 (1993) 1–13. https://doi.org/https://doi.org/10.1016/0022-0248(93)90002-E.

[29] K. Chow, H.G. McKnight, The growth and characterization of pure and rare-earth-substituted YVO_4, Mater. Res. Bull. 8 (1973) 1343–1350. https://doi.org/https://doi.org/10.1016/0025-5408(73)90018-4.

[30] J.R. O'Connor, UNUSUAL CRYSTAL-FIELD ENERGY LEVELS AND EFFICIENT LASER PROPERTIES OF YVO_4:Nd, Appl. Phys. Lett. 9 (1966) 407–409. https://doi.org/10.1063/1.1754631.

[31] R.A. Fields, M. Birnbaum, C.L. Fincher, Highly efficient Nd:YVO4 diode-laser end-pumped laser, Appl. Phys. Lett. 51 (1987) 1885–1886. https://doi.org/10.1063/1.98500.

[32] E. Hertel, Crystal structures, von Ralph W. G. Wyckoff. Interscience Publishers, Inc., New YorkInterscience Publishers, Inc., New York, 1953. https://doi.org/https://doi.org/10.1002/ange.19530650914.

[33] K. Robinson, G. V Gibbs, P.H. Ribbe, The Structure of Zircon: A Comparison With Garnet, Am. Mineral. 56 (1971) 782–790.

[34] H.C. Schopper, W. Urban, H. Ebel, Measurements of the temperature dependence of the lattice parameters of some rare earth compounds with zircon structure, Solid State Commun. 11 (1972) 955–958. https://doi.org/10.1016/0038-1098(72)90297-9.

[35] C. Vishnu Vardhan Reddy, K. Satyanarayana Murthy, P. Kistaiah, X-ray study of the thermal expansion anisotropy in YVO4 and YAsO4 compounds, Solid State Commun. 67 (1988) 545–547. https://doi.org/https://doi.org/10.1016/0038-1098(84)90179-0.

[36] E. Broch, The Journal of Physical Chemistry, J. Phys. Chem. B. 20 (1933) 345.

[37] V.E. Kisel, A.E. Troshin, N.A. Tolstik, V.G. Shcherbitsky, N. V Kuleshov, V.N. Matrosov, T.A. Matrosova, M.I. Kupchenko, Spectroscopy and continuous-wave diode-pumped laser action of Yb^{3+}:YVO_4, Opt. Lett. 29 (2004) 2491–2493. https://doi.org/10.1364/OL.29.002491.

[38] D. Zhong, B. Teng, J. Li, S. Zhang, B. Zhang, C. Wang, X. Tian, J. Liu, Growth and laser action of Yb: YVO_4 crystals with low Yb doping concentration, J. Cryst. Growth. 358 (2012) 16–19. https://doi.org/https://doi.org/10.1016/j.jcrysgro.2012.07.029.

[39] J.A. Capobianco, P. Kabro, F.S. Ermeneux, R. Moncorgé, M. Bettinelli, E. Cavalli, Optical spectroscopy, fluorescence dynamics and crystal-field analysis of Er^{3+} in YVO_4, Chem. Phys. 214 (1997) 329–340.

https://doi.org/https://doi.org/10.1016/S0301-0104(96)00318-7.

[40] X. Yan, X. Wu, J. Zhou, Z. Zhang, J. Wang, Growth of laser single-crystals Er:YVO_4 by floating zone method, J. Cryst. Growth. 220 (2000) 543–547. https://doi.org/https://doi.org/10.1016/S0022-0248(00)00872-1.

[41] N. Ter-Gabrielyan, V. Fromzel, T. Lukasiewicz, W. Ryba-Romanowski, M. Dubinskii, Nearly quantum-defect-limited efficiency, resonantly pumped, Er^{3+}:YVO_4 laser at 1593.5 nm, Opt. Lett. 36 (2011) 1218–1220. https://doi.org/10.1364/OL.36.001218.

[42] C. Brandt, V. Matrosov, K. Petermann, G. Huber, In-band fiber-laser-pumped Er:YVO_4 laser emitting around 1.6 μm, Opt. Lett. 36 (2011) 1188–1190. https://doi.org/10.1364/OL.36.001188.

[43] S. Ganesamoorthy, I. Bhaumik, R. Bhatt, A. Saxena, A.K. Karnal, P.K. Gupta, Spectroscopic analysis on the basis of Judd–Ofelt theory along [001] of Er:YVO_4 grown by optical floating zone technique, Mater. Res. Bull. 48 (2013) 1132–1136. https://doi.org/https://doi.org/10.1016/j.materresbull.2012.12.003.

[44] T. Tsuboi, Emission spectroscopy of Er^{3+}/Yb^{3+}-codoped YVO_4 crystals, Phys. B Condens. Matter. 293 (2000) 84–90. https://doi.org/https://doi.org/10.1016/S0921-4526(00)00533-0.

[45] R. Liu, Y. Zhan, L. Liu, Y. Liu, D. Tu, Morphology analysis and luminescence properties of YVO_4:Sm^{3+},Eu^{3+} prepared by molten salt synthesis, Opt. Mater. (Amst). 100 (2020) 109633. https://doi.org/https://doi.org/10.1016/j.optmat.2019.109633.

[46] G. Zhang, Y. Wang, Z. Jiao, D. Li, J. Wang, Z. Chen, Tungsten disulfide saturable absorber for passively Q-Switched YVO_4/Nd:YVO_4/YVO_4 laser at 1342.2 nm, Opt. Mater. (Amst). 92 (2019) 95–99. https://doi.org/https://doi.org/10.1016/j.optmat.2019.04.024.

[47] R.F. Likerov, V.F. Tarasov, A.A. Sukhanov, R.M. Eremina, K.B. Konov, I. V Yatsyk, A. V Shestakov, Y.D. Zavartsev, S.A. Kutovoi, Investigation of neodymium doped YVO_4 by EPR method, Opt. Mater. (Amst). 85 (2018) 414–417. https://doi.org/https://doi.org/10.1016/j.optmat.2018.09.003.

[48] Y.C. Liu, C.M. Chen, J.Q. Hsiao, Y.Y. Pan, C.H. Tsou, H.C. Liang, Y.F. Chen, Compact efficient high-power triple-color Nd:YVO_4 yellow-lime-green self-Raman lasers, Opt. Lett. 45 (2020) 1144–1147. https://doi.org/10.1364/OL.388266.

[49] Y.F. Chen, Y.Y. Pan, Y.C. Liu, H.P. Cheng, C.H. Tsou, H.C. Liang, Efficient high-power continuous-wave lasers at green-lime-yellow wavelengths by using a Nd:YVO_4 self-Raman crystal, Opt. Express. 27 (2019) 2029–2035. https://doi.org/10.1364/OE.27.002029.

[50] W. Su-Mei, D. Shi-Feng, L. Jian, Z. Dong-Xiang, F. Bao-Hua, Spectroscopic investigation of a new crystal: Nd^{3+} ,Yb^{3+} :YVO_4, Chinese Phys. 16 (2007) 1786–1789. https://doi.org/10.1088/1009-1963/16/6/052.

[51] Z. Long, Z. Jun-jie, H. He-fang, L. Feng-ying, Fluorescence mechanisms of Tm^{3+} - and Yb^{3+} /Tm^{3+} doped AlF_3 -based fluoride glass, Chinese Phys. 10 (2000)

58–64. https://doi.org/10.1088/1009-1963/10/1/313.

[52] A. Rudenkov, V. Kisel, V. Matrosov, N. Kuleshov, 200 kHz 5.5W Yb^{3+}: YVO_4-based chirped-pulse regenerative amplifier, Opt. Lett. 40 (2015) 3352–3355. https://doi.org/10.1364/OL.40.003352.

[53] M.J. Weber, Optical Properties of $Y^{3+}$and Nd^{3+}-Yb^{3+}Energy Transfer in YAl_3, Phys. Rev. B. 4 (1971) 3153–3159. https://doi.org/10.1103/PhysRevB.4.3153.

[54] D. Jaque, M. de la O Ramirez, L. Bausá, A. Speghini, M. Bettinelli, E. Cavalli, Influence of Nd^{3+} and Yb^{3+} concentration on the $Nd^{3+}\rightarrow Yb^{3+}$ energy-transfer efficiency in the $YAl_3(BO_3)_4$ nonlinear crystal: determination of optimum concentrations for laser applications, J. Opt. Soc. Am. B. 21 (2004) 1203–1209. https://doi.org/10.1364/JOSAB.21.001203.

[55] F. Liégard, J.L. Doualan, R. Moncorgé, M. Bettinelli, $Nd^{3+} \rightarrow Yb^{3+}$ energy transfer in a codoped metaphosphate glass as a model for Yb^{3+} laser operation around 980 nm, Appl. Phys. B. 80 (2005) 985–991. https://doi.org/10.1007/s00340-005-1829-y.

[56] M.O. Ramirez, D. Jaque, L.E. Bausá, I.R. Martín, F. Lahoz, E. Cavalli, A. Speghini, M. Bettinelli, Temperature dependence of $Nd^{3+}\leftrightarrow Yb^{3+}$ energy transfer in the $YAl_3(BO_3)_4$ nonlinear laser crystal, J. Appl. Phys. 97 (2005) 93510. https://doi.org/10.1063/1.1886887.

[57] V. Lupei, A. Lupei, A. Ikesue, Transparent Nd and (Nd, Yb)-doped Sc_2O_3 ceramics as potential new laser materials, Appl. Phys. Lett. 86 (2005) 111118. https://doi.org/10.1063/1.1886897.

[58] M. Higuchi, H. Sagae, K. Kodaira, T. Ogawa, S. Wada, H. Machida, Float zone growth of Nd:$GdVO_4$ single crystals along [110] direction and their laser performance, J. Cryst. Growth. 264 (2004) 284–289. https://doi.org/https://doi.org/10.1016/j.jcrysgro.2003.12.058.

[59] K. Onodera, T. Ogawa, H. Itagaki, H. Machida, S. Wada, Crystal quality and optical properties for Nd:$GdVO_4$ single crystals by a floating zone method, Opt. Mater. (Amst). 26 (2004) 343–345. https://doi.org/10.1016/j.optmat.2003.12.017.

[60] H. Zhang, J. Liu, J. Wang, C. Wang, L. Zhu, Z. Shao, X. Meng, X. Hu, M. Jiang, Y.T. Chow, Characterization of the laser crystal Nd:$GdVO_4$, J. Opt. Soc. Am. B. 19 (2002) 18–27. https://doi.org/10.1364/JOSAB.19.000018.

[61] M. Soharab, I. Bhaumik, R. Bhatt, A. Saxena, A.K. Karnal, P.K. Gupta, S. Bhattacharya, S. Singh, A. Das, S. Basu, Growth and investigation of Nd doped $GdVO_4$ single crystals grown by OFZ technique, AIP Conf. Proc. 1832 (2017) 100018. https://doi.org/10.1063/1.4980620.

[62] J. Su, Q.-L. Zhang, S.-T. Yin, C.-X. Guo, Growth and spectral properties of Nd:$GdVO_4$ laser crystal, Phys. B Condens. Matter. 403 (2008) 3002–3008. https://doi.org/https://doi.org/10.1016/j.physb.2008.03.002.

[63] Y. Sato, T. Taira, Comparative study on the spectroscopic properties of Nd:$GdVO_4$ and Nd:YVO_4 with hybrid process, IEEE J. Sel. Top. Quantum Electron. 11 (2005) 613–620. https://doi.org/10.1109/JSTQE.2005.850569.

[64] V. Ostroumov, T. Jensen, J.-P. Meyn, G. Huber, M.A. Noginov, Study of luminescence concentration quenching and energy transfer upconversion in Nd-doped $LaSc_3(BO_3)_4$ and $GdVO_4$ laser crystals, J. Opt. Soc. Am. B. 15 (1998) 1052–1060. https://doi.org/10.1364/JOSAB.15.001052.

[65] H.R. Xia, H.D. Jiang, W.Q. Zheng, G.W. Lu, X.L. Meng, H.J. Zhang, X.S. Liu, L. Zhu, J.Y. Wang, Optical parameters and luminescent properties of Nd:$GdVO_4$ crystals, J. Appl. Phys. 90 (2001) 4433–4436. https://doi.org/10.1063/1.1407307.

[66] H.-D. Jiang, H.-J. Zhang, J.-Y. Wang, H.-R. Xia, X.-B. Hu, B. Teng, C.-Q. Zhang, Optical and laser properties of Nd:$GdVO_4$ crystal, Opt. Commun. 198 (2001) 447–452. https://doi.org/https://doi.org/10.1016/S0030-4018(01)01539-5.

[67] A.A. Danilov, V.L. Evstigneev, N.N. Il'ichev, A.A. Malyutin, M.Y. Nikol'skiĭ, A.F. Umyskov, I.A. Shcherbakov, Compact GSGG:Cr^{3+}:Nd^{3+}laser with passiveQswitching, Sov. J. Quantum Electron. 17 (1987) 573–574. https://doi.org/10.1070/qe1987v017n05abeh008975.

[68] B. Jiang, Z. Zhao, X. Xu, P. Song, J. Xu, Study of the effects of Cr ions on Nd in self-Q-switched laser crystal Cr^{4+},Nd^{3+}:$Gd_3Ga_5O_{12}$, in: Proc.SPIE, 2005. https://doi.org/10.1117/12.569952.

[69] J. Dong, K. Ueda, Observation of repetitively nanosecond pulse-width transverse patterns in microchip self-Q-switched laser, Phys. Rev. A. 73 (2006) 53824. https://doi.org/10.1103/PhysRevA.73.053824.

[70] J. Dong, P. Deng, Y. Lu, Y. Zhang, Y. Liu, J. Xu, W. Chen, Laser-diode-pumped Cr^{4+},Nd^{3+}:YAG with self-Q-switched laser output of 1.4 W, Opt. Lett. 25 (2000) 1101–1103. https://doi.org/10.1364/OL.25.001101.

[71] S. Zhou, K.K. Lee, Y.C. Chen, S. Li, Monolithic self-Q-switched Cr,Nd:YAG laser, Opt. Lett. 18 (1993) 511–512. https://doi.org/10.1364/OL.18.000511.

[72] J. Dong, K. Ueda, Longitudinal-mode competition induced instabilities of Cr^{4+},Nd^{3+}:$Y_3Al_5O_{12}$ self-Q-switched two-mode laser, Appl. Phys. Lett. 87 (2005) 151102. https://doi.org/10.1063/1.2089153.

[73] H. Yu, H. Zhang, Z. Wang, J. Wang, Y. Yu, W. Gao, X. Tao, J. Liu, X. Zhang, M. Jiang, Cr^{5+}:$GdVO_4$ as a saturable absorber for a diode-pumped Nd:$Lu_{0.5}Gd_{0.5}VO_4$ laser, Opt. Express. 15 (2007) 11679–11684. https://doi.org/10.1364/OE.15.011679.

[74] S.A. Zolotovskaya, K. V Yumashev, N. V Kuleshov, V.N. Matrosov, T.A. Matrosova, M.I. Kupchenko, Absorption saturation properties and laser Q-switch performance of Cr^{5+}-doped YVO4 crystal, Appl. Phys. B. 86 (2007) 667–671. https://doi.org/10.1007/s00340-006-2521-6.

[75] H. Zhang, H. Kong, S. Zhao, J. Jiu, J. Wang, Z. Wang, L. Gao, C. Du, X. Hu, X. Xu, Z. Shao, M. Jiang, Growth of new laser crystal Nd:$LuVO_4$ by the Czochralski method, J. Cryst. Growth. 256 (2003) 292–297. https://doi.org/https://doi.org/10.1016/S0022-0248(03)01356-3.

[76] S. Zhao, H. Zhang, Y. Lu, J. Liu, J. Wang, X. Xu, H. Xia, M. Jiang, Spectroscopic characterization and laser performance of Nd:$LuVO_4$ single crystal, Opt. Mater.

(Amst). 28 (2006) 950–955. https://doi.org/https://doi.org/10.1016/j.optmat.2005.05.004.

[77] H. Zhang, J. Liu, J. Wang, X. Xu, M. Jiang, Continuous-wave laser performance of Nd:$LuVO_4$ crystal operating at 1.34 μm, Appl. Opt. 44 (2005) 7439–7441. https://doi.org/10.1364/AO.44.007439.

[78] S. Zhao, H. Zhang, J. Liu, J. Wang, X. Xu, Z. Zhao, J. Xu, M. Jiang, Growth of excellent-quality Nd:$LuVO_4$ single crystal and laser properties, J. Cryst. Growth. 279 (2005) 146–153. https://doi.org/https://doi.org/10.1016/j.jcrysgro.2005.02.044.

[79] Efficient continuous-wave lasing operation of Nd:KGd(WO4)2 at 1.067 μm with diode and Ti:sapphire laser pumping, Opt. Lett. 20 (1995) 1538–1540. https://doi.org/10.1364/OL.20.001538.

[80] N.P. Barnes, M.E. Storm, P.L. Cross, M.W. Skolaut, Efficiency of Nd laser materials with laser diode pumping, IEEE J. Quantum Electron. 26 (1990) 558–569. https://doi.org/10.1109/3.52133.

[81] D.G. Matthews, J.R. Boon, R.S. Conroy, B.D. Sinclair, A comparative study of diode pumped microchip laser materials: Nd-doped YVO_4, YOS, SFAP and SVAP, J. Mod. Opt. 43 (1996) 1079–1087. https://doi.org/10.1080/09500349608233268.

[82] Thermo-optic coefficients and thermal lensing in Nd-doped $KGd(WO_4)_2$ laser crystals, Appl. Opt. 49 (2010) 6651–6659. https://doi.org/10.1364/AO.49.006651.

[83] N.U. Wetter, 12 - Neodymium doped lithium yttrium fluoride (Nd:$YLiF_4$) lasers, in: B. Denker, E.B.T.-H. of S.-S.L. Shklovsky (Eds.), Woodhead Publ. Ser. Electron. Opt. Mater., Woodhead Publishing, 2013: pp. 323–340. https://doi.org/https://doi.org/10.1533/9780857097507.2.323.

[84] G.E. Khalil, G.A. Fattah, M.S. Shafik, Y.A. Badr, Comparison of CW laser performance of Nd:YAG and Nd:YLF under laser diode pumping, in: Third Work. Photonics Its Appl. Egypt. Eng. Fac. Institutes (Cat. No.02EX509), 2002: pp. 123–140. https://doi.org/10.1109/PAIA.2002.995085.

[85] 1053-nm-wavelength selection in a diode-laser-pumped Nd:YLF laser, Appl. Opt. 33 (1994) 6942–6946. https://doi.org/10.1364/AO.33.006942.

[86] K. Kopczynski, Z. Mierczyk, S.M. Kaczmarek, Properties of crystals for diode-pumped solid state laser devices, in: Proc.SPIE, 1996. https://doi.org/10.1117/12.233018.

[87] Comparative spectroscopic and thermo-optic study of Tm:LiLnF4 (Ln = Y, Gd, and Lu) crystals for highly-efficient microchip lasers at ~2 μm, Opt. Mater. Express. 7 (2017) 844–854. https://doi.org/10.1364/OME.7.000844.

[88] R.L. Aggarwal, D.J. Ripin, J.R. Ochoa, T.Y. Fan, Measurement of thermo-optic properties of $Y_3Al_5O_{12}$, $Lu_3Al_5O_{12}$, $YAlO_3$, $LiYF_4$, $LiLuF_4$, BaY_2F_8, $KGd(WO_4)_2$, and $KY(WO_4)_2$ laser crystals in the 80–300K temperature range, J. Appl. Phys. 98 (2005) 103514. https://doi.org/10.1063/1.2128696.

[89] A.A. Demidovich, A.N. Kuzminz, G.I. Ryabtev, M.B. Danailov, W. Strek, A.N. Titov, Dependence of Yb:KYW minilaser performance on Yb concentration, in: Conf. Dig. 2000 Conf. Lasers Electro-Optics Eur. (Cat. No.00TH8505), 2000: p. 1 pp. https://doi.org/10.1109/CLEOE.2000.909664.

[90] A. Pirri, G. Toci, D. Alderighi, M. Vannini, Yb-doped YLF and CaF_2 crystal laser at room temperature, Opt. Mater. (Amst). 33 (2010) 200–204. https://doi.org/https://doi.org/10.1016/j.optmat.2010.07.019.

[91] X. Tian, Z. Zhou, Q. Dai, W. Han, J. Liu, H. Zhang, Study of Yb:YVO_4 lasers end-pumped by a 985-nm diode laser, Laser Phys. 22 (2012) 688–692. https://doi.org/10.1134/S1054660X12040238.

[92] H. Qiu, P. Yang, J. Dong, P. Deng, J. Xu, W. Chen, The influence of Yb concentration on laser crystal Yb:YAG, Mater. Lett. 55 (2002) 1–7. https://doi.org/https://doi.org/10.1016/S0167-577X(01)00608-5.

[93] F.D. Patel, E.C. Honea, J. Speth, S.A. Payne, R. Hutcheson, R. Equall, Laser demonstration of $Yb_3Al_5O_{12}$ (YbAG) and materials properties of highly doped Yb:YAG, IEEE J. Quantum Electron. 37 (2001) 135–144. https://doi.org/10.1109/3.892735.

[94] H.H. Yu, H.J. Zhang, J.Y. Wang, Growth and Characterization of Vanadate Laser Crystals, Acta Phys. Pol. A. 124 (2013) 301–304. https://doi.org/10.12693/APhysPolA.124.301.

[95] A.A. Demidovich, A.P. Shkadarevich, M.B. Danailov, P. Apai, T. Gasmi, V.P. Gribkovskii, A.N. Kuzmin, G.I. Ryabtsev, L.E. Batay, Comparison of cw laser performance of Nd:KGW, Nd:YAG, Nd:BEL, and Nd:YVO_4 under laser diode pumping, Appl. Phys. B. 67 (1998) 11–15. https://doi.org/10.1007/s003400050467.

[96] Crystallisation, 4th Edition By J. W. Mullin. 2001. Butterworth Heinemann: Oxford, UK. 600 pp. £75.00. ISBN 075-064-833-3., Org. Process Res. Dev. 6 (2002) 201–202. https://doi.org/10.1021/op0101005.

[97] T.F. Hans J. Scheel, Crystal Growth Technology, John Wiley & Sons, New York, 2005.

[98] A.R.M. Gilbert J. Sloan, Techniques of Melt Crystallization, John Wiley & Sons, New York, 1988.

[99] Front Matter, Introd. to Cryst. Growth Charact. (2014) I–XIV. https://doi.org/doi:10.1002/9783527689248.fmatter.

[100] 5. J.W. Gibbs, On the Equilibrium of Heterogeneous Substances, Longmans Green, New York, 1928.

[101] H.J.S. D. Elwell, Crystal growth from high-temperature solutions, Academic, London, 1975. https://doi.org/https://doi.org/10.3929/ethz-a-006779537.

[102] M.D. Govindhan Dhanaraj, Kullaiah Byrappa, Vishwanath Prasad, Springer Handbook of Crystal Growth, Springer, Berlin, Heidelberg, 2010. https://doi.org/https://doi.org/10.1007/978-3-540-74761-1.

[103] H.L. Bhat, Introduction to Crystal Growth, Principles and Practice, CRC Press,

2015.

[104] K.-T. Wilke, I. Tarjan, M. Matrai. Laboratory Manual on Crystal Growth. Akademiai Kiado, Budapest 1972 250 Seiten, zahlreiche Abbildungen, Preis Ft. 150.-, Krist. Und Tech. 8 (1973) K11–K11. https://doi.org/10.1002/crat.19730080516.

[105] P.H. Keck, W. Van Horn, J. Soled, A. MacDonald, Floating Zone Recrystallization of Silicon, Rev. Sci. Instrum. 25 (1954) 331–334. https://doi.org/10.1063/1.1771057.

[106] P.H. Keck, M.J.E. Golay, Crystallization of Silicon from a Floating Liquid Zone, Phys. Rev. 89 (1953) 1297. https://doi.org/10.1103/PhysRev.89.1297.

[107] W.L. Bragg, X-Rays and Crystal Structure, Philos. Trans. R. Soc. London. Ser. A. 215 (1915) 253.

[108] K.N.T. J. Pickworth Glusker, Crystal Structure Analysis, A premier, Oxford University press, New York, 1985.

[109] B.D. Cullity, Elements of X-Ray Diffraction, Osmania University, Addison-Wesley Publishing Company, Inc., 1978.

[110] Front Matter, Elem. Mod. X-ray Phys. (2011) i–xii. https://doi.org/doi:10.1002/9781119998365.fmatter.

[111] R. Selvamani, G. Singh, V. Sathe, V.S. Tiwari, P.K. Gupta, Dielectric, structural and Raman studies on (Na0.5Bi0.5TiO3)(1 −x)(BiCrO3)xceramic, J. Phys. Condens. Matter. 23 (2011) 55901. https://doi.org/10.1088/0953-8984/23/5/055901.

[112] S.K.D. A.K. Sinha, A. Sagdeo, P. Gupta, A. Kumar, M.N. Singh, R.K. Gupta, S. R. Kane, Commissioning of angle dispersive x-ray diffraction beamline on Indus-2, 55th DAE Solid State Phys. Symp. (2010) paper D48.

[113] U.K. Goutam, R.K. Sharma, J. Singh, K. Dutta, U.S. Sule, R. Pradeep, S.C. Gadkari, HAXPES beamline PES-BL14 at the Indus-2 synchrotron radiation source., J. Synchrotron Radiat. 25 (2018) 1541–1547. https://doi.org/10.1107/S1600577518008408.

[114] P. Wobrauschek, H. Aiginger, Total-reflection x-ray fluorescence spectrometric determination of elements in nanogram amounts, Anal. Chem. 47 (1975) 852–855. https://doi.org/10.1021/ac60356a034.

[115] M.K. Tiwari, A.K. Singh, K.J.S. Sawhney, Analysis of stainless steel samples by energy dispersive X-ray fluorescence (EDXRF) spectrometry, Bull. Mater. Sci. 24 (2001) 633–638. https://doi.org/10.1007/BF02704012.

[116] I. Bhaumik, R. Bhatt, S. Ganesamoorthy, A. Saxena, A.K. Karnal, P.K. Gupta, A.K. Sinha, S.K. Deb, Temperature-dependent index of refraction of monoclinic Ga_2O_3 single crystal, Appl. Opt. 50 (2011) 6006–6010. https://doi.org/10.1364/AO.50.006006.

[117] H. Onodera, I. Awai, J. Ikenoue, Refractive-index measurement of bulk materials: prism coupling method, Appl. Opt. 22 (1983) 1194–1197. https://doi.org/10.1364/AO.22.001194.

[118] T.A.N. Douglas A. Skoog, F. James Holler, Principles of Instrumental Analysis, Saunders College Publishing, Philadelphia, 1988.

[119] M. Soharab, I. Bhaumik, R. Bhatt, A. Saxena, A.K. Karnal, S. Satapathy, P.K. Gupta, Effect of Yb doping on the crystal structure, polarization dependent optical absorption and photoluminescence of Yb:YVO_4 single crystal grown by optical floating zone technique, J. Alloys Compd. 649 (2015) 766–771. https://doi.org/https://doi.org/10.1016/j.jallcom.2015.07.183.

[120] X. Ming, F. Lu, H. Liu, M. Chen, L. Wang, Formation and characterization of ZnO : Tm^+optical waveguides fabricated by $Tm^+$and O^+ion implantation, J. Phys. D. Appl. Phys. 42 (2009) 165303. https://doi.org/10.1088/0022-3727/42/16/165303.

[121] D.-L. Zhang, Q.-Z. Yang, P.-R. Hua, H.-L. Liu, Y.-M. Cui, L. Sun, Y.-H. Xu, E.Y.-B. Pun, Sellmeier equation for doubly Er/Mg-doped congruent $LiNbO_3$ crystals, J. Opt. Soc. Am. B. 26 (2009) 620–626. https://doi.org/10.1364/JOSAB.26.000620.

[122] G.J. Edwards, M. Lawrence, A temperature-dependent dispersion equation for congruently grown lithium niobate, Opt. Quantum Electron. 16 (1984) 373–375. https://doi.org/10.1007/BF00620081.

[123] H.Y. Shen, X.L. Meng, G. Zhang, J.J. Qin, W. Liu, L. Zhu, C.H. Huang, L.X. Huang, M. Wei, Sellmeier's equation and the expression of the thermal refractive-index coefficient for a $Nd_{0.007}Gd_{0.993}VO_4$ crystal, Appl. Opt. 43 (2004) 955–960. https://doi.org/10.1364/AO.43.000955.

[124] W.M. Dean, Instrumental Methods of Analysis, D.Van Nostrad publications, Toronto, 1974.

[125] M. Fox, Optical Properties of Solids, Oxford University Press, 2010.

[126] J. C. Tauc, Optical Properties of Solids, North-Holland, Amsterdam, 1978.

[127] . M. Soharab, I. Bhaumik, R. Bhatt, A. Saxena, A.K. Karnal, S. Satapathy, and P.K. Gupta, Effect of Yb concentration on the optical properties of Yb:YVO_4 single crystal grown by optical floating zone technique, Kiran. 24 (2013) 30.

[128] R. Bhatt, I. Bhaumik, S. Ganesamoorthy, A.K. Karnal, M.K. Swami, H.S. Patel, P.K. Gupta, Urbach tail and bandgap analysis in near stoichiometric $LiNbO_3$ crystals, Phys. Status Solidi. 209 (2012) 176–180. https://doi.org/10.1002/pssa.201127361.

[129] R. Bhatt, S. Ganesamoorthy, I. Bhaumik, A.K. Karnal, P.K. Gupta, Optical bandgap and electrical conductivity studies on near stoichiometric $LiNbO_3$ crystals prepared by VTE process, J. Phys. Chem. Solids. 73 (2012) 257–261. https://doi.org/https://doi.org/10.1016/j.jpcs.2011.10.033.

[130] D.M.J. and T.L. Hazlett, Biophysical and Biochemical Aspects of Fluorescence Spectroscopy, Plenum Press, New York, 1991.

[131] T. Henningsen, N.B. Singh, Crystal characterization by use of birefringence interferometry, J. Cryst. Growth. 96 (1989) 114–118. https://doi.org/https://doi.org/10.1016/0022-0248(89)90281-9.

[132] R. Bhatt, S. Ganesamoorthy, I. Bhaumik, A. Sexana, A.K. Karnal, P.K. Gupta, J. George, K. Ranganathan, Photorefractive properties of Fe, Zn co-doped near stoichiometric $LiNbO_3$ crystals at moderate intensities (0.5–6W/cm^2), Opt. Laser Technol. 50 (2013) 112–117. https://doi.org/https://doi.org/10.1016/j.optlastec.2013.02.019.

[133] M.J. Weber, Probabilities for Radiative and Nonradiative Decay of Er^{3+} in LaF_3, Phys. Rev. 157 (1967) 262–272. https://doi.org/10.1103/PhysRev.157.262.

[134] W.T. Carnall, P.R. Fields, K. Rajnak, Spectral Intensities of the Trivalent Lanthanides and Actinides in Solution. II. Pm^{3+}, Sm^{3+}, Eu^{3+}, Gd^{3+}, Tb^{3+}, Dy^{3+}, and Ho^{3+}, J. Chem. Phys. 49 (1968) 4412–4423. https://doi.org/10.1063/1.1669892.

[135] O.F. Bartolo, Baldassare Di, Advances in Spectroscopy for Lasers and Sensing, Department of PhysicsBoston College Chestnut HillUSA, 2006. https://doi.org/https://doi.org/10.1007/1-4020-4789-4.

[136] W. Krupke, Induced-emission cross sections in neodymium laser glasses, IEEE J. Quantum Electron. 10 (1974) 450–457. https://doi.org/10.1109/JQE.1974.1068162.

[137] L. Zundu, C. Xueyuan, Z. Tingjie, Judd-Ofelt parameter analysis of rare earth anisotropic crystals by three perpendicular unpolarized absorption measurements, Opt. Commun. 134 (1997) 415–422. https://doi.org/https://doi.org/10.1016/S0030-4018(96)00386-0.

[138] M. Soharab, I. Bhaumik, R. Bhatt, A. Saxena, A.K. Karnal, Effect of Yb co-doping on the spectral properties of Er:YVO_4 single crystal: A Judd Ofelt analysis, J. Lumin. 200 (2018) 280–286. https://doi.org/https://doi.org/10.1016/j.jlumin.2018.03.050.

[139] M. Soharab, I. Bhaumik, R. Bhatt, A. Saxena, S. Khan, U.K. Goutam, A.K. Karnal, Investigation of optical and spectroscopic properties of Nd co-doped Yb:YVO_4 single crystals grown by OFZ method, J. Lumin. 231 (2021) 117736. https://doi.org/https://doi.org/10.1016/j.jlumin.2020.117736.

[140] M. Soharab, I. Bhaumik, R. Bhatt, A. Saxena, S. Khan, A. Sagdeo, A.K. Karnal, Growth and optical investigation of Nd co-doped Yb:YVO_4 crystal: A promising material for laser gain medium, Opt. Mater. (Amst). 109 (2020) 110183. https://doi.org/https://doi.org/10.1016/j.optmat.2020.110183.

[141] M. Soharab, I. Bhaumik, R. Bhatt, A. Saxena, A.K. Karnal, P.K. Gupta, Effect of Yb doping on the refractive index and thermo-optic coefficient of YVO_4 single crystals, Appl. Opt. 56 (2017) 1682–1688. https://doi.org/10.1364/AO.56.001682.

[142] M. Soharab, I. Bhaumik, R. Bhatt, A. Saxena, A.K. Karnal, A.J. Singh, S.K. Sharma, C. Mukherjee, K. Rajiv, M.P. Kamath, Fabrication of “a-cut” laser element from in-house grown Nd doped $GdVO_4$ crystals and demonstration of lasing, AIP Conf. Proc. 2265 (2020) 30416. https://doi.org/10.1063/5.0018467.

[143] M. Soharab, I. Bhaumik, R. Bhatt, A. Saxena, S. Khan, A.K. Karnal, Spectroscopic properties and Judd-Ofelt analysis of Nd doped $GdVO_4$ single

crystals grown by OFZ method, Opt. Mater. (Amst). 92 (2019) 379–385. https://doi.org/https://doi.org/10.1016/j.optmat.2019.04.059.

[144] M. Soharab, I. Bhaumik, R. Bhatt, A. Saxena, A.K. Karnal, Effect of Nd doping on the refractive index and thermo-optic coefficient of $GdVO_4$ single crystals, Appl. Phys. B. 125 (2019) 84. https://doi.org/10.1007/s00340-019-7194-z.

[145] www.webelements.com and the references there in., (n.d.).

[146] Optical Spectroscopy of Inorganic Solids, J. Mod. Opt. 37 (1990) 1688. https://doi.org/10.1080/09500349014551901.

[147] M.F. Reid, Electronic Structure and Transition Intensities in Rare-Earth Materials, University of Canterbury Christchurch New Zealand, Department of Physics and Astronomy University of Canterbury Christchurch New Zealand, 2019. https://doi.org/http://www2.phys.canterbury.ac.nz/~mfr24/.

[148] J. Cardin, D. Leduc, Determination of refractive index, thickness, and the optical losses of thin films from prism-film coupling measurements, Appl. Opt. 47 (2008) 894–900. https://doi.org/10.1364/AO.47.000894.

[149] C.W. Teng, J.F. Muth, Ü. Özgür, M.J. Bergmann, H.O. Everitt, A.K. Sharma, C. Jin, J. Narayan, Refractive indices and absorption coefficients of $Mg_xZn_{1-x}O$ alloys, Appl. Phys. Lett. 76 (2000) 979–981. https://doi.org/10.1063/1.125912.

[150] I.G. Kim, S. Takekawa, Y. Furukawa, M. Lee, K. Kitamura, Growth of $Li_xTa_{1-x}O_3$ single crystals and their optical properties, J. Cryst. Growth. 229 (2001) 243–247. https://doi.org/https://doi.org/10.1016/S0022-0248(01)01131-9.

[151] A.J. Bosman, E.E. Havinga, Temperature Dependence of Dielectric Constants of Cubic Ionic Compounds, Phys. Rev. 129 (1963) 1593–1600. https://doi.org/10.1103/PhysRev.129.1593.

[152] P.H. and L. Avrami, Some physics of the Grüneisen parameter, 1972.

[153] Y.K. Kshetri, C. Regmi, H.-S. Kim, S.W. Lee, T.-H. Kim, Microwave hydrothermal synthesis and upconversion properties of Yb^{3+}/Er^{3+} doped YVO_4 nanoparticles, Nanotechnology. 29 (2018) 204004. https://doi.org/10.1088/1361-6528/aab2bf.

[154] A. Szczeszak, M. Runowski, R.J. Wiglusz, T. Grzyb, S. Lis, Up-conversion green emission of Yb^{3+}/Er_{3+} ions doped YVO_4 nanocrystals obtained via modified Pechini's method, Opt. Mater. (Amst). 74 (2017) 128–134. https://doi.org/https://doi.org/10.1016/j.optmat.2017.03.032.

[155] E.P. Perkin, Elmer, Handbook of X-Ray Photoelectron Spectroscopy, 1979.

[156] M. Kruczek, E. Talik, H. Sakowska, W. Szyrski, Z. Ujma, D. Skrzypek, XPS investigations of YVO_4: Tm,Yb single crystal, J. Cryst. Growth. 275 (2005) e1715–e1720. https://doi.org/https://doi.org/10.1016/j.jcrysgro.2004.11.250.

[157] I. Bhaumik, S. Ganesamoorthy, R. Bhatt, A. Saxena, M. Soharab, A.K. Karnal, P.K. Gupta, Doped YVO_4 single crystals: Growth issues in the OFZ technique and investigation of spectroscopic properties, AIP Conf. Proc. 1591 (2014) 18–23. https://doi.org/10.1063/1.4872475.

[158] H.R. Xia, L.X. Li, H.J. Zhang, X.L. Meng, L. Zhu, Z.H. Yang, X.S. Liu, J.Y. Wang, Raman spectra and laser properties of Yb-doped yttrium orthovanadate crystals, J. Appl. Phys. 87 (1999) 269–273. https://doi.org/10.1063/1.371855.

[159] L. Qin, X. Meng, J. Zhang, L. Zhu, H. Zhang, B. Xu, H. Jiang, Growth and defects of Nd:$GdVO_4$ single crystal, J. Cryst. Growth. 242 (2002) 183–188. https://doi.org/https://doi.org/10.1016/S0022-0248(02)01371-4.

[160] M. Zhu, W. Liu, T. Zhang, Calculation of electron wave functions and refractive index of Ne, Sci. China Ser. G Physics, Mech. Astron. 51 (2008) 1489–1495. https://doi.org/10.1007/s11433-008-0158-7.

[161] L.J. Qin, X.L. Meng, H.Y. Shen, L. Zhu, B.C. Xu, L.X. Huang, H.R. Xia, P. Zhao, G. Zheng, Thermal conductivity and refractive indices of Nd:$GdVO_4$ crystals, Cryst. Res. Technol. 38 (2003) 793–797. https://doi.org/https://doi.org/10.1002/crat.200310097.

[162] D.E. Zelmon, J.M. Northridge, J.J. Lee, K.M. Currin, D. Perlov, Optical properties of Nd-doped rare-earth vanadates, Appl. Opt. 49 (2010) 4973–4978. https://doi.org/10.1364/AO.49.004973.

[163] P.K. Mukhopadhyay, A. Nautiyal, P.K. Gupta, K. Ranganathan, J. George, S.K. Sharma, T.P.S. Nathan, Experimental determination of the thermo-optic coefficient (dn/dT) and the effective stimulated emission cross-section (σe) of an a-axis cut 1.-at. % doped Nd:$GdVO_4$ crystal at 1.06 μm wavelength, Appl. Phys. B. 77 (2003) 81–87. https://doi.org/10.1007/s00340-003-1242-3.

[164] Y. Sato, T. Taira, Highly accurate interferometric evaluation of thermal expansion and dn/dT of optical materials, Opt. Mater. Express. 4 (2014) 876–888. https://doi.org/10.1364/OME.4.000876.

[165] R. Soulard, A. Zinoviev, J.L. Doualan, E. Ivakin, O. Antipov, R. Moncorgé, Detailed characterization of pump-induced refractive index changes observed in Nd:YVO_4, Nd:$GdVO_4$ and Nd:KGW, Opt. Express. 18 (2010) 1553–1568. https://doi.org/10.1364/OE.18.001553.

[166] M. Soharab, I. Bhaumik, R. Bhatt, A. Saxena, A.K. Karnal, Unusual absorption and emission characteristics of Cr co−doped Nd:GdVO4 laser gain crystal, J. Alloys Compd. 886 (2021) 161182. https://doi.org/https://doi.org/10.1016/j.jallcom.2021.161182.

[167] I. Bhaumik, M. Soharab, R. Bhatt, A. Saxena, K. Gupta, A.K. Karnal, Anomalous effect of growth ambience on the optical absorption characteristics of Cr-co-doped Nd:YVO_4 crystal, Appl. Phys. A. 125 (2019) 347. https://doi.org/10.1007/s00339-019-2637-2.

[168] D. Millers, H.M. Yochum, V. Pankratov, P. Potera, L. Grigorjeva, Transient and near-edge absorption in YVO_4 crystals, Phys. Status Solidi C. 4 (2007) 1155–1158. https://doi.org/https://doi.org/10.1002/pssc.200673835.

[169] M.F. Hazenkamp, A.C. Stückl, E. Cavalli, H.U. Güdel, Optical Spectroscopy and Density Functional Calculations of Chromium(V)-Doped YVO_4 and YPO_4: Influence of the Second Coordination Sphere, Inorg. Chem. 39 (2000) 251–254. https://doi.org/10.1021/ic990949q.

[170] Y. Nobe, H. Takashima, T. Katsumata, Decoloration of yttrium orthovanadate laser host crystals by annealing, Opt. Lett. 19 (1994) 1216–1218. https://doi.org/10.1364/OL.19.001216.

Annexure-I

1. Introduction to Judd-Ofelt Theory

Judd-Ofelt theory describes the line strengths or intensities of lanthanide as well as the actinide transitions in solid materials and solutions. In the year 1962, two identical formulations of a theory on transition of rare earth ions doped solids, in the literature were described simultaneously as well as independently namely one by Brian R. Judd at the University of California at Berkeley and the other by a Ph.D. student, George S. Ofelt, at the Johns Hopkins University in Baltimore. Although there are small differences in these two formulations but their approach, assumptions and final-results are more likely similar. These two formulations were published originally by Judd and Ofelt and theory is known as the Judd-Ofelt theory for the intensities of rare earth ions. J.H. Van Vleck published an article titled "The Puzzle of Rare-Earth Spectra in Solids" in 1937 and called it a puzzle because the rare earths showed sharp spectral lines of the transitions. These sharp spectral features are expected due to the various transitions between the $4f$ electronic shell of the rare earth ion. The f - f transitions of rare earth ions are generally forbidden by the Laporte selection rule of transitions, which tells that the states or wave functions of active ions having even parity are linked with the electric dipole (ED) transitions only with states of odd parity of the state, and similarly the odd states are connected with even ones only. The electric dipole transitions are forbidden for transitions within the $4f$ shell of rare earth ion, but the magnetic dipole (MD) and electric quadrupole (EQP) transitions are allowed by Laporte selection rule. The terms forbidden and allowed for particular transitions are not strictly accurate. The presence of relatively strong intensities and sharp spectral features of rare earth spectra are due to the following possibilities:

1. $4f$ to 5d transitions.
2. Magnetic dipole (MD) or electric quadrupole transitions (EQP).
3. Electric dipole transitions (ED).

The magnetic dipole transitions are considerably strong for some particular transitions and gives strong contribution in the intensity. Quadrupole transitions give its contributions for all the transitions, but EQP transitions are too weak and give very less contributions in the observed intensities. Only ED transitions give the strong contribution in the observed intensity but ED transitions is not allowed by Laporte

selection rule. The allowed solution of ED transitions of rare earth ions can be described with significant distortion of the electronic wave functions by crystalline fields in solids and this effect can be observed for particular crystalline fields or symmetry of site. The crystalline field must be noncentrosymmetric so that the even wave functions can mix with odd parity and odd wave functions with even parity.

The odd-order terms of the crystalline field do the change of parity of states, the odd-order terms can be expressed as a power series of the displacement from equilibrium of elections, in the perturbations. The above terms vanish for a central field or centrosymmetric materials, and does not change the parity of states. The coupling between odd and even states can be forced by the odd-order terms of a noncentral crystalline field, which results in the mixed parity states and moderates the Laporte's rule.

An active ion in a solid (crystalline and amorphous) can be considered as an impurity ion, which is embedded in a solid host material and usually found in small quantities. The impurity ions replace ions of the host substitutionally and form optically active centers. The host lattice shows an important role for determining the nature of the observed spectra of the optically active ions. The theory for calculation of wave-functions of the active ion is known as Ligand field theory or crystal field theory for the ordered periodic lattice.

The impurities or dopant ions are transition metal or lanthanide series ions which have been characterized by unfilled shells in the interior of the active ion. All lanthanide ions are characterized by a Xe core, an unfilled $4f$ shell, and the outer shells of $4f$ are screened by other shells from outside perturbing influences. This screening effect upto some level protects the optically active electrons from the influence of the crystal field and provides characteristic sharp and well defined spectral features of the lanthanides. In the case of transition metals, which have unfilled 3d shell and is not well screened due to presence of only a single outer shell. Therefore, the transition metals shows broad and undefined features of spectral line.

Hence, the crystal field plays a very important role to the features of optical spectra of active ion and also plays an observable role in the Stark effect regarding the splitting of energy levels of ions in solids. The crystalline field or ligand field is totally external to

the optically active dopant ion and is determined by the symmetry and chemical composition of the host.

In the ionic crystals, the optically active ions feel the repulsion to crystal host ions via electrons, and an attraction with nuclei of the crystal host. These influences of crystal host can be considered as a net electric field, which act on the active ions and known as the crystalline field.

The crystalline field plays a fundamental role for making many laser transitions possible in the laser host gain medium. To find out the maximum extension of energy levels splitting as well as the number of energy levels generation by the crystal field, let us consider the free ion Hamiltonian;

$$H_F = -\frac{\hbar^2}{2m}\sum_{i=1}^{N}\nabla_i^2 - \sum_{i=1}^{N}\frac{e^2}{r_i} + \sum_{i<j}^{N}\frac{Ze^2}{r_{ij}} + \sum_{i=1}^{N}\xi(r_i)(s_i.l_i) \quad \ldots\ldots\ldots\ldots\ldots\ldots.(A.1)$$

In the above equation (A.1) the first term gives the sum of the kinetic energies of all the electrons of a 4f ion. The second term provides the potential energy of all the electrons in the field of the nucleus. The third term represents the repulsive Coulomb potential of the interactions between pairs of electrons. The last term denotes the spin-orbit interaction, which accounts for coupling between the spin angular momentum and the orbital angular momentum.

According to the central field approximation, each electron of active ion is assumed to be moving independently in the field of the nucleus and in a spherically averaged potential of all the electrons. The Coulomb interaction of electrons generates different spin and orbital angular momentum (SL) terms with different energies, but these interactions do not effect on the total angular momentum (J) of the electrons. Simply we can say that the spin-orbit interaction allows only coupling between states of different SL (spin and orbital angular momentum) and not on the total angular momentum. In other words we can say that the Coulomb interaction removes degeneracy in S and L and the spin orbit interaction removes degeneracy in J. The degeneracy in M_J remains. This can be only removed by the crystal field or ligand field. Therefore, the free atom provides the spherical symmetry and each levels have 2J+1 degeneracy. When the active ion is placed in a crystal environment and non-centrosymmetric site then each level lifts their detergency under the influence of the

crystal field. In fact, the spherical symmetry is reduced to the point symmetry at the ion site. The degree of removing 2J+1 degeneracy, depends on the point symmetry of the surrounding ions. The perturbed total Hamiltonian for an active ions in a crystal field can be written as

$$H_T = H_F + V_{CF} \dots\dots\dots\dots\dots\dots (A.2)$$

where V_{CF} is Hamiltonian of the perturbation by crystal field and is potential energy created by the crystalline environment of host ions around the active ion. The eigen functions of free atom possess complete spherical symmetry and their Hamiltonian can be expressed in terms of spherical harmonics. Therefore, the perturbation Hamiltonian V_{CF} can be written in terms of spherical harmonics:

$$V_{CF} = \sum_{Kq} A_{kq} \sum_i r_i^k Y_{kq}(\vartheta_i, \varphi_i) \dots\dots\dots\dots\dots\dots (A.3)$$

$$H_F = -\frac{\hbar^2}{2m}\sum_{i=1}^{N} \nabla_i^2 - \sum_{i=1}^{N} \frac{e^2}{r_i} + \sum_{i<j}^{N} \frac{Ze^2}{r_{ij}} + \sum_{i=1}^{N} \xi(r_i)(s_i . l_i) + \sum_{Kq} A_{kq} \sum_i r_i^k Y_{kq}(\vartheta_i, \varphi_i) \dots\dots (A.4)$$

The summation "i" has been taken for all the electrons of the ion of interest in the equation (A.4). The A_{kq} term represents the structural q parameters in the static crystal field expansion and depends only on the crystal host. This term can be calculated in a point charges lattice by using crystallographic data and charges of the host lattice. In the point charge model it has to assumed that the all the charges of the host lattice act as a point charges. For the calculation of matrix elements $\langle \alpha | V_{CF} | \beta \rangle$, their resultant matrix elements in the form of $\langle nl | r^k | nl \rangle$ represents the average value of $\langle r^k \rangle$.This term corresponds to lifting of Stark levels. The term A_{kq} can be expressed as:

$$B_{kq} = A_{q_e} \langle r^k \rangle \dots\dots\dots\dots\dots\dots (A.5)$$

Further, if the initial and final wave function of active ion have the same parity, then value of k must be even and otherwise value of k must be odd for opposite parity of initial and final wave function. If both conditions are not satisfied then the matrix

elements of V_{CF} will be zero. Therefore, if an operator of rank k of a matrix element are connected with angular momenta ℓ and ℓ' then the triangle condition, $\ell + \ell' \geq k \geq |\ell - \ell'|$, must be hold. The 4f electrons of rare earth ion have $\ell = \ell' = 3$, and therefore the value of k must be even for allowed transitions within the f^n shell. The k value is limited to k = 0, 2, 4, 6. Further, if eigen function of the f^n shell of rare earth are connected with opposite parity states of higher lying configurations for example $4f^{(n-1)}5d$, then $\ell = 3$ and $\ell' = 2$. Now for this condition the value of k should be odd and is limited to k = 1, 3, 5. These odd-order terms show an important role in the Judd-Ofelt theory for the calculation of forced electric dipole transitions intensity in lanthanide and actinide ions in solids. The values for k and q also depend on the point symmetry of the ion and are limited. Hence, nonzero terms in the perturb Hamiltonian depends on the point symmetry of active ion.

The Hamiltonian of active ion must be invariant under operations of the point symmetry group. Therefore, the crystal field must also show the same symmetry as the point symmetry of the active ion, which is also part of the total Hamiltonian.

The value corresponding to k = 0 and q = 0 indicates the spherically symmetry and affects all energy levels in the same manner and results in an uniform shift of all energy levels in the configuration.

2. Principles of Judd-Ofelt Theory

The Judd-Ofelt theory is based on three approximations namely the static, free-ion and single configuration approximations. The first approximation called the static model says that the active or central ions are affected by the surrounding host ions through a static electric field. The static electric flied interaction between active ion and host are called as the ligand or crystal field. The second approximation called the free-ion model says that the host ions produce static crystal field on the active ions, and acts as a perturbation on the free-ion Hamiltonian of active ion. Third approximations called the single configuration model says that the electron-electrons interactions are neglected. Judd-Ofelt theory provides a theoretical expression for the line strength of transition of rare earth ion and is given as

$$S_{J\to J'} = \sum_{i=2,4,6} \Omega_i \left|\langle [S\ L], J \| U^i \| [S'\ L'], J' \rangle\right|^2 \ldots\ldots\ldots\ldots\ldots\ldots (A.6)$$

where Ω_λ corresponds to the Judd-Ofelt parameters. The bracket terms represent the doubly reduced matrix elements for intermediate coupling approximations. The intermediate coupling approximations states that the interaction of mutual repulsion between 4f electrons of rare earth ion is of the same order of magnitude of the spin-orbit coupling. The above effect can be be used for expanding the wave-functions of the $4f$ states in a linear combination of Russel-Saunders, or LS-coupled states. Further, the full intermediate coupled wave-functions $\langle f^n|SL|f^n\rangle$ and the coupling coefficients can be obtained by diagonalizing the combined electrostatic, spin orbit and configuration interaction energy matrices. In case of free ions, the electric dipole transitions are forbidden within the $4f$ shell of lanthanide ions. If opposite parity states from higher lying configurations outside the $4f$ shell are mixed into the upper state, then forbidden electric dipole transitions get modified and become allowed and are called as forced electric dipole transitions. The above phenomenon happen, when the active ions are situated in a non-centrosymmetric site of the perturbing crystal field of a host lattice. However, for a central field or centrosymmetric materials the transition is not allowed and the Hamiltonian of the system is invariant under coordinate inversion, and the wave function retain definite parity. The odd-order terms of the crystal field, can be expanded in a series of spherical harmonics. This perturbs the system and produces mixed parity states because of which the electric dipole transitions become allowed. Now considering crystal field as a first-order perturbation by is, then the initial $\langle\psi_a|$ and final mixed parity states $|\psi_b\rangle$ of rare earth ion can be written as

$$\langle\psi_a| = \langle\varphi_a| + \sum_\beta \frac{\langle\varphi_a|V_{CF}|\varphi_\beta\rangle}{E_a - E_\beta} \langle\varphi_\beta| \dots\dots\dots\dots\dots\dots (A.7)$$

$$|\psi_b\rangle = |\varphi_b\rangle + \sum_\beta \frac{\langle\varphi_\beta|V_{CF}|\varphi_b\rangle}{E_b - E_\beta} |\varphi_\beta\rangle \dots\dots\dots\dots\dots\dots (A.8)$$

where $\langle\psi_a|$ |and $|\psi_a\rangle$, are the initial and final states of single parity. The $|\varphi_\beta\rangle$ are states of higher β energy having opposite parity configurations. The electric dipole matrix elements can written as,

$$D = \langle\psi_a|P|\psi_b\rangle \dots\dots\dots\dots\dots\dots (A.9)$$

where P denotes the electric dipole (ED) operator and given by,

$$P = -e\sum_i r_i \dots\dots\dots\dots\dots\dots (A.10)$$

$$D = \langle \psi_a | P | \psi_b \rangle$$

$$= \sum_{\beta} \left[\frac{\langle \varphi_a | V_{CF} | \varphi_\beta \rangle \langle \varphi_\beta | P | \varphi_b \rangle}{E_a - E_\beta} + \frac{\langle \varphi_a | P | \varphi_\beta \rangle \langle \varphi_\beta | V_{CF} | \varphi_b \rangle}{E_b - E_\beta} \right] \ldots\ldots\ldots\ldots\ldots (A.11)$$

It is suitable to introduce the tensor forms of the crystal field and ED operator because these operators can be easily combined into a single effective tensor operator. The crystal field and ED operators can be written in the tensor operator forms as:

$$D_q^{(1)} = \sum_i r_i \left[C_q^{(1)} \right]_i \ldots\ldots\ldots\ldots\ldots (A.12)$$

$$D_p^{(t)} = \sum_{tp} A_{tp} \sum_i r_i^t \left[C_q^{(t)} \right]_i \ldots\ldots\ldots\ldots\ldots (A.13)$$

The $C_q^{(k)}$ are tensor operators that can be expressed in form of spherical harmonics

$$C_q^{(k)} = \left[\frac{4\pi}{2k+1} \right]^{1/2} Y_{kq} \ldots\ldots\ldots\ldots\ldots (A.14)$$

A couple of assumptions can now be made to simplify the problem:

1. The states of $|\varphi_\beta\rangle$ are completely degenerate in J.
2. The energy term in denominators are equal ($E_a - E_\beta = E_b - E_\beta$).

Once closure condition of wave function is applied then the angular parts of the crystal field $C_p^{(t)} = \langle \ell || C^t || \ell' \rangle U_Q^t$ and electric dipole operator $C_q^{(1)} = \langle \ell || C^1 || \ell' \rangle U_Q^1$ can be combined into an effective tensor operator such as,

$$U_q^{(1)} U_p^{(t)} = \sum_{\lambda Q} (-1)^{1+t+\lambda+Q} (2\lambda+1) \begin{Bmatrix} 1 & t & \lambda \\ l' & l & l'' \end{Bmatrix} \begin{pmatrix} 1 & t & \lambda \\ q & p & Q \end{pmatrix} U_Q^{(\lambda)} \ldots\ldots\ldots\ldots\ldots (A.15)$$

where Q = – (q + p), and λ = 1 + t. The 3j symbol ( ) corresponds to the coupling probability for two angular momenta. The 6j symbol { } corresponds to the coupling probability for 3 angular momenta. These notations are known as Wigner symbols. The Wigner 3j and 6j symbols represents Clebsch-Gordon coefficients. The above equation (A.15) can be further simplified by applying the Wigner-Eckart theorem:

$$\left\langle JM\left|U_Q^{(\lambda)}\right|J'M'\right\rangle = (-1)^{J-M}\begin{pmatrix} J & \lambda & J' \\ -M & Q & M' \end{pmatrix}\langle J||U^{(\lambda)}||J'\rangle \ldots\ldots\ldots\ldots\ldots (A.16)$$

$U^{(\lambda)}$ is the reduced matrix element. The complete solution can be written as

$$D = -e\sum_{tp}\sum_{\lambda Q}(-1)^{J-M-Q}\,(2\lambda + 1)\,A_{tp}Y(t,\lambda)\begin{pmatrix} 1 & t & \lambda \\ q & p & Q \end{pmatrix}\begin{pmatrix} J & \lambda & J' \\ -M & Q & M' \end{pmatrix}\langle \varphi_a||U^{(\lambda)}||J\varphi_b\rangle \ldots\ldots\ldots\ldots\ldots (A.17)$$

The $Y(t,\lambda)$ term is expressed as

$$Y(t,\lambda) = 2\sum_{nl}\frac{\langle 4f|r|nl\rangle\langle nl'|r'|4f\rangle}{\Delta E_{nl}}\langle \mathrm{f}||C^{(1)}||l\rangle\langle \mathrm{l}||C^{(t)}||f\rangle\begin{Bmatrix} 1 & t & \lambda \\ l' & l & l'' \end{Bmatrix} \ldots\ldots\ldots\ldots\ldots (A.18)$$

Where A_{tp} are parameters of the static crystal field expansion. The equation (A.17) and (A.18) provide the full solution of the Judd-Ofelt theory.

The form of equation (A.17) can be used to calculate electric dipole matrix elements between mixed parity states of individual Stark level transitions. ΔE_{nl} is the energy difference between the $4f$ and opposite parity, nl configuration.

The equation (A .17) and (A .18) is suitable for calculating transitions between individual Stark levels. However, initially Judd and Ofelt took interest in active ions embedded in the solution where individual Stark level transitions cannot be distinguished. Therefore, further they simplified the problem and derived the formula for manifold-to-manifold transitions, which is valid for active ions embedded in the crystals as well as glasses. Additional assumptions are needed further to simplify the problem:,

3. The ground manifold of all Stark energy levels are equally populated.

4. The host material is considered as optically isotropic.

For the quantitative analysis, the solution can be defined in the form of oscillator strength, which is basically the cross section of the particular transitions. These transitions are connected with multipole transitions and analogous to classical damped oscillators. The oscillator strength (f-number) or line strength for an electric dipole transition is well-defined as.

$$f = \frac{8\pi^2 mc}{h\bar{\lambda}e^2} n \left(\frac{n^2+2}{3n}\right)^2 \sum_{MM'} |\langle \alpha \mathrm{JM}||P||\alpha \mathrm{J'M'}\rangle|^2 \ldots\ldots\ldots\ldots\ldots (A.19)$$

The equation (A.17) can be simplified according the assumption three and it allows the sum to be carried out a sum over M and M′ Stark split levels.

$$\sum_{MM'} \begin{pmatrix} J & \lambda & J' \\ -M & Q & M' \end{pmatrix} \begin{pmatrix} J & \lambda' & J' \\ -M & Q' & M' \end{pmatrix} = \frac{1}{2\lambda+1} \delta_{\lambda\,\lambda'} \delta_{Q\,Q'} \ldots\ldots\ldots\ldots (A.20)$$

The equation (A.17) can be simplified according the assumption four and it allows the sum over q, the polarization term.

$$\sum_{q} \begin{pmatrix} 1 & t & \lambda \\ q & p & Q \end{pmatrix} \begin{pmatrix} 1 & t' & \lambda \\ q & p' & Q \end{pmatrix} = \frac{1}{2t+1} \delta_{t\,t'} \delta_{pp'} \ldots\ldots\ldots\ldots (A.21)$$

Where q=0, ±1 for different state of polarizations.

Now the equation (A.19) can written as

$$f = \frac{8\pi^2 mc}{3h\bar{\lambda}e^2(2J+1)} n \left(\frac{n^2+2}{3n}\right)^2 \sum_{\lambda=2,4,6} \sum_{p} \sum_{t=1,3,5} (2\lambda + 1) \frac{|A_{tp}|^2}{2t+1} Y^2(t,\lambda) \left|\langle \varphi_a || U^{(\lambda)} || \varphi_b \rangle\right|^2 \ldots\ldots\ldots\ldots\ldots (A.22)$$

The Judd-Ofelt parameters can be defined as

$$\Omega_\lambda = \sum_{p} \sum_{t=1,3,5} (2\lambda+1) \frac{|A_{tp}|^2}{2t+1} Y^2(t,\lambda) \ldots\ldots\ldots\ldots\ldots (A.23)$$

The Ω_λ, therefore, contain of odd-order parameters of the crystal field, radial integrals over wave functions of the $4f^n$ and perturbing, opposite parity wave functions of higher energy, and energies separating these states in terms of perturbation energy denominators. The oscillator strength can be written as

$$f = \frac{8\pi^2 mc}{3h\bar{\lambda}e^2(2J+1)} n \left(\frac{n^2+2}{3n}\right)^2 \sum_{\lambda=2,4,6} \Omega_\lambda \left|\langle \varphi_a || U^{(\lambda)} || \varphi_b \rangle\right|^2 \ldots\ldots\ldots\ldots\ldots (A.24)$$

The summation over λ is known as the line strength. This is the approximate solution of the Judd-Ofelt theory, which is used to find the ED matrix elements between mixed parity states for manifold-to-manifold transitions.

3. Methodology of Judd-Ofelt Theory for calculation of spectral parameters

Judd-Ofelt theory can be used for the calculation of manifold to manifold transition probabilities for absorption and emission lines of active ion. Also the radiative lifetimes and branching ratios of various emission line of active ion can be determined. The accurate absorption measurements specifically the integrated absorption cross section over the wavelength range of a number of manifolds are necessary for a Judd-Ofelt analysis. The line-strength, S_m can be calculated from the integrated absorption cross section using following formula,

$$S_m = \frac{\int \alpha(\lambda) d\lambda}{\frac{8\pi^3 \rho \bar{\lambda} e^2}{9ch(2J+1)}\left[\frac{(n^2+2)^2}{3n}\right]} \quad \ldots\ldots\ldots\ldots\ldots (A.25)$$

where J denotes the total angular momentum of the initial ground manifold, can be found from the $^{2S+1}L_J$ designation. σ(λ) represents the absorption cross section as a function of wavelength. The mean wavelength λ, can be calculated by the first moment of the absorption cross section data.

Judd-Ofelt theory is used to determine a set of phenomenological parameters, Ω_λ (λ = 2, 4, 6), by using the equation (A.25), which is fitted with the experimental optical absorption, and equation (A.6). This can be done most efficiently by a least squares fitting method in the following way

$$S'_J = \sum_{i=1}^{3} M_{ij}\, \Omega_{\lambda j} \quad \ldots\ldots\ldots\ldots\ldots (A.26)$$

Where, M_{ij} represents the components of a N x 3 matrix for the square matrix elements of $U^{(2)}$,$U^{(4)}$ and $U^{(6)}$. The Ω_κ denotes components of a 1 x 3 matrix for the Judd-Ofelt parameters (Ω_2, Ω_4 and Ω_6). N is the number of total transitions to fit and it is decided by the number of measured absorption manifolds. There are only three Judd-Ofelt parameters then N should be equal or more than 3. Now the sum of the squared difference of both line strengths for minimization is given as below

$$\sigma^2 = \sum_{j=1}^{N} \left| S_j^m - \sum_{i=1}^{3} M_{ij}\, \Omega_{\lambda j} \right|^2 \quad \ldots\ldots\ldots\ldots\ldots (A.26)$$

Now take the derivative with respect to Ω for minimization and become equal to zero.

$$\frac{\partial \sigma^2}{\partial \Omega_k} = -2 \sum_{j=1}^{N} M_{ik} \left(S_j^m - \sum_{i=1}^{3} M_{ij}\, \Omega_{\lambda j} \right) = 0 \ldots\ldots\ldots\ldots\ldots (A.26)$$

The set of Judd-Ofelt parameters, which minimize the sum of the squared difference between the measured and theoretical line strength, can be obtained. The matrix form of it can be written as, $\Omega^{(0)} = (M^{\dagger}M)^{-1}M$, where $M^{\dagger}$ is the adjoint of M. The large number of calculations are required for obtaining the parameters, therefore be computer based calculations has been done. Once the Judd-Ofelt parameters are calculated by computer based programmed, then it can be used to estimate transition probabilities, A(J; J′), of all excited states from the following equation,

$$A(J \to J') = \frac{64\pi^4 e^2}{3h(2J+1)\bar{\lambda}^3} \left(\left[\frac{n(n^2+2)^2}{9} \right] \sum_{i=2,4,6} \Omega_i \left| \langle [S\ L], J \| U^i \| [S'L'], J' \rangle \right|^2 + n^2 S_{MD} \right) \ldots\ldots\ldots\ldots\ldots (A.27)$$

$$S_{ED} = \left[\frac{n(n^2+2)^2}{9} \right] \sum_{i=2,4,6} \Omega_i \left| \langle [S\ L], J \| U^i \| [S'L'], J' \rangle \right|^2 \ldots\ldots\ldots\ldots\ldots (A.28)$$

where n denotes the refractive index of the solid, S_{ED} and S_{MD} represent the electric and magnetic dipole line strengths respectively. J′ symbol describes the total angular momentum of the upper excited state of rare earth ions. Electric dipole line strengths, (S_{ED}) from each excited manifold to all lower lying manifolds are calculated using equations (A. 6), matrix elements ($U^{(\lambda)}$) and Judd-Ofelt parameters.

Magnetic dipole (MD) transition are generally found to smaller orders of magnitude to that the electric dipole (ED) transitions for free ions, but the electric dipole (ED) transitions becomes allowed for active ions in solids as a result of a crystals field perturbation. Therefore, S_{ED} intensities are much smaller to the free ions. In the particular ion sometimes, the magnetic dipole transitions make substantial contributions to the observed intensities of active ion.

Now, the equation for calculation of the radiative lifetimes, τ_r, and the branching ratio, β is given by,

$$\tau = \frac{1}{\sum A(J \rightarrow J')} \qquad \ldots\ldots\ldots\ldots\ldots (A.29)$$

$$\beta(J \rightarrow J') = \frac{A(J \rightarrow J')}{\sum A(J \rightarrow J')} \qquad \ldots\ldots\ldots\ldots\ldots (A.30)$$

Further, the emission cross-sections for the particular manifold-to-manifold transition of rare earth ion are also estimated as per following formula.

$$\sigma_e(\lambda) = \frac{\bar{\lambda}^4}{8\pi n^2 c \Delta\lambda_{eff}} A(J \rightarrow J') \qquad \ldots\ldots\ldots\ldots\ldots\ldots\ldots\ldots\ldots\ldots (A.31)$$

$$\Delta\lambda_{eff} = \frac{\int I(\lambda) d\lambda}{I_{max}} \qquad \ldots\ldots\ldots\ldots\ldots\ldots\ldots\ldots\ldots\ldots (A.32)$$

The whole procedure of a Judd-Ofelt analysis for spectral parameters can be represented by simple flow chart.

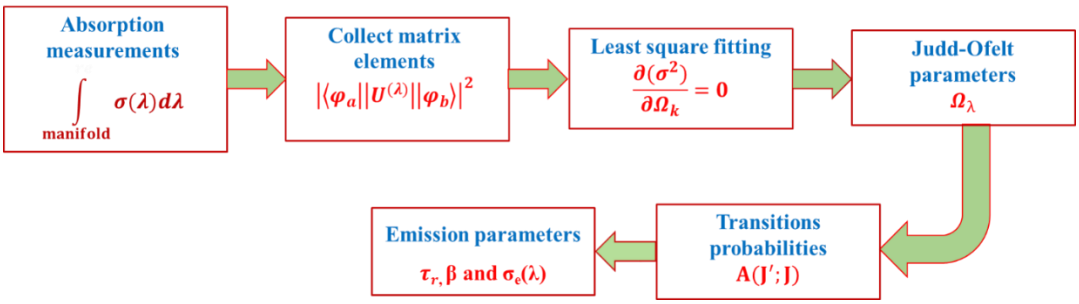

References

1. Van Vleck, J. H. The puzzle of rare earth spectra in solids, J. Phys. Chem. 41 (1937) 67-80.
2. B.M. Walsh, Advances in Spectroscopy for Lasers and Sensing, Springer (2006) p. 403.
3. Judd, B.R. Optical absorption intensities of rare-earth ions, Phys. Rev. 127 (1962) 750-761.
4. Ofelt, G.S. Intensities of crystal spectra of rare-earth ions, J. Chem. Phys. 37 (1962) 511-520.
5. R.C. Powell, Physics of Solid State Laser Materials, Springer (1998).

6. Nielson, C.W. and Koster, G.F. Spectroscopic coefficients of the p^n, d^n,*and* f^n configurations, (1963) The M.I.T. Press, Cambridge.
7. Leavitt, R.P. and Morrison, C.A. Crystal-field analysis of triply ionized rare earth ions in lanthanum fluoride. II. Intensity calculations, J. Chem. Phys. 73 (1980) 749-757.

Annexure-II

MATLAB program for calculation of spectral parameters for Nd or Er ion using Judd-Ofelt theory.

In this section, MATLAB program written only for Nd ion to calculate the spectral parameters is described. MATLAB program is same for the calculation of the spectral parameters of Er ion, only difference is to change the matrix element, energy levels for Er ion and refractive index for corresponding the doped host materials.

A. Calculation of line strengths and Judd-Ofelt parameters

```
clear all
clc
c=3*10^10;
e=4.8032*10^(-10);
h=6.6262*10^(-27);
p=3.142;
C=(27*c*h)/(8*p^3*e^2);
w=0.808;%wavelength in um
x=808;%wavelength in nm

%%%%% Refractive index calculations for σ-polarization
no=sqrt(3.77834+ (0.069736 / (w^2 - 0.04724)) - 0.0108133*w^2);

% %%% or %%%%%
% %%% Refractive index calculations π-polarization

ne=sqrt(4.59905 +(0.110534 /(w^2 - 0.04813)) - 0.0122676*w^2);

N=0.992*10^20;%concentration/cc
J=9/2;% initial J value or ground state of Nd ion

%%%%%%% % integrated absorption calculations %%%%%%
Ab=133.76374; %integrated absorption for π or σ-polarization

%  %%%%%%%%%  experimentally  Line  strength  for  π or σ-polarization
%%%%%%%%%%%%%%%

Sm=(C*(2*J+1)*ne*Ab)/(N*x*((ne^2)+2)^2);

% %%%%%%%%% measured Line strength %%%%%%%%%%%%%

S=[Sm];% for all the transitions of Nd ions and make it as matrix
form/%%

% % % matrix element for calculation of JO parameters %%%%%%%
 U=[0.0000 0.0381 0.000;0.0010 0.0431 0.0361;0.0597 0.2180 0.0954;...
     0.8968 0.4049 0.0355;0.0010 0.0096 0.0381;...
     0.0010 0.0447 0.6603; 0.0101 0.2437 0.5169; 0 0.2299 0.0547];

%Judd Ofelt parameters X10^-20 for π or σ-polarization
disp('Judd-Ofelt Parameter X10^-20');
```

```
JOP=U\S;

AA=[JOP]*10^-20;
% % %    A=[12.629;4.828;8.425]* 10^-20;

% %%%%%%%% calculated Line strength %%%%%%%%%%%%%%

 UU=[0.0000 0.0381 0.000;0.0010 0.0431 0.0361;0.0597 0.2180 0.0954;...
     0.8968 0.4049 0.0355;0.0010 0.0096 0.0381;...
     0.0010 0.0447 0.6603; 0.0101 0.2437 0.5169; 0 0.2299 0.0547];

% %%%%%%%% UU is matrix elements of Nd ion %%%%%%%%%%%%%%

disp('S calulated')
Scal=UU*AA; % *10^20cm^2
Sscal= Scal*10^20;
% % %%%%%%%%%%%
%%%%%% error calculation %%%%%%
Line strength=[S  Sscal];

MM=S-Sscal;
Ms=[sqrt(sum(MM.^2)/n-1)]*10^-20; %%%%%% n is number transitions %%%%%%
```

B. Calculation of emission line strengths

```
clear all
clc
clear

% % % calculation of effective Judd-Ofelt parameters

 OmP=[10.4957; 6.7350; 7.8825]; % % % taken as example
 OmSig=[9.5331; 4.1574; 5.4806]; % % % taken as example

 OmegaEff=[[OmP]+2*[OmSig]]/3;

 AS=[OmegaEff]* 10^-20;

%%%% Estimation of emission spectral parameters %%%%

US=[0 0.2296 0.0563; 0 0.1423 0.4070; 0 0 0.2117; 0 0 0.0275];
%%%%% matrix element of emission of Nd ion

disp('S calculated for emission line')
Sem=US*AS;
disp('S for Nd   ---- at.% . %')

Scal_em=Sem*10^20 %%%%% Line strength of emission line of Nd ion%%
```

C. Calculation of radiative lifetime and branching ratio

```
clear
clc
```

```
clear all
c=3*10^10;
e=4.8032*10^(-10);
h=6.6261*10^(-27);
p=3.142;

x=1.064; %in um

w=1064; %in nm

% % calculated line strength of emission line of Nd ion

S=3.2455*10^(-20);

% % excited state of Nd ion from which emission occurs%%%

J=3/2; % % excited state J value %%%

 % % % Refractive index calculation %%%%%

ne=sqrt(4.59905 + (0.110534 / (x^2 - 0.04813)) - 0.0122676*x^2);


no=sqrt(3.77834+ (0.069736 / (x^2 - 0.04724)) - 0.0108133*x^2);

 % % % Average of refractive index calculation %%%%%

n=(ne+2*no)/3;


X1=(64*p^4*e^2*n1*(((n1^2)+2)^2)*S1)/(27*h*(2*J+1)*(w1*10^-7)^3);
```

Note: calculate for all transition from state $^4F_{3/2}$ and J=3/2

```
% Einstein A-coefficient %%%%%

AA=[X1;X2;X3;X4]
AT=X1+X2+X3+X4;

% Radiative life time %%%%%

Lifetime= (1/AT)*1000000 %(umsec)
```

D. Calculation of emission cross section

```
clear all
clc
clear
x=1.064; %in um
w=1064*10^-7; %in nm  %wavelength
p=3.142;
c=3*10^10;
W=[W1;W2;W3;W4]*10^-7; % emission Width for all the transitions

% % A coefficient taken as example
```

```
A1=[5.4997]*1000;
A2=[4.5163]*1000;
A3=[5.0743]*1000;
A4=[4.7065]*1000;

% % % Refractive index calculation %%%%%

no=sqrt(3.8357+(0.0725/(x1^2-0.0426))-0.0116*x1^2);
ne=sqrt(4.7038+(0.1032/(x1^2-0.06398))-0.01857*x1^2);

n=(ne+2*no)/3;

% % % calculation of emission cross section%%%%

L1=w1^4*A1;
L2=w1^4*A2;
L3=w1^4*A3;
L4=w1^4*A4;
M1=8*c*p*(n1^2);
M2=8*c*p*(n2^2);
M3=8*c*p*(n3^2);
M4=8*c*p*(n4^2);
N1=M1*W1;
N2=M2*W2;
N3=M3*W3;
N4=M4*W4;
C1=L1/N1;
C2=L2/N2;
C3=L3/N3;
C4=L4/N4;

% % % emission cross section is given as %%%%

Cross-section=[C1;C2;C3;C4]*10^19;
```